



**HAL**  
open science

# Photoswitchable fluorescence hysteresis based on multichromophoric architectures

Yang Zhou

► **To cite this version:**

Yang Zhou. Photoswitchable fluorescence hysteresis based on multichromophoric architectures. Other. Université Paris-Saclay, 2022. English. NNT : 2022UPASF039 . tel-04368487

**HAL Id: tel-04368487**

**<https://theses.hal.science/tel-04368487v1>**

Submitted on 1 Jan 2024

**HAL** is a multi-disciplinary open access archive for the deposit and dissemination of scientific research documents, whether they are published or not. The documents may come from teaching and research institutions in France or abroad, or from public or private research centers.

L'archive ouverte pluridisciplinaire **HAL**, est destinée au dépôt et à la diffusion de documents scientifiques de niveau recherche, publiés ou non, émanant des établissements d'enseignement et de recherche français ou étrangers, des laboratoires publics ou privés.

# Hystérésis de fluorescence photocommutable grâce à des architectures multichromophoriques

*Photoswitchable fluorescence hysteresis based on multichromophoric  
architectures*

**Thèse de doctorat de l'Université Paris-Saclay**

École doctorale n° 571 Sciences Chimiques : Molécules, Matériaux, Instrumentation et  
Biosystèmes (2MIB)  
Spécialité de doctorat : Chimie  
Graduate School : Chimie. Référent : ENS Paris-Saclay

Thèse préparée dans l'unité de recherche **PPSM (Université Paris-Saclay, ENS Paris-Saclay, CNRS)**, sous la direction de **Rémi MÉTIVIER**, directeur de recherche, la co-direction de **Joanne XIE**, professeur, le co-encadrement de **Stéphane MAISONNEUVE**, ingénieur de recherche

**Thèse soutenue à Gif-sur-Yvette, le 20 mai 2022, par**

**Yang ZHOU**

## Composition du Jury

<b>François MAUREL</b> Professeur, Université Paris Cité (Laboratoire ITODYS, CNRS 7086)	Président
<b>Martial BOGGIO-PASQUA</b> Directeur de Recherche, Université Paul Sabatier (Laboratoire LCPO, CNRS 5626)	Rapporteur
<b>Lucie NOREL</b> Maître de Conférences, Université de Rennes 1 (Laboratoire ISCR, CNRS 6226)	Rapporteur
<b>Christophe COUDRET</b> Directeur de Recherche, Université Paul Sabatier (Laboratoire IMRCP, CNRS 5623)	Examineur
<b>Isabelle LERAY</b> Directrice de Recherche, ENS Paris-Saclay (Laboratoire PPSM, CNRS 8531)	Examinatrice
<b>Rémi MÉTIVIER</b> Directeur de Recherche, ENS Paris-Saclay (Laboratoire PPSM, CNRS 8531)	Directeur de thèse
<b>Joanne XIE</b> Professeur, ENS Paris-Saclay (Laboratoire PPSM, CNRS 8531)	Co-directrice de thèse
<b>Stéphane MAISONNEUVE</b> Ingénieur de Recherche, ENS Paris-Saclay (Laboratoire PPSM, CNRS 8531)	Co-encadrant de thèse



# Acknowledgement

This dissertation is accomplished in the « Laboratoire de Photophysique et Photochimie Supramoléculaires et Macromoléculaires (PPSM) » in École Normale Supérieure Paris-Saclay (ENS Paris-Saclay), Université Paris-Saclay. I express my sincere gratitude to all the people for giving me the help and supports during the journey to finish the thesis.

First and foremost, I would like to express my gratitudes to my advisors, Dr. Rémi Métivier, Pr. Joanne Xie and Dr. Stéphane Maisonneuve. They offered me the opportunity to work at ENS de Cachan and latter relocated ENS Paris-Saclay and gave me the guidance from the spectroscopic and laboratory synthetic perspectives. We also spent a lot of time on private topics about every side of life here. And thank you Stéphane for translations of many of my troubles sometimes. I hope I have left a “good student” image to you all, maybe not so diligent, but smart.

As an important part of my collaboration in the project, I would like to thank Dr. Nicolò Baggi, Dr. Yu Pei and Dr. Anne Léaustic from Institut de Chimie Moléculaire et des Matériaux d'Orsay (ICMMO), Université Paris-Saclay. The diarylethene molecule synthesized by Dr. Baggi helps to accomplish the 4<sup>th</sup> chapter of the thesis. And we have good private relationship with each other, for example, taking the 1<sup>st</sup> injection of COVID-19 vaccines together in l'Orangerie au Château de Versailles.

I would like to express my gratitude to the project collaborator, as well as the president of the defense, Pr. François Maurel, for helping the theoretical perspectives and encouraging me in the simulation works. For this dissertation, I would like to thank all the committee members: Dr. Isabelle Leray, Dr. Lucie Norel, Dr. Martial Boggio-Pasqua, Dr. Stéphane Maisonneuve, Pr. Joanne Xie and Dr. Rémi Métivier.

I would like to thank all the faculty members and staff in PPSM: Pr. Keitaro Nakatani, Dr. Gilles Clavier, Dr. Clémence Allain, Dr. Laurent Galmiche, Dr. Nicolas Bogliotti, Dr. Victor Brasiliense, Dr. Cédric Mongin, Dr. Fabien Miomandre, Elise Michel, Christian Jean-Baptiste, Ayano Tanaka, Jean-Frédéric Audibert. Arnaud Brosseau, Jacky Formont.

I would also like to acknowledge the members of PPSM: Jinbiao Jiao, Gaoyu Li, Zhaoxin Wang, Dr. Lorenzo Casimiro, Dr. Nicolas Fabre, Dr. Jonathan Long, Dr. Benjamin Poggi, Dr. Luca Polacchi, Dr. Clément Polese, Dr. Ayedah Tariq, Dr. Céline, Dr. Jan Patrick Calupitan, Céline Jegat, Aurélie Dijan, Enzo Dalloz, Clément Barois, Margarita Bosmi, Elodie Deschamps, Magin Ferrer, Julien Malletroit, Suzanne Veda. Thank you all during the period. Some of you have already obtained the doctoral degrees, and some of you are approaching. Wish you all good results and bright futures.

I am a person who likes to be alone and isolated to store energy at most time. To laboratory members, thank you for raising topics with me, and I feel grateful of it. During the period, I also find something new to me. I found it happy to go boating after the COVID-19 lockdown and thank you for people who sometimes come with me in summer. My parallel parking skills improves a lot here in the city. Perhaps I will go for a manual license and a manual transmission, because I found it interesting to disassembly or polish in automobile knowledges and crafts. I would like to share the happiness from it with you in the future, etc.

Finally, my mum and dad, support me all the time. It was a pity that I had long time not possible to go back to see you and urge your health progresses. Love you always.



Yang ZHOU

ENS Paris-Saclay à Gif-sur-Yvette





**Titre :** Hystérésis de fluorescence photocommutable grâce à des architectures multichromophoriques

**Mots clés :** fluorescence, hystérésis, photocommutable, FRET, photoisomérisation, multichromophorique

**Résumé :** Les matériaux fluorescents photocommutables ont des applications potentielles dans le domaine du stockage optique de l'information ou de l'imagerie super-résolution, ce qui attire des développements considérables en recherche. Dans de tels systèmes moléculaires, les différentes voies de photoisomérisation accessibles et les cinétiques compétitives associées, sous irradiation en lumière UV et visible, correspondant à des réactions photoinduites aller et retour, doivent permettre d'ouvrir un cycle d'hystérésis de fluorescence. Dans ce but, nous cherchons à générer des effets d'hystérésis de fluorescence avec des architectures multichromophoriques à base de plateformes cyclodextrines multivalentes portant plusieurs dendrons, comportant un nombre variable d'unités photocommutables et/ou fluorescentes. Le travail effectué au cours de cette thèse couvre les études d'un fluorophore photoisomérisable  $E \leftrightarrow Z$  (dérivé du dicyanométhylène-4H-pyran, DCM), des systèmes multichromophoriques contenant plusieurs DCM (multi-DCMs), ou une combinaison de DCM et d'unités photochromes (diaryléthènes, DAE). Après une présentation générale de la photocommutation de fluorescence (chapitre 1), le DCM lui-même a été étudié par des techniques spectroscopiques (stationnaires, résolues en temps) et des approches théoriques (Théorie de la Fonctionnelle de la Densité Spin-Flip, SF-DFT) afin d'élucider les processus conduisant aux propriétés de fluorescence photocommutable, en particulier à travers l'identification des intersections coniques (chapitre 2).

Dans le chapitre 3, plusieurs DCM photoisomérisables et fluorescents ont ensuite été combinés ensemble par des stratégies de chimie click en petites molécules dendritiques (multi-DCMs) et leurs études spectroscopiques indiquent des processus efficaces de transfert d'énergie résonant de type Förster (FRET) intramoléculaire. Des mesures d'anisotropie de fluorescence et des simulations de dynamique moléculaire ont été réalisées pour confirmer les modèles FRET dans ces multi-DCMs. Enfin, le chapitre 4 décrit les efforts déployés pour synthétiser des DAE combiné à des unités DCM, conduisant à un système "trichromophorique" (1 DAE, 2 DCM), assemblé ensuite en multichromophores 12-valents et 42-valents. Ces systèmes multichromophoriques complexes révèlent des voies FRET intramoléculaires efficaces et démontrent l'effet d'hystérésis de fluorescence, qui dépend du nombre de chromophores. De telles caractéristiques d'hystérésis de fluorescence, démontrées au moyen de multichromophores intelligents photocommutables et fluorescents, sont très prometteuses pour un large éventail de développements futurs, puisque nous pouvons envisager des modalités de stockage de données optique complexe à plusieurs états ou des biosystèmes photosensibles capables de se greffer par chimie click pour une imagerie de fluorescence sophistiquée, via un contrôle précis par la lumière.

**Title :** Photoswitchable fluorescence hysteresis based on multichromophoric architectures

**Keywords :** fluorescence, hysteresis, photochromism, FRET, photoisomerization, multichromophoric

**Abstract :** Photoswitchable fluorescent materials have potential applications in optical information storage or super-resolution imaging area, attracting considerable research developments. In such molecular systems, competitive photoisomerization pathways and kinetics under UV and visible light irradiation, corresponding to forward and backward photoinduced reactions, are expected to open a fluorescence hysteresis cycle. With this goal in mind, we aim to generate fluorescence hysteresis effects with multichromophoric architectures based on cyclodextrin multivalent platforms bearing several dendritic linkers, substituted by a variable number of photoswitchable and/or fluorescent units. The work carried out in this PhD covers the studies on a  $E/Z$  photoisomerizable fluorophore (derived from dicyanomethylene-4H-pyran, DCM), multichromophoric systems holding multiple DCM (multi-DCMs), or a combination of DCM and photochromic units (diarylethenes, DAE). After a general review of fluorescence photoswitching (chapter 1), the DCM itself has been investigated by spectroscopic techniques (steady state, time-resolved) and theoretical approaches (Spin-Flip Density Functional Theory, SF-DFT) to unravel the processes leading to photoswitchable fluorescence properties, especially through its conical intersections (chapter 2).

In chapter 3, several photoisomerizable and fluorescent DCM have been then combined together by click chemistry strategies into small dendritic molecules (multi-DCMs) and their spectroscopic studies indicate effective intramolecular Förster resonance energy transfer (FRET) processes. Fluorescence anisotropy and molecular dynamics simulations have been carried out to confirm and support the FRET models in such multi-DCMs. Finally, the chapter 4 describes our efforts to synthesize DAE combined with DCM units, leading to a “trichromophore” system (1 DAE, 2 DCM), further assembled into 12-valent and 42-valent multichromophores. These complex multichromophoric systems show efficient intramolecular FRET pathways and demonstrate the fluorescence hysteresis effect, which depends on the number of chromophores. Such fluorescence hysteresis features, demonstrated by means of smart photoswitchable and fluorescent multichromophores, are very promising for a wide range of future developments, since we can envision complex multi-state optical data storage or photoactive biosystems capable to be grafted by click chemistry for smart fluorescence imaging, via precise control by light.

# ACRONYMS, NOTATIONS & ABBREVIATIONS

## A, B, C

---

Abs	<b>A</b> bsorption
Ac	<b>A</b> cetyl
AIE	<b>A</b> ggregation- <b>I</b> nduced <b>E</b> mission
Asc	<b>A</b> scorbate

---

B3LYP	Hybrid DFT functional: <b>B</b> ECKE, 3-parameter, <b>L</b> EE- <b>Y</b> ANG- <b>P</b> ARR
BODIPY	<b>B</b> oron- <b>d</b> ipyrrromethene
BTD	<b>B</b> enzothiadiazole
Bu	<b>B</b> utyl

---

CAM- B3LYP	<b>C</b> oulomb- <b>A</b> ttenuating <b>M</b> ethod- <b>B</b> ECKE, 3-parameter, <b>L</b> EE- <b>Y</b> ANG- <b>P</b> ARR (DFT functional)
CD	<b>C</b> yclodextrin
CI	<b>C</b> onical intersection
CoSy	<b>C</b> orrelation <b>S</b> pectroscopy
CuAAC	<b>C</b> opper(I)-catalyzed <b>A</b> zide- <b>A</b> lkyne <b>C</b> ycloaddition

## D, E, F

---

d	<b>D</b> oublet (NMR)
DAE	<b>D</b> iarylethene
DCM	<b>D</b> icyanomethylene, or compound 4-Dicyanomethylene-2-methyl-6-(p-dimethylaminostyryl)-4 <i>H</i> -pyran, in this thesis the common solvent dichloromethane writes in its full name
dd	<b>D</b> oublet of <b>d</b> oublets (NMR)
DFT	<b>D</b> ensity <b>F</b> unctional <b>T</b> heory
DMAP	4-( <b>D</b> imethylamino)pyridine
DMF	<i>N,N</i> - <b>d</b> imethylformamide
DMSO	<b>D</b> imethyl sulfoxide
DTE	<b>D</b> ithienylethene

---

EDTA	<b>E</b> thylenediaminetetraacetic acid
em	<b>E</b> mission
ESI	<b>E</b> lectron <b>S</b> pray <b>I</b> onization
Et	<b>E</b> thyl
ET	<b>E</b> nergy <b>T</b> ransfer
ES	<b>E</b> xcited state
equiv.	Molar <b>e</b> quivalent
exc	<b>E</b> xcitation

---

FEL	<b>F</b> ree <b>E</b> nergy <b>L</b> andscape
FRET	<b>F</b> örster <b>R</b> esonance <b>E</b> lectron <b>T</b> ransfer

## G, H, I, J

---

GAFF	<b>G</b> eneral <b>A</b> MBER force field
GS	<b>G</b> round state

---

HF	<b>H</b> artree- <b>F</b> ock
HMQC	<b>H</b> eteronuclear <b>M</b> ultiple <b>Q</b> uantum <b>C</b> oherence
HPLC	<b>H</b> igh <b>P</b> erformance <b>L</b> iquid <b>C</b> hromatography
HRMS	<b>H</b> igh <b>R</b> esolution <b>M</b> ass <b>S</b> pectroscopy

---

ICT	<b>I</b> nternal <b>C</b> harge <b>T</b> ransfer
IEFPCM	<b>I</b> ntegral <b>E</b> quation <b>F</b> ormalism <b>P</b> olarized <b>C</b> ontinuum <b>M</b> odel
Irr	<b>I</b> rradiation

---

<i>J</i>	Scalar coupling constant, expressed in Hz (NMR)
----------	---

## K, L, M, N, O, P

---

<b>m</b>	<b>M</b> ultiplet (NMR)
<b>MD</b>	<b>M</b> olecular <b>d</b> ynamics
<b>Me</b>	<b>M</b> ethyl
<b>MECI</b>	<b>M</b> inimum <b>e</b> nergy <b>c</b> onical <b>i</b> ntersection
<b>MS</b>	<b>M</b> ass <b>S</b> pectroscopy
<b>MW</b>	<b>M</b> icro- <b>W</b> ave or <b>M</b> olecular <b>W</b> eight

---

<b>NMR</b>	<b>N</b> uclear <b>M</b> agnetic <b>R</b> esonance
<b>NPT</b>	constant number ( <b>N</b> ), volume ( <b>V</b> ), and temperature ( <b>T</b> )
<b>NVT</b>	constant number ( <b>N</b> ), pressure ( <b>P</b> ), and temperature ( <b>T</b> )

---

<b>OLED</b>	<b>O</b> rganic <b>L</b> ight- <b>E</b> mitting <b>D</b> iode
-------------	---

---

<b>PBE</b>	<b>P</b> erdew- <b>B</b> urke- <b>E</b> rnzerhof
<b>PCM</b>	<b>P</b> olarizable <b>C</b> ontinuum <b>M</b> odel
<b>PE</b>	<b>P</b> etroleum <b>e</b> ther
<b>PEC</b>	<b>P</b> otential <b>e</b> nergy <b>c</b> urve
<b>PES</b>	<b>P</b> otential <b>e</b> nergy <b>s</b> urface
<b>PET</b>	<b>P</b> hotoinduced <b>e</b> lectron <b>t</b> ransfer
<b>pH</b>	<b>P</b> otential of <b>h</b> ydrogen
<b>Ph</b>	<b>P</b> henyl
<b>PMMA</b>	<b>P</b> oly <b>m</b> ethyl <b>m</b> ethacrylate
<b>ppm</b>	<b>P</b> arts <b>p</b> er <b>m</b> illion
<b>PSS</b>	<b>P</b> hoto <b>S</b> ationary <b>S</b> tate

## Q, R, S, T

---

<b>q</b>	<b>Q</b> uadruplet (NMR)
----------	--------------------------

---

<b>RET</b>	<b>R</b> esonance <b>E</b> nergy <b>T</b> ransfer
<b>R<sub>f</sub></b>	<b>R</b> etention <b>f</b> actor
<b>rt</b>	<b>R</b> oom <b>t</b> emperature

---

<b>s</b>	<b>S</b> inglet (RMN)
----------	-----------------------

---

<b>SF-TDDFT</b>	<b>S</b> pin- <b>F</b> lip <b>T</b> ime- <b>D</b> eendent <b>D</b> FT
<b>S<sub>n</sub></b>	<b>S</b> inglet state on the state <i>n</i>

---

<b>t</b>	<b>T</b> riplet (NMR)
<b>T<sub>n</sub></b>	<b>T</b> riplet state on the state <i>n</i>
<b><i>t</i>-Bu</b>	<b><i>t</i></b> ert- <b>b</b> utyl
<b>TBAF</b>	<b>T</b> etra <b>b</b> utylammonium <b>f</b> luoride
<b>TBAI</b>	<b>T</b> etra- <i>n</i> - <b>b</b> utylammonium <b>i</b> odide
<b>TBDMS</b>	<b><i>t</i></b> ert-butyl <b>d</b> imethyl <b>s</b> ilyl
<b>TDDFT</b>	<b>T</b> ime- <b>D</b> eendent <b>D</b> FT
<b>THF</b>	<b>T</b> etra <b>h</b> ydro <b>f</b> uran
<b>TLC</b>	<b>T</b> hin <b>L</b> ayer <b>C</b> hromatography
<b>TMS</b>	<b>T</b> etra <b>m</b> ethyl <b>s</b> ilane (NMR)
<b>TPE</b>	<b>T</b> etra <b>p</b> henyl <b>e</b> thane
<b>TS</b>	<b>T</b> ransition <b>s</b> tate

## U, V, W, X, Y, Z

---

<b>UV</b>	<b>U</b> ltra- <b>V</b> iolet
<b>Vis</b>	<b>V</b> isible

## Units and Symbols

---

<b>a.u</b>	<b>A</b> rbitrary <b>u</b> nit
<b>°C</b>	<b>D</b> egrees <b>C</b> elsius

eV	Electron-volt
g	Gram
h	Hour
Hz	Hertz
L	Liter
m	Meter
M	Represents the unit <b>mol L<sup>-1</sup></b>
mol	<b>Molar</b>
s	Second
v/v	Volume to <b>v</b> olume
w/v	<b>W</b> eight to <b>v</b> olume
$\delta$	Chemical shift expressed in ppm (NMR)
$\Delta H$	Variation of the enthalpy
$\Delta G$	Variation of Gibbs Free Energy
$\Delta S$	Variation of the entropy
$\Phi$	Quantum yield
$\Phi_F$	Fluorescence quantum yield
$\lambda$	Wavelength number expressed in <b>nm</b>



# TABLE OF CONTENTS

ACRONYMS, NOTATIONS & ABBREVIATIONS.....	7
TABLE OF CONTENTS .....	11
GENERAL INTRODUCTION.....	13
<b>1 CHAPTER I – FROM PHOTOCHROMISM AND FLUORESCENCE TO MULTICHROMOPHORIC ARCHITECTURES AND HYSTERESIS.....</b>	<b>17</b>
1.1 PHOTOCROMISM.....	17
1.1.1 Principles.....	17
1.1.2 Main families of photochromic compounds.....	18
1.1.2.1 Spiropyrans/merocyanines (SP/MC).....	18
1.1.2.2 Diarylethenes (DAE).....	19
1.1.2.3 Azobenzenes (Azo) .....	20
1.1.2.4 DASA .....	21
1.2 FLUORESCENCE .....	22
1.2.1 Principles.....	22
1.2.2 Fluorophores .....	22
1.3 INTERACTIONS BETWEEN CHROMOPHORES .....	23
1.3.1 Förster resonance energy transfer (FRET).....	23
1.3.2 The different fluorophore-photochrome associations .....	24
1.3.3 DCM photoswitchable fluorophore.....	27
1.4 MULTICHROMOPHORIC SYSTEMS .....	28
1.4.1 Dendrimeric multichromophoric systems .....	29
1.4.2 Multiphotochromic systems.....	32
1.5 HYSTERESIS EFFECTS.....	34
1.5.1 Principles.....	34
1.5.2 Some examples of hysteresis effect in scientific developments .....	34
1.5.3 Towards photoswitchable fluorescence hysteresis effect .....	35
1.5.3.1 The pioneering exploration .....	36
1.5.3.2 Fluorescence hysteresis implementations.....	36
1.5.3.3 Further developments of photoswitchable fluorescence hysteresis .....	38
1.6 SYNTHETIC TACTICS.....	38
1.6.1 Dendritic linkers .....	39
1.6.2 CuAAC in multivalent systems.....	40
1.7 OBJECTIVES OF THESIS .....	44
1.7.1 General interests.....	44
<b>2 CHAPTER II – PHOTOPHYSICAL AND THEORETICAL STUDIES OF DCM .....</b>	<b>51</b>
2.1 INTRODUCTION .....	51
2.2 PAPER MANUSCRIPT #1 (PHYS. CHEM. CHEM. PHYS.).....	52
2.3 APPENDIX: THEORETICAL TECHNIQUES.....	79
2.3.1 Choice of the functionals and basis sets .....	79
2.3.2 Calculations of absorption and emission energies, solvent effects.....	80
2.3.3 Principles of Spin-Flip TDDFT (SF-TDDFT).....	82
2.4 CONCLUSIONS AND PERSPECTIVES.....	85
<b>3 CHAPTER III – SYNTHESIS AND INVESTIGATION OF MULTI-DCM SYSTEMS.....</b>	<b>88</b>
3.1 INTRODUCTION .....	88
3.2 STRATEGIES TO DESIGN MULTI-DCM COMPOUNDS .....	89
3.2.1 Pentaerythritol scaffold .....	89
3.2.2 $\beta$ -Cyclodextrin scaffold .....	90
3.3 PRINCIPLES OF MOLECULAR DYNAMICS SIMULATIONS.....	96
3.3.1 Classical molecular dynamics.....	96
3.3.2 Trajectory based clustering analysis .....	98
3.3.3 Principal component analysis (PCA).....	98
3.3.3.1 Principles of PCA.....	99
3.3.3.2 Free energy landscape (FEL) .....	99
3.3.4 Markov state models (MSMs).....	100



3.4	PAPER MANUSCRIPT #2 (CHEM. EUR. J.) .....	102
3.5	SYNTHESIS DETAILS OF MULTI-DCM COMPOUNDS .....	131
3.5.1	<i>Preparation of dendritic linkers</i> .....	131
3.5.2	<i>Preparation of <math>\beta</math>-CDs</i> .....	132
3.5.3	<i>Preparation of multi-DCMs</i> .....	135
<b>4</b>	<b>CHAPTER IV – MULTI-DAE/DCM SYSTEMS, TOWARDS FLUORESCENCE HYSTERESIS .....</b>	<b>143</b>
4.1	THE DIFFERENT TYPES OF FLUORESCENCE HYSTERESIS .....	143
4.2	TOWARDS A NEW TYPE OF HYSTERESIS EFFECT .....	144
4.2.1	<i>Molecular architectures</i> .....	144
4.2.2	<i>Spectroscopic and theoretical description of the new DAE</i> .....	145
4.2.2.1	Spectroscopic studies .....	145
4.2.2.2	Theoretical studies .....	146
4.3	SYNTHESIS OF THE DENDRITIC STRUCTURES FOR HYSTERESIS EFFECT .....	149
4.3.1	<i>Synthesis of the azido-dendron</i> .....	149
4.3.2	<i>Synthesis of the trichromophoric dendron</i> .....	151
4.3.3	<i>Synthesis of the dendritic architectures</i> .....	151
4.4	FLUORESCENCE HYSTERESIS MEASUREMENTS.....	155
4.4.1	<i>Prerequisites for fluorescence hysteresis measurements</i> .....	155
4.4.1.1	Experimental measurement prerequisites .....	155
4.4.1.2	Previous experiment considerations .....	156
4.4.2	<i>Steady-state measurements</i> .....	158
4.4.2.1	Photophysical properties.....	158
4.4.2.2	Demonstration of the photoswitchable fluorescence hysteresis behavior of YN-3c.....	159
4.4.3	<i>Dual photokinetics hysteresis measurement</i> .....	160
4.4.3.1	Setup description.....	160
4.4.3.2	Improvement of the setup with the multichromophoric compounds.....	161
4.5	MOLECULAR DYNAMICS SIMULATIONS ON DENDRON YN-3C.....	163
4.5.1	<i>Trajectory-based analysis</i> .....	163
4.5.2	<i>MSM analysis</i> .....	169
4.6	APPENDIX: MSM VALIDATIONS .....	171
4.7	CONCLUSION AND PERSPECTIVES .....	174
	<b>GENERAL CONCLUSION AND PERSPECTIVES .....</b>	<b>176</b>
<b>5</b>	<b>EXPERIMENTAL SECTION .....</b>	<b>181</b>
5.1	GENERAL EXPERIMENTAL DETAILS .....	181
5.1.1	<i>Materials and characterizations</i> .....	181
5.1.2	<i>Synthesis catalog</i> .....	181
5.1.2.1	2DCM.....	181
5.1.2.2	3DCM.....	182
5.1.2.3	4DCM.....	184
5.1.2.4	14DCM.....	185
5.1.2.5	YN-3c .....	186
5.1.2.6	YN-12c .....	190
5.1.2.7	YN-42c .....	191

## GENERAL INTRODUCTION

Multichromophoric systems are envisioned as a promising category of innovative functional architectures for light-harvesting systems, optoelectronic devices, adjustable polymers, photoactive supramolecular nanomaterials, etc. With the growing demand in the field of materials science, the basic studies on organic molecules are highly active. In particular, multichromophores including photochromes and fluorophores can exhibit specific features, such as photoswitchable multi-colors, high-contrast fluorescence *via* resonance energy transfer (RET), and they can serve as multi-dimensional logic gates or induce supramolecular structural rearrangements beyond just two forms. To the best of our knowledge, photoswitchable fluorophores incorporated in multichromophoric systems have not been explored to date. Following the previous research carried out in the PPSM laboratory, this PhD work takes place in the field of multichromophoric molecules involving both fluorescent and photoisomerizable chromophores, which may lead to the discovery of new photophysical and photochemical effects, especially those based on hysteresis.

For induce and enhance fluorescence hysteresis effects, we aim at building proper multichromophoric systems bearing appropriate photoactive dyes. In this project, a dicyanomethylene-4*H*-pyran (DCM) analog and a diarylethene (DAE) derivative are selected as the key molecules to design the molecular architectures and realize the final implementations. Beyond the former results, at the beginning of the PhD, there were several unexplored fields: theoretical studies on mono-DCM were missing, energy transfer patterns inside the multi-DCM/DAE still required some photophysical and theoretical rationalization, and the design of straightforward and efficient large multichromophoric DAE/DCM systems had to be defined. Therefore, the whole PhD dissertation follows this sequence of implementation of the project, with the characterization of the mono-DCM molecule, and then the synthesis and investigation of multi-DCM and multi-DCM/DAE molecules. The background of this work covers the synthesis, the photophysics, and the theoretical chemistry of such systems, in order to build the most promising and effective systems to bring out the desired fluorescence hysteresis effect.

To better understand this manuscript which covers several fields from the organic synthesis to the molecular dynamic, through the photochemistry, it is of interest to summarize the genesis of the project called *photoswitchable fluorescence hysteresis*.

To the origin of the photoswitchable fluorescence hysteresis effect, a first research proposal based on the design of a new category of cyclodextrin-based multichromophoric molecules was envisioned by Pr J. Xie's groups and Pr K. Nakatani's group since 2007 to target applications such as reversible optical data storage systems. After several attempts, the project was finally granted by the *Agence Nationale pour la Recherche* (ANR) five years after the first submission, to address new related nano-objects for applications in the field of super-resolution imaging (ANR JCJC AZUR 2012-2015, coord. Dr R. Métivier). More precisely, these new multichromophoric systems involved in a same molecular architecture several fluorescent and photochromic units. The fluorescent units were employed in order to increase the contrast and the brightness, while the photochromic units were used as internal photoactivatable quenchers using the resonance energy transfer phenomenon. The unexpected *photoswitchable hysteresis effect* was first discovered by serendipity in 2013 at the PPSM during the study of these multichromophoric molecules containing fluorescent diarylethene (DAE) units and/or dicyanomethylene-4*H*-pyran (DCM) units: it appeared that the systems were more complicated than expected. To better understand the structure-property relationships of the photochemical and photophysical behaviors of such molecular architectures, a careful methodological approach was established: the control of the ratio between the DAE and the DCM units. This approach has also considerably changed the way of thinking of the group and has initiated the revisiting of the DCM fluorophore as to be considered as a photoswitchable fluorescent unit, as demonstrated by Dr S. Maisonneuve during his PhD work dedicated to this new phenomenon in 2016. Aware of the importance of the number of chromophoric units and the ratio between the different types of photoswitchable chromophores, several aspects were still unexplored and are of primary importance for the understanding of this effect. To develop this new research field further, the ANR program granted the SWIST project ("Switchable fluorescence hysteresis by light", 2017-2022, coord. Dr R. Métivier), which provides the playground of this PhD work.

This dissertation is composed of four chapters. **Chapter I** of this manuscript is devoted to the bibliographic work covering the knowledge of photochromism, fluorescence, multichromophoric systems, hysteresis effects and state-of-the-art of the whole work. This first chapter introduces the connections of the photophysical and photochemical properties brought by the DCM, the DAE and the multichromophoric systems, which contribute to the final fluorescence hysteresis targets.

The **Chapter II** is devoted to photophysical and theoretical studies on one of the photoisomerizable fluorophore, the so-called **DCM-azide** (previously synthesized by Dr S. Maisonneuve)<sup>1,2</sup> Since the **DCM-*o*-propargyl**<sup>3,4</sup> showed the presence of several possible isomers/conformers, the photoisomerization process of **DCM** series was still unclear in the description of the relaxation from the excited state to the ground state. This chapter focuses on the four isomers and conformers of the **DCM-azide**, elucidating their connections in the isomerization process through fluorescence spectroscopic evidence and excited state calculations by the spin-flip density functional theory method with the help of Pr F. Maurel in ITODYS laboratory at Univ. Paris Cité (ANR collaborator).

Based on the background of multichromophoric systems already prepared in the PPSM laboratory by Dr S. Maisonneuve, showing some first evidence of photoswitchable fluorescence hysteresis effect, combined systems involving several DCM fluorophores were expected to optimize this phenomenon. However, the possible resonance energy transfer among DCM molecules was not identified nor clarified yet. In the **Chapter III**, we have synthesized the array of mono-, di-, tri-, tetra-, and tetradeca-DCMs (1-, 2-, 3-, 4-, 14-DCMs) based on the molecule **DCM-azide** investigated in **Chapter I**, using the “click chemistry” strategy. The photophysical characterizations on the simplest elements, **DCM-azide**, **2DCM**, and **3DCM**, revealed the photoisomerization process of **2DCM** and **3DCM**. Intramolecular resonance energy transfer was demonstrated to play a great role within DCM units of these two compounds. Particularly on **2DCM**, molecular dynamics simulations studies have been performed, and the corresponding statistical analyses were implemented to conclude that the energy transfer processes depend on the conformational structure of the **2DCM** molecule. The simulation and analysis workflows were built and taken into the Chapter IV, serving the RET explanations on combined multichromophores.

In the **Chapter IV**, the target of the project of realizing the photoswitchable fluorescence hysteresis is shown with the DCM/DAE combined multichromophoric system. This work aims at optimizing and interpreting the phenomenon with optimized molecular building blocks: the  $\beta$ -cyclodextrin platform, re-designed linkers, and a new non-fluorescent DAE synthesized by Dr P. Yu’s group in ICMMO laboratory at Univ. Paris-Saclay (N. Baggi’s PhD work, ANR SWIST collaborators). The non-fluorescent DAE and the fluorescent **DCM-*o*-propargyl** were gathered at the ratio of 2:1 first to form the basic trichromophoric system **YN-3c**. Further, the **YN-3c** is synthesized into **YN-12c** and **YN-42c** by the “click chemistry” procedure inherited from Chapter II. Absorption and fluorescence correlation experiments were carried out to characterize the different systems, providing the photoswitchable fluorescence hysteresis demonstration and its dependence on the multichromophoric dimensions. Theoretical investigations were also involved in this section, including the **DAE** DFT / TDDFT calculations, and molecular dynamics simulations on **YN-3c** to describe the intramolecular resonance energy transfer pathways taking place in the system.

# Chapter I



# 1 CHAPTER I – FROM PHOTOCHROMISM AND FLUORESCENCE TO MULTICHROMOPHORIC ARCHITECTURES AND HYSTERESIS

---

This chapter introduces the basic principles underlying the fluorescence hysteresis effect. Photochromism and fluorescence from specific molecules are key features to bring out the photoswitchable fluorescence hysteresis effect. Furthermore, photochromic and fluorescent molecules can affect each other through resonance energy transfer processes. These building blocks and mutual interactions are all involved in multichromophoric systems, resulting in novel specific features, such as the photoswitchable fluorescence hysteresis effect.

## 1.1 PHOTOCHROMISM

### 1.1.1 Principles

Photochromism is a phenomenon existing in several classes of chemical compounds which can undergo reversible conversions between two species upon light illumination. In the process, the two species have different absorption spectra, causing the change of the color upon the exposure to different wavelength ranges of light, where the backward process can be driven by either light or heat (**Figure 1**).

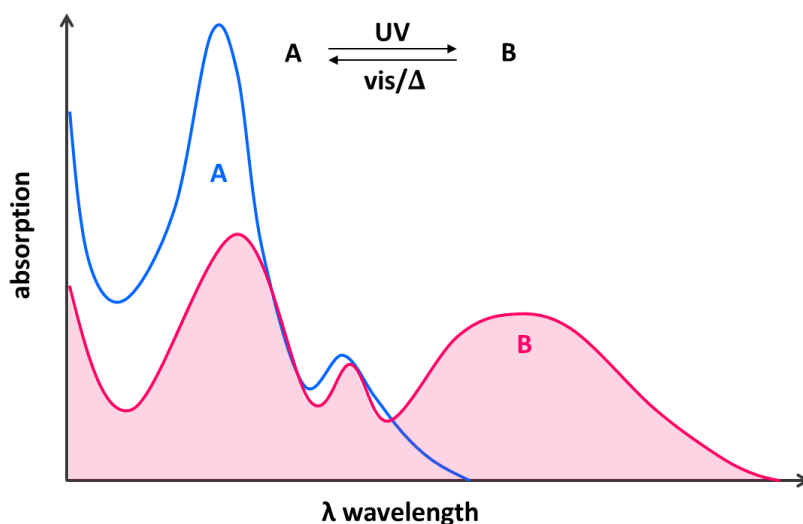


**Figure 1:** Illustration of the photochromism and corresponding state changes. Due to the shift of the absorption band under light irradiation or heating, the color of the substance's changes.

Positive photochromic compounds have a blue-shifted absorption spectrum in the stable state A (e.g. colorless), and a red-shifted absorption spectrum in the metastable state B (colored). The situation is opposite for negative photochromic molecules, for which the transition occurs from the colored state (A, stable) to the colorless state (B, metastable). The most familiar natural photochromic system is rhodopsin (also named as "visual purple"), a protein present in the human eyes. It exists in the rods of the retina and is a G-protein-coupled receptor.<sup>5,6</sup>

The chemical compounds that possess the property of photochromism have already entered our daily life in the form of functional or decorative usage. As shown in the **Figure 2**, the most common commercial examples are the photochromic ophthalmic lenses. They can act as multiple lenses just all-in-one by blending a combination of photochromic molecules in the coating. The photochromic material responds to different intensity of sunlight outdoor to adjust the light transmittance. More recently, photochromic

materials are also used in the fabrication of smartphones. Compared to the electrochromism, photochromism has a more natural looking, and saves precious battery life of the mobile device. With pre-injection molding masks or enclosure cases, users can easily customize and show off the back surface of their own personalities without invasive surface etchings.<sup>7</sup>



**Figure 2:** (a) Photochromic lenses: the lenses can self-adjust the color corresponding to the outdoor light intensity. Photo credit: Brahmox Lens.<sup>8</sup> (b) Smartphone with a photochromic back design: the color evolves by shielding the sunlight by masks to create customized effects.<sup>7</sup>

The photochromic materials can be composed of inorganic, organic or hybrid molecules. Among them there is a classification of the type of the photochromism, namely the P type (the backward reaction can be induced by light or by temperature) and T type (the backward reaction is only induced thermally). The organic molecular systems are the richest and easily to be modified for the specific demands. The photochemical reactions include double bonds  $E \leftrightarrow Z$  (or  $cis \leftrightarrow trans$ ) photoisomerizations, but also photocycloadditions, photocyclizations, intramolecular hydrogen transfer, electron transfer (oxidation-reduction), dissociations, etc., which are the basic mechanisms of the main families of photochromic molecules. The investigations on photochromic molecules are not only restricted to the development of new molecules with extended excitation wavelengths, P or P/T type and colors, but depending on the target applications, the research efforts are also oriented towards improved fatigue resistance, conversion and quantum yields of isomerization, fast or slow thermal back reaction, etc. Although the definition of photochromism is extended by introducing increasing sub-classifications, photochromism is still one subset of the photochemical reactions. The applications of photochromism now cover the self-adapting sunglasses, 3D optical data storage, solar energy storage, as well as novel photoactive supramolecular architectures.<sup>9-13</sup>

### 1.1.2 Main families of photochromic compounds

Several major families of photochromic molecules have been developed. Even within the last few decades, new families are still emerging. The prevalent spiropyrans, diarylethenes and azobenzenes are already top stars from long time ago. By modifying the chemical structures, specific applicative targets can be fulfilled under most circumstances.

#### 1.1.2.1 Spiropyran/merocyanines (SP/MC)

The spiropyran/merocyanines (SP/MC) is the pair name of the two forms of this category of photochromes upon light irradiations. It plays a pivotal role in the field of photochromism since the concept was established. The closed form spiropyran features an indoline and another aromatic moiety which are separated by a  $sp^3$ -hybridized "spiro" junction carbon " $C_{\text{spiro-O}}$ " bond. The two moieties are perpendicularly oriented to each other. When the SP structure is irradiated under UV, the transformation starts with the cleavage of the  $C_{\text{spiro-O}}$  bond, resulting in an intermediate *cis*-MC structure. This process is detectable to the ultrafast transient absorption citations.<sup>14</sup> The MC structure will finally reach a *trans*-form by rotating the central C-C bond. The  $SP \leftrightarrow MC$  isomerization can also be induced by near-infrared (NIR) *via* two-photon excitation, which enables less photo-degradation and wider biological usages with

longer penetration length. The reverse MC→SP occurs spontaneously and can be accelerated in the visible light range. In summary, spiropyrans are able to realize photochromism, acidochromism and thermochromism all together. The combined features allow SPs to play versatile roles in photosensitive, thermosensitive and chemosensitive applications. As shown in **Figure 3**, Kortekaas et al. and Klajin have described the SP chromophore evolutions and related materials in details.<sup>15, 16</sup>

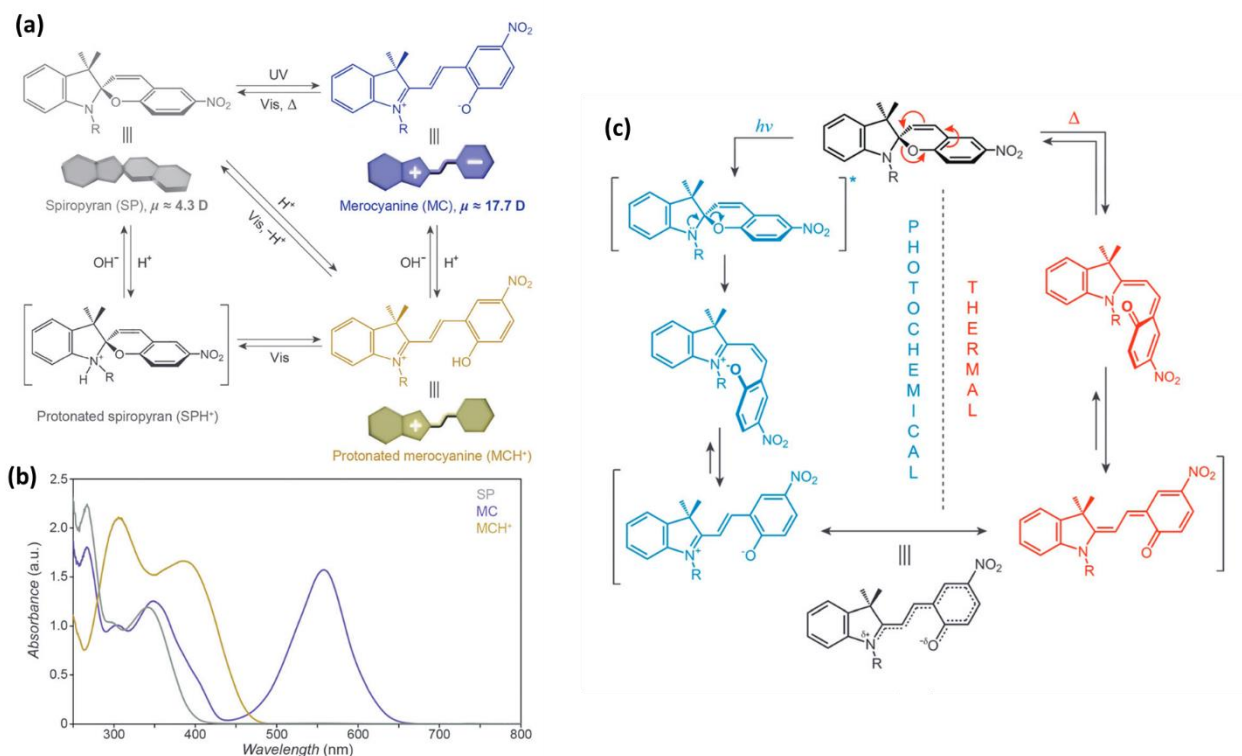
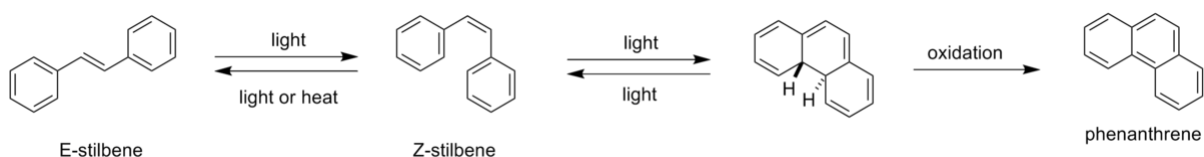


**Figure 3:** (a) Reversible transformations among four states of SP↔MC. (b) UV-Vis absorption spectra of the parent SP(1',3',3'-trimethyl-6-nitrospi[chromene-2,2'-indoline]) before (grey line) and after (purple line) UV irradiation, and after the addition of HCl (yellow line). (c) Mechanism of photochemical and thermal isomerization of SP.<sup>15, 16</sup>

### 1.1.2.2 Diarylethenes (DAE)

This family of photochromes was first discovered by serendipity and introduced by Irie *et al.*<sup>17</sup>. Since then, they grew up rapidly due to their high thermodynamic stabilities. DAE are derived from the stilbene motif, which is the simplest photoisomerizable model possessing aromatic groups bridged by a C=C bond (**Scheme 1**).



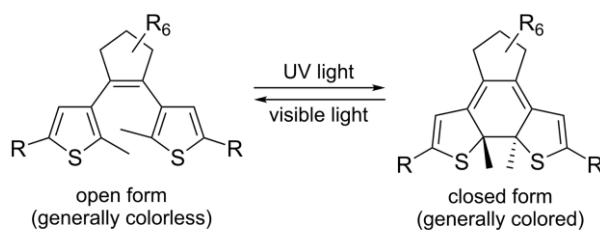
**Scheme 1:** The stilbene isomerizations upon light irradiations.

Under the light irradiation, the stilbene can undergo two sorts of reversible isomerizations:

1. **E↔Z isomerization.** This is a C=C double bond isomerization, which goes through an excited state energy minimum where the aromatic groups are not in the same plane anymore (usually perpendicular to each other). The conformation will distribute into Z and E forms when it relaxes from the excited state to the ground state.



2. **Open and close isomerization.** The Z-stilbene can further isomerize by rearranging the aromatic system itself (6- $\pi$  electrocyclization mechanism), then be oxidized into the stable phenanthrene. However, the quantum yield of the reaction is usually low under the circumstance of pure stilbenes.



**Scheme 2:** General scheme of DAE OF↔CF isomerization.

As **Scheme 2** shows, the DAE has substituted C=C double bond and phenyl groups on the stilbene. The five-membered heterocyclic rings with low aromatic stabilization energies are often utilized in place of phenyl groups, such as thiophene or furan rings. This type of molecules can undergo photoisomerization between the open form (OF) and the closed form (CF). On the left, two heterocyclic rings have only non-bonded interactions. After isomerization, on the right, the bonds are rearranged, so that the electronic structure is influenced by the  $\pi$ -conjugation on the planar plane. In addition, the central ring structure prevents the  $E \leftrightarrow Z$  isomerization like the stilbene, providing stable two states. The reasons that DAE families are prevalent in many research fields are:

1. DAE offers a stable P-type photochromism, whereby the dye switches *via* light irradiation at different wavelengths. Compared to the T-type photochromes, which thermally revert back in the absence of light to the original states, P-types are extremely popular due to their apparent bistability: the thermal stability of well-designed DAE derivatives can reach a half-life at room temperature over 470,000 years.<sup>18</sup>

2. Solid state photochromism. Many DAEs show photochromism in the crystalline form, which is a rare property among the photochromic molecules. The general types can only switch in solution or in gel state.<sup>19, 20</sup>

3. The high performance of the fatigue resistance. The strong fatigue resistance makes DAE resilient between two states until thousands of cycles.<sup>20</sup>

The structural modifications can be made on many positions, which enable DAEs suitable for vast application scenarios by changing the physical features, such as the color, solubility, hydrophobicity, etc. The *ortho*-substitution on aromatic rings helps the stabilization against the oxidation, and the lowering of the whole aromaticity results in a high thermal stability of the closed form.

### 1.1.2.3 Azobenzenes (Azo)

Azobenzenes is another important family of photochromic molecules, or photoswitches. It is composed of two phenyl rings conjugated with a central N=N double bond. Azobenzene commonly refers to the wide class of molecules containing the core structure and functional group modifications on the phenyl rings or their substitution by heterocycles.<sup>21</sup> As it is ascribed to the through double bond isomerization, one typical azobenzene has one *cis*-isomer and the other *trans*-isomer. The conversion between the two isomers can be induced by different wavelengths of lights. The UV corresponding to the energy gap of the  $\pi \rightarrow \pi^*$  transition ( $S_0 \rightarrow S_2$ ) transforms the *trans*-isomer into *cis*, and *vice versa*, the blue light (or longer wavelength) irradiation can induce the *cis*→*trans* isomerization, *i.e.*,  $n \rightarrow \pi^*$  transition ( $S_0 \rightarrow S_1$ ). Generally, the *trans*-isomers are more stable. The basic structural and spectroscopic information are shown in **Figure 4**.

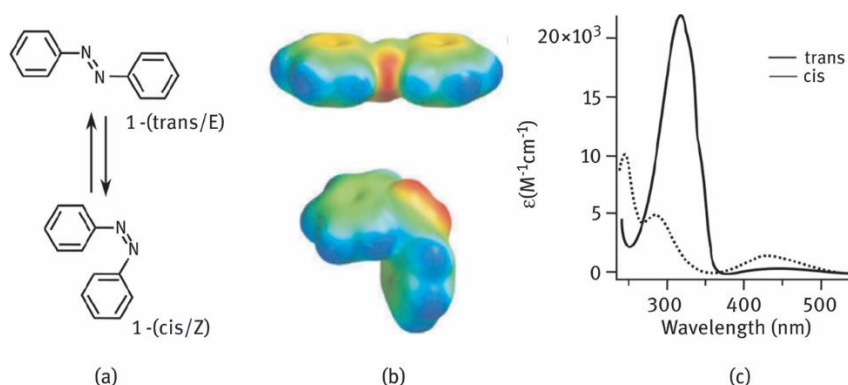


**Figure 4:** (a) Structures of trans- and cis isomers of azobenzene. (b) Space filling models are colored by electrostatic potential (red—negative to blue—positive). (c) Absorption spectra of the trans and cis isomers of azobenzene dissolved in ethanol.<sup>22</sup>

#### 1.1.2.4 DASA

The donor–acceptor Stenhouse adduct (DASA) has been developed as molecular switches since 2014.<sup>23, 24</sup> The **Figure 5** shows the general scheme of DASA and corresponding color changes. DASA can switch freely between extended linear and compact circular forms under different light or thermal conditions, accompanied with changes in molecular dimension and polarity. The DASA possesses a neutral open  $\pi$ -extended color form, which can be converted to a  $4\pi$ -electrocyclic zwitterionic closed colorless form. The backward reaction is driven by thermal activation due to the instability of the zwitterionic closed form. It is worthy to note that DASA molecule here exhibits the negative photochromism.

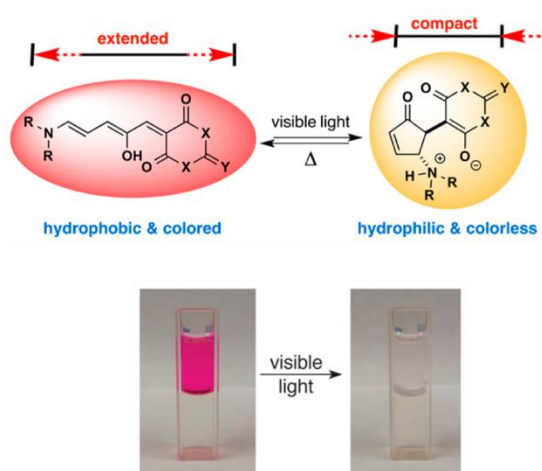


**Figure 5:** DASA photochromism.<sup>23</sup>

Compared to the other photoswitchable structures presented above, DASA molecules can get rid of UV conditions, which can damage the biological tissues. Therefore, the medical applications of DASA molecules are increasing.<sup>25, 26</sup>

## 1.2 FLUORESCENCE

### 1.2.1 Principles

Fluorescence is another essential topic in the world of photoscience. By definition, it represents the light emitted by a substance after absorption of light or electromagnetic radiation.

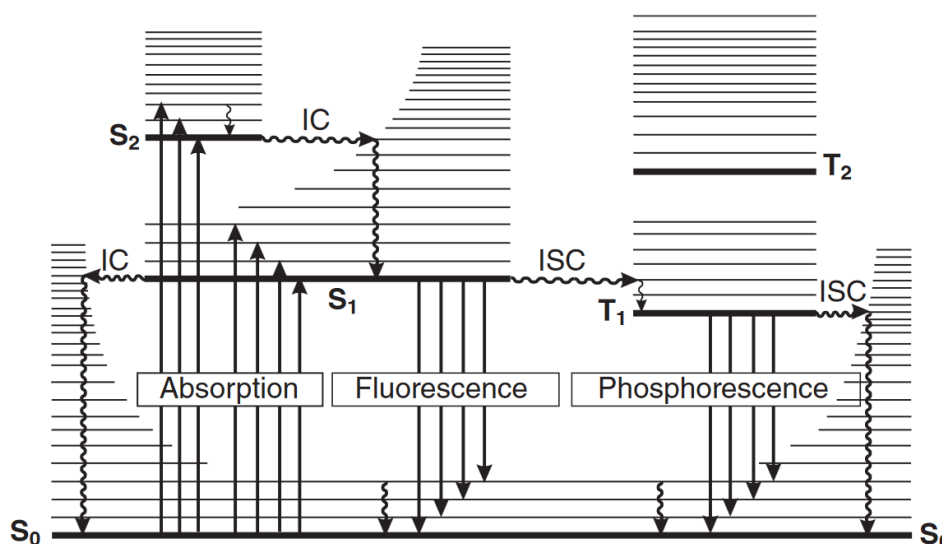


Figure 6: Basic mechanism illustration of the Perrin-Jablonski diagram.<sup>27</sup>

The basic mechanism of fluorescence is shown in the **Figure 6**. In the figure, the ground state and the first and second electronic excited states are depicted as  $S_0$ ,  $S_1$  and  $S_2$ , respectively. The first triplet state is denoted as  $T_1$ . The transition  $S_0 \rightarrow S_n$  displays the process of *light absorption*, which occurs in the femtosecond timescale. The  $S_n$  excited state quickly relaxes to the lowest vibrational level of  $S_1$  (the black bars) through *vibrational relaxation* and *internal conversion* and usually takes place in the picosecond-nanosecond timescales. The *fluorescence* corresponds to the radiative  $S_1 \rightarrow S_0$  transition, in the nanosecond timescale. Further, the  $S_1$  can undergo *intersystem crossing* down to the triplet state with a spin conversion. The relaxation from the lowest triplet state  $T_1$  to the ground state  $S_0$ , which is “forbidden” (kinetically unfavored) in quantum mechanics due to the different spin multiplicity, takes significantly longer time, releasing the long-life phosphorescence, which usually lasts longer than milliseconds. Beyond the simplest illustration above, molecules can also absorb more than one photon at a time, which is called multiphoton excitation, which enables many practical uses such as microscopic bio-imaging or tissue penetrations.

### 1.2.2 Fluorophores

The fluorescent molecules are commonly called fluorophores. According to the demands of specific colors, many fluorophores are developed to emit light covering all the visible wavelengths. As shown in **Figure 7**, I previously synthesized two BODIPY® fluorophores with different chemical modifications, possessing different fluorescent colors.



**Figure 7:** Two modified BODIPY® fluorophores in dichloromethane upon UV excitation.

Interestingly, chemical modifications enable the photochromes introduced above to show fluorescence properties as well under some circumstances, usually connecting or disconnecting the  $\pi$ -conjugation in the molecules, allowing ON/OFF fluorescence trigger effects.<sup>28-30</sup> Moreover, when photochromic molecules are linked to fluorophores, due to the existence of interactions between the photoactive units, the photochromism and fluorescence are not simply independent to each other. In the next section, we introduce the resonance energy transfer (RET) that can occur between chromophores.

## 1.3 INTERACTIONS BETWEEN CHROMOPHORES

Photochromic and fluorescent molecules can connect and interact each other by resonance energy transfer (RET) process.<sup>30</sup> Fundamentally, RET involves an excited donor part, which transfers its energy to the acceptor part in its ground state.

### 1.3.1 Förster resonance energy transfer (FRET)

In applications that connect the photochromism and the fluorescence, Förster Resonance Energy Transfer (FRET) is an important mechanism describing the energy transfer between two light-sensitive chromophores, dividing the pair into a donor chromophore and an acceptor chromophore. Under the framework of FRET, the excited donor transfers its excitation energy to the acceptor part through a non-radiative dipole-dipole coupling between the two electronic transitions. This means that FRET is a distance and orientation dependent process. In multichromophoric systems, FRET can usually be a highly efficient process, due to the close distance between chromophores.

The prerequisites of the FRET process require the spectral overlap of the donor emission and the acceptor absorption. When the FRET process is effective, the emission intensity of the donor is reduced (quenched) and *vice versa*, the emission of the acceptor is enhanced (if the acceptor is fluorescent).

The spectral overlap ( $J$ ) can be calculated following the equation

$$J = \int_0^{\infty} I_F(\lambda) \epsilon_A(\lambda) \lambda^4 d\lambda$$

where,  $I_F(\lambda)$  and  $\epsilon_A$  represent the normalized donor emission spectrum and the acceptor molar extinction coefficient.

The FRET process is largely relying on the distance between the donor and the acceptor. The quantification of the FRET efficiency  $E_{\text{FRET}}$  from the donor to the acceptor is expressed by the equation:

$$E_{\text{FRET}} = \frac{1}{1 + (R_{\text{DA}}/R_0)^6}$$

where  $R_0$  is the Förster radius of the involved D-A pair, *i.e.*, the distance at which the FRET efficiency is 50%. The  $R_0$  can be written by the equation:

$$R_0^6 = \frac{9000(\ln 10)\kappa^2 Q_D}{128\pi^5 N_A n^4} J$$

where  $Q_D$  is the fluorescence quantum yield of the donor in the absence of the acceptor,  $\kappa^2$  is the dipole-dipole orientation factor,  $n$  is the refractive index of the medium and  $N_A$  is the Avogadro constant. The dipole-dipole orientation factor  $\kappa^2$  can be calculated by the following equation:

$$\kappa^2 = (\cos\theta_T - 3\cos\theta_D\cos\theta_A)^2 = (\sin\theta_D\sin\theta_A\cos\phi - 2\cos\theta_D\cos\theta_A)^2$$

where the  $\theta_T$  is the angle between the vector of donor dipole and the vector of the acceptor dipole, and the  $\phi$  is the dihedral between the D-A pair. The factor can be calculated in either way according to the more convenient readouts.

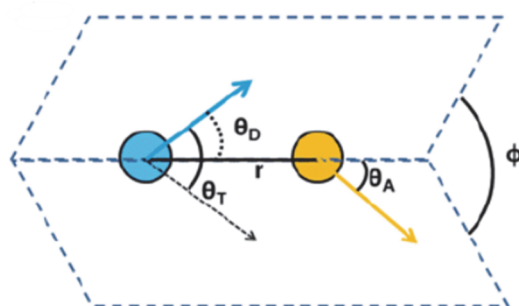


**Figure 8:** Mechanism Illustration of the dipole-dipole orientations on the two panels. The  $\kappa^2$  is calculated by either the vectors or the dihedral.

Mathematically, the  $\kappa^2$  ranges from 0 (perpendicular transition dipoles) to 4 (colinear transition dipoles).  $\kappa^2$  is equal to 2/3 when both the donor and the acceptor are freely rotating in the medium and can be considered as randomly oriented during the FRET process.

All in all, the main FRET principles are:

1. FRET can only occur if the emission spectrum of the donor overlaps the excitation spectrum of the acceptor. This overlap is defined by an overlap integral  $J$ .
2. FRET is generally observed if the distance between the two fluorophores is less than twice the Förster radius ( $R_0$ ), the latter defining the donor-acceptor distance at which the energy transfer efficiency is 0.5.
3. Favorable relative orientation of the donor and acceptor transition dipoles is necessary for the energy transfer process (better if parallel or colinear, canceled if perpendicular).

### 1.3.2 The different fluorophore-photochrome associations

We divide the fluorophore-photochrome associations into three categories. The criterion of the classification is based on the association type between the units.

**Type I:** refers to intrinsic fluorescent photochromic molecules. The type I photochromes can also be called photoswitchable fluorophores, and they can trigger ON/OFF fluorescence themselves or different colors of fluorescence. **Figure 9** displays an example of high-performance photochromic-fluorescent DAE developed by Uno *et al.*,<sup>31</sup> which is a typical type I photochrome. In addition, the photoswitch delivered by

photochromism structures can not only trigger ON/OFF fluorescence, but two different emission colors as well. As shown in **Figure 10**, a DAE molecule developed by our group displayed photoswitchable blue and green fluorescence.<sup>32</sup>

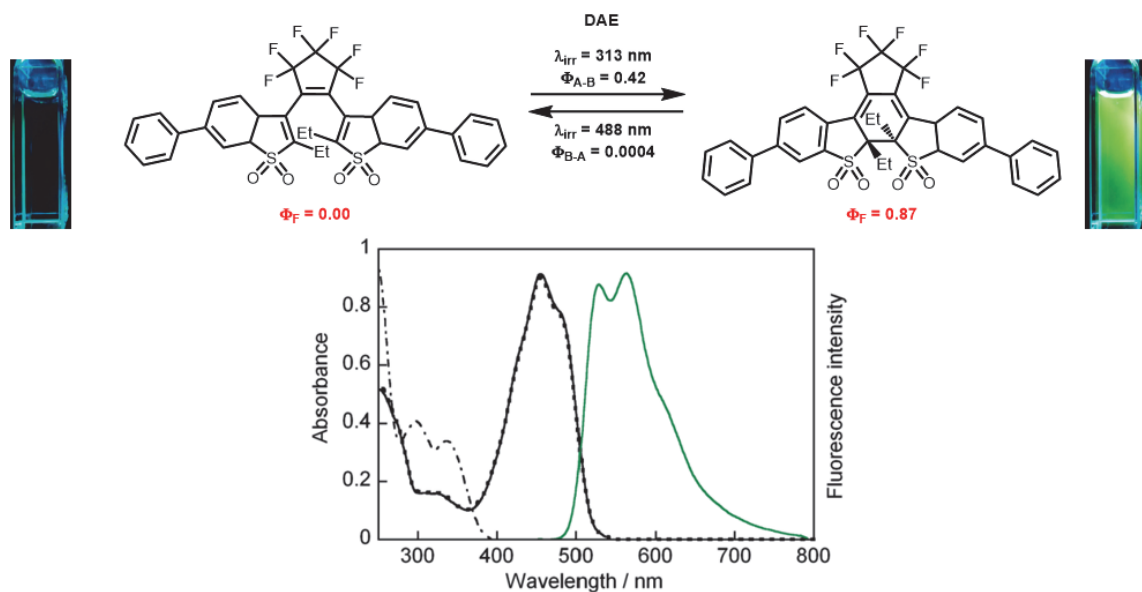


**Figure 9:** The structures of the fluorescent DAE reported by Uno et al. to obtain the fluorescence quantum yield as high as 0.87 and its corresponding absorption fluorescence profile.<sup>31</sup>

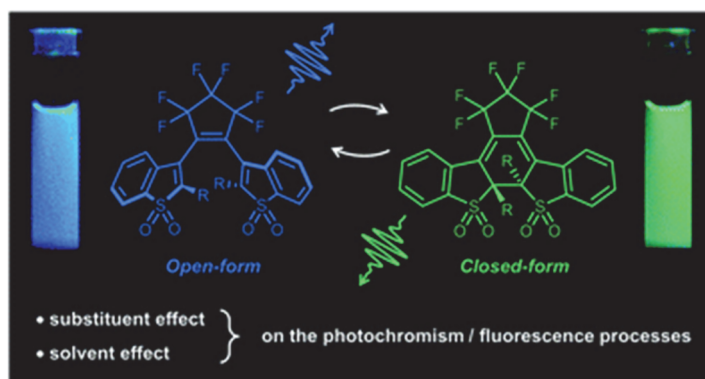


**Figure 10:** Photochromic-fluorescent DAE of OF-blue and CF-green dual states.<sup>32</sup>

**Type II:** refers to covalently linked photochromic and fluorescent molecules. The type II systems usually take advantage of the FRET between the photochrome and the fluorophore, presenting a molecule in a dyad form. Usually, the photochromic part acts as the fluorescence quencher in one of its two forms, by means of a FRET process (or sometimes a photoinduced electron transfer process), to switch ON/OFF the emission of the fluorophore.

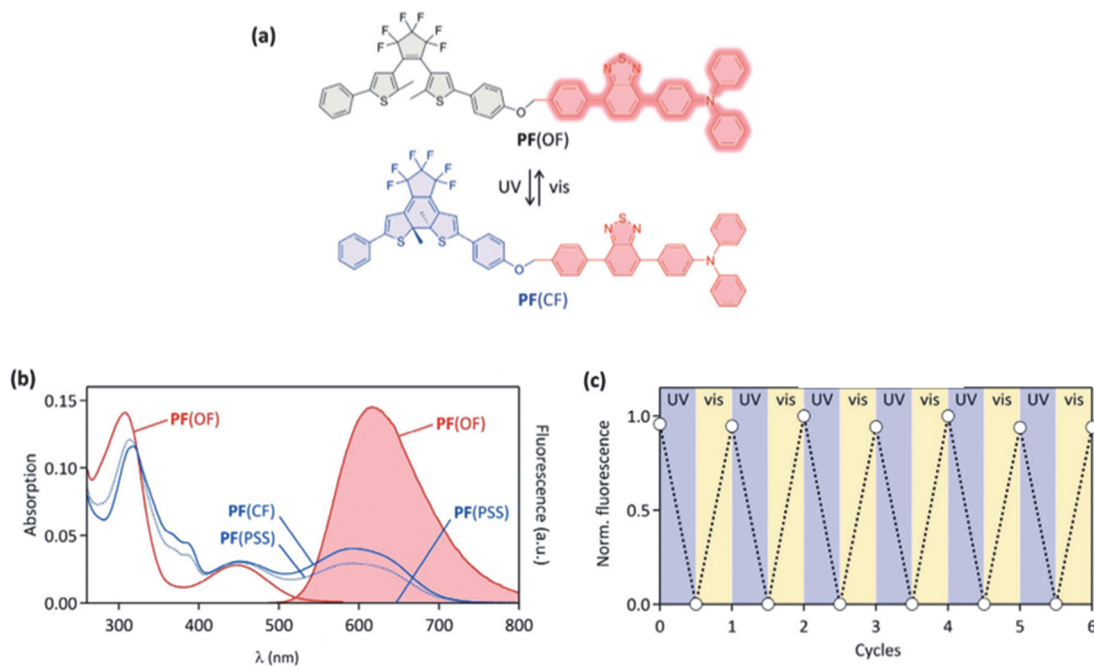


**Figure 11:** (a) Chemical structure of the PF dyad (DAE in blue, BTD in red). (b) Absorption and emission spectra. (c) The ON/OFF fluorescence performance by photochromism of DAE moiety.<sup>33</sup>

As shown in **Figure 11**, the PF dyad developed in Fukaminato's group and studied in our group<sup>33</sup> belongs to the **Type II**, composed of a photochromic DAE and a benzothiadiazole (BTD) fluorophore. By switching the DAE between its OF and CF, the dyad realizes the ON/OFF fluorescence photoswitching, thanks to an efficient FRET when the DAE is in the CF. The **Type II** dyads must obey the rules of the spectral overlap, *i.e.*, the emission of the fluorophore must overlap the absorption of one form (only) of the photochrome part. In addition, a suitable excitation wavelength is also necessary and must be carefully considered.

**Type III:** refers to non-covalently linked photochromes and fluorophores, in systems such as micelles or nanoparticles. As for the example shown in **Figure 12**, FRET can occur between the DAE and the Cy3 fluorophore at the surface of the dendritic nanoclusters.

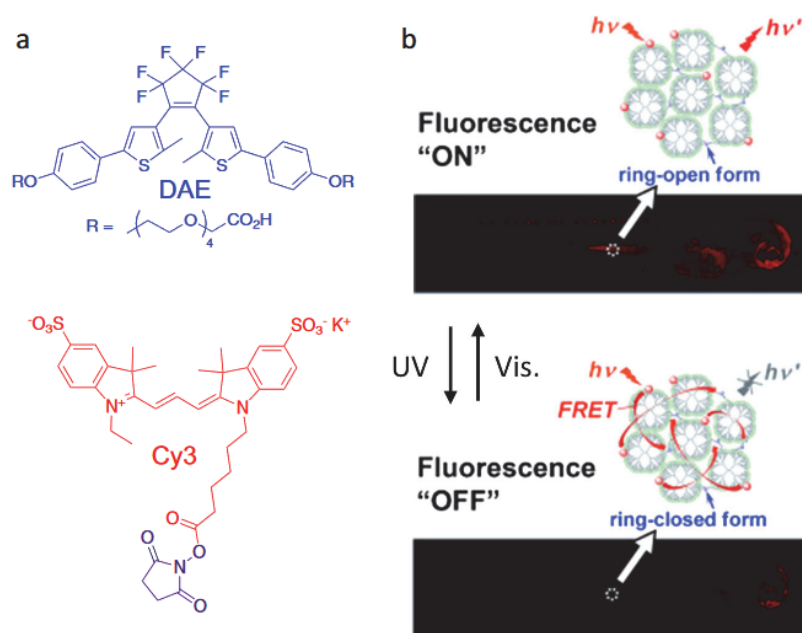


**Figure 12:** (a) Molecular structures of a DAE switching unit and a fluorophore Cy3. (b) Photoswitching experiments, performed on



living zebrafish with dendritic nanoclusters internalized by permeation, upon alternate irradiation with UV/visible light. Red circles represent the Cy3.<sup>34</sup>

### 1.3.3 DCM photoswitchable fluorophore

The DCM abbreviation refers to 4-dicyanomethylene-2-methyl-6-(4-dimethylaminostyryl)-4*H*-pyran, which has been known as red laser dye since the last century.<sup>35-38</sup> Some DCM-derivatives (bis-dimethylaminostyryl and 4-(dicyanomethylene)-2-4-*tert*-butyl-6-(1,1,7,7-tetramethyljulolidin-4-yl-vinyl)-4*H*-pyran DCJTB) are actively used in the fabrications of dye sensitive solar cells (DSSCs) and organic light emitting diodes (OLEDs).<sup>39-41</sup> In DSSCs, the DCM derivatives are used as the interface substances retarding the charge recombination between the donors and the acceptors. In OLEDs, they are used as the dopant to the red emissive layer to provide stable red emission with electric circuits.

At a glance of the structural composition, DCM has an aniline conjugated to the electron-withdrawing dicyanomethylene-pyranyl moiety, providing its charge transfer character and subsequent solvatochromism. At the very beginning, it was discovered to have the high tuning range and great dye efficiency compared to other fluorophores, *e.g.*, rhodamine 6G or cresyl violet. Its thermal stability is also remarkable with a boiling point over 200°C. Therefore, DCM finds applications in a variety of fields: logic gates, non-linear optical material developments, chemo- or biosensors as well. The studies on DCM have already demonstrated the strong photoinduced intramolecular charge transfer nature of its emissive excited state with time-resolved spectroscopic techniques and theoretical calculations.<sup>42, 43</sup>

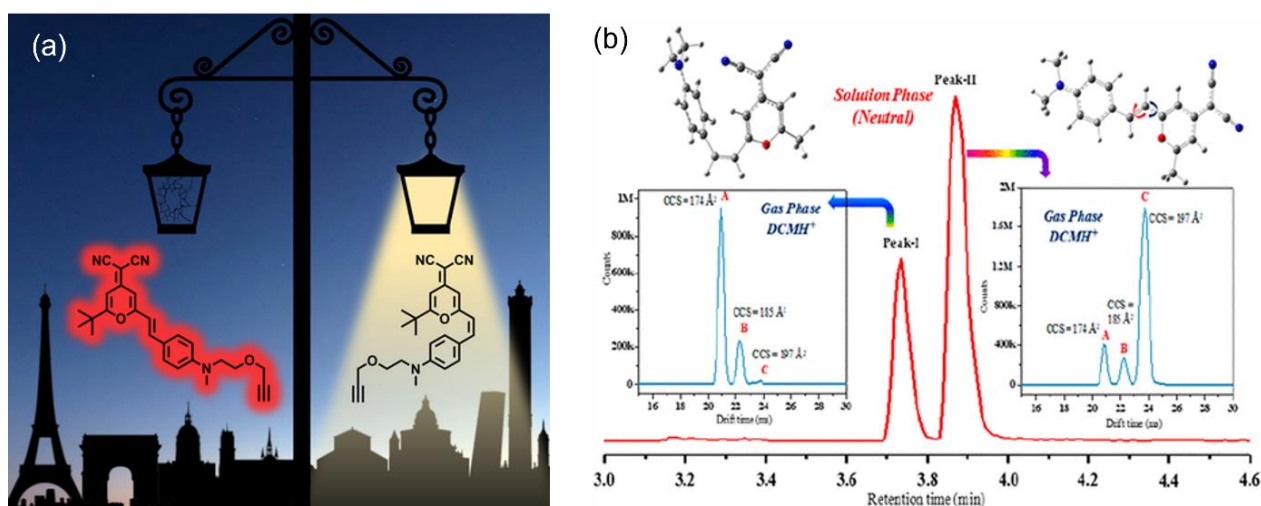


**Figure 13:** (a) Illustration of ON/OFF fluorescence of a E↔Z photoisomerizable DCM derivative in solution.<sup>3</sup> (b) Ion-mobility mass spectroscopies chromatograms of the DCM isomers and rotamer in methanol at gas phase.<sup>44</sup>

However, investigations of DCM in solution have been updated by our group in 2020.<sup>3</sup> As shown in **Figure 13 (a)**, the C=C double bond bridging the dicyanomethylene moiety and the aniline part of the molecule makes DCM photoisomerizable. The C=C double bond isomerization and the different *s-cis* and *s-trans* conformations by the adjacent C-C single bond rotation led to four isomers and conformers of DCM. Different isomers are also detectable with the help of modern ion-mobility spectrometry mass spectrometry (IMS-MS) in 2020, which is shown in **Figure 13 (b)**.<sup>44</sup>



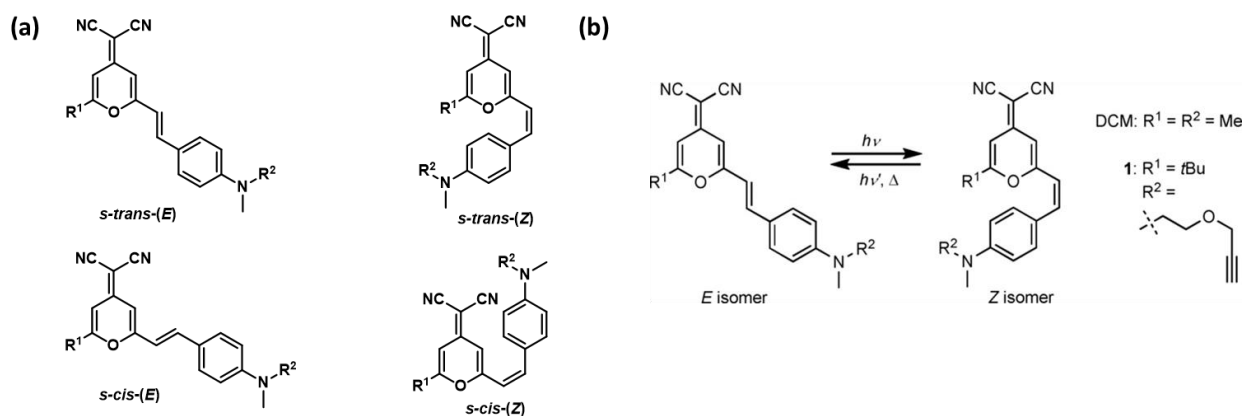


**Figure 14:** (a) The four stable isomers and conformers of DCM derivatives. (b) Scheme of the DCM photoisomerization.<sup>3</sup>

The best solvent for the photoisomerization of DCM was identified to be THF, as a trade-off between fluorescence and photoisomerization properties. The photoinduced Z-isomers, isolated by high performance liquid chromatography (HPLC), have a much lower molar absorption coefficient (at 467 nm in THF) compared to the synthesized E-forms. The fluorescence lifetime measured by a time-correlated single-photon counting (TCSPC) technique recorded the fluorescent components unchanged before and after the light irradiation, which solidly provides the evidence of the non-emissive property of Z-isomers.<sup>3</sup>

As the conclusion of this work, the DCM derivative can act as a photoswitchable fluorophore with rather high efficiency in given conditions. We ascribe DCM and its derivatives into **Type I** photochromic-fluorescent system (**Chapter 1.3.2**).

## 1.4 MULTICHROMOPHORIC SYSTEMS

When talking about multichromophoric systems, the most famous categories are the biological photosynthesis and the light-harvesting systems. They are composed of chromophoric molecules that absorb light efficiently, with featured arrangements. For example, the naturally existing light-harvesting complex II (LHC II) inspired artificial photosynthetic mimics that have been studied for years.<sup>45, 46</sup>

Therefore, chemists design and manufacture multichromophores not only for the biological mimics, but also to prepare high-performance optical and optoelectronic materials. Gathering multiple chromophores, novel properties could be obtained, such as wider emission wavelengths,<sup>47</sup> ultrafast excitation energy transfer,<sup>48</sup> etc. Like the LHCs in the natural photosynthesis system, the chemically synthesized multichromophores, e.g., **Figure 15**, enable the light absorbing donor chromophores and the light emitting acceptor chromophores to work in a wider range of absorbing light, facilitating the efficiency of the photophysical processes.<sup>49</sup>

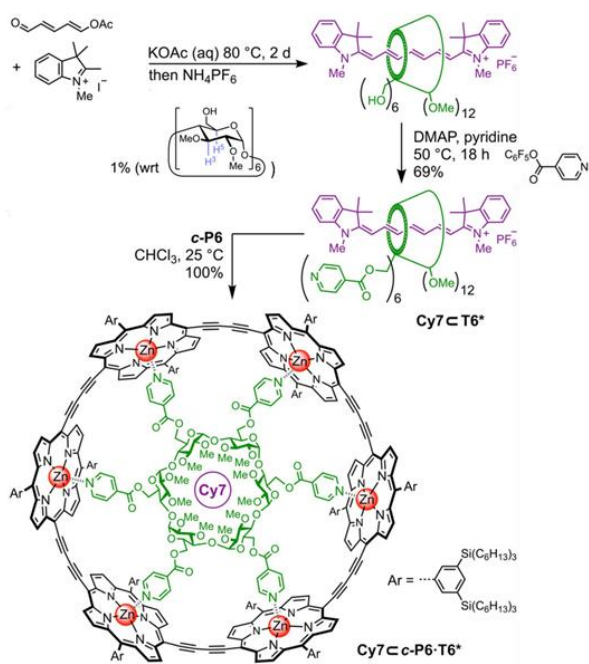


**Figure 15:** A synthesized model light-harvesting system comprising a cyanine dye rotaxane and a porphyrin nanoring.<sup>49</sup>

In bio-imaging applications, multichromophores can have bi-color luminescence depending on the location of biological systems.<sup>50</sup> The dye sensitive solar cells are also welcoming the design concept, especially for the category of organic photovoltaics (OPV) to be used in soft materials in weak light environments, absorbing the larger band of ambient light.<sup>51, 52</sup>

### 1.4.1 Dendrimeric multichromophoric systems

For the enhancement of light absorption, photosynthetic systems and their light-harvesting mimics are usually constructed in the way of dendrimer topologies. The reaction center is usually placed in the center of one structure, and the light-harvesting fragments are branched outside to grow as many chromophores as possible to enhance the absorption efficiency. In the light-harvesting complexes (LHC) and most artificial mimics, almost all the energy is absorbed at the periphery followed by energy transfer to the core center. The resonance type energy transfer pathways in the dendrimers have two typical models: the direct RET and the successive RET shown in **Figure 16**.<sup>53</sup> The former sees all the branching units as the same and transfer the energy to the core center with identical probability. The latter one is more efficient due to the formation of an excitation energy gradient. The higher energy branching units transfer their excitation energy to the intermediate node branching units, and the lowest energy core reaction center accepts the excitation energy from the intermediates.

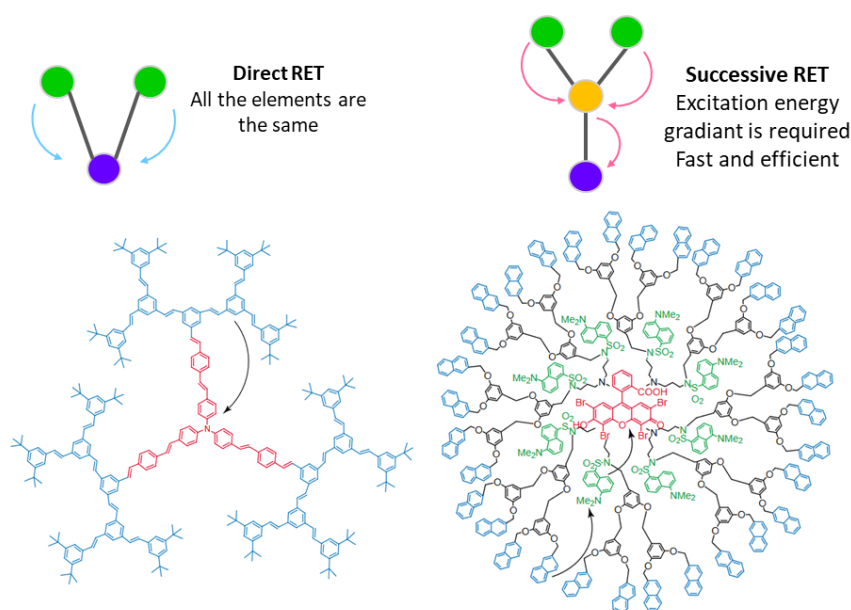


**Figure 16:** The direct RET shown in the left is functionalized by the equivalent branching unit to the end reaction center. The successive RET shown on the right has a surface unit layer and the higher energy intermediate to occur layer to layer ET.<sup>53</sup>

The mechanisms of RET in dendrimers can be Dexter and Förster type. Especially due to the existence of the direct RET type dendrimers, the FRET is the most popular in the field. The studies about the structural D-A pairs in the multichromophoric systems are developing along with the growing interest for these systems and the computational power to simulate them. For instance, I. Oh *et al.* have quantified the donor number and D-A pair distance effects in a multichromophoric system.<sup>54</sup> Porphyrin dendrimers were designed into different D-D distance and D-A numbers to observe their influence on the FRET efficiency inside the multichromophores, as shown in the **Figure 17**. As a result, keeping the structural heterogeneity and increasing the number of donors will facilitate the FRET efficiency.<sup>54</sup>

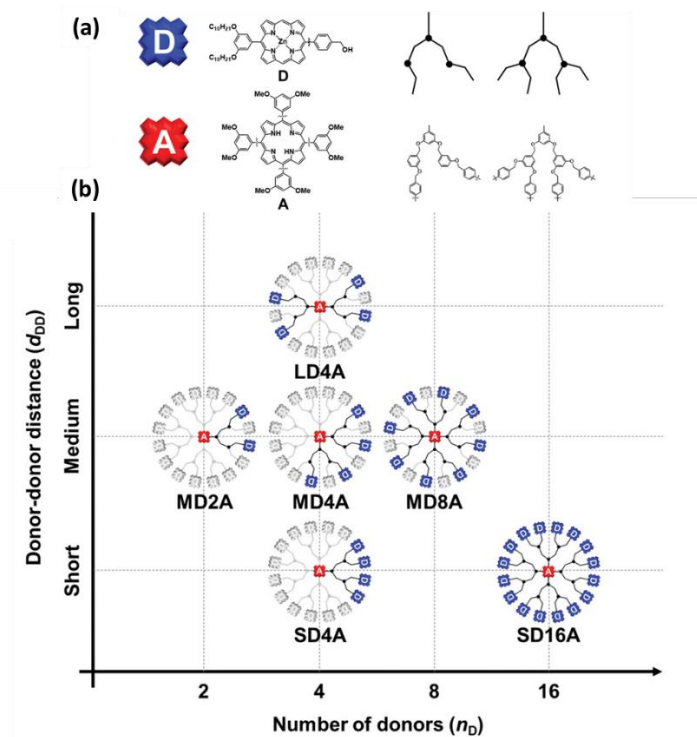


**Figure 17:** The multichromophoric system studies by I. Oh *et al.*<sup>54</sup> (a) The chemical structures of the donor, the acceptor, and the linker. (b) Structures of multiporphyrin dendrimers represented as a function of the number of donors and the donor-donor

distance. The actual structures are sphere 3D rather than the 2D planar. Each Zinc porphyrin donor (D, blue) is connected to a free-base porphyrin acceptor (A, red) by the linker.

Beyond the multichromophoric systems consisting of traditional donors and acceptors, the perspective to embed photoswitchable units represents another strong interest. The photochromic units can be used as photoswitches to turn ON/OFF or enhance/lower the intramolecular FRET, and following, influence the whole system. For example, in the **Figure 18**, stilbenes or azobenzenes can adopt a bent structure upon illumination and drag the other chromophores closer to (or further from) the dendrimer cores.<sup>55-57</sup>

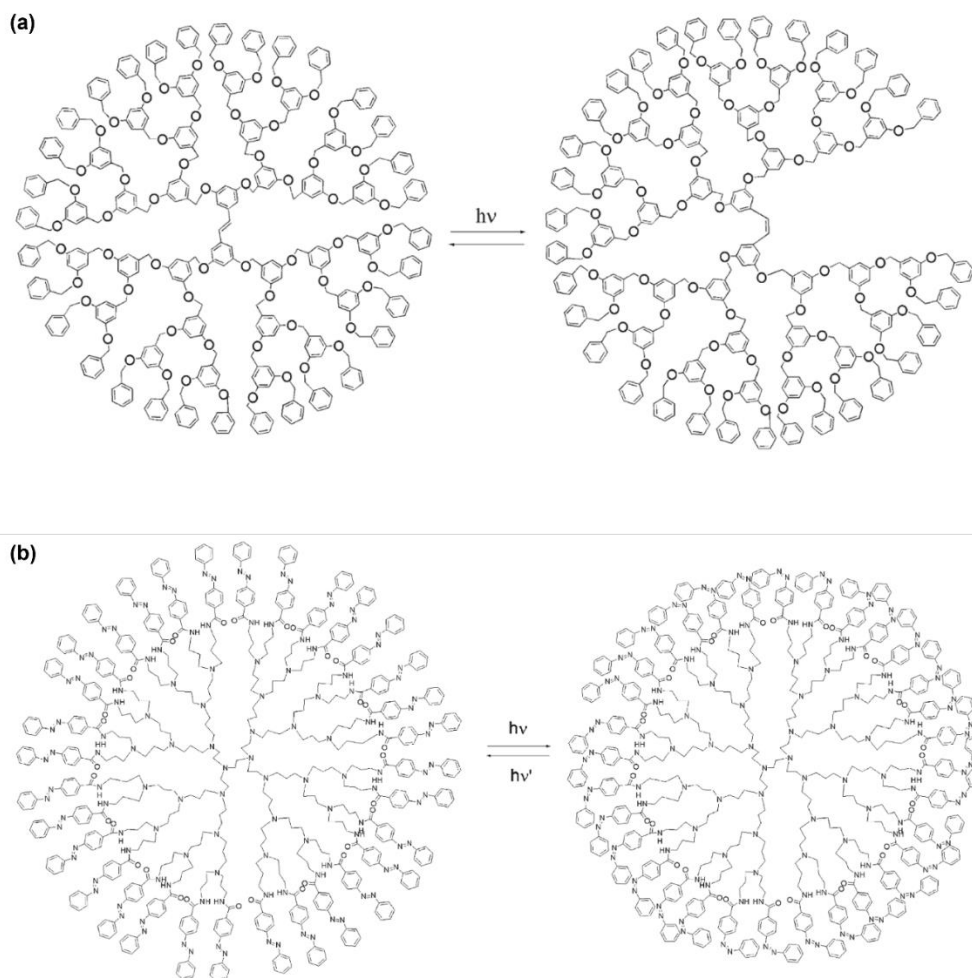


**Figure 18:** (a) One example of central stilbene, able to change the topology of the whole dendrimeric molecule under light irradiation.<sup>57</sup> If intramolecular energy process exists, the efficiency will be affected correspondingly.<sup>55</sup> (b) Multiple photoisomerizable azobenzene located in the outer part of the dendrimeric multiphotochrome system.<sup>58</sup>

## 1.4.2 Multiphotochromic systems

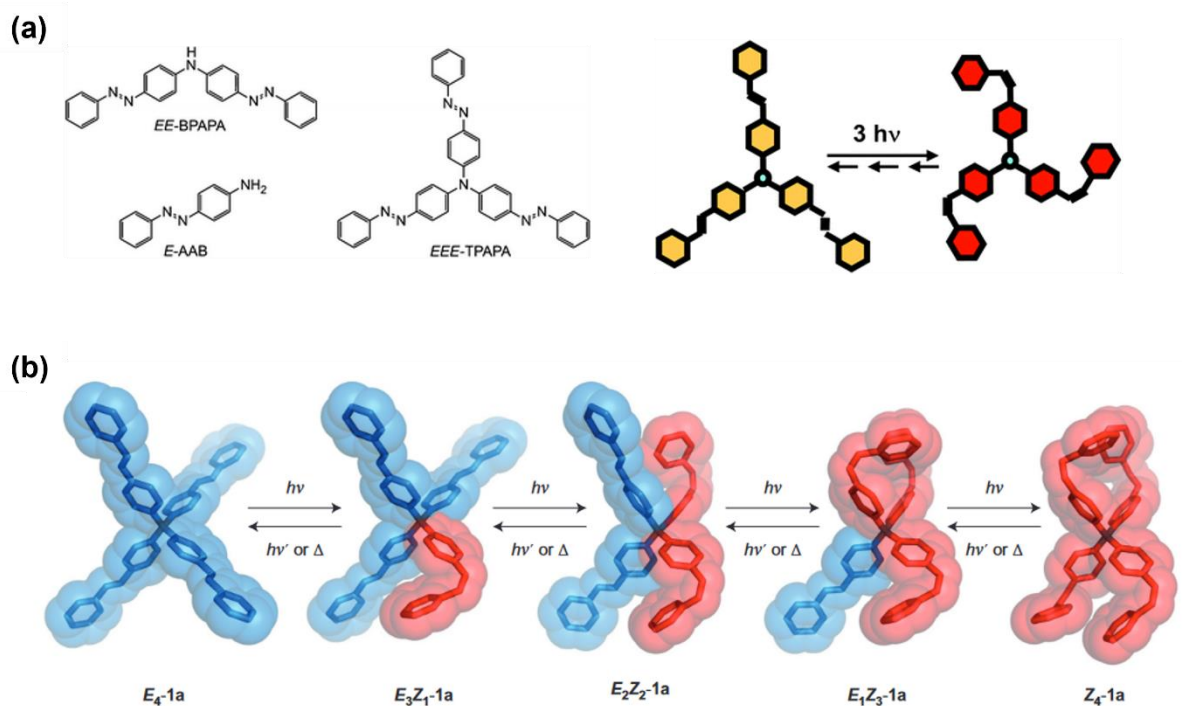


**Figure 19:** (a) The azobenzene (*E*)-AAB and multi-azobenzenes (*EE*)-BPAPA, (*EEE*)-TPAPA.<sup>59</sup> (b) The molecular mechanics (MM3) optimized interconverting *E*↔*Z* of azobenzene tetramer.<sup>60</sup>

Besides the giant dendrimeric molecules with numerous chromophores inside or outside, the multiphotochromes in dyads or triads, composed of several photoisomerizable molecules, are often studied as multi-state photoswitches.<sup>61</sup> J. Bahrenburg *et al.* have reported a series of multi-azobenzenes which shows non-linear photoswitching effects in solution.<sup>59</sup> An azobenzene tetramer reported by M. Baroncini *et al.* shown in **Figure 19** enables the reversible conversion between the molecular crystal porosity in *E*-configuration capturing CO<sub>2</sub> from gas phase and the amorphous melt phase in *Z*-configuration.<sup>60</sup> With heterogenous composition of chromophores, F. G. Erko *et al.* have reported a triphotochromic naphthopyran flanked by two DAEs which is capable of switching the naphthopyran and the diarylethene independently or with constraints by sequential isomerizations displayed in **Figure 20**.<sup>62</sup>

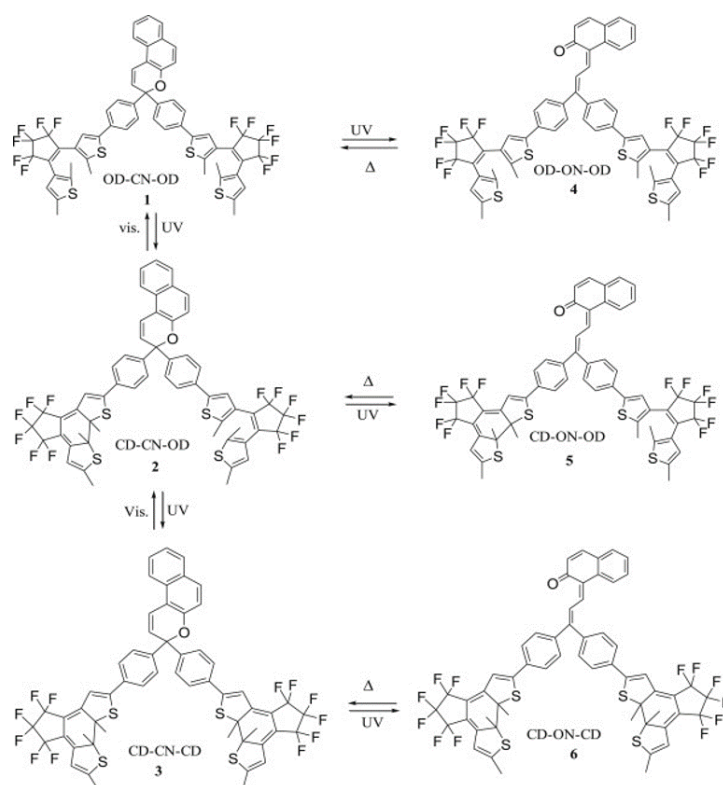


**Figure 20:** Photochemical and thermal interconversion of the six states of triphotochromic naphthopyran with diarylethenes.<sup>62</sup>

From the literature, we can note that constructing a multichromophoric system with photoisomerizable molecules is a challenging work, especially to coordinate the subunits together. Regarding the design of suitable energy transfer processes between donor and acceptor pairs, the work could be even more complex. To build photoswitchable system, multichromophoric structures could be used to enhance the desired performance, *i.e.*, the fluorescence ON/OFF contrast or the light harvesting efficiency to exploit broader visible light range, for instance.

The design of the multichromophoric systems presented in this PhD dissertation includes either homogeneous or heterogeneous chromophoric constitutions. The intramolecular FRET processes within the molecules are the focus point to be investigated. Especially, the heterogeneous ones with two photoisomerizable units interacting through FRET, the competition between the photoisomerization and the intramolecular FRET will lead to novel photophysical effects and optical properties, such as the recent discovery of our laboratory: the *photoswitchable fluorescent hysteresis effect*.

## 1.5 HYSTERESIS EFFECTS

Before introducing the concept of *photoswitchable fluorescent hysteresis effect*, it is of primary importance to describe the hysteresis effect, its impact for future scientific developments, and the main important criteria for the design of our new molecular multichromophoric architectures.

### 1.5.1 Principles

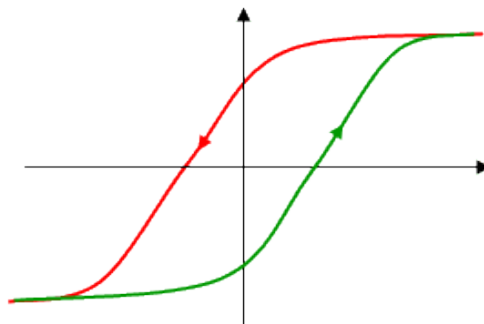


**Figure 21:** The curves form a hysteresis loop.

Hysteresis effect refers to the delayed pathway from one state to another. Like the difference between routes, the national road and the highway express both can reach the destination, however, the same tank load of oil as the input will not reach the same reaching time if you plot the remaining oil vs. remaining range.

### 1.5.2 Some examples of hysteresis effect in scientific developments

The more scientific definition of the hysteresis effect describes that the nature of a system not only depends on the current input parameters but relies on its history and pathways. In nature, hysteresis effects are often caused by phase transitions which are accompanied by abrupt changes of some of the involved physical quantities, as well as by the absorption or release of energy in the form of latent heat. Hysteresis effect is ubiquitous, and in scientific scenarios it exists as magnetic hysteresis,<sup>63, 64</sup> ferroelectric hysteresis,<sup>65</sup> mechanical force hysteresis,<sup>66</sup> adsorption hysteresis,<sup>67, 68</sup> optical hysteresis,<sup>69, 70</sup> charge transfer hysteresis,<sup>71</sup> etc.

The visualization chart to describe a hysteresis effect is usually expressed as a closed loop shape formed by two independent variables from a system. In the daily life, one of the most common occasions to meet the hysteresis effects is probably the lithium-ion battery charge-discharge process in the following **Figure 22**.

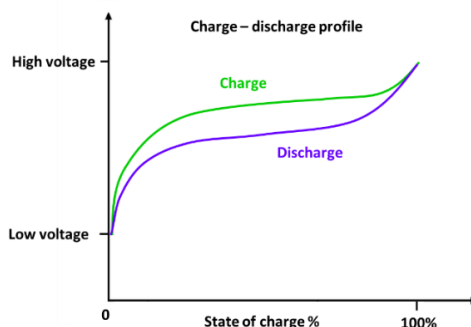


**Figure 22:** The illustration of a hysteresis effect in a lithium-ion battery.



During the charging process, the chemical reaction lags behind the input of charging voltage and *vice versa* during the discharging process. The input from the outside electricity supply and the inside battery load are in advance accompanied with an energy loss depending on the chemical reaction, causing the hysteresis effect. The modern battery management system (BMS) chip designs aim to smartly adjust the charge-discharge tactics according to extra environmental variables to reduce but not to eliminate the voltage hysteresis effect.<sup>72</sup>

The hysteresis effect has miscellaneous great applications in physics, material science and biology, especially existing with nano materials.<sup>73-75</sup> Fluorescence hysteresis is a phenomenon sometimes observed in optoelectronics. Hania *et al.*<sup>76</sup> reported the fluorescence hysteresis of poly(2-methoxy-5-(2-ethylhexyloxy)-1,4-phenylene-vinylene (MEH-PPV) embedded in polar poly(methyl methacrylate) (PMMA) matrix by means of a electric field. Zhou *et al.*<sup>77</sup> further reported one model with squaraine-derived rotaxanes embedded in PMMA shown in **Figure 23**, successfully induced fluorescence hysteresis under the electric field.

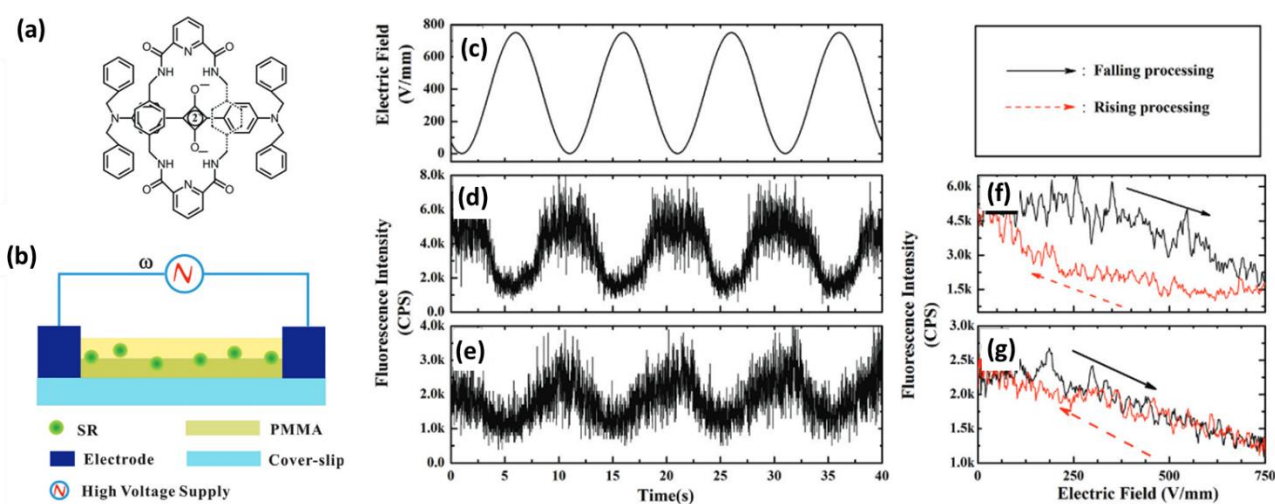


**Figure 23:** (a) Chemical structure of SR. (b) The side view of the electric field applied substrate structure. SRs are spin-coated on the spin-coated PMMA and covered by another layer with the same method. (c) Periodic sine wave of electric field applied on the SR. (d) and (e) are two typical fluorescence response trajectories of SR SMs in PMMA matrix under the varying electric field with the maximum strength of 750 V/mm, respectively. (f) and (g) are the electric field-fluorescence intensity curves for asymmetric and symmetric fluorescence quenching and recovering processing by averaging the fluorescence profiles from (b) and (c), respectively. Considerable hysteresis effect can be observed in (f).<sup>77</sup>

By adding a sine wave intensity of electric field, both the non-instantaneous and instantaneous fluorescence responses are recorded. The author explains it with an electron transfer theory between the electron acceptor PMMA and the donor SR. The ambient of SR caused different anisotropy of SRs will change the fluorescence response, and the non-instantaneous responses show the fluorescence hysteresis effect as function of the electric field.<sup>77</sup>

### 1.5.3 Towards photoswitchable fluorescence hysteresis effect

To the best of our knowledge, the photoswitchable fluorescence hysteresis effect has not been reported to date. In this section, we will introduce the previous work, the implementation methodology, and the characterizations of realizing the photoswitchable fluorescence hysteresis with a multichromophoric architectures.

We have talked about the RET, the connection of photochromism and fluorescence, and the photoisomerizable species in multichromophoric systems. If we want to realize the photoinduced fluorescence hysteresis, it requires distinct photochromic and photoisomerizable fluorescent units, ideally in a multichromophoric system to favor efficient FRET. The simplest way to reach this effect is to find a



photoisomerizable fluorophore that can undergo ON/OFF fluorescence photoswitching by itself (**Type I**, cf. **Section 1.3.2**) and interact with another photochrome by means of FRET (**Type II**, cf. **Section 1.3.2**).

By the knowledge and availability in our laboratory, the dicyanomethylene-4*H*-pyran is chosen to play the role of the intrinsic photoisomerizable fluorophore. The photochromic counterpart is based on the diarylethene unit, synthesized by Dr P. Yu's group (ICMMO, Univ. Paris-Saclay).

### 1.5.3.1 The pioneering exploration

The previous research in the group related to the combination of these two units was first a simple DCM-DAE dyad.<sup>2</sup> At that time, the photoisomerizable nature of DCM was not yet identified. Nevertheless, the photophysical characterization showed that the DCM-DAE dyad worked as a fluorescence photoswitch with a highly efficient FRET.

Then, Maisonneuve *et al.* reported a sugar-based tetrachromophoric compound (**Figure 24**),<sup>78</sup> for which the increasing number of DCM units improved the fluorescence signal, thanks to the brightness of DCM. The original intention on this work was to induce the full quenching effect in the working wavelengths to obtain a [0 1] logical write-erase effect with only one tetrachromophoric composition shown in **Figure 24**.

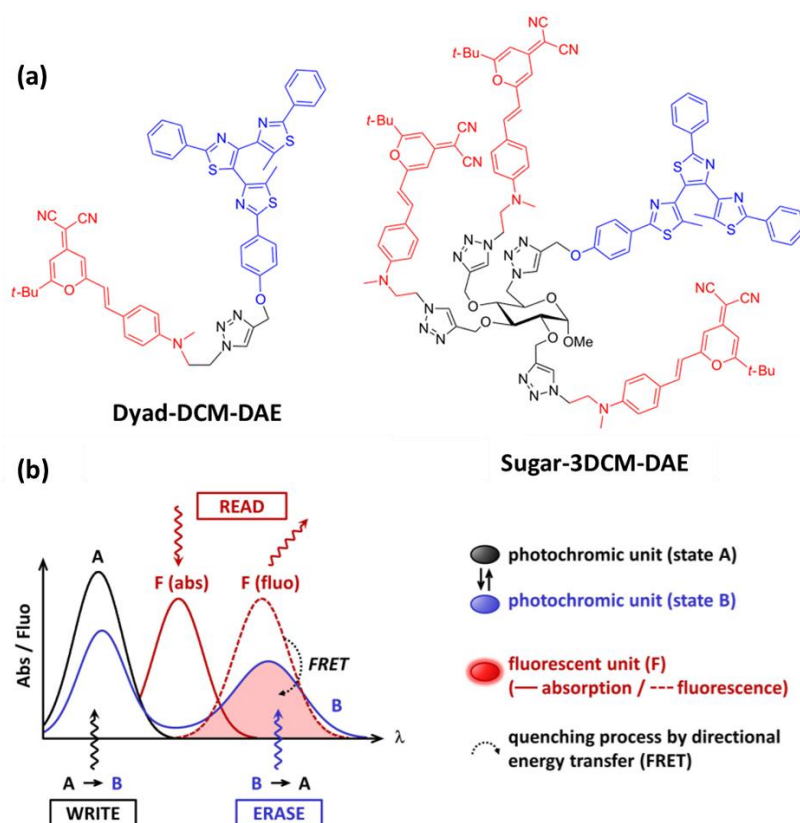


**Figure 24:** (a) Chemical structures synthesized previously in the PPSM laboratory.<sup>2, 78</sup> (b) Conceptual illustration of the fluorescence photoswitching of DCM based on FRET processes with the DAE in the CF.<sup>78</sup>

### 1.5.3.2 Fluorescence hysteresis implementations

In the following research described in Dr S. Maisonneuve's PhD work, the synthesis of a series of multi-DAE molecules, including mono-, tri- and hepta-DAEs was made, based on a glycoside and a  $\beta$ -cyclodextrin platform.<sup>79</sup>

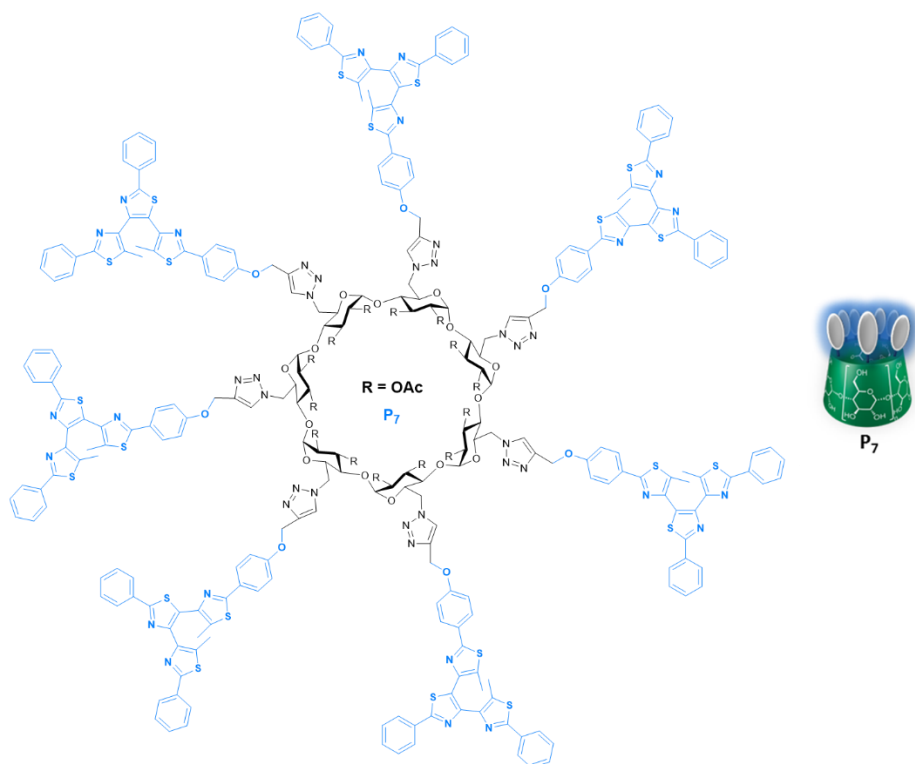


**Figure 25:** Chemical structure of the 7-DAE  $P_7$  molecule synthesized by Dr S. Maisonneuve.<sup>79</sup>

These multi-DAE molecules showed an efficient and reversible fluorescence photoswitching upon illumination, the fluorescence quenching efficiency being enhanced by the increasing number of DAE units. In addition, a non-linear effect was demonstrated between the fluorescence quenching under UV irradiation, due to multiple FRET processes. Moreover, the forward (under UV irradiation) and backward (under visible irradiation) pathways are not equivalent, as shown in the fluorescence vs. conversion yield plot displayed in **Figure 26**, leading to a hysteresis cycle. This is the first generation of photoswitchable fluorescence hysteresis molecules.

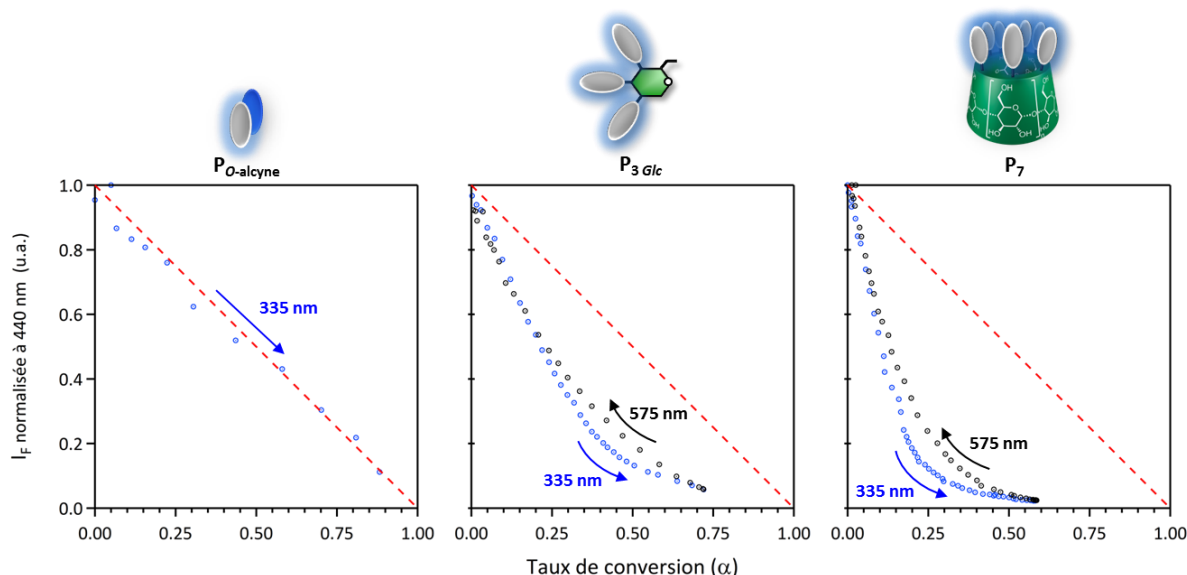


**Figure 26:** Demonstration of the fluorescence hysteresis of the 7-DAE molecule, exhibiting the non-linearity under the irradiation of 335 nm (forward) and 575 nm (backward).<sup>79</sup>

### 1.5.3.3 Further developments of photoswitchable fluorescence hysteresis

Thanks to the DCM fluorophore, which we have mentioned above to photoisomerize through C=C double bond  $E \leftrightarrow Z$  photoisomerization, some improvements were already obtained on the photoswitchable fluorescence hysteresis: the combination of a single DCM unit with three DAE could lead to a very interesting molecular system (**Figure 27**). It involves DCM, which can be photoisomerized between its  $E$  (emissive) and  $Z$  (non-emissive) states, DAE which can be photoswitched between its OF and CF, and FRET processes, which can induce fluorescence quenching of the DCM fluorophore when at least one DAE is in its CF. Such a combination of molecular units and interchromophoric interactions led to a much larger fluorescence hysteresis shape, as shown in **Figure 27**. This is the second generation of photoswitchable fluorescence hysteresis molecules.

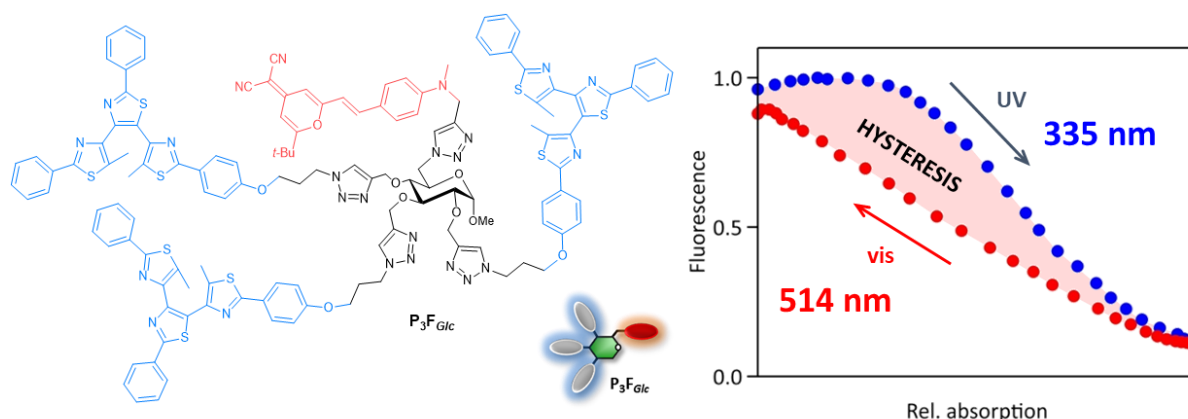


**Figure 27:** The chemical structure of  $P_3F_{Glc}$  and its fluorescence hysteresis shape at the 335/514 nm irradiation combination. (unpublished result)<sup>79</sup>

In the next stage, as well as the main target of this PhD work, we would like to synthesize the third generation of photoswitchable fluorescence hysteresis molecules. Given the previous experience of the group, we would like to have:

1. A higher number of DAE units connected together, with a lower number of DCM units in a FRET allowed distance range.
2. More efficient fluorescence quenching of DCM by the DAE units, while not disturbing the working wavelengths.
3. Non-fluorescent DAE to reduce the complexity of the fluorescence hysteresis system and help to set up the theory more solidly based on the FRET mechanism.

Additionally, the ON/OFF fluorescence contrast cannot be solely attributed to the DAE in the CF, but also to the photoisomerizable property of DCM. Therefore, the studies on homogenous multiple DCM units will be advantageously discussed in the Chapter III as the fulfillment of the studies and the methodology presets for the Chapter IV.

In summary, the implementation of fluorescence hysteresis requires an optimal combination of the DCM-DAE in multichromophoric configurations, allowing efficient intramolecular FRET processes between the different chromophores.

## 1.6 SYNTHETIC TACTICS

Despite the DCM and DAE chromophores, the multichromophoric systems need platforms to link these chromophores covalently together. We are particularly interested in synthesis of dendritic linkers which are versatile for general uses, and in synthesizing larger molecules by utilizing the concept of *Click Chemistry*.

## 1.6.1 Dendritic linkers

Dendritic architectures in chemistry represent now an important area of conventional polymer chemistry and glycobiology.<sup>80, 81</sup> The classification of these chemical structures can be divided into three main structurally controlled categories: dendrigrafts, dendrons and dendrimers.<sup>82-85</sup> The dendrigrafts are centered with a linear polymer axis chain able to connect the branches of the co-axis chains. Dendrons and dendrimers are the most investigated subsets of dendritic chemical structures. Dendrons have focal points, which are chemically addressable groups, and they are growing in a way like a tree diagram. Because of the existence of the focal points, the dendrons are also capable of being constructed to form a dendrimer. Dendrimers are regularly branched structures. An ideal dendrimer possesses a center, a spherical topology, monodisperse and repetitive chemical units. They are quite different to the conventional polymers, since the dendrimers can control the product dimension, the molecular weight, etc. The chemical properties are controllable to some extents by substituting the building blocks.

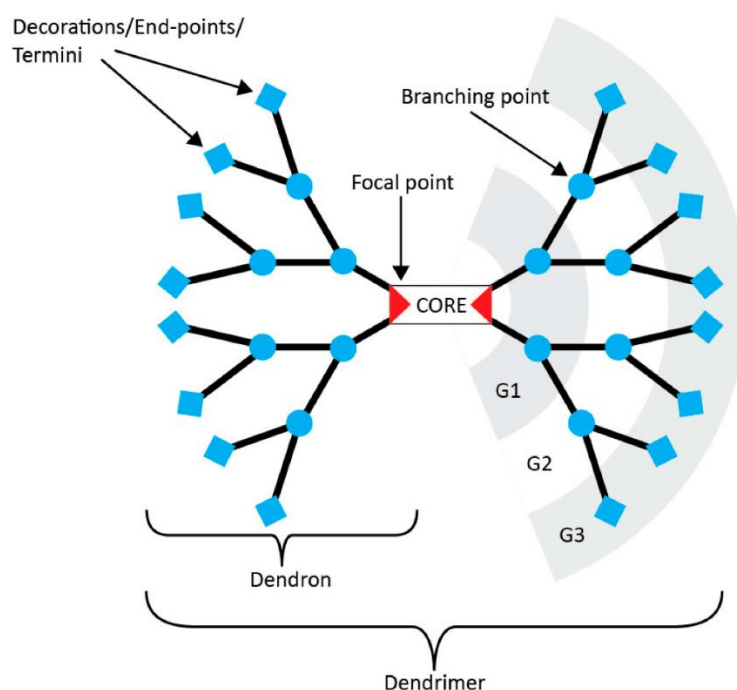


**Figure 28:** Anatomy of a dendrimer. This is an example where each branch is made of a monomer A (blue circle) that splits into two B monomers (blue square). "G" stands for generation.<sup>86</sup>

Dendrimers consist of 3 domains: the core, the branching units and the terminal groups.<sup>86-88</sup> Relying on the layers of the branching units, the denotation rules categorize the homologous building blocks as the "generations", naming  $G_n$  from the core till the termini. Building dendrimers usually involve two synthetic strategies: the divergent strategy and the convergent strategy. The former one follows a step-by-step, layer-by-layer growth workflow, building from the core and linking with every external component group by deprotection-activation/protection-deactivation schemes. Finally, the divergent strategy ends up with the connections of terminal groups. The convergent approach requires monodisperse dendrons with connection interface to be generated firstly. A well-designed functional focal point is responsible to dock on the core. The docking surface dendrons or surface groups are easy to investigate their properties as a "monomer" at first. However, regardless of the approach applied in the practical synthesis, the increasing generation of dendrimers or dendrons will bring about the problem of the steric hindrance, which limits the molecular dimensions and the yield.

In this study, we follow the typical dendrimer synthetic strategies to construct multichromophoric systems. By understanding the synthetic routes, we turn the focus point onto the docking implementations in the synthesis. The synthetic tactic to construct the multichromophores as dendrons

and dendrimers we applied here is the copper(I)-catalyzed azide-alkyne 1,3-dipolar cycloaddition (CuAAC) reaction. Under the frame of CuAAC, we plan to synthesize the interface components, *i.e.*, the corresponding azides and alkynes, so as to obtain the target multichromophores.

## 1.6.2 CuAAC in multivalent systems

K. Barry Sharpless, Hartmuth Kolb and M. G. Finn of the Scripps Research Institute have systematically defined the term "click chemistry".<sup>89</sup> Click chemistry refers to a wide concept of attaching small modular units onto the target substances, and usually they are both biocompatible. *Click reactions* in chemistry set several criteria: modularity, one-pot high product yields, insensitivity to solvent parameters, insensitivity towards ambient water and oxygen, "spring-loaded", *i.e.*, characterized by a high thermodynamic driving force to favor one-way product, high atom economy, minimal and non-toxic byproducts, etc. These criteria make one chemical reaction nearly "perfect". There are plural chemical reactions existing which fulfill the click reaction standards, including Cu(I)-catalyzed Huisgen 1,3-dipolar cycloaddition, thiol-ene reaction, Diels-Alder reaction, etc. Among them, the commonly denoted "click reaction" in this dissertation refers to copper(I)-catalyzed azide-alkyne 1,3-dipolar cycloaddition (CuAAC), whose application is the broadest, including conventional in-solution organic synthesis, *in vivo* biosynthesis and solid phase synthesis.

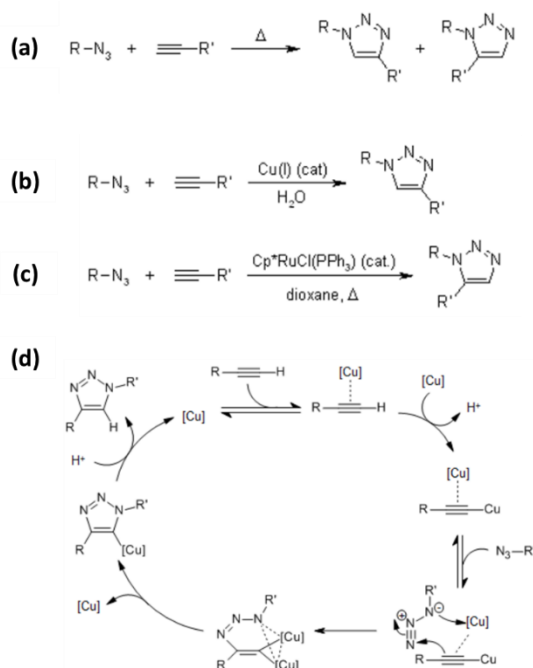
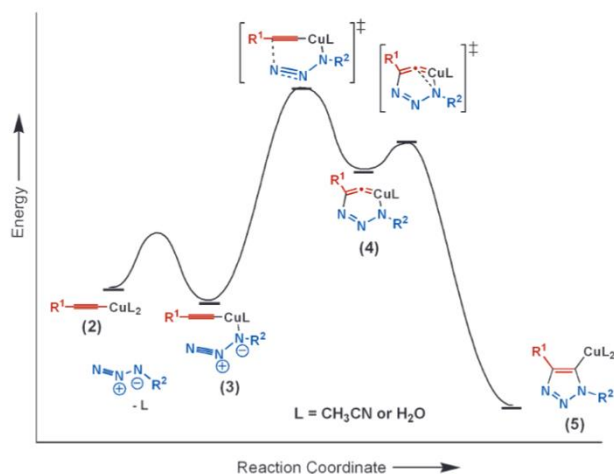


**Figure 29:** (a) Huisgen's 1,3-dipolar cycloaddition. (b) CuAAC produces the pure 1,4-triazole product. (c) RuAAC produces the pure 1,5-triazole product. (d) The proposed mechanism in CuAAC catalytic cycle.<sup>90</sup>

Huisgen's 1,3-dipolar cycloaddition produces 1,4- and 1,5-triazole mixtures, whereas the CuAAC leads to the regioselective 1,4-triazole product exclusively (**Figure 29**). On the other side, the ruthenium catalyzed cycloaddition (RuAAC) only produces 1,5-triazole products. In this dissertation, we adopt CuAAC as the synthetic method. As one of the best and widest click reaction to date, it features an enormous acceleration rate of reaction over  $10^7$  compared to the naturally occurred Huisgen's 1,3-dipolar cycloaddition.<sup>91</sup> The reaction itself suits a wide range of temperature condition as well, corresponding to the rich solvent pair choices. The active Cu(I) catalyst is from Cu(I) source directly or generated from the Cu(II) source. The most commonly used salts are copper (I) iodide and copper (II) sulfate paired with sodium ascorbate as the reducing agent.



Figure

Figure 30: Energy profile diagram for CuAAC based on DFT studies (L = CH<sub>3</sub>CN or H<sub>2</sub>O) by K. B. Sharpless et al.<sup>91</sup>

After the coordination of Cu(I) to the alkyne in the reaction system, a  $\sigma$ -bound copper acetylide bearing a  $\pi$ -bond copper coordinates with the azide, forming an anomalous six-membered copper metallacycle. The second copper atom in the ring (**Figure 29 (d)**) works as the stabilizing donor ligand. The ring then contracts into a triazolyl-copper derivative. In the end, the protonolysis process produces the final 1,4-triazole product and releases the copper catalyst. As the **Figure 30** showed, according to the reaction process, the reactant will reach a higher platform for rearranging the 6-membered ring. After the final step, the 1,4-triazole form much more stable 5-membered ring when joining the azido reactant.

There exists a long history in applying the CuAAC reaction in Pr J. Xie's group at PPSM laboratory since 2004, not far away of its discovery. In addition to have discovered a new fluoroionophore (the triazolyl-pyridyl), they have reported various conditions of CuAAC on different platforms since then.<sup>92-94</sup> The multichromophoric effects on the  $\beta$ -cyclodextrin are extraordinarily attracting for the photochemical applications, which can be easily obtained *via* CuAAC reaction with high yields. David *et al.* reported a multivalency construction with  $\beta$ -cyclodextrin (**Figure 31**).<sup>92</sup> This multichromophore exhibited Zn<sup>2+</sup>-sensitive fluorogenic chelating properties with a significant fluorescence enhancement and a large red-shift in emissions.

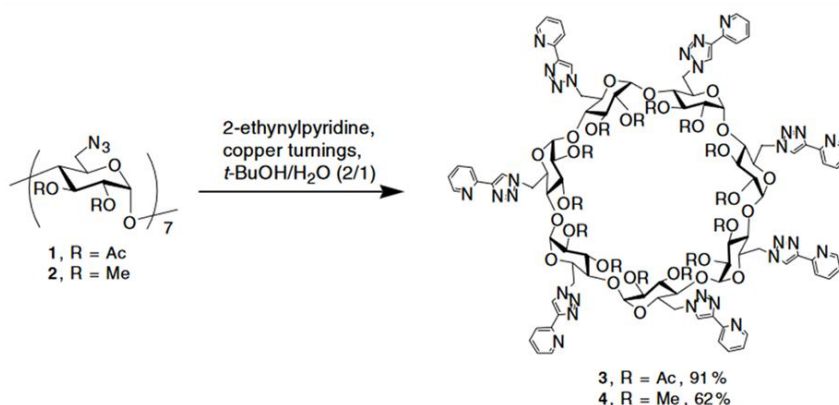
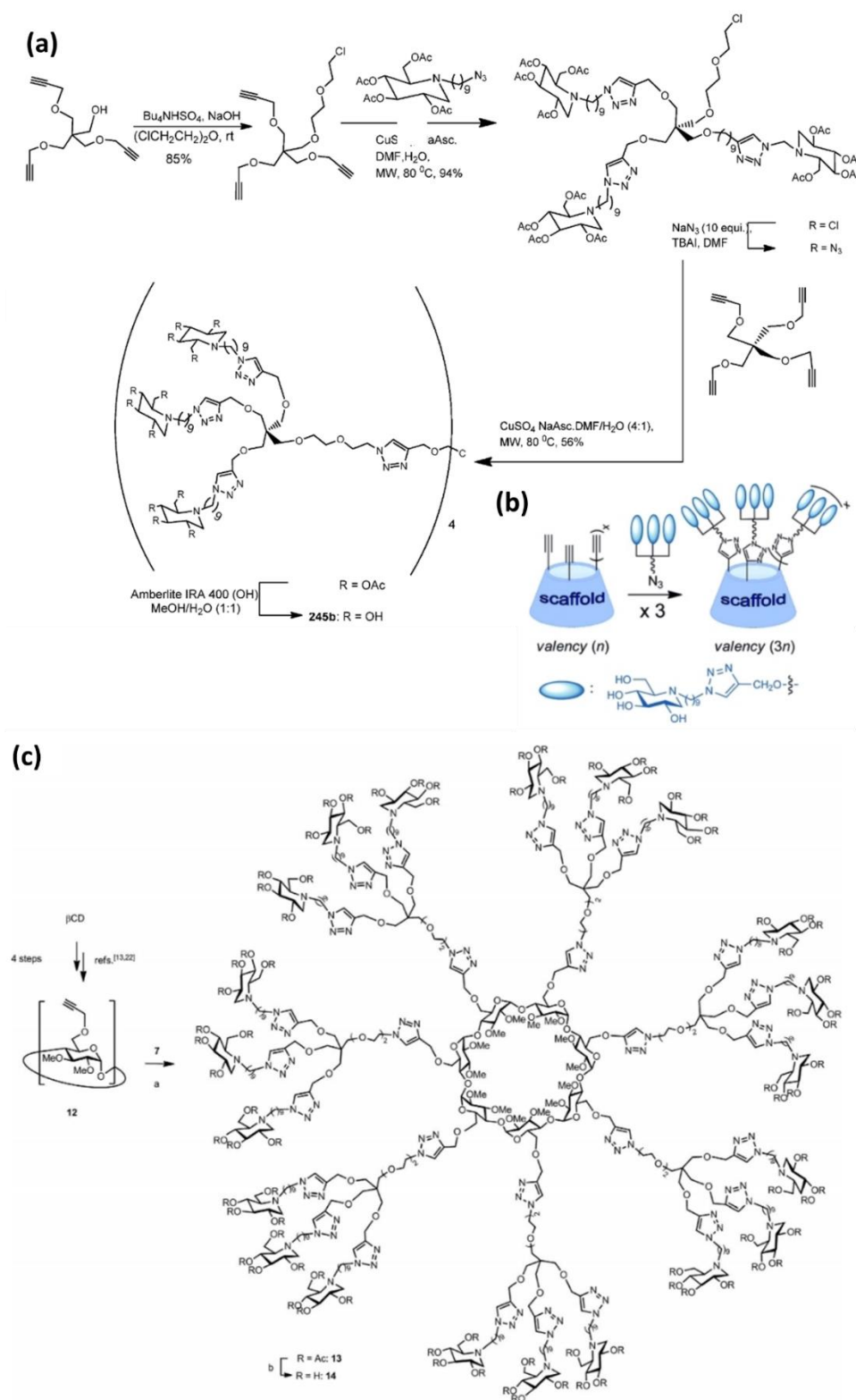


Figure 31: (a) The first reported example of CuAAC using a Cu(0) source to form the pyridyl-triazolyl chromophores on  $\beta$ -cyclodextrin. (b) Fluorescence spectra obtained during the titration of **3** in MeOH with Zn(ClO<sub>4</sub>)<sub>2</sub> (from 0 to  $3 \times 10^{-6}$  M).  $\lambda_{ex} = 280$  nm. Inset: titration curve of the integrated fluorescence as a function of Zn<sup>2+</sup> concentration.

CuAAC reaction has found wide application in glycoscience,<sup>95,96</sup> and offers a high degree of freedom to build big molecules with proper dendrons, dendritic linkers, and sugars. Joosten *et al.*<sup>97</sup> reported a series of multivalent compounds obtained with different CuAAC conditions. The three and four propargyl linkers allow the 12-valent compound (**Figure 32 (a)**). The trivalent dendron can click with the  $\beta$ -cyclodextrin to



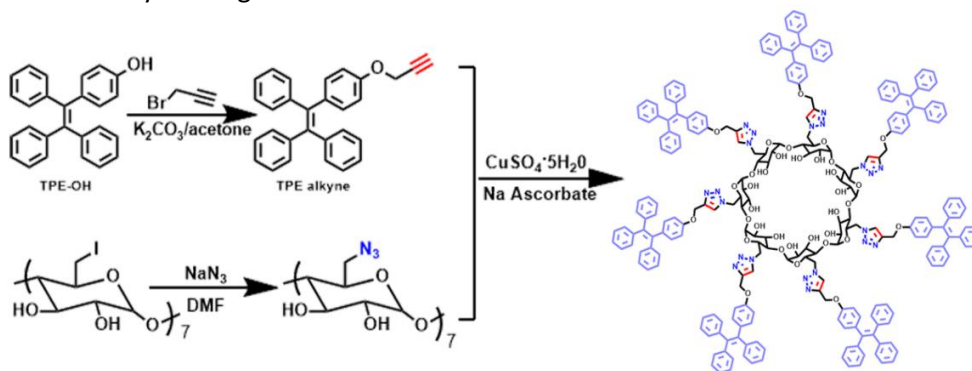
form a 21-valent compound (**Figure 32 (b,c)**). According to our experience, by modifying the dendritic linkers or the sugar, we can endow these structures with photoswitchable capabilities.



**Figure 32:** (a) Synthetic scheme of the trivalent and tetra-valent dendritic linkers to click out a 12-valent compound. (b) Illustration of the trivalent compound to click with proper scaffold to have the (3n)-valent product. (c) Scheme of the real case of 21-valent compound.<sup>97</sup>

In the situation of constructing the multichromophoric systems, CuAAC is a prevalent reaction widely applied in this field of research. Increasing the homogenous fluorophores to obtain more fluorescent

molecule is a well-known strategy. Zhao *et al.* reported that the 7 TPE on the  $\beta$ -cyclodextrin in **Figure 33** can enhance the AIE to yield brighter fluorescence.<sup>98</sup>



Figure

**Figure 33:** The AIE enhanced fluorescence multi-TPE synthetic scheme by CuAAC.<sup>98</sup>

To generate the heterogenous chromophoric system with CuAAC reaction, it usually involves the protection-deprotection strategy. In the **Figure 34**, Tafriouch *et al.* reported  $\alpha$ -hydroxy- $\beta$ -azidotetrazole scaffold to build a FRET capable trichromophoric structure with coumarin, BODIPY® and distyryl BODIPY®.<sup>99</sup> It is worth noting that the 1,4-triazole formed *via* CuAAC did not disturb the independent fluorophore or chromophore functions. The coumarin and BODIPY can retain their working wavelength regardless of the linkers. In addition, the multichromophoric systems constructed in a similar way are in the favorable distance to allow the FRET processes to occur.

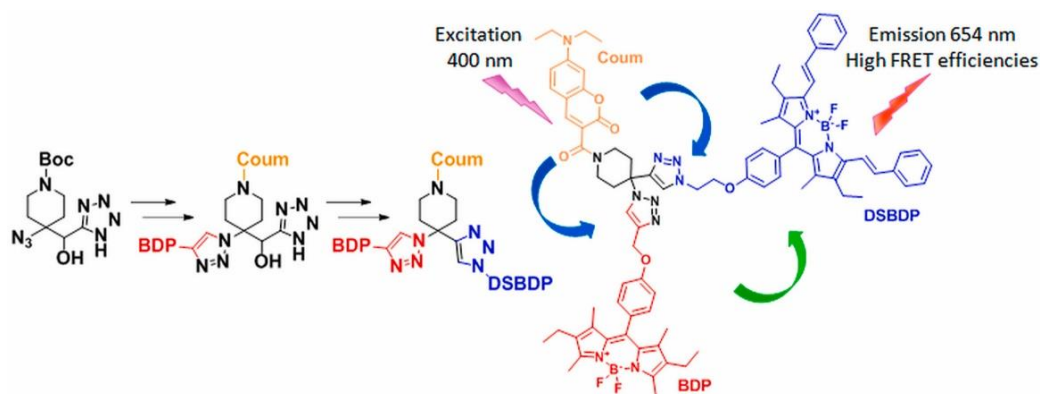


**Figure 34:** The FRET directions inside the trichromophoric system.<sup>99</sup>



## 1.7 OBJECTIVES OF THESIS

### 1.7.1 General interests

The aim of this work is to build a molecular platform which is able to accommodate as many as possible the chromophores and fluorophores together. The designed system should take the advantage of the number of the photoswitchable units to realize the hysteresis effect, based on FRET processes. In particular, based on the pioneering exploration demonstrated in the **Section 1.5.3**, the molecular designs will focus on two chromophores, DCM and DAE. The DCM is a photoisomerizable fluorescent unit and DAE is a photochromic unit, playing the role of the acceptor when it is in the CF state. We intend to accommodate together as many DCM and DAE as possible, with a proper platform, for example,  $\beta$ -cyclodextrin to realize the fluorescence hysteresis loop.

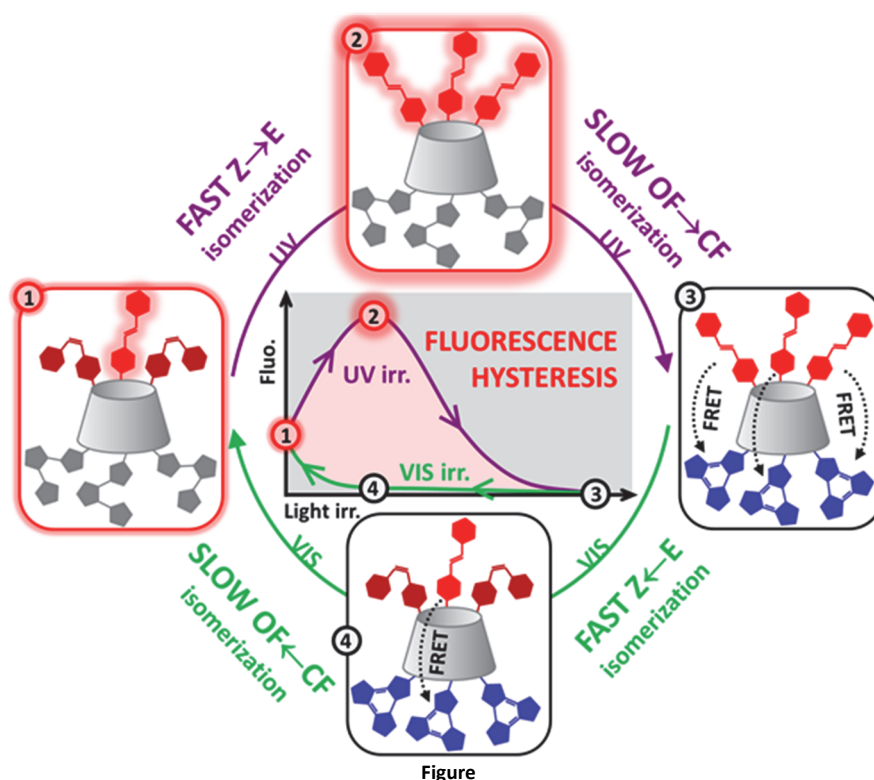


**Figure 35:** The design concept of a multichromophoric system to realize fluorescence hysteresis

In the PhD dissertation, we need to first understand the photochrome and the fluorophore, which are the model compounds at the basis of the implementation of the photoswitchable fluorescence hysteresis. Besides the prerequisites elucidated in **Chapter 1.3**, since we have known the photoisomerization of DCM, the competition of the isomerization rates of DCM and DAE is another key point to be properly elucidated. This leads to the conclusion that we need a “fast” isomerizing DCM fluorophore, and a “slow” isomerizing DAE photochrome.

Based on the understanding of the photoisomerizable DCM and DAE, the schematic concept of the photoswitchable fluorescence hysteresis effect is represented in the **Figure 35**:

**(1)** Starting from a photostationary state (PSS) of the DCM with all DAE under their open form, a fast  $Z \rightarrow E$  isomerization of DCM under UV irradiation leads to the more fluorescent  $E$ -DCM, enhancing the fluorescence.

(2) UV irradiation induces the slow OF→CF of DAE and enables the FRET to occur from *E*-DCM fluorescence emission to DAE absorption, accelerating the quenching of fluorescence.

(3) Fast *E*→*Z* isomerization of DCM under visible light irradiation leads to the non-fluorescent *Z*-DCM, then reducing the fluorescence emission.

(4) Visible light irradiation induces the slow CF→OF DAE back to the initial PSS.

The fluorescence hysteresis loop is constituted based on the different rates of isomerization under light irradiation and the influence of FRET. In the same irradiation input at any time point, the real population in the system of *E*- or *Z*-DCM, OF- or CF-DAE is unknown. The contribution to the fluorescence can be reduced by the light irradiation or the intramolecular FRET arbitrarily, which is in accordance with the hysteresis effect definition of the system history dependence.

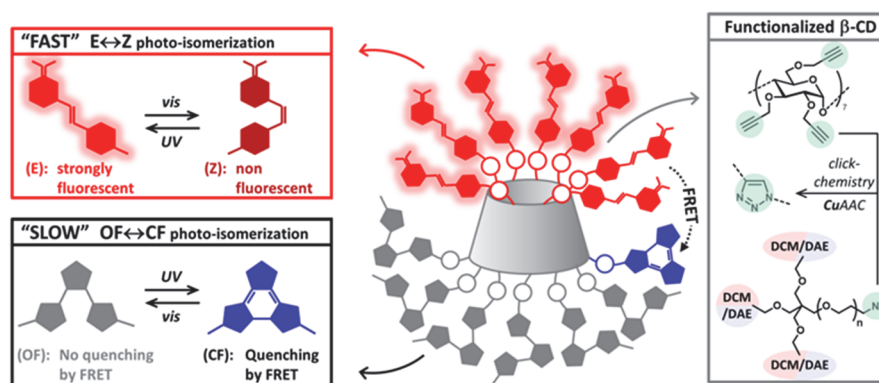


**Figure 36:** The composition of the implementation of the fluorescence hysteresis in the end. The photoswitchable DCM and DAE should be improved and synthesized to a platform which allow them to occur FRET between each other as many as possible.

Thanks to the hydroxyl functions on the cyclodextrin (see **Chapter III** for details), a series of multichromophoric cyclodextrins (CDs) can be proposed in the **Figure 37**. We could either first functionalize the small ring surface (with primary hydroxyl groups) of CD for installing DCM and the larger ring surface (with secondary hydroxyl groups) for DAE, or both could be installed simultaneously at the same ring. However, in the synthetic point of view, these options cannot be easily controlled.

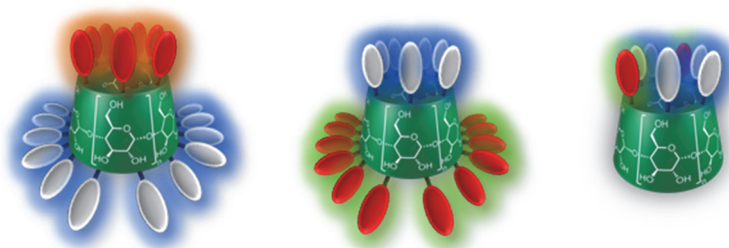


**Figure 37:** Possible composition of the final fluorescence hysteresis capable compounds. Red beans represent the DCMs and grey beans represent the DAEs.

After evaluation of the DAE prepared at ICMMO laboratory (N. Baggi, PhD under supervision of Dr P. Yu), we have decided to choose a 2:1 ratio for DAE and DCM to form the basic dendron unit and use the CuAAC reaction to synthesize compounds with a higher number of chromophoric units. Therefore, the target compounds in this PhD work will be a series of 3-, 12-, 42-chromophores, as shown in **Figure 38** and denoted **YN-3c**, **YN-12c** and **YN-42c**. This new generation of molecules represents finally a multivalent version of the historical compound of the second generation of photoswitchable fluorescence hysteresis effect. We can consequently expect a fluorescence quenching within the dendron but also between the dendrons.

effect. We can consequently expect a fluorescence quenching within the dendron but also between the dendrons.

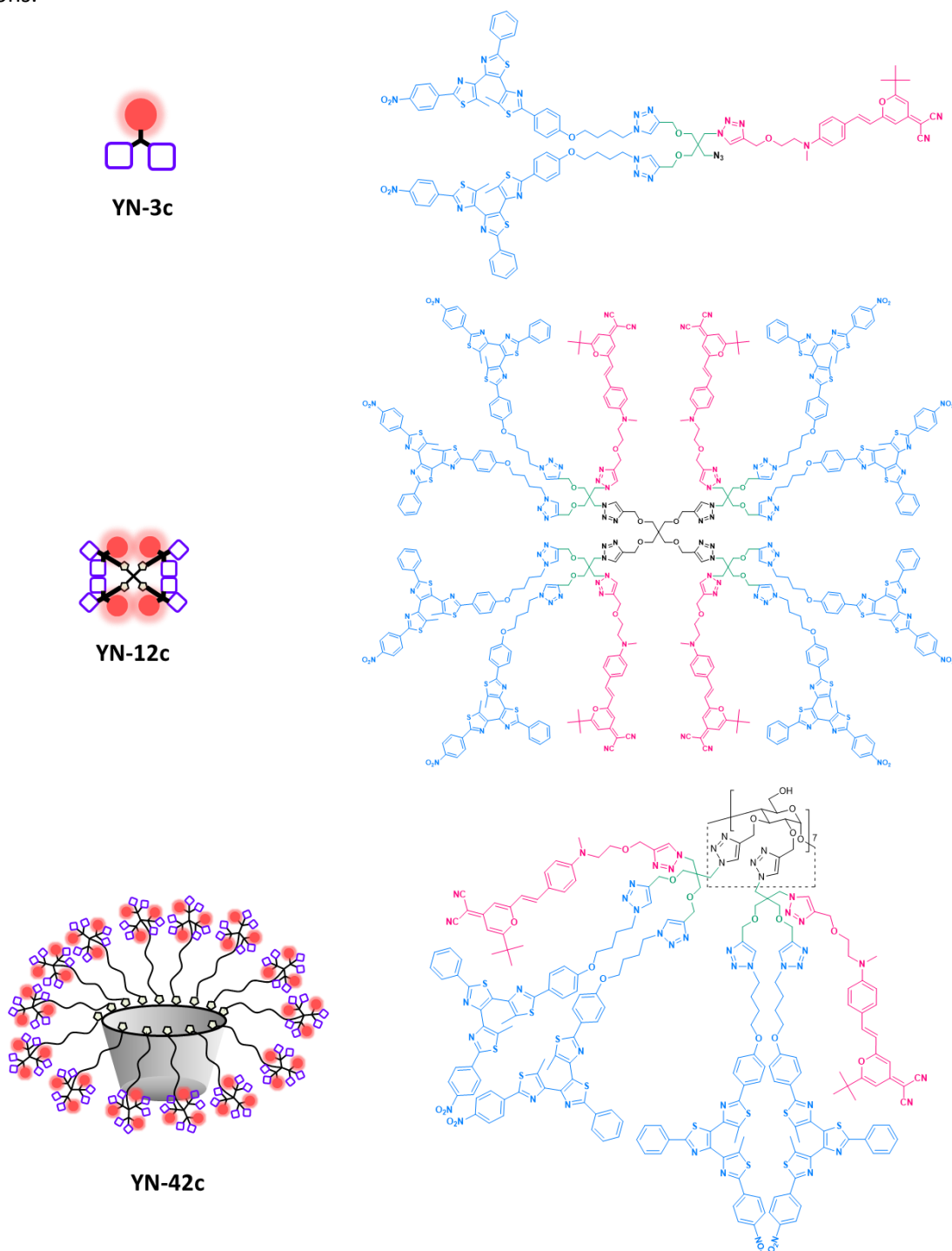


**Figure 38:** Compounds designed for the photoswitchable fluorescence hysteresis effect prepared in this thesis.

In particular, **Chapter II** will focus on spectroscopic and theoretical studies on the compound **DCM-azide** shown in the **Figure 39**. In **Chapter III**, the synthesis of compounds **2DCM**, **3DCM**, **4DCM**, and **14DCM** will be described and the **DCM-azide**, **2DCM**, and **3DCM** were compared through spectroscopic and theoretical studies. All these results have as common objective: the proper understanding of the multi-DCM behavior.

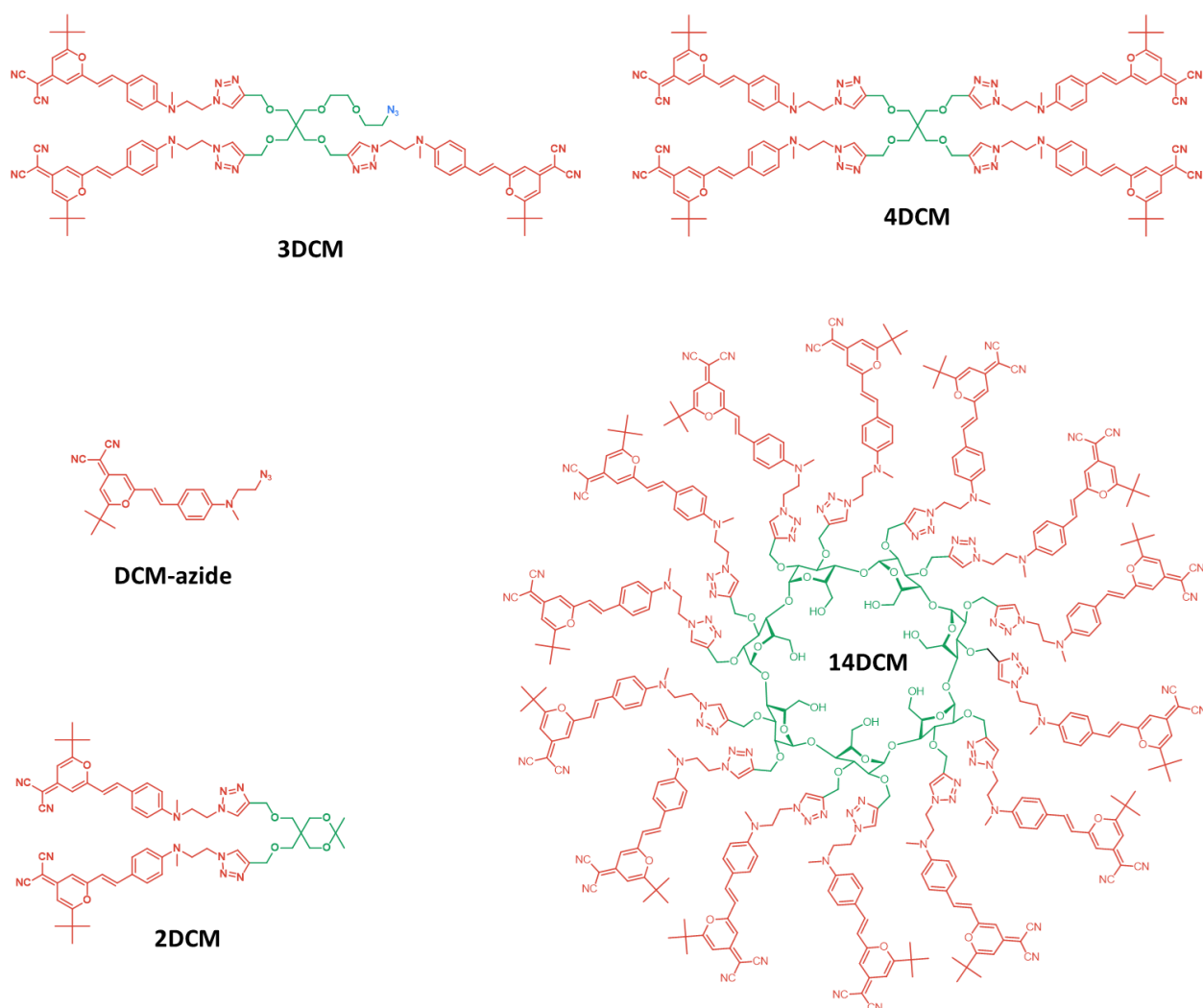


**Figure 39:** The structures studied in the **Chapter II** and **Chapter III**.

Finally, **Chapter IV** will be devoted to photochromic-fluorescent triads and multichromophoric systems (**YN-3c**, **YN-12c**, and **YN-42c**, **Figure 38**), involving the theoretical studies of subunits, the synthesis and the improvement of the combined photochromic-fluorescent molecules, the spectroscopic characterization with photoswitchable fluorescence hysteresis demonstration, and the simulation studies to unveil the FRET processes among the photochromic-fluorescent subunits.

The full workflows of the thesis on building a multichromophoric system which is capable of fluorescence hysteresis cover the synthesis technique explorations, the theoretical studies from quantum to simulation levels and the spectroscopic characterizations.



# Chapter II



## 2 CHAPTER II – PHOTOPHYSICAL AND THEORETICAL STUDIES OF DCM

### 2.1 INTRODUCTION

In **Chapter I**, molecular photoswitchable chromophores have been introduced. In a nutshell, these refer to a sort of compounds which can be interconverted by light stimuli between at least two states, resulting in different photochemical and photophysical properties. Light-induced reactions involve photoinduced electrocyclization, cycloreversion, dimerization, photoinduced bond cleavage,  $E \leftrightarrow Z$  or  $trans \leftrightarrow cis$  isomerizations. Among these mechanisms, the double-bond  $E \leftrightarrow Z$  or  $trans \leftrightarrow cis$  photoisomerization is prevailing in light-driven molecular switches, rotors and sensors due to its synthetic flexibility and easy structural modification.<sup>100-103</sup> The tunable optical and mechanical properties upon irradiation provided by the double-bond isomerization allow applications such as light-sensitive sensors and functional materials.<sup>60, 104, 105</sup> The N=N, C=N and C=C bonds are the most common photoswitchable groups in azobenzenes<sup>106, 107</sup>, acylhydrazones<sup>108, 109</sup>, and stilbenes<sup>110</sup>, respectively.

Besides, 4-dicyanomethylene-2-methyl-6-(*p*-dimethylamino-styryl)-4*H*-pyran (DCM) analogs belongs to the category of C=C double bond isomerization introduced in the **Chapter I**. Its donor- $\pi$ -acceptor structure confers it a noticeable intramolecular charge transfer character and consequently, a strong solvatochromism.<sup>40, 41, 111-113</sup> Although in the common knowledge, DCM is a highly efficient fluorophore active in the application field of red-emissive laser dyes, molecular sensors or photoactive solid state materials, the photoisomerization properties of DCM in solution have been ignored in the vast majority of reports, with a few notable exceptions.<sup>3, 38, 114-118</sup> The  $E \leftrightarrow Z$  photoisomerization studies and the related conversion yield quantification of a DCM analog (**DCM-*o*-alkyne**) have been reported by Casimiro *et al.*<sup>3</sup> The steady-state spectroscopy, HPLC analysis, conversion yield and photostationary states (PSSs), characterization of the *E*-form and *Z*-form have been carried out under illumination, at different wavelengths and in different solvents. The most important feature among the previous studies is that the *E*-forms of **DCM-*o*-alkyne** are identified fluorescent, whereas the *Z*-forms are non-emissive. Therefore, the fluorescence modulation associated to the photoisomerization demonstrates the high potential of DCM analogs as intrinsic photoswitchable fluorophores.

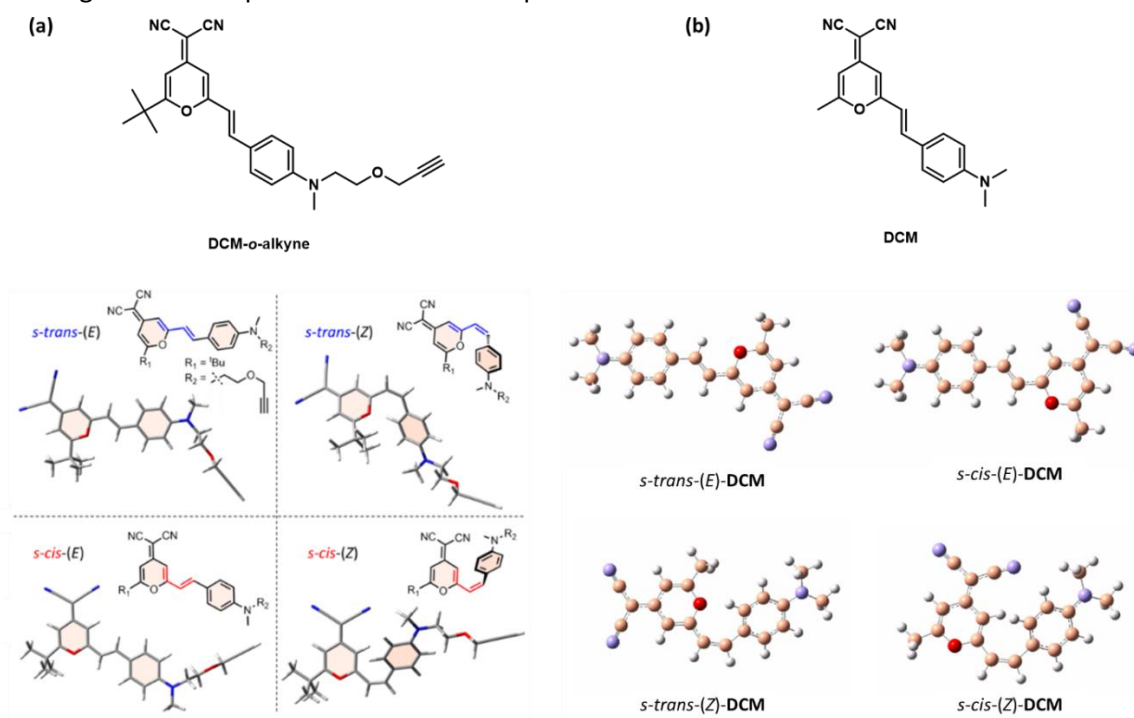


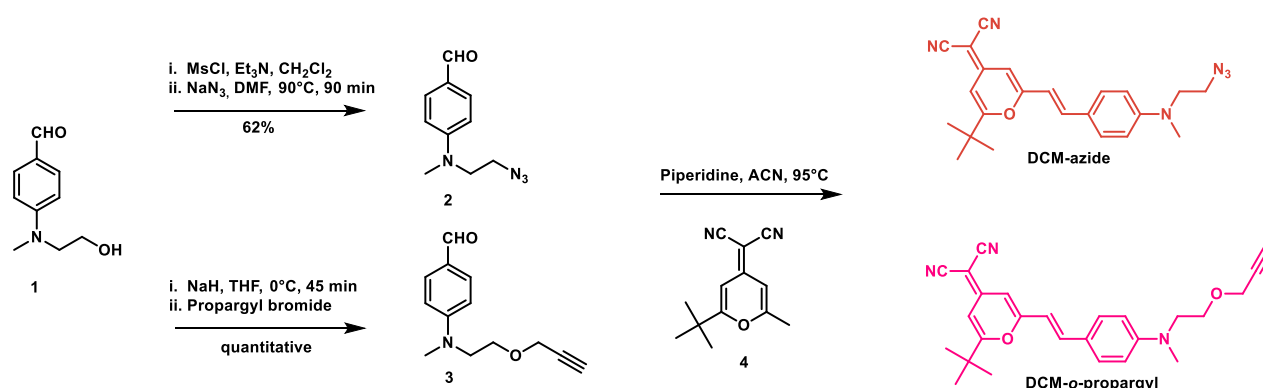
**Figure 40:** (a) Chemical and PBE0/6-311+G(d,p) in vacuo level DFT optimized molecular structures of **DCM-*o*-alkyne** in its different isomers and conformers by the studies from L. Casimiro and S. Maisonneuve *et al.*<sup>3</sup> (b) Chemical structure and the DFT



optimized same four isomers and conformers of commercially available DCM studied by X. Xu et al.<sup>119</sup>

The previous studies on DCM as shown in **Figure 40**, using spectroscopic or quantum chemical calculations, indicated the existence of four isomers (*E*- and *Z*-forms) and conformers (*s-cis*- and *s-trans*-forms) and their possible interconversions.<sup>3, 119</sup> Another DCM analog, **DCM-azide** was studied 10 years ago as a part of the photochrome–fluorophore dyad in our laboratory.<sup>2</sup> At that time, the importance of the *E*↔*Z* photoisomerization from the **DCM-azide** part was not demonstrated yet. Like other molecular systems with dissymmetric stilbene core, the detailed description of photochemical behaviors of the DCM analogs were not properly understood. Since we already knew about the main photochemical and photophysical behavior of **DCM-*o*-alkyne**, we selected the **DCM-azide** compound as the precursor to be involved in the multichromophoric systems *via* CuAAC reaction and decided to investigate in detail its peculiar properties.

The synthesis of **DCM-azide** and **DCM-*o*-alkyne** are all based on the Knoevenagel condensation in the final stage. The benzaldehydes of *o*-alkyne and azido derivatives are prepared first and react with the *tert*-butyl dicyanomethylene. It is just because of the sensitive *E*↔*Z* photoisomerization, the regenerations are dealt with in the ambient light shielded environment, and the products are all in the *E*-forms.



**Scheme 3:** The preparation of **DCM-azide** and the previous reported **DCM-*o*-propargyl** by the Knoevenagel condensation reaction.

The more advanced spectroscopic and theoretical investigations have been done on the **DCM-azide** in this Chapter. We report here the experimental and theoretical studies of **DCM-azide** involving its four forms, to bring in-depth description of its photophysical and photochemical properties. X-ray structures, steady-state and time-resolved spectroscopy data, as well as quantum chemical computations in the ground state, the excited state, or at conical intersections, provide important information on the photoisomerization pattern of **DCM-azide**.

## 2.2 PAPER MANUSCRIPT #1 (PHYS. CHEM. CHEM. PHYS.)



Cite this: *Phys. Chem. Chem. Phys.*,  
2022, 24, 6282

# Photoisomerization of a 4-dicyanomethylene-2-methyl-6-(*p*-dimethylaminostyryl)-4*H*-pyran analog dye: a combined photophysical and theoretical investigation†

Yang Zhou,<sup>a</sup> Stéphane Maisonneuve,<sup>ib</sup><sup>a</sup> Lorenzo Casimiro,<sup>ib</sup><sup>a</sup>  
Pascal Retailleau,<sup>ib</sup><sup>b</sup> Juan Xie,<sup>ib</sup><sup>a</sup> François Maurel<sup>\*c</sup> and Rémi Métivier<sup>ib</sup><sup>\*a</sup>

A combination of experimental and theoretical investigations of a photoisomerizable analog of 4-dicyanomethylene-2-methyl-6-(*p*-dimethylaminostyryl)-4*H*-pyran (DCM) dye molecule is presented. We provide evidence that the 4 main isomers and conformers of DCM contribute to its photochemical and photophysical processes. The absorption and emission spectra, as well as time-resolved fluorescence experimental results, are discussed and compared to DFT/TDDFT calculations. The *E* ↔ *Z* isomerization is induced photochemically, whereas the *s-cis* ↔ *s-trans* conformational interconversion is a thermal process which may also happen during irradiation. The photoreaction pathways from the first excited state down to the ground state are shown to be mediated by two conical intersections, as revealed using spin-flip TDDFT calculations. The rationalization of these isomerization schemes provides important insights into the photophysical properties of DCM, responsible for its photoswitchable fluorescence.

Received 11th November 2021,  
Accepted 28th January 2022

DOI: 10.1039/d1cp05170a

rsc.li/pccp

## Introduction

Molecular photoswitchable systems consist of chromophores that can be interconverted upon light stimuli between at least two states, resulting in different photochemical and photophysical properties. Light-induced reactions involve photoinduced electrocyclization, cycloreversion, dimerization, photoinduced bond cleavage, and *E* ↔ *Z* or *cis* ↔ *trans* isomerization. Among these mechanisms, double-bond *E* ↔ *Z* photoisomerization occurs in light-driven molecular switches, rotors and sensors due to its flexibility and embeddability.<sup>1–4</sup> The tunable optical and mechanical properties upon irradiation provided by the double-bond isomerization allow applications such as light-sensitive sensors and functional materials.<sup>5–7</sup> The N=N, C=N and C=C bonds are the most common photoswitchable groups in azobenzenes,<sup>8,9</sup> acylhydrazones,<sup>10–12</sup> and stilbenes<sup>13</sup>, respectively.

In addition, 4-dicyanomethylene-2-methyl-6-(*p*-dimethylaminostyryl)-4*H*-pyran (DCM) analogs are well-known red-emitting dyes, which are used in lasers,<sup>15–17</sup> in capping layers of organic light emitting diodes (OLEDs) and in dye-sensitized solar cells (DSSCs).<sup>18–22</sup> Its donor–π–acceptor structure confers it a noticeable intermolecular charge transfer character and consequently, strong solvatochromism. Because of its central C=C double-bond, DCM can undergo *E* ↔ *Z* isomerization under irradiation. However, the photoisomerization properties of DCM have been ignored in the vast majority of reports, with a few notable exceptions.<sup>14,23–29</sup> The *E* ↔ *Z* photoisomerization studies and the related conversion yield quantification of a DCM analog (DCM-*o*-alkyne) have been reported by our group.<sup>14</sup> In our previous article, we described steady-state spectroscopy, HPLC analysis, conversion yields, photostationary states (PSSs), and characterization of the *E*-form and *Z*-form, under illumination, at different wavelengths and in different solvents.

Indeed, the *E*-forms of DCM-*o*-alkyne were found to be fluorescent, and not the *Z*-forms. Thus, the fluorescence modulation associated with the photoisomerization demonstrates the high potential of DCM analogs to act as intrinsic photoswitchable fluorophores. Previous studies on DCM, using spectroscopic or quantum chemical calculations, indicated the existence of 4 stable isomers (*E*- and *Z*-forms) and conformers (*s-cis*- and *s-trans*-forms) and their possible interconversions.<sup>14,29</sup>

In the present paper, we focus our attention on the DCM-azide,<sup>30</sup> an azido variant of the previously studied DCM-*o*-alkyne, allowing further functionalization. The molecular

<sup>a</sup> Université Paris-Saclay, ENS Paris-Saclay, CNRS, Photophysique et Photochimie Supramoléculaires et Macromoléculaires, 91190 Gif-sur-Yvette, France.  
E-mail: remi.metivier@ens-paris-saclay.fr

<sup>b</sup> Université Paris-Saclay, CNRS, Institut de Chimie des Substances Naturelles, UPR 2301, Gif-sur-Yvette, France

<sup>c</sup> Université de Paris, ITODYS, CNRS, F-75006 Paris, France  
E-mail: maurel@univ-paris-diderot.fr

† Electronic supplementary information (ESI) available: X-ray diffraction analyses, details of DFT/TDDFT and conical intersection calculations. CCDC 2120494 and 2121293. For ESI and crystallographic data in CIF or other electronic format see DOI: 10.1039/d1cp05170a

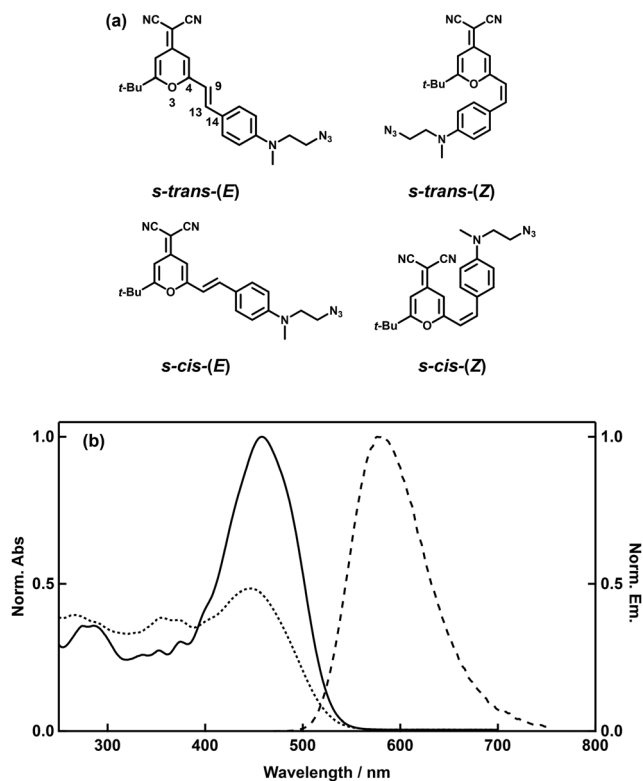


**Fig. 1** (a) Molecular structures of DCM-azide in its different isomers and conformers, denoted as *s-trans*-(*E*), *s-cis*-(*E*), *s-trans*-(*Z*), and *s-cis*-(*Z*) according to our previous study.<sup>14</sup> Dihedral ( $O_3-C_4-C_9=C_{13}$ ) involving a C–C single bond is defined as *D1* and dihedral ( $C_4-C_9=C_{13}-C_{14}$ ) involving C=C double bond is defined as *D2*. (b) Absorption spectra of the *E*-isomer (full line on the left) and the *Z*-isomer (dotted line on the left) together with *E*-isomer emission (dashed line on the right) are recorded in THF solution.

structures of the four isomers/conformers of DCM-azide are shown in Fig. 1. Like other molecular systems with an asymmetric stilbene core, a detailed description of the behavior of DCM-azide under illumination in its different isomers/conformers is not straightforward, and the interconversion modes between the four geometries are still not clearly understood. In this context, the combination of spectroscopic and computational approaches can be helpful to rationalize the properties of DCM-azide. We report here the experimental and theoretical studies of DCM-azide involving its four forms to bring in-depth description of its photophysical and photochemical properties. X-ray structures, steady-state and time-resolved spectroscopy data, as well as quantum chemical computations in the ground state, the excited state, or at conical intersections, provide important information on the photoisomerization pattern of DCM-azide.

## Results and discussion

### Structural studies

The DCM-azide has been synthesized as the pure *E*-form according to the previously reported procedures<sup>30</sup> by shielding the reaction and post-procedures from ambient UV-visible light

exposures. Under different eluent conditions on column chromatographies, the DCM-azide can be obtained as a red crystalline powder. In the following, we denote two key dihedral angles,  $O_3-C_4-C_9=C_{13}$  and  $C_4-C_9=C_{13}-C_{14}$  of the molecular layout in Fig. 1, as *D1* and *D2*, respectively.

After recrystallizing the crystalline powder, two different polymorphs were obtained as single crystals. The corresponding structures were successfully solved by X-ray diffraction (XRD) analyses, as shown in Fig. 2 and in the ESI† (Fig. S1 and Table S1): the first one crystallizes in the triclinic  $P\bar{1}$  space group, whereas the second one adopts an orthorhombic *Pnma* space group. The molecular packing mainly influences the orientation of the azido substituent, while the whole structure is in both cases thoroughly planar across the central double bond of DCM-azide, shown in the *s-trans*-(*E*) configuration, for both structures (see Fig. S2, ESI†). The two polymorphs differ mainly in the intermolecular contacts, as shown by the Hirshfeld surface analyses described in the ESI† (Fig. S3–S5). The molecular geometry of DCM-azide is defined by the two main dihedral angles *D1* and *D2* ( $D1 = 4.7^\circ$  and  $D2 = 179.9^\circ$  for the triclinic form, and  $D1 = 0.0^\circ$  and  $D2 = 180.0^\circ$  for the orthorhombic form), and the corresponding  $C_4-C_9$  single-bond (length = 1.440 Å and 1.434 Å for triclinic and orthorhombic forms, respectively) and  $C_9=C_{13}$  double-bond (length = 1.335 Å and 1.340 Å for triclinic and orthorhombic forms, respectively). These geometrical parameters are fully in line with the previously described DCM-*o*-alkyne derivative.<sup>14</sup>

In a previous study on DCM-*o*-alkyne, the THF solvent (medium polarity) was revealed to be an ideal trade-off between the fluorescence quantum yield and the *E* → *Z* photoisomerization conversion yield, outperforming acetonitrile and toluene in terms of fluorescence photoswitching benchmark. Therefore, we decided to employ THF as the main solvent in the present study of DCM-azide. In the steady-state UV-visible measurements, DCM-azide shows an absorption  $\lambda_{\max}$  at 459 nm in THF, with a molar absorption coefficient recorded at  $\epsilon_{459\text{nm}} = 48\,700 \text{ L mol}^{-1} \text{ cm}^{-1}$ . After reaching a photostationary state under irradiation at 485 nm (PSS485), the  $\lambda_{\max}$  was shortened and the absorption bands around 350–450 nm were flattened. Furthermore, from the PSS485 solution, we extracted the *Z*-form of DCM-azide by thin layer chromatography (TLC), and recorded its absorption spectrum in THF. The

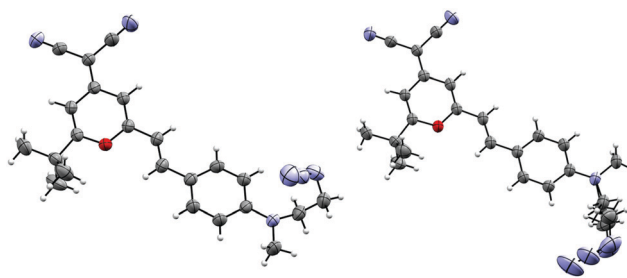


**Fig. 2** X-ray diffraction structures in the triclinic form (left) and in the orthorhombic form (right) of the *s-trans*-(*E*) form of DCM-azide obtained after crystallization.

corresponding dotted absorption spectrum shown in Fig. 1 presents a much weaker and blue-shifted band at 447 nm, and the absorption is stronger in the 300–400 nm range than that in the spectrum of the synthesized *E*-form.

The fluorescence spectrum of DCM-azide in the *E*-form is broad and intense around 590 nm, and its emission quantum yield is appreciable ( $\Phi_f = 0.25$ ) but lower than that of the DCM-*o*-alkyne ( $\Phi_f = 0.32$ ),<sup>14</sup> due to its azido lateral part. Fluorescence decay curves of DCM-azide were recorded at different excitation wavelengths using the time-correlated single-photon counting (TCSPC) technique (Fig. 3). The fluorescence decays were fitted by a global analysis procedure using a bi-exponential function, which was necessary to obtain acceptable curve fitting ( $\chi_R^2 < 1.2$ ). Two decay-times were identified: the first decay-component ( $\tau_1$ ) is found at 0.84 ns contributing to the major part of the fluorescence (large pre-exponential factor  $\alpha_1 > 0.88$  and fraction of intensity  $f_1 > 0.97$ ), whereas the second decay-time is shorter ( $\tau_2 = 0.20$  ns) and has a minor contribution to the fluorescence intensity ( $\alpha_2 < 0.12$  and  $f_2 < 0.03$ ). We collected the fluorescence decays at different excitation wavelengths from 315 nm to 450 nm and irradiated the DCM-azide sample at 485 nm to make cross comparisons, and further evaluated the possible contributions of the *Z*-isomer to the emission. As a result, the change in excitation wavelength or irradiation did not influence the collected fluorescence decays:  $\tau_1$  and  $\tau_2$  were found to be identical, and  $\alpha_1 = 0.91 \pm 0.03$ ,  $\alpha_2 = 0.09 \pm 0.03$  were similar for all the measurements, as shown in Fig. 3 and Table 1. Therefore, the two decay-time components are not related to the *E* ↔ *Z* photoisomerization process. The results from Table 1 fully confirm the

**Table 1** Time-resolved fluorescence parameters of DCM-azide in the *E*-form, determined in THF

$\lambda_{\text{ex}}$ (nm)	$\tau_1$ (ns)	$\alpha_1$ ( $f_1$ )	$\tau_2$ (ns)	$\alpha_2$ ( $f_2$ )
315	0.84	0.89(0.97)	0.20	0.11(0.03)
350	0.84	0.93(0.98)	0.20	0.07(0.02)
400	0.84	0.88(0.97)	0.20	0.12(0.03)
400 <sup>a</sup>	0.84	0.89(0.97)	0.20	0.11(0.03)
450	0.86	0.92(0.98)	0.17	0.08(0.02)

<sup>a</sup> After irradiation at 485 nm (PSS485).

interpretation reported in our previous paper.<sup>14</sup> From fluorescence decays collected at different excitation wavelengths, with or without irradiation, we can conclude that the *Z*-forms of DCM-azide are completely non-emissive, and the fluorescence components ( $\tau_1$  and  $\tau_2$ ) identified by fluorescence decays correspond to *s-trans*(*E*) and *s-cis*(*E*) conformers.

### Absorption and emission electronic transitions of the *s-trans*(*E*) isomer

From the X-ray structure of DCM-azide, we assume that the *s-trans*(*E*) isomer corresponds to its most stable isomer. Moreover, the steady-state and time-resolved fluorescence results demonstrated that the *s-trans*(*E*) isomer is considered to represent the main contribution to the fluorescence. Therefore, absorption and emission energy calculations at the level of density functional theory (DFT) and time-dependent density functional theory (TDDFT) were first performed for this isomer. Computations with the polarizable continuum model (PCM) for THF, three functionals (PBE0, CAM-B3LYP, and  $\omega$ B97X-D), and the 6-311+G(d,p) Pople basis set were performed for DCM-azide in the *s-trans*(*E*) form. All electronic transition energies were calculated by the linear-response method. Other non-equilibrium solvation calculations were also investigated, as reported in the ESI† (corrected linear-response and state-specific, see Table S6).

By screening the DFT functionals, PBE0 shows the most accurate estimation of the DCM-azide absorption ( $\lambda_{\text{abs}} = 463$  nm, compared to the experimental value  $\lambda_{\text{max}} = 459$  nm) and at the same time rather acceptable emission estimation compared to the experiment ( $\lambda_{\text{em}} = 521$  nm vs. experimental  $\lambda_{\text{max}} = 576$  nm). Despite the donor–acceptor character of DCM-azide,  $\omega$ B97X-D and CAM-B3LYP did not provide better absorption or emission energies compared to PBE0, with systematic overestimation of the transition energies and shorter maximum wavelengths than those measured experimentally (Table 2). Only the Stokes shift is more accurately described with the long-range corrected CAM-B3LYP. Considering all the functional screenings and computational costs, we decided to select PBE0 as the main functional for the DFT studies, for more intuitive comparisons and uniformity over the whole theoretical investigation (see the “Excited state computations” paragraph below).

We analyzed the frontier molecular orbitals of the four isomers/conformers of DCM-azide at the PBE0/6-311G++(d,p) level with the PCM model of the THF solvent, as reported in the

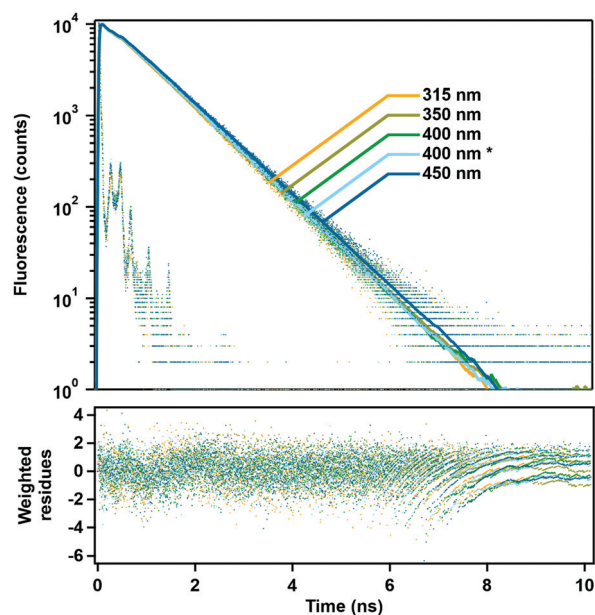


**Fig. 3** Fluorescence decay curves, instrumental response function, bi-exponential fitting and weighted residuals of DCM-azide at different excitation wavelengths (315 nm, 350 nm, 400 nm and 450 nm) in THF. The marked decay (\*) corresponds to a DCM-azide THF solution irradiated at 485 nm.

**Table 2** Absorption and emission transition energies of the *s-trans-(E)* form of DCM-azide, calculated using TDDFT with the 6-311G++(d,p) basis set in THF, together with the experimental data recorded for the *E*-form in THF solution

	PBE0		CAM-B3LYP		$\omega$ B97X-D		Exp. data	
	(eV)	(nm)	(eV)	(nm)	(eV)	(nm)	(eV)	(nm)
$\lambda_{\text{abs}}$	2.68	463	3.06	405	3.15	394	2.70	459
$\lambda_{\text{em}}$	2.38	521	2.44	509	2.45	507	2.15	576
Stokes shift	2404 cm <sup>-1</sup>		5045 cm <sup>-1</sup>		5657 cm <sup>-1</sup>		4425 cm <sup>-1</sup>	

ESI<sup>†</sup> (Fig. S6). For all forms, the highest occupied molecular orbitals (HOMOs) and the lowest unoccupied molecular orbitals (LUMOs) are the main orbitals involved in the first electronic transition  $S_0 \rightarrow S_1$ . The HOMOs (respectively LUMOs) have a clear  $\pi$  (respectively  $\pi^*$ ) character. Therefore, the  $S_0 \rightarrow S_1$  transition has a  $\pi \rightarrow \pi^*$  nature, with a limited charge-transfer character due to a small electronic delocalization from the methylamino-styryl moiety to the dicyano-pyran moiety. Multiple contributions of the HOMO-1, HOMO, LUMO and LUMO+1 to the  $S_0 \rightarrow S_2$  and  $S_0 \rightarrow S_3$  electronic transitions are noted. In a similar manner, such features were also identified for the other functionals tested, namely  $\omega$ B97X-D and CAM-B3LYP, and other polar solvents (see Fig. S7–S10, ESI<sup>†</sup>).

### Ground-state potential energy surface

As previously described, the four stable forms of DCM derivatives are denoted as *s-trans-(E)*, *s-cis-(E)*, *s-trans-(Z)*, and *s-cis-(Z)*. Their corresponding ground state geometries and energies were optimized at the DFT PBE0/6-311G++(d,p) level (Tables S2–S5, ESI<sup>†</sup>). *s-trans-(E)* shows the lowest energy, which confirms the X-ray structure analysis. Both *E*-forms have straight planar geometries across the double-bond moiety.

Within a PCM model of the THF solvent, the dipole moment of *s-trans-(E)* records the highest value at 20.0 D, while *s-cis-(Z)* has the lowest dipole moment at 12.8 D amongst the four forms (Fig. S6, ESI<sup>†</sup>). The dipole moments were enhanced in more polar solvents such as acetonitrile and DMSO (see Fig. S9 and S10, ESI<sup>†</sup>) with more stabilized energies.

The ground-state pathway of the interconversion between the *s-trans* and *s-cis* conformers can be followed by rotating the  $C_4$ – $C_9$  single-bond, thus changing the  $D1$  dihedral angle, the *E*-isomer being transformed into its corresponding *Z*-isomer by changing the  $D2$  dihedral angle (rotation around the  $C_9$ = $C_{13}$  double bond). The scanning plot of these energy minimized paths along the two rotating dihedral angles  $D1$  and  $D2$  is presented in Fig. 4. For the *s-cis*  $\leftrightarrow$  *s-trans* interconversion, the energy barriers are calculated to be 0.41 eV and 0.16 eV for the *E*-side and the *Z*-side, respectively. Regarding the *E*  $\leftrightarrow$  *Z* reaction, the curves show that the closed-shell formalism cannot be used for double-bond rotation but clearly illustrate that the *E*  $\leftrightarrow$  *Z* barrier of isomerization is much higher than the *s-cis*  $\leftrightarrow$  *s-trans* process, as expected. Therefore, the ground-state *s-cis*  $\leftrightarrow$  *s-trans* transformation can occur spontaneously at room temperature, whereas the *E*  $\leftrightarrow$  *Z* requires external energy input to take place, such as photon absorption. The  $C_4$ – $C_9$  and  $C_9$ = $C_{13}$  bond lengths vs. scan coordinates  $D1$  and  $D2$  are shown in the ESI<sup>†</sup> (Fig. S11, blue and red lines, respectively), presented by the blue and red lines, respectively. Along the *s-cis*  $\leftrightarrow$  *s-trans* interconversion, the double bond remains almost unaffected, whereas the single bond is elongated to a maximum at the transition states, then shortened at the four stable isomers and conformers structures. Along the *E*  $\leftrightarrow$  *Z* isomerization paths, the double bond is elongated and the single bond is shortened to reach comparable bond lengths at the transition states ( $C_9$ = $C_{13}$  max. = 1.419 Å,

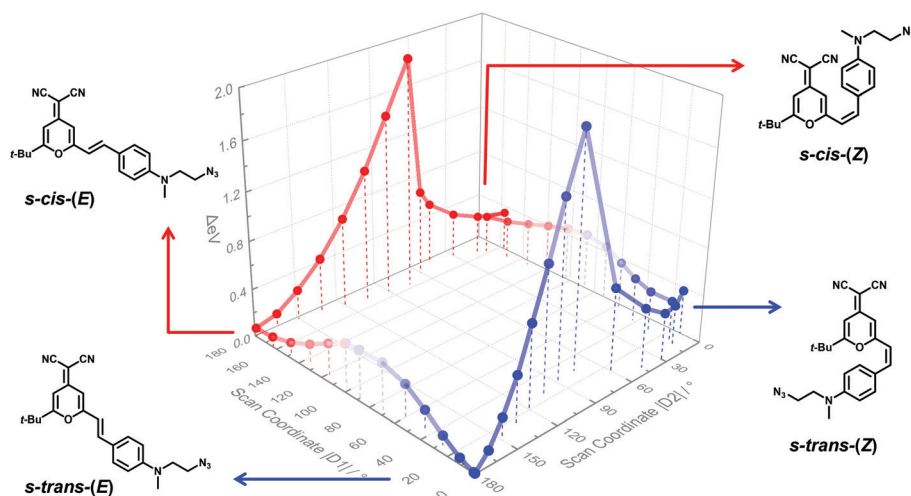


**Fig. 4** The  $S_0$  potential energy curves of the DCM-azide isomer/conformer interconversion by rotating the main dihedral angles  $D1$  and  $D2$ , with  $D1$  corresponding to the  $O_3$ – $C_4$ – $C_9$ – $C_{13}$  scan coordinate and  $D2$  corresponding to the  $C_4$ – $C_9$ – $C_{13}$ – $C_{14}$  scan coordinate (see Fig. 1). DFT calculations were performed at the PBE0/6-311+G(d,p) PCM:THF level of theory. The calculated scans were performed along the following coordinate directions: *s-cis-(E)*  $\rightarrow$  *s-cis-(Z)*, *s-cis-(E)*  $\rightarrow$  *s-trans-(E)*, *s-trans-(E)*  $\rightarrow$  *s-trans-(Z)* and *s-cis-(Z)*  $\rightarrow$  *s-trans-(Z)*. The *s-cis* side is shown in red color and the *s-trans* side is shown in blue color. NB: the final states reached at the end of the scans may slightly differ from the fully optimized forms (as visible e.g. for *s-cis-(Z)* and *s-trans-(Z)*).



$C_4-C_9$  min. = 1.399 Å). When the molecule is distorted around  $D_2 = 75^\circ$ , the  $C_4-C_9=C_{13}-C_{14}$  loses the alternate single-double-single bond character at this peculiar geometry. Indeed, the  $E \leftrightarrow Z$  transformation is a configurational isomerization, which requires that the double bond adopts a “single bond” character. In the present case, these elements lead us to assume that the  $E \leftrightarrow Z$  photoisomerization is allowed in the excited state (see below).

### Excited-state computations

The role of the dihedral angle  $D_1$  corresponding to the  $s$ -*cis*  $\leftrightarrow$   $s$ -*trans* interconversion processes was first investigated in the excited state. We performed the relaxed scan optimization of their lowest excited-state  $S_1$  PECs with a downsized def2-SVP basis set, as well as the  $S_1$  vertical excitation energies (VEEs), as shown in the ESI† (Fig. S12). By examining the  $s$ -*cis*  $\leftrightarrow$   $s$ -*trans* excited-state interconversion, the optimized  $S_1$  energy levels are only slightly lower than the  $S_1$  VEEs *i.e.*, the lowest excited-state geometries are almost identical to the Frank-Condon ones. The scan optimizations of the  $S_1$  states imply even higher energy barriers than the ground states for the two conformational interconversions: 0.70 eV in the  $S_1$  *vs.* 0.44 eV in the  $S_0$  ( $s$ -*cis*( $E$ )  $\rightarrow$   $s$ -*trans*( $E$ )) and 0.40 eV in the  $S_1$  *vs.* 0.17 eV in the  $S_0$  ( $s$ -*cis*( $Z$ )  $\rightarrow$   $s$ -*trans*( $Z$ )). On the other hand, regarding the  $E \leftrightarrow Z$  isomerization, TDDFT optimizations could not be performed due to the possible conical intersection (CI) encountered, which requires other multi-determinant methods.

As an extension to explore the potential energy surface (PES) along the  $E \leftrightarrow Z$  isomerization, we searched the possible

existence of CIs on the reaction path by using the spin-flip TDDFT (SF-TDDFT) method.<sup>31,32</sup> SF-TDDFT is a single reference method that is easy to carry out to compensate for the inability of TDDFT to localize  $S_0/S_1$  CIs.<sup>33,34</sup> Taking a higher triplet state with two unpaired  $\alpha$ -electrons as the reference state instead of the ground state used in TDDFT, SF-TDDFT is able to describe doubly excited electron configurations *via*  $\alpha \rightarrow \beta$  spin-flipped excitations necessary to calculate CIs where the Born-Oppenheimer approximation breaks down. However, we need to pay attention to the spin contamination problem brought by the single reference method. When applied to double-bond molecular systems, *e.g.* stilbene or azobenzene, the SF-TDDFT method with different algorithms has successfully yielded results close to the CASSCF/CASPT2 level of calculations at a rather lower computational cost.<sup>33-35</sup> In the present case, we adapted SF-TDDFT with the penalty constrained algorithm to DCM-azide, which is a 54-atom dimension system, searching for the minimum energy CIs on the  $S_0/S_1$  PES.<sup>33</sup>

To localize the CI, we firstly implemented a  $S_0$  PES scan map with a reduced basis set size at 6-31G(d) *in vacuo*. The global  $S_0$  PES is shown in Fig. 5. Despite slight energy differences, the results are well-compatible with the larger basis set used with the PCM solvation model (Fig. 3). Then we assumed the CIs to be located close to the maximum energy barrier between the  $E$ - and  $Z$ -forms. We defined a set of initial geometries corresponding to the  $S_0$  PES map, with  $D_2 = -75^\circ$  and  $D_1$  ranging from  $-180^\circ$  and  $+180^\circ$ , sampling one structure every  $15^\circ$ . With this methodology, two CI( $S_0/S_1$ ) geometries were successfully identified as depicted in Fig. 5 and detailed in the ESI† (Tables S7 and S8), of the  $s$ -*cis* type (CI-1:  $D_1 = 176.66^\circ$ ,  $D_2 = -78.58^\circ$ )

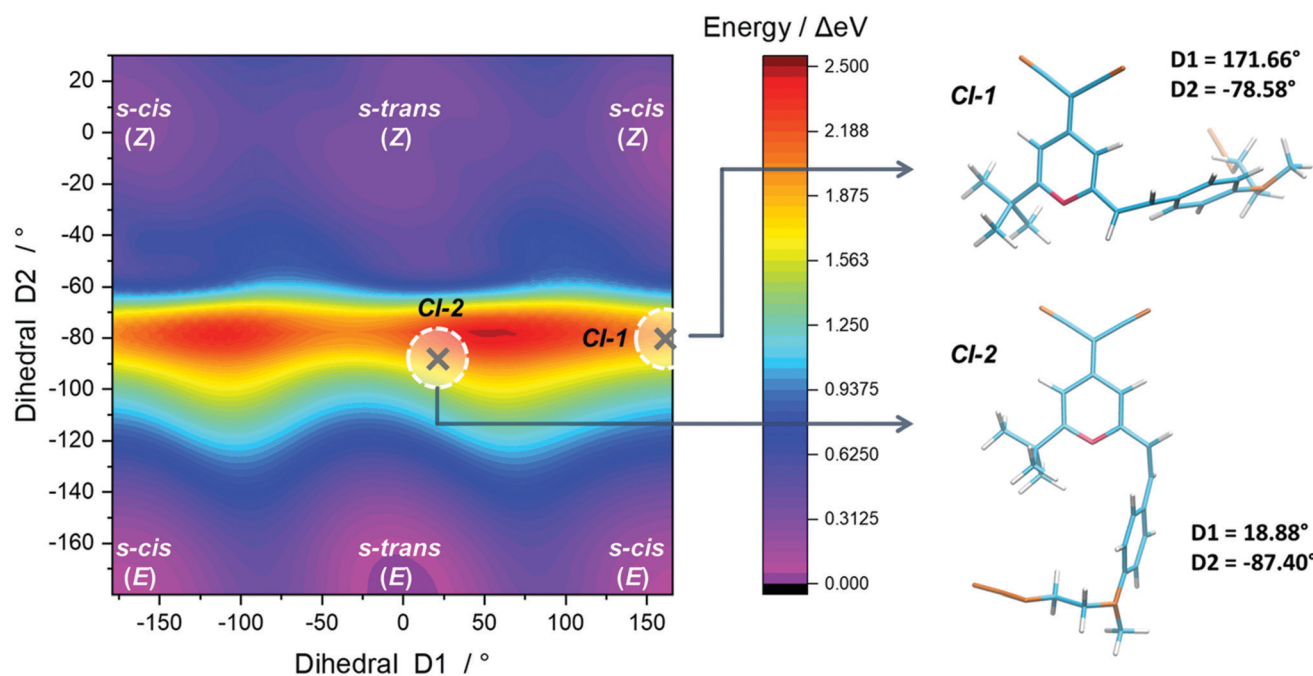


Fig. 5 Ground-state potential energy surface (PES) calculated using DFT (PBE0/6-31G(d)) *in vacuo* as a function of  $D_1$  and  $D_2$  dihedral angles (color map), and minimum energy conical intersection (CI) geometries localized in the  $S_0$  PES map, calculated by the SF-TDDFT method at the PBE0/6-31G(d) *in vacuo* level of theory.

**Table 3** Energies and dihedral angles of optimized  $S_1$  and CI, computed at the SF-PBE0/6-31G(d) level

	$\Delta E$ of $S_1$ (eV)	$D1$ ( $^\circ$ )	$D2$ ( $^\circ$ )
$S_1$ of <i>s-trans</i> -( <i>E</i> )	—	0.12	179.41
$S_1$ of <i>s-cis</i> -( <i>E</i> )	0.058	-179.32	179.74
$S_1$ of <i>s-trans</i> -( <i>Z</i> )	0.290	4.66	18.63
$S_1$ of <i>s-cis</i> -( <i>Z</i> )	0.088	-171.35	23.92
CI-1 ( <i>s-cis</i> )	0.512	171.66	-78.58
CI-2 ( <i>s-trans</i> )	0.511	18.88	-87.40

and *s-trans* type (CI-2:  $D1 = 18.88^\circ$ ,  $D2 = -87.40^\circ$ ), respectively. At first glance, the CIs are close to the location of the highest energy barrier structures of the  $S_0$  PES. The *s-cis* CI-1 is geometrically close to the ground state geometry taken at the transition state between *s-cis*-(*E*) and *s-cis*-(*Z*) as shown in Fig. 5. The CI-2 geometry found on the *s-trans* side is more displaced from the saddle point of the ground state between the *s-trans*-(*E*) and *s-trans*-(*Z*). However, the two CIs identified by SF-TDDFT have a similar  $S_0/S_1$  energy at this calculation level (CI-1:  $S_0/S_1 = -1292.8950/-1292.8935$  a.u. and CI-2:  $S_0/S_1 = -1292.8945/-1292.8935$  a.u., respectively), with comparable single  $C_4-C_9$  and double  $C_9=C_{13}$  bond lengths (CI-1: 1.399/1.464 Å and CI-2: 1.395/1.456 Å, respectively). Both CI-1 and CI-2 most probably originate from the same seam of intersection between  $S_0$  and  $S_1$ , along the  $D1$  dihedral angle rotation. In addition, it is interesting to note that the electronic nature of the  $S_1$  state at the crossing could be provided by the SF-TDDFT method and was found to have an ionic HOMO  $\rightarrow$  LUMO character.

Moreover, we computed the  $S_1$  minima for the *s-trans*-(*E*), *s-cis*-(*E*), *s-trans*-(*Z*), and *s-cis*-(*Z*) forms, at the SF-PBE0/6-31G(d) level in a vacuum, to be compared with CI-1 and CI-2. Their relative energies and dihedral angles ( $D1$  and  $D2$ ), together with those of CI-1 and CI-2, are gathered in Table 3. The energy difference between the optimized  $S_1$  state and the CI is higher for the *s-trans*-(*E*) form ( $\Delta E = 0.51$  eV). The lowest energy differences are obtained for the *Z*-forms ( $\Delta E = 0.22-0.42$  eV). The *s-cis*-(*E*) is located at an intermediate level ( $\Delta E = 0.45$  eV). Additionally, the optimized  $S_1$  states for both *E*-forms show a fully planar geometry, whereas they appear more tilted for the *Z*-forms, with  $5-9^\circ$  away from planarity for  $D1$ , and  $18-24^\circ$  for  $D2$ . The geometries of the excited state of the *Z*-forms are closer to the CI ones, compared to the planar *E*-forms; we can therefore expect a much lower energy barrier in the excited state landscape to reach the CI after excitation and return non-radiatively to the ground state, possibly along with photoisomerization. Consequently, we can deduce that the DCM-azide molecule has several pathways to relax from the excited states to the ground state. When DCM-azide is excited, it can undergo isomerization in the excited state, through the CI to reach the ground state, which is fully compatible with the experimental evidence of the  $E \leftrightarrow Z$  photoisomerization. Besides, the relaxed excited states of DCM-azide can return to the ground state by radiative deactivation. Since the  $S_1$  excited state of the *s-trans*-(*E*) form has a larger energy difference than the *s-cis*-(*E*) form to reach the CI, it could explain its much larger contribution to the overall emission and its longer lifetime. The  $S_1$  excited

states of the *Z*-forms are much closer to the CI (in geometry and energy), which is fully in line with the absence of observed fluorescence from these species, as well as the higher photoisomerization quantum yield measured previously for the  $Z \rightarrow E$  reaction, compared to the  $E \rightarrow Z$  reaction.<sup>14</sup>

As a unified general picture, after light absorption, the *E*-forms may experience a competition between fluorescence deactivation,  $E \rightarrow Z$  isomerization reaction (through CIs), and other non-radiative deactivation pathways. Regarding the *Z*-forms, which are not emissive, only the  $Z \leftrightarrow E$  isomerization reaction (through CIs) and other non-radiative deactivation paths can be considered. It is worth noting that DCM is expected to have both locally excited and internal charge-transfer states in solution, at the origin of its well-known solvatochromism in emission. In the present CI determination *in vacuo*, the solvent could not be taken into account and consequently, the role of the internal charge transfer state could not be properly modeled. The solvent effect is beyond the scope of our computational investigation.

## Conclusions

The photoisomerization of a DCM analog (DCM-azide) was investigated experimentally and theoretically, shining light on its  $E \leftrightarrow Z$  isomerization, which was demonstrated previously.<sup>14</sup> The relationships between the four isomers and conformers of DCM-azide were clarified by both experimental evidence (X-ray structures and spectroscopic data) and a full set of theoretical calculations (geometries, energies, electronic transitions, isomerization and interconversion patterns) *in vacuo* or including the solvent medium.

The fluorescence decay experiments confirmed that only the *E*-forms of DCM-azide are emissive. The emissive species in the fluorescence decay experiments were assigned to the *s-trans*-(*E*) (longer decay-time) and *s-cis*-(*E*) (shorter decay-time) forms of DCM-azide. The DFT/TDDFT and SF-TDDFT calculations of the four isomers and conformers provided a general pattern of the isomerization and interconversion paths in the ground and the excited states. Two conical intersections were identified, explaining the relaxation from the lowest excited state to the ground state, at the origin of the  $E \leftrightarrow Z$  photoisomerization. They obviously play a great role in the competition between the fluorescence relaxation and the  $E \leftrightarrow Z$  photoreaction, and also in the *s-trans*  $\leftrightarrow$  *s-cis* conformational interconversion.

## Experimental section and methods

### Materials

All solvents used for steady-state spectroscopies were of pure spectroscopic grade reagents from Carlo Erba Reagents. The DCM-azide compound was prepared according to literature procedures.<sup>30,36,37</sup>

### Steady-state absorption and emission spectroscopy

Steady-state spectroscopic absorption measurements were carried out with Agilent Technologies Cary 4000 and Cary 5000 spectrophotometers. The emission spectra were recorded with a Horiba Jobin-Yvon Fluorolog FL3-221 fluorescence spectrometer. The fluorescence quantum yield was determined by using Coumarin 153 in ethanol ( $\phi_{\text{em}} = 0.544^{38}$ ) as a standard reference from Sigma-Aldrich.

### Time-resolved fluorescence spectroscopy

Fluorescence decay curves were obtained by the time-correlated single-photon counting (TCSPC) method. The setup is composed of a titanium sapphire Ti:Sa oscillator (Spectra Physics, Mai Tai) emitting pulses of 100 fs duration for the fundamental laser beam, at an 80 MHz frequency. The laser pulses then pass through a pulse picker which implements an acousto-optic modulator to reduce the repetition rate down to 4 MHz. Non-linear SHG/THG crystals generate the desired wavelength (GWU Lasertechnik, UHG-23-PSK), then the beam is directed to the sample solution after adjusting the excitation power with an intensity attenuator filter wheel. Fluorescence photons are detected at  $90^\circ$  through a polarizer at the magic angle and a monochromator, by means of a micro-channel plate photomultiplier (MCP-PMT R3809U-50, Hamamatsu), connected to a TCSPC module (SPC-630, Becker & Hickl). Time-correlated fluorescence decay data are finally processed and analysed with the help of software which implements reconvolution analysis and the global nonlinear least-squares minimization method (Globals, Laboratory for Fluorescence Dynamics at the University of California, Irvine).

### X-ray crystallographic analysis

X-ray crystallographic analysis was carried out on the DCM-azide crystals. The isolated crystals were dried under vacuum at room temperature and shielded from ambient light. X-ray diffraction was carried out using a Rigaku XtaLabPro diffractometer equipped with a Mo microfocus sealed tube generator coupled to a double-bounce Max-Flux multilayer optic and a HPAD PILATUS3 R 200K detector. Data collections were carried out using the software CrysAlisPro 1.171.41.96a.<sup>39</sup> The SCALE3 ABSPACK scaling algorithm implemented within CrysAlisPro was applied to the processed data for the empirical absorption correction using spherical harmonics. The two structures were readily solved by intrinsic phasing methods (SHELXT program)<sup>40</sup> and refined by full-matrix least-squares methods on  $F^2$  using SHELXL.<sup>41</sup> Molecular graphics were prepared with ORTEP.<sup>42</sup>

### Computational details

All the DFT and TDDFT calculations were performed using the Gaussian 16 software package.<sup>43</sup> The Pople 6-311+G(d,p), 6-311+G(d,p) and 6-31G(d) basis sets were adopted and the solvent effects were implemented with integral equation formalism of the polarizable continuum model (IEFPCM). The  $S_0$  geometries of the four isomers and conformers were optimized at the PBE0/6-311+G(d,p) level. Regarding the computational cost, reduced size def2-SVP and 6-31G(d) basis sets were used

for the excited states explorations and corresponding comparisons. The comparison of functionals and the basis set dependencies are shown in the ESI.† From all optimized geometries, the vertical excitation energies and emission energies were calculated by the TDDFT method. The linear response (LR) method was implemented in the TDDFT calculations. The minimum energy CI calculations of  $S_0/S_1$  in the  $E \leftrightarrow Z$  isomerization process were located by the SF-TDDFT method with the penalty-constrained (PC) optimization algorithm.<sup>33,34,44,45</sup> The SF-TDDFT/PC CI localizations were carried out at the PBE0/6-31G(d) level in the gas phase by GAMESS-US (version 30 SEP 2020 (R2)).<sup>46</sup> All visualizations were implemented by GaussView 6 and VMD 1.9.3.<sup>47,48</sup>

## Author contributions

Conceptualization: R. M., F. M., S. M. (equal), and J. X. (supporting); data curation: Y. Z. and P. R. (equal); formal analysis: Y. Z. (lead), P. R., and F. M. (supporting); funding acquisition: R. M.; investigation: Y. Z. (lead), P. R., R. M., F. M., S. M., and L. C. (supporting); methodology: Y. Z. (lead), R. M., F. M., S. M., and P. R. (supporting); project administration: R. M. (lead), F. M., S. M., and J. X. (supporting); resources: R. M., J. X., S. M., and A. B. (equal); software: Y. Z.; supervision: R. M., and F. M. (equal); validation: Y. Z., R. M., and F. M. (equal), S. M. (supporting); visualization: Y. Z. and R. M. (equal); writing – original draft: Y. Z. and R. M. (equal), P. R. (supporting); writing – review and editing: Y. Z., R. M. (equal), F. M., and L. C. (supporting).

## Conflicts of interest

There are no conflicts to declare.

## Acknowledgements

The authors acknowledge Arnaud Brosseau for his kind help and support during the time-resolved fluorescence measurements. This work was performed by using HPC resources from the “Mésocentre” computing center of Centrale-Supélec and the École Normale Supérieure Paris-Saclay supported by the CNRS and the Région Ile-de-France (<http://mesocentre.centrale-supelec.fr/>). Funding from the Agence Nationale de la Recherche (ANR-17-CE07-0056-01) is acknowledged.

## Notes and references

- 1 D. Bléger and S. Hecht, *Angew. Chem., Int. Ed.*, 2015, **54**, 11338–11349.
- 2 M. Baroncini, M. Canton, L. Casimiro, S. Corra, J. Groppi, M. La Rosa, S. Silvi and A. Credi, *Eur. J. Inorg. Chem.*, 2018, 4589–4603.
- 3 D. Roke, S. J. Wezenberg and B. L. Feringa, *Proc. Natl. Acad. Sci. U. S. A.*, 2018, **115**, 9423–9431.
- 4 C. T. Kornman, L. Li, A. O. Weldeab, I. Ghiviriga, K. A. Abboud and R. K. Castellano, *Chem. Sci.*, 2020, **11**, 10190–10197.



- 5 M. Baroncini, S. d'Agostino, G. Bergamini, P. Ceroni, A. Comotti, P. Sozzani, I. Bassanetti, F. Grepioni, T. M. Hernandez, S. Silvi, M. Venturi and A. Credi, *Nat. Chem.*, 2015, **7**, 634–640.
- 6 F. Castiglioni, W. Danowski, J. Perego, F. K.-C. Leung, P. Sozzani, S. Bracco, S. J. Wezenberg, A. Comotti and B. L. Feringa, *Nat. Chem.*, 2020, **12**, 595–602.
- 7 S. L. Oscurato, M. Salvatore, P. Maddalena and A. Ambrosio, *Nanophotonics*, 2018, **7**, 1387–1422.
- 8 G. Das, T. Prakasam, M. A. Addicoat, S. K. Sharma, F. Ravaux, R. Mathew, M. Baias, R. Jagannathan, M. A. Olson and A. Trabolsi, *J. Am. Chem. Soc.*, 2019, **141**, 19078–19087.
- 9 K. Müller, A. Knebel, F. Zhao, D. Bléger, J. Caro and L. Heinke, *Chem. – Eur. J.*, 2017, **23**, 5434–5438.
- 10 P. M. Toro, D. H. Jara, A. H. Klahn, D. Villaman, M. Fuentealba, A. Vega and N. Pizarro, *Photochem. Photobiol.*, 2021, **97**, 61–70.
- 11 W. A. de Oliveira, D. Z. Mezalira and E. Westphal, *Liq. Cryst.*, 2021, **48**, 88–99.
- 12 B. Bai, M. Zhang, N. Ji, J. Wei, H. Wang and M. Li, *Chem. Commun.*, 2017, **53**, 2693–2696.
- 13 H. Karimi-Alavijeh, F. Panahi and A. Gharavi, *J. Appl. Phys.*, 2014, **115**, 093706.
- 14 L. Casimiro, S. Maisonneuve, P. Retailleau, S. Silvi, J. Xie and R. Métivier, *Chem. – Eur. J.*, 2020, **26**, 14341–14350.
- 15 P. Hammond, *Opt. Commun.*, 1979, **29**, 331–333.
- 16 E. Marason, *Opt. Commun.*, 1981, **37**, 56–58.
- 17 J.-C. Mialocq and M. Meyer, *Laser Chem.*, 1990, **10**, 067392.
- 18 M.-k. Leung, C.-C. Chang, M.-H. Wu, K.-H. Chuang, J.-H. Lee, S.-J. Shieh, S.-C. Lin and C.-F. Chiu, *Org. Lett.*, 2006, **8**, 2623–2626.
- 19 Y.-S. Yao, J. Xiao, X.-S. Wang, Z.-B. Deng and B.-W. Zhang, *Adv. Funct. Mater.*, 2006, **16**, 709–718.
- 20 H. J. Yun, D. Y. Jung, D. K. Lee, A. K.-Y. Jen and J. H. Kim, *Dyes Pigm.*, 2015, **113**, 675–681.
- 21 J. Y. Kim, S. S. Yoon and Y. S. Kim, *J. Nanosci. Nanotechnol.*, 2013, **13**, 1–4.
- 22 Z. Guo, W. Zhu and H. Tian, *Chem. Commun.*, 2012, **48**, 6073–6084.
- 23 M. Meyer, J. C. Mialocq and B. Perly, *J. Phys. Chem.*, 1990, **94**, 98–104.
- 24 M. Lesiecki, F. Asmar, J. Drake and D. M. Camaioni, *J. Lumin.*, 1984, **31**, 546–548.
- 25 J. Drake, M. L. Lesiecki and D. M. Camaioni, *Chem. Phys. Lett.*, 1985, **113**, 530–534.
- 26 M. Meyer, J. Mialocq and M. Rougee, *Chem. Phys. Lett.*, 1988, **150**, 484–490.
- 27 W. Rettig and W. Majenz, *Chem. Phys. Lett.*, 1989, **154**, 335–341.
- 28 J. Mialocq, X. Armand and S. Marguet, *J. Photochem. Photobiol., A*, 1993, **69**, 351–356.
- 29 X. Xu, R. Zhang, Z. Cao and Q. Zhang, *J. Theor. Comput. Chem.*, 2008, **7**, 719–736.
- 30 K. Ouhenia-Ouadahi, R. Métivier, S. Maisonneuve, A. Jacquart, J. Xie, A. Léaustic, P. Yu and K. Nakatani, *Photochem. Photobiol. Sci.*, 2012, **11**, 1705–1714.
- 31 Y. Shao, M. Head-Gordon and A. I. Krylov, *J. Chem. Phys.*, 2003, **118**, 4807–4818.
- 32 F. Wang and T. Ziegler, *J. Phys. Chem.*, 2004, **121**, 12191–12196.
- 33 N. Minezawa and M. S. Gordon, *J. Phys. Chem. A*, 2009, **113**, 12749–12753.
- 34 N. Minezawa and M. S. Gordon, *J. Phys. Chem. A*, 2011, **115**, 7901–7911.
- 35 M. Winslow, W. B. Cross and D. Robinson, *J. Chem. Theory Comput.*, 2020, **16**, 3253–3263.
- 36 S. Maisonneuve, R. Métivier, P. Yu, K. Nakatani and J. Xie, *Beilstein J. Org. Chem.*, 2014, **10**, 1471–1481.
- 37 Y. Yu, N. Bogliotti, S. Maisonneuve, J. Tang and J. Xie, *Tetrahedron Lett.*, 2013, **54**, 1877–1883.
- 38 K. Rurack and M. Spieles, *Anal. Chem.*, 2011, **83**, 1232–1242.
- 39 O. D. Rigaku, *CrysAlis PRO*, Rigaku Oxford Diffraction, Yarnton, Oxfordshire, England, 2015.
- 40 G. M. Sheldrick, *Acta Crystallogr. A*, 2015, **71**, 3–8.
- 41 G. M. Sheldrick, *Acta Crystallogr. C*, 2015, **71**, 3–8.
- 42 M. N. Burnett and C. K. Johnson, *ORTEP-III*, ORNL-6895, Oak Ridge National Laboratory, Tennessee, USA, 1996.
- 43 M. J. Frisch, G. W. Trucks, H. B. Schlegel, G. E. Scuseria, M. A. Robb, J. R. Cheeseman, G. Scalmani, V. Barone, G. A. Petersson, H. Nakatsuji, X. Li, M. Caricato, A. V. Marenich, J. Bloino, B. G. Janesko, R. Gomperts, B. Mennucci, H. P. Hratchian, J. V. Ortiz, A. F. Izmaylov, J. L. Sonnenberg, D. Williams-Young, F. Ding, F. Lipparini, F. Egidi, J. Goings, B. Peng, A. Petrone, T. Henderson, D. Ranasinghe, V. G. Zakrzewski, J. Gao, N. Rega, G. Zheng, W. Liang, M. Hada, M. Ehara, K. Toyota, R. Fukuda, J. Hasegawa, M. Ishida, T. Nakajima, Y. Honda, O. Kitao, H. Nakai, T. Vreven, K. Throssell, J. A. Montgomery, Jr., J. E. Peralta, F. Ogliaro, M. J. Bearpark, J. J. Heyd, E. N. Brothers, K. N. Kudin, V. N. Staroverov, T. A. Keith, R. Kobayashi, J. Normand, K. Raghavachari, A. P. Rendell, J. C. Burant, S. S. Iyengar, J. Tomasi, M. Cossi, J. M. Millam, M. Klene, C. Adamo, R. Cammi, J. W. Ochterski, R. L. Martin, K. Morokuma, O. Farkas, J. B. Foresman and D. J. Fox, *Gaussian 16 Revision C.01*, Gaussian Inc., Wallingford CT, 2016.
- 44 B. G. Levine, C. Ko, J. Quenneville and T. J. Martínez, *Mol. Phys.*, 2006, **104**, 1039–1051.
- 45 B. G. Levine, J. D. Coe and T. J. Martínez, *J. Phys. Chem. B*, 2008, **112**, 405–413.
- 46 G. M. J. Barca, C. Bertoni, L. Carrington, D. Datta, N. De Silva, J. E. Deustua, D. G. Fedorov, J. R. Gour, A. O. Gunina, E. Guidez, T. Harville, S. Irle, J. Ivanic, K. Kowalski, S. S. Leang, H. Li, W. Li, J. J. Lutz, I. Magoulas, J. Mato, V. Mironov, H. Nakata, B. Q. Pham, P. Piecuch, D. Poole, S. R. Pruitt, A. P. Rendell, L. B. Roskop, K. Ruedenberg, T. Sattasathuchana, M. W. Schmidt, J. Shen, L. Slipchenko, M. Sosonkina, V. Sundriyal, A. Tiwari, J. L. Galvez Vallejo, B. Westheimer, M. Wloch, P. Xu, F. Zahariev and M. S. Gordon, *J. Chem. Phys.*, 2020, **152**, 154102.
- 47 R. Dennington, T. A. Keith and J. M. Millam, *GaussView Version 6*, Semichem Inc., Shawnee Mission, KS, 2019.
- 48 W. Humphrey, A. Dalke and K. Schulten, *J. Mol. Graph. Model.*, 1996, **14**, 33–38.

# Supporting Information

## Photoisomerization of a 4-dicyanomethylene-2-methyl-6-(*p*-dimethylaminostyryl)-4*H*-pyran analog dye: a combined photophysical and theoretical investigation

Yang Zhou,<sup>a</sup> Stéphane Maisonneuve,<sup>a</sup> Lorenzo Casimiro,<sup>a</sup> Pascal Retailleau,<sup>b</sup> Juan Xie,<sup>a</sup> François Maurel,<sup>\*c</sup> and Rémi Métivier<sup>\*a</sup>

<sup>a</sup> Université Paris-Saclay, ENS Paris-Saclay, CNRS, Photophysique et Photochimie Supramoléculaires et Macromoléculaires, 91190 Gif-sur-Yvette, France.

<sup>b</sup> Université Paris-Saclay, CNRS, Institut de Chimie des Substances Naturelles, UPR 2301, Gif-sur-Yvette, France.

<sup>c</sup> Université de Paris, ITODYS, CNRS, 75006 Paris, France.

<b>Table of contents</b>		<b>Page</b>
<b>1</b>	Crystallographic data collection, structure determination and refinement	2-6
<b>2</b>	DFT calculations	7-16
<b>3</b>	Cartesian coordinates of conical intersections	17-18

## 1. Crystallographic data collection, structure determination and refinement

The compound (*E*)-2-(2-(4-((2-azidoethyl)(methyl)amino)styryl)-6-(tert-butyl)-4H-pyran-4-ylidene) malononitrile was obtained in similar red solid forms suitable to Single Crystal X-ray Diffraction analyses. Both crystal forms could be mounted upon a nylon loop with a drop of paratone oil to be irradiated at room temperature using a RIGAKU XtaLabPro diffractometer equipped with a Mo microfocus sealed tube generator coupled to a double-bounce confocal Max-Flux® multilayer optic and a HPAD PILATUS3 R 200K detector. Data collections were carried out using the software *CrysAlisPro* 1.171.41.96a<sup>1</sup>. SCALE3 ABSPACK scaling algorithm implemented within *CrysAlisPro* was applied to the processed data for the empirical absorption correction using spherical harmonics. The two structures were readily solved by intrinsic phasing methods (*SHELXT* program)<sup>2</sup> and refined by full-matrix least-squares methods on  $F^2$  using *SHELXL*.<sup>3</sup> One form was refined in the centrosymmetric triclinic space group (**form I**) while the second one crystallized in an orthorhombic unit cell (**form II**). Although the normalized structure factor distribution was in favor of a centrosymmetric structure, the non-centrosymmetric  $Pna2_1$  space group, which is consistent with the systematic absences, was first tested to deal with the azido disorder in the course of the structure refinement. The ethyl azido atoms were therefore refined over two sites whose occupancy factors converged to a value close to 0.5 and were thus fixed to half occupancy. However, to ensure satisfactory refinement of that disorder and avoid chemically unreasonable ellipsoids, rigid-body restraints (*SHELXL* commands DELU and SIMU with esd 0.005 and 0.01 Å<sup>2</sup> respectively) were applied to atoms of the ethylazido group with resort to displacement parameters constrained to be identical (command EADP upon the following pair of atoms C21-C21B, and C22-C22B), as well as similar distance restraints (DFIX, DANG and SADI with esd ranging from 0.001 to 0.01 Å<sup>2</sup>). If the *checkCIF* implementation of *PLATON*<sup>4</sup> ADDSYM could not fail to detect the mirror plane instead of  $2_1$  axis, the refinement of the model after *b-c* axes permutation in the higher symmetry space group *Pnma* with ADDYM-exact worsened the model statistics (see Table S1), the weighting scheme refinement and the electron residuals on both side of the mirror with or without application of ADP or bond length restraints. Nevertheless, the refined model was kept in the holohedral group *Pnma* -whose  $Pna2_1$  is an hemihedral subgroup- in link with the molecular geometry, which does not eventually affect the packing structure interaction type analyses. In both cases, anisotropic refinement improved all parameters of non-hydrogen atoms of the molecule of interest. If most of the H atoms were identified in difference maps, methyl H atoms were idealized and included as rigid groups allowed to rotate but not tip and refined with  $U_{iso}$  set to  $1.5U_{eq}(C)$  of the parent carbon atom. All other H atoms bound to carbon atoms were positioned geometrically and refined with  $U_{iso}$  set to  $1.2U_{eq}(C)$  of the parent carbon atom. Both polymorphic crystal structures are shown in Ortep<sup>5</sup> representation in Figure S1. It has to be noticed that in both crystal forms the *s-trans*-(*E*) configuration was unveiled. The triclinic structure appears slightly the most accurate one with no static disorder. It is made of one conformer in the asymmetric unit, featuring regular geometry parameters except a short terminal triple bond distance of 1.131(2) Å leading to a |Z-score| value of 4.681 after a Mogul<sup>6</sup> check. Unsurprisingly for such (*E*)-2-(2-styryl-4H-pyran-4-ylidene) malononitrile core as observed in 15 previous hits found in the Cambridge Structural Database<sup>7</sup> (CSD version 5.42, updated Sep 2021), the DCM platform is indeed quasi-planar in the triclinic form and would be constrained to be lying within the mirror plane

<sup>1</sup> Rigaku OD (2015). *CrysAlis PRO*. Rigaku Oxford Diffraction, Yarnton, Oxfordshire, England.

<sup>2</sup> Sheldrick, G. M. (2015). *Acta Crystallogr.*, **A71**, 3-8.

<sup>3</sup> Sheldrick, G. M. (2015). *Acta Crystallogr.*, **C71**, 3-8.

<sup>4</sup> Spek, A. L. (2009). *Acta Cryst.* **D65**, 148–155.

<sup>5</sup> Burnett, M. N. & Johnson, C. K. (1996). *ORTEP III*. Report ORNL-6895. Oak Ridge National Laboratory, Tennessee, USA.

<sup>6</sup> Bruno, I. J., Cole, J. C., Kessler, M., Luo, J., Motherwell, W. D. S., Purkis, L. H., Smith, B. R., Taylor, R., Cooper, R. I., Harris, S. E. & Orpen, A. G. (2004). *J. Chem. Inf. Comput. Sci.* **44**, 2133-2144.

<sup>7</sup> Groom, C. R., Bruno, I. J., Lightfoot, M. P. & Ward, S. C. (2016). *Acta Cryst.* **B72**, 171–179.

perpendicular to [0 1 0] in the putative *Pnma* orthorhombic space group. This putative mirror bisects the tert-butyl group and the two sites between which the azido-ethyl chain is allowed to swing. In the triclinic form the mean plane is allowed to slightly wave (rmsd of 0.094 Å for 22 atoms and C21 out of the mean plane by 0.62 Å) and the dihedral angle between the two central six-membered rings is 9.6°. More striking structural differences between the two polymorphs are the relative switch of the azidoethyl chain with respect to the pyran-4-ylidene substituents and its conformation which points almost perpendicular to the molecule mean plane in the triclinic form. An overlay of both conformers is shown in Figure S2 to underscore these crystal structure differences. As expected, the molecules are in each form assembled in layers parallel to the (2 1 1) or (1 0 1) plane respectively for the triclinic case and the orthorhombic one. The interplanar distance is slightly longer in the triclinic form (3.6 Å vs 3.54 Å) probably due to the anchorage of azidoethyl chains in-between the layers. Furthermore, in the triclinic packing all the molecules aligned along the [0 1 -1] direction in an anti-parallel manner, both on the top of each other and within the same plane making pairwise non-conventional H-bonds between C4-H4 ... N1 to develop infinite 1D ribbons bordered in the 2D-sheets by van der Waals interactions through tert-butyl groups and adjacent aromatic H atoms, and stacking interactions in the third dimension. In the orthorhombic form, the molecules viewed down the *b* axis pack in a herringbone arrangement, which is staggered from one layer to another one. The relevance of different intermolecular interactions describing the polymorphism can be established *via* Hirshfeld surface (HS) analysis.<sup>8</sup> These surfaces, along with the two-dimensional fingerprint (FP) plots,<sup>9</sup> were evaluated using *Crystal Explorer 17.5*.<sup>10</sup> The red spots, corresponding to contacts that are shorter than the van der Waals radii sum of the closest atoms, are observed in few spots in the triclinic HS: two weak ones at the opposite long side of the molecule, the N2 atom and C22-H22B atom whose successive N/H interactions link the molecules in 1D-chain along the [0 1 -1] direction, and two intense ones at C5-H5 and N1 as pairwise interaction location to propagate the 2D network. They are more numerous in the orthorhombic HS (Figure S3) regularly scattered at the periphery of the molecule, involving in particular the nitrogen atoms of the disordered azido group and the acetonitrile groups. The surfaces mapped with curvedness, a function of the root-mean-square curvature of the surface show the large green flat region of the molecule core separated by dark blue edges (large positive curvature). In the triclinic CS, these surfaces are on the top of each other in adjacent asu but the shorter centroid to centroid distance is not below 4.0 Å. In the second form, it is even longer (5 Å) due to shifted overlaps with adjacent molecules in the *b* direction.

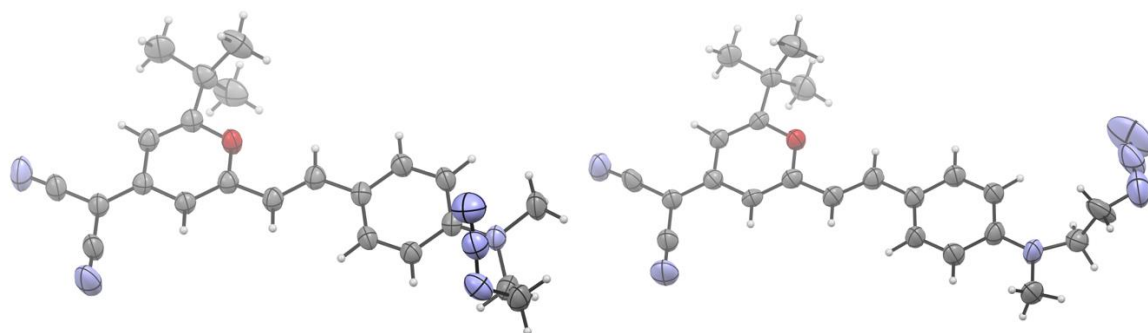
The fingerprint plots (Figure S5) depict the various interactions (*All*) in the two polymorphs and the individual contributions of the different interactions, the grey shadow being an outline of the complete fingerprint plot. The upper spike corresponds to the donor, spike with the lower spike representing the acceptor. Significant differences between the molecular interactions in the two polymorphs are reflected in the distribution of scattered points in the fingerprint plots which appeared more condensed in the orthorhombic form region of 1.0 Å-2.4 Å ( $d_e+d_i$ ) vs 1.0 Å-2.8 Å ( $d_e+d_i$ ) for the triclinic one. It is observed that the relative contributions of H/H and N/H are comparable in both forms and account for 2/3 of the interactions. It is followed by a significant number of C-H $\cdots$  $\pi$  or  $\pi$ - $\pi$  interactions whose proportions differ noticeably between the two forms (13.7 % vs 16.1 % and 9% vs 5%). Another contribution specific to the form II is C/N contacts (3%). Structure refinement statistics are reported in Table S1.

<sup>8</sup> Spackman, M. A. & Jayatilaka, D. (2009). *CrystEngComm*, **11**, 19–32.

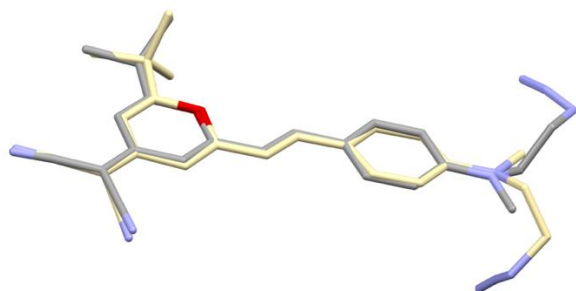
<sup>9</sup> McKinnon, J. J., Jayatilaka, D. & Spackman, M. A. (2007). *Chem. Commun.* pp. 3814–3816.

<sup>10</sup> Turner, M. J., McKinnon, J. J., Wolff, S. K., Grimwood, D. J., Spackman, P. R., Jayatilaka, D. & Spackman, M. A. (2017). *CrystalExplorer17*. University of Western Australia. <http://hirshfeldsurface.net>.

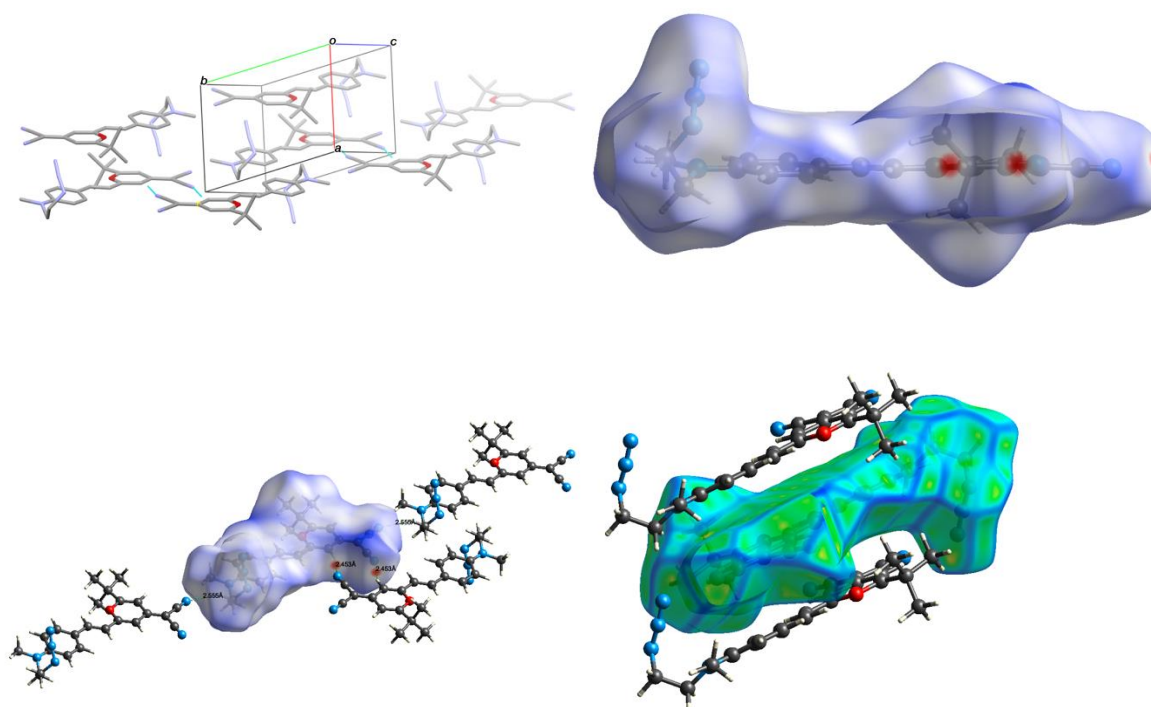
CCDC 2120494 and 2121293 (**triclinic** form and **orthorhombic** form respectively) contain the supplementary crystallographic data for this paper. These data can be obtained free of charge from The Cambridge Crystallographic Data Centre via [www.ccdc.cam.ac.uk/data\\_request/cif](http://www.ccdc.cam.ac.uk/data_request/cif).



**Figure S1** Ortep plot of one conformer (the disorder of the azido moiety is not shown for clarity) of the **triclinic form** (form I, left), and crystal structure of the **orthorhombic form** (form II, right). Ellipsoids are drawn at 50% of probability and hydrogen atoms, with sphere radius of arbitrary size.

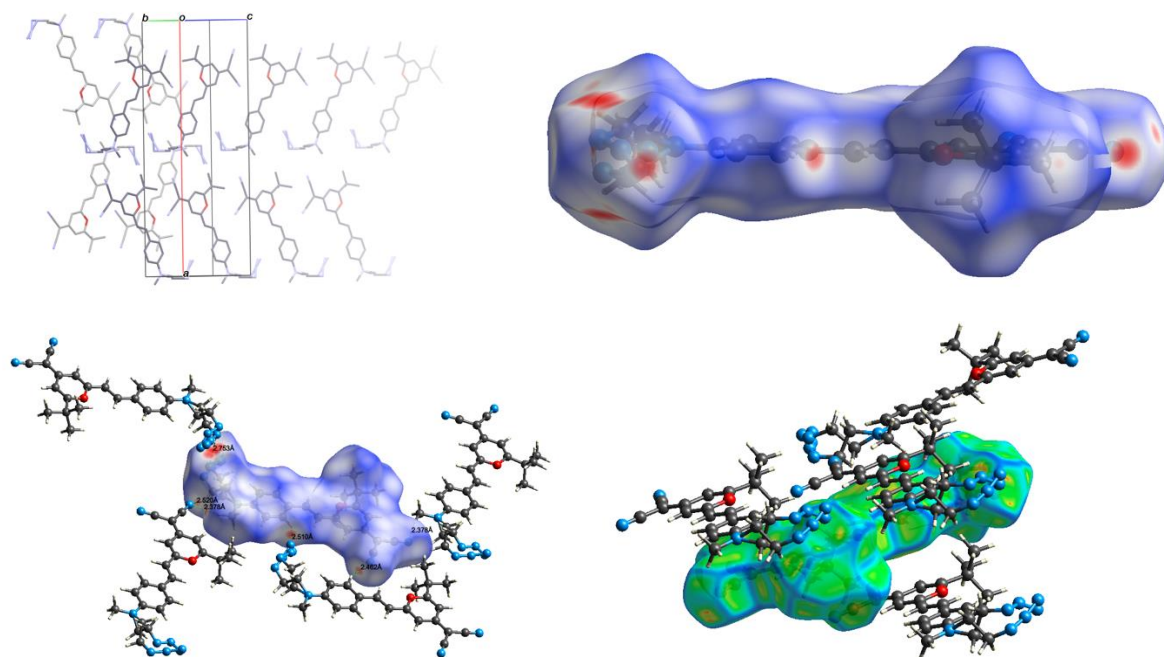


**Figure S2** (Left) Overlay plot of the two forms (carbon atoms in yellow belong to the triclinic structure, grey ones are those of the orthorhombic structure).

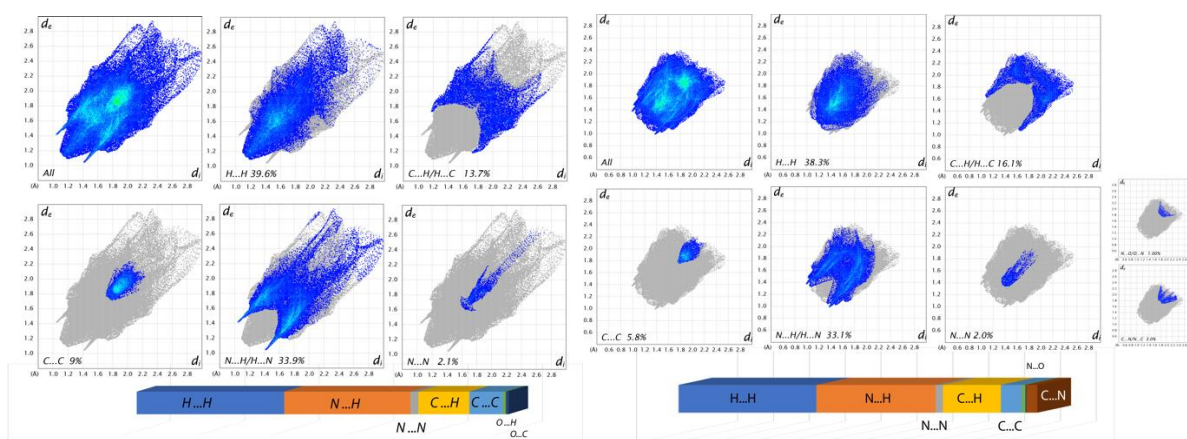




**Figure S3** (a) Partial view of the triclinic crystal showing the molecular association in linear ribbon along the [0 1 -1] direction (b) Hirshfeld surface for form I mapped with  $d_{\text{norm}}$  over the range -0.13 to 2.08. (c) Neighboring molecules associated with close contacts are shown along with distances between the atoms involved (d)

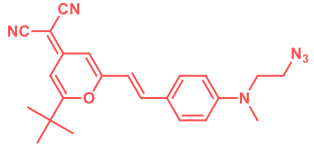


**Figure S4** (a) Partial view down the  $b$  axis of the orthorhombic crystal showing the herringbone pattern waving along the  $a$  direction. (b) Hirshfeld surface for form II mapped with  $d_{\text{norm}}$  over the range -0.22 to 1.20. (c) Neighbouring molecules associated with close contacts are shown along with distances between the atoms involved and (d) the map with curvedness



**Figure S5** Fingerprint plots for the molecule in form I (triclinic, left) and in form II (orthorhombic, right), broken down into contributions from specific pairs of atom-types. For each plot the grey shadow is an outline of the complete fingerprint plot (upper left plot). Below the histograms for the major atom-type/atom-type contacts represent the percentage contributions to the Hirshfeld surface area for the various close intermolecular contacts for molecules in forms I and II.

**Table S1** Crystal data and structure refinement of *s-trans-(E)* conformer of DCM-azide obtained in **Form I** (triclinic) and **Form II** (orthorhombic).

CRYSTAL DATA				
Identification code		<b>Form I</b>		<b>Form II</b>
Name		<i>(E)</i> -2-(2-(4-((2-azidoethyl)(methyl)amino)styryl)-6-(tert-butyl)-4H-pyran-4-ylidene)malononitrile		
Structure				
Empirical formula		C <sub>23</sub> H <sub>24</sub> N <sub>6</sub> O		
Formula weight		400.48		
Crystal system, Space group		Triclinic, P -1		Orthorhombic,
				Pna21
				P nma
Unit cell dimensions (Å, °)	a   Å	7.3618(4)	29.8656(17)	29.8656(17)
	b	9.7239(5)	10.0461(5)	7.1127(4)
	c	16.0733(8)	7.1127(4)	10.0461(5)
	α   °	86.088(4)	90	90
	β	83.182(4)	90	90
	γ	74.189(4)	90	90
Volume (Å <sup>3</sup> )		1098.48(10)	1537.41(16)	
Z,		2,	4,	
Calculated density (Mg/m <sup>3</sup> )		1.211	1.246	
Absorption coefficient (mm <sup>-1</sup> )		0.078	0.081	
F(000)		424	848	
Crystal size (mm)		0.32 x 0.16 x 0.03	0.35 x 0.22 x 0.05	
DATA COLLECTION				
Diffractometer		Rigaku XtaLabPro mm003 diffractometer with Pilatus 200K Hybrid pixel array detector (HPAD)		
Wavelength (Å)		0.71073		
Temperature (K)		293(2)		
θ range for data collection (°)		2.483 to 26.022	2.881 to 26.019	
Limiting indices		-9 ≤ h ≤ 9, -11 ≤ k ≤ 11, -19 ≤ l ≤ 19	-31 ≤ h ≤ 36, -12 ≤ k ≤ 12, -7 ≤ l ≤ 8	-31 ≤ h ≤ 36, -8 ≤ l ≤ 7, -12 ≤ k ≤ 12,
Reflections collected / unique R(int)		22812 / 4312 0.0294	13702 / 3751 0.0192	13711 / 3748 0.0186
Completeness to θ <sub>full</sub> (%)		99.8	99.6	99.7
Absorption correction		Semi-empirical from equivalents		
Max. and min. transmission		1.000 and 0.270	1.000 and 0.686	
REFINEMENT				
Refinement method		Full-matrix least-squares on F <sup>2</sup>		
		IAM	HAR	IAM
Data / restraints / parameters		4310 / 0 / 275	4310 / 0 / 487	3745 / 52 / 308 2280 / 0 / 188
Goodness-of-fit on F <sup>2</sup>		1.021	1.1751	1.114 1.091
Final R indices [I > 2σ(I)]		0.0454, 0.1262	0.294, 0.0709	0.0543, 0.1537 0.0659, 0.2012
R indices (all data)		0.0527, 0.1314	0.0367, 0.0736	0.0626, 0.1631 0.0731, 0.2093
Largest diff. peak and hole (e. Å <sup>3</sup> )		0.168 and -0.187	0.185 and -0.112	0.544 and -0.317 0.724 and -0.510
CCDC deposit number		2120494	-	- 2121293

## 2. DFT calculations

Optimized Cartesian coordinates of four stable isomers and conformers of DCM-azide at PBE0/6-311G++(d,p) level with IEFPCM model of THF solvent.

**Table S2. *s-trans-(E)*** (most stable form)

C	-4.947723	0.057511	0.15126	N	7.712552	1.773028	0.104317
C	-4.11564	-1.004332	0.23043	N	8.149488	2.415586	1.045255
O	-2.780855	-0.850768	0.084059	N	8.60965	3.079201	1.837116
C	-2.236153	0.364733	-0.144102	H	-6.011285	-0.093864	0.272526
C	-3.029965	1.475348	-0.234036	H	-2.557655	2.432335	-0.41783
C	-4.433456	1.371799	-0.089661	H	-0.383969	1.362671	-0.454061
C	-5.280329	2.485738	-0.175496	H	-6.232062	-3.651739	0.81559
C	-4.488504	-2.443792	0.479503	H	-6.379982	-2.027256	1.490703
C	-0.809914	0.380945	-0.276519	H	-6.53791	-2.286138	-0.260684
C	-5.999886	-2.598426	0.638937	H	-4.26476	-4.338109	-0.535927
C	-4.011208	-3.289087	-0.712768	H	-2.929625	-3.21681	-0.847058
C	-3.787388	-2.916072	1.763885	H	-4.497994	-2.972109	-1.63962
C	-0.030887	-0.723436	-0.192355	H	-2.701195	-2.838218	1.678273
C	1.403604	-0.792565	-0.310723	H	-4.11048	-2.327665	2.627552
C	2.042084	-2.038985	-0.210091	H	-4.041842	-3.963191	1.950195
C	3.411537	-2.175489	-0.31349	H	-0.527522	-1.675387	-0.017107
C	4.236998	-1.050042	-0.531594	H	1.43935	-2.928066	-0.045805
C	3.597666	0.211438	-0.621934	H	3.845423	-3.163203	-0.228688
C	2.230094	0.326859	-0.518165	H	4.178643	1.113367	-0.767008
N	5.591283	-1.186774	-0.652311	H	1.79468	1.318003	-0.593686
C	6.457616	-0.048746	-0.863579	H	7.358883	-0.390475	-1.377785
C	6.209451	-2.484286	-0.464335	H	5.981512	0.675042	-1.529616
C	6.850696	0.631349	0.442609	H	5.99974	-2.89638	0.529258
C	-4.766116	3.777629	-0.413813	H	5.868421	-3.20359	-1.217325
N	-4.328447	4.83324	-0.610108	H	7.288904	-2.37857	-0.564977
C	-6.677263	2.358701	-0.026792	H	5.957413	0.97393	0.977576
N	-7.824327	2.242106	0.097404	H	7.386884	-0.073905	1.088286

**Table S3. *s-cis-(E)*** ( $\Delta E = 0.0027$  eV compared to *s-trans-(E)*)

c	-4.958722	0.429697	0.096962	N	7.670186	1.669825	0.154393
C	-4.119842	1.466543	-0.119852	N	8.112276	2.292464	1.106219
O	-2.787001	1.268631	-0.208161	N	8.573628	2.941758	1.909182
C	-2.243946	0.033677	-0.084462	H	-6.022065	0.613173	0.16398
C	-3.048166	-1.050456	0.137682	H	-2.597658	-2.02944	0.236567
C	-4.449701	-0.900517	0.238463	H	-0.404873	1.064337	-0.374267
C	-5.304676	-1.990403	0.466064	H	-6.218557	4.184335	-0.312169
C	-4.482735	2.920167	-0.290123	H	-6.532549	2.572711	-0.960872
C	-0.814139	0.071661	-0.215741	H	-6.377288	2.8165	0.792897
C	-5.993123	3.122517	-0.184363	H	-4.025954	4.792198	0.688107
C	-3.778989	3.733679	0.808233	H	-2.693456	3.627483	0.750434
C	-3.999537	3.388022	-1.672608	H	-4.107008	3.417675	1.802795
C	-0.008123	-1.014085	-0.158015	H	-2.918107	3.275572	-1.777019
C	1.426506	-1.043115	-0.282163	H	-4.486932	2.821857	-2.471674
C	2.095431	-2.276284	-0.218592	H	-4.248019	4.444985	-1.803325
C	3.466845	-2.376172	-0.332015	H	-0.465277	-1.989988	-0.004759
C	4.263479	-1.225195	-0.523119	H	1.515345	-3.184015	-0.076818
C	3.593209	0.022813	-0.575237	H	3.92487	-3.354974	-0.276844
C	2.224199	0.101981	-0.462038	H	4.151487	0.942295	-0.697617
N	5.619314	-1.325302	-0.654026	H	1.764426	1.083863	-0.507664
C	6.456056	-0.161799	-0.845236	H	7.360689	-0.469487	-1.374626
C	6.270185	-2.612556	-0.50861	H	5.956868	0.565684	-1.489974
C	6.844029	0.496702	0.473442	H	6.075712	-3.059159	0.47292
C	-4.796734	-3.298417	0.605786	H	5.942654	-3.316699	-1.281608
N	-4.361972	-4.3677	0.718446	H	7.346134	-2.477059	-0.610875
C	-6.700849	-1.819887	0.564313	H	5.947393	0.801623	1.025366
N	-7.847953	-1.66748	0.643396	H	7.405868	-0.208903	1.09644



**Table S4. *s-trans*-(Z) ( $\Delta E = 0.0127$  eV compared to *s-trans*-(E))**

C	-3.588794	-0.97489	0.446582	N	5.754888	-2.197641	-1.05191
C	-2.314873	-0.68066	0.791639	N	6.310045	-2.483008	-2.100424
O	-1.70949	0.437834	0.328009	N	6.82279	-2.860054	-3.035407
C	-2.381228	1.3223	-0.441909	H	-4.045865	-1.874224	0.834966
C	-3.668035	1.067823	-0.828789	H	-4.173628	1.80135	-1.444354
C	-4.331408	-0.112796	-0.417761	H	-2.437267	3.296929	-1.142213
C	-5.641454	-0.413466	-0.812671	H	-1.541149	-3.113853	3.094302
C	-1.4115	-1.509349	1.673077	H	-2.992198	-2.103212	3.059814
C	-1.732889	2.571272	-0.746847	H	-2.687958	-3.286052	1.768511
C	-2.217544	-2.560488	2.437808	H	0.285329	-2.822159	1.406608
C	-0.380512	-2.220855	0.780641	H	0.23006	-1.504468	0.22895
C	-0.691869	-0.594077	2.674548	H	-0.872906	-2.886528	0.066261
C	-0.47076	3.024979	-0.546323	H	-0.06676	0.143836	2.168065
C	0.770692	2.3791	-0.175898	H	-1.408527	-0.066209	3.310807
C	1.771767	3.146119	0.4427	H	-0.051211	-1.203091	3.318174
C	2.995142	2.613685	0.795331	H	-0.363725	4.095871	-0.715925
C	3.308365	1.265949	0.509785	H	1.575051	4.191262	0.665378
C	2.328201	0.510812	-0.175576	H	3.718605	3.250983	1.286966
C	1.099977	1.052421	-0.492298	H	2.534246	-0.506845	-0.482734
N	4.515106	0.733771	0.87409	H	0.391247	0.443542	-1.041253
C	4.870774	-0.630762	0.55858	H	5.60094	-0.977362	1.29377
C	5.527038	1.576542	1.478924	H	4.000252	-1.283812	0.660051
C	5.461159	-0.77284	-0.83971	H	5.827113	2.398275	0.818071
C	-6.366898	0.451105	-1.659506	H	5.177494	2.003508	2.425391
N	-6.951026	1.170893	-2.355767	H	6.408859	0.972429	1.689223
C	-6.285033	-1.591964	-0.379804	H	4.749052	-0.416019	-1.592808
N	-6.803243	-2.563959	-0.017737	H	6.377034	-0.176601	-0.925155

**Table S5. *s-cis*-(Z) ( $\Delta E = 0.0121$  eV compared to *s-trans*-(E))**

C	3.336382	1.159432	0.130299	N	-4.960518	2.246765	-1.162243
C	4.039371	0.043045	-0.167512	N	-4.828768	3.355124	-0.668926
O	3.465787	-1.175629	-0.087464	N	-4.743106	4.427185	-0.318794
C	2.174774	-1.326898	0.298781	H	3.817559	2.124553	0.053271
C	1.428528	-0.23651	0.634412	H	0.412497	-0.387026	0.973695
C	1.973366	1.068423	0.551429	H	2.682975	-3.372839	0.498372
C	1.220747	2.208109	0.868553	H	7.145724	1.246559	-1.022853
C	5.477985	-0.042044	-0.611455	H	5.592594	1.981913	-1.426396
C	1.818074	-2.724594	0.387427	H	6.108743	1.855403	0.269768
C	6.106772	1.347411	-0.698839	H	7.298838	-0.971394	0.089342
C	6.255174	-0.892947	0.406385	H	5.843912	-1.902137	0.479946
C	5.526443	-0.713621	-1.993579	H	6.234213	-0.43512	1.399626
C	0.599282	-3.313336	0.419375	H	5.103938	-1.720366	-1.963592
C	-0.733051	-2.791336	0.181643	H	4.976332	-0.127131	-2.735238
C	-1.826765	-3.40143	0.814449	H	6.566805	-0.788473	-2.322063
C	-3.117643	-2.934638	0.662093	H	0.620947	-4.374075	0.666139
C	-3.396803	-1.834584	-0.17843	H	-1.65368	-4.253274	1.466423
C	-2.303985	-1.262005	-0.871912	H	-3.916392	-3.428659	1.199762
C	-1.021076	-1.729549	-0.690948	H	-2.456724	-0.439986	-1.559586
N	-4.674263	-1.366992	-0.32585	H	-0.22052	-1.265796	-1.25684
C	-4.954787	-0.165223	-1.08022	H	-4.373885	-0.150402	-2.005825
C	-5.745698	-1.933388	0.468771	H	-6.004763	-0.184992	-1.38029
C	-4.680788	1.103585	-0.280197	H	-5.572481	-1.809681	1.544791
C	-0.132484	2.105696	1.255199	H	-6.677038	-1.429251	0.213924
N	-1.245859	2.004866	1.563325	H	-5.873533	-3.000616	0.259418
C	1.782549	3.500219	0.798539	H	-5.328091	1.138183	0.604008
N	2.256235	4.55683	0.736855	H	-3.638521	1.130291	0.057764

**Table S6.** Absorption and emission transition energies of *s-trans-(E)* form of DCM-azide, calculated by TDDFT with the 6-311G++(d,p) basis set in THF (IEFPCM), using the default Linear Response equilibrium (LR), corrected Linear-Response (cLR) and State-Specific (SS) solvation models, together with experimental data recorded for the *E*-form in THF solution.

	Calc. values						Exp. data	
	PBE0		CAM-B3LYP		$\omega$ B97-XD		(ev)	(nm)
	(eV)	(nm)	(eV)	(nm)	(eV)	(nm)		
Abs LR	2.68	463	3.06	405	3.15	394		
Abs cLR	2.71	457	3.11	402	3.31	386	2.70	459
Abs SS	2.42	512	2.85	436	2.98	416		
Em LR	2.38	521	2.44	509	2.45	507		
Em cLR	2.60	478	2.71	457	2.74	452	2.15	576
Em SS	2.42	528	2.56	485	2.56	482		
Stokes shift LR	2404 cm <sup>-1</sup>		5045 cm <sup>-1</sup>		5657 cm <sup>-1</sup>			
Stokes shift cLR	947 cm <sup>-1</sup>		3236 cm <sup>-1</sup>		4609 cm <sup>-1</sup>		4425 cm <sup>-1</sup>	
Stokes shift SS	607 cm <sup>-1</sup>		2350 cm <sup>-1</sup>		3336 cm <sup>-1</sup>			

**Figure S6.** Molecular orbitals involved in the main excited states of the 4 conformations *s-trans*-(*E*), *s-cis*-(*E*), *s-trans*-(*Z*), *s-cis*-(*Z*) at the PBE0/6-311G++(d,p) level with IEFPCM model of THF solvent.

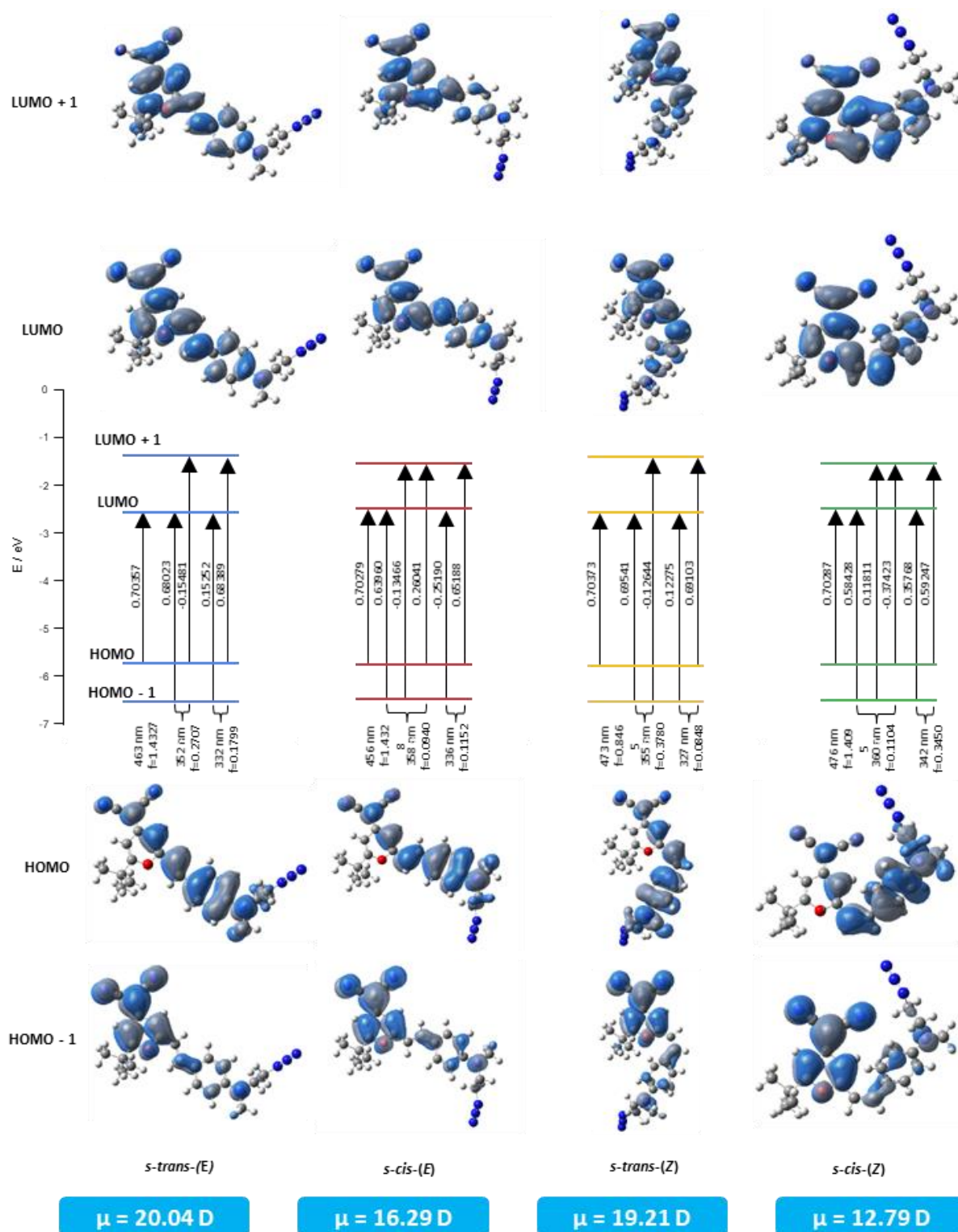


**Figure S7.** Molecular orbitals involved in the main excited states of the 4 conformations *s-trans*-(*E*), *s-cis*-(*E*), *s-trans*-(*Z*), *s-cis*-(*Z*) at the CAM-B3LYP/6-311G++(d,p) level with IEFPCM model of THF solvent.

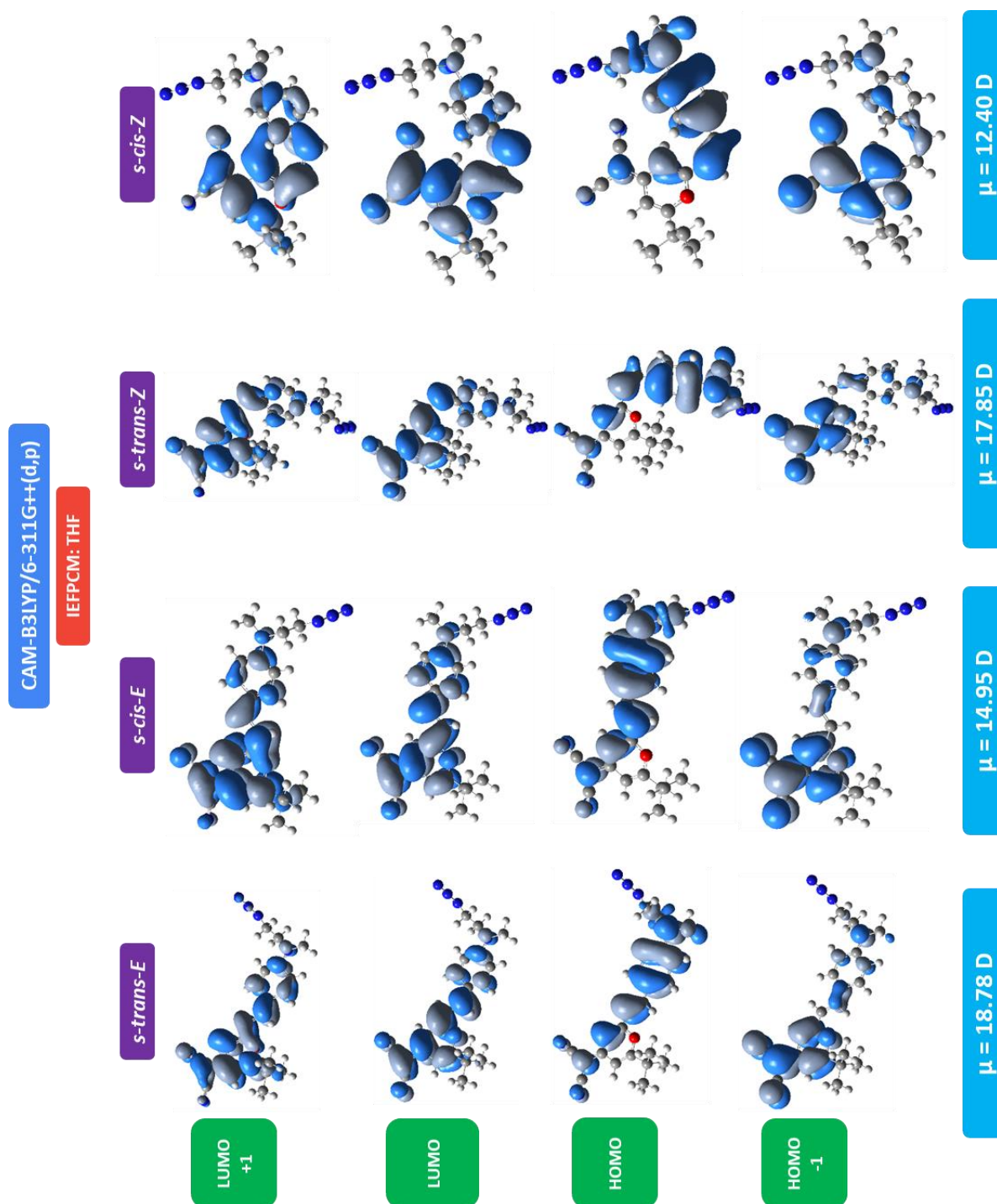


**Figure S8.** Molecular orbitals involved in the main excited states of the 4 conformations *s-trans*-(E), *s-cis*-(E), *s-trans*-(Z), *s-cis*-(Z) at the  $\omega$ B97X-D/6-311G++(d,p) level with IEFPCM model of THF solvent.

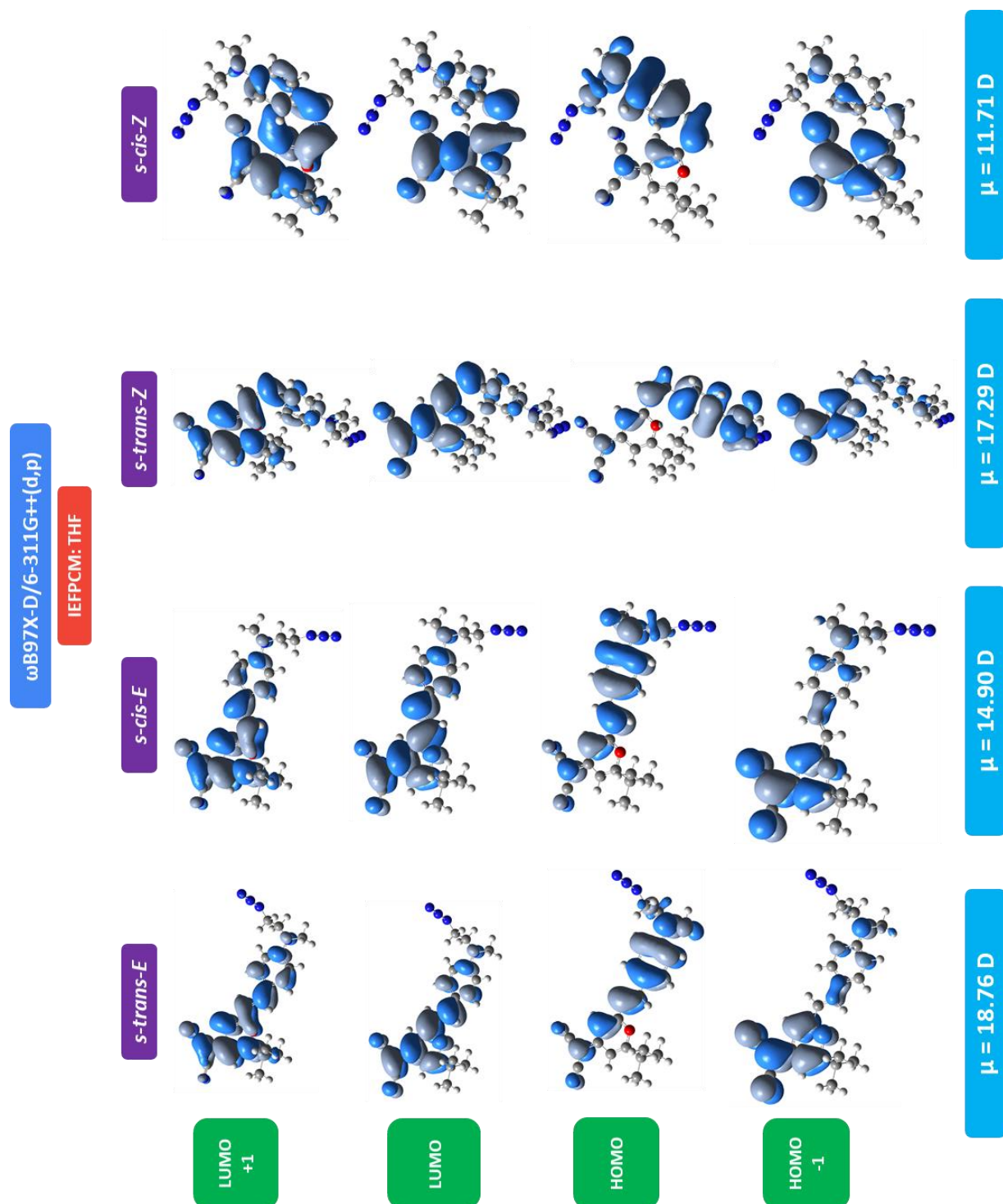




**Figure S9.** Molecular orbitals involved in the main excited states of DCM-azide *E*-forms calculated by DFT at the PBE0/6-311G++(d,p) level with IEFPCM model of DMSO, acetonitrile and THF solvent.

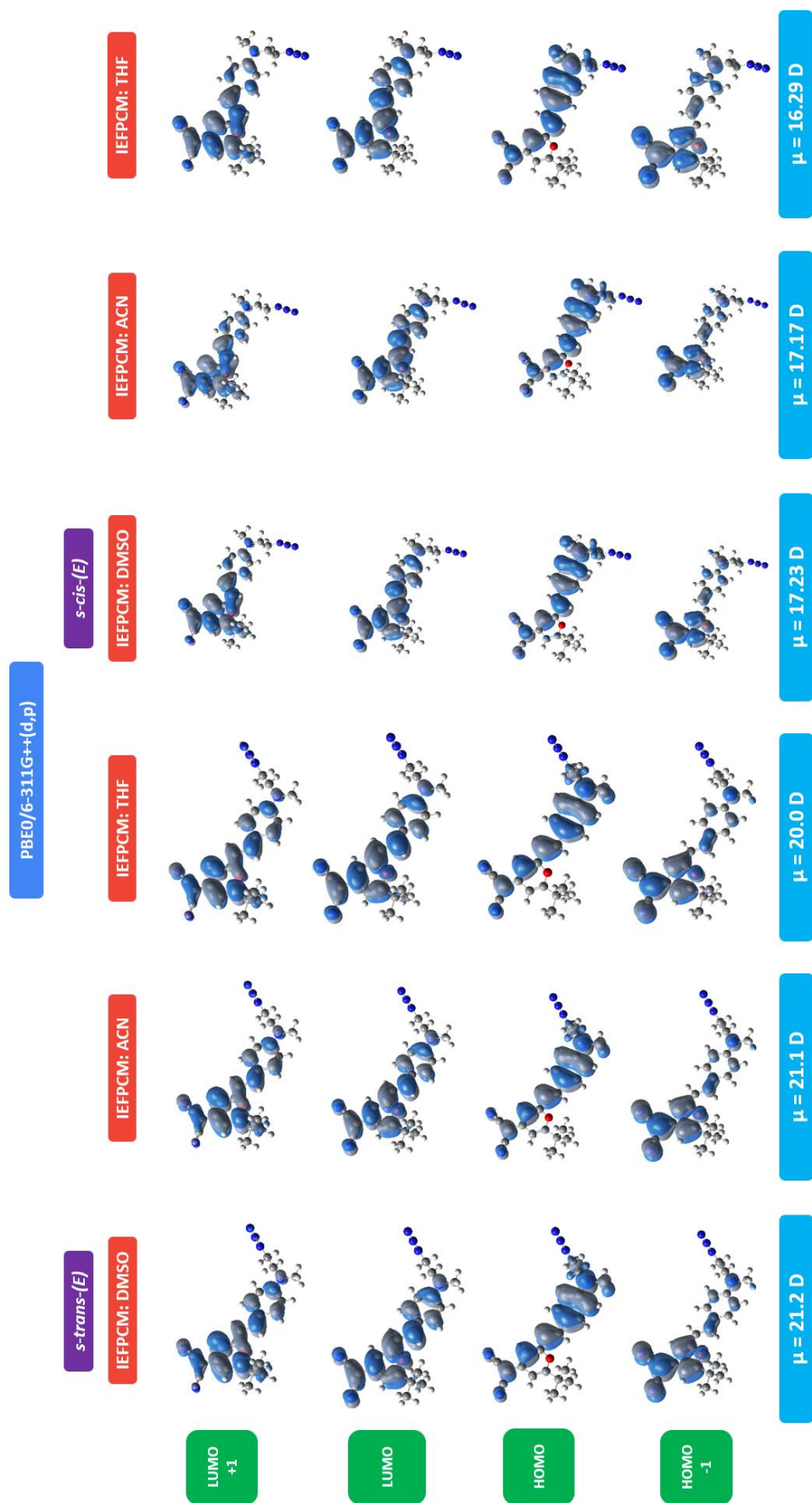


**Figure S10.** Molecular orbitals involved in the main excited states of DCM-azide Z-forms calculated by DFT at the PBE0/6-311G++(d,p) level with IEFPCM model of DMSO, acetonitrile and THF solvent.

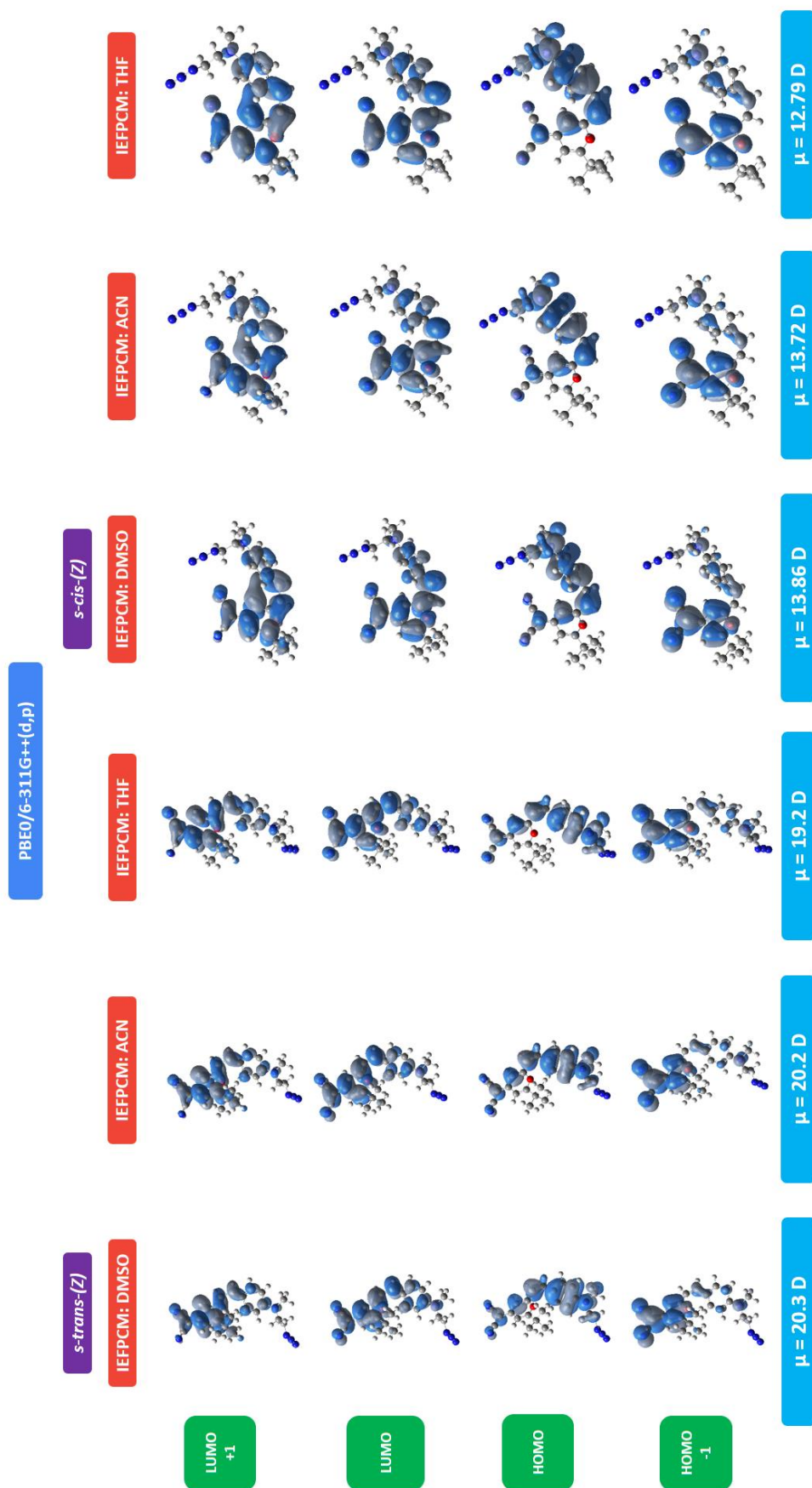


**Figure S11.** The bond lengths  $C_4-C_9$  and  $C_9=C_{13}$  vs. scan coordinates D1 and D2 (dihedral angles, see main text, Figure 1) for DCM-azide calculated at the PBE0/6-311G+(d,p) level with IEFPCM model of THF solvent.

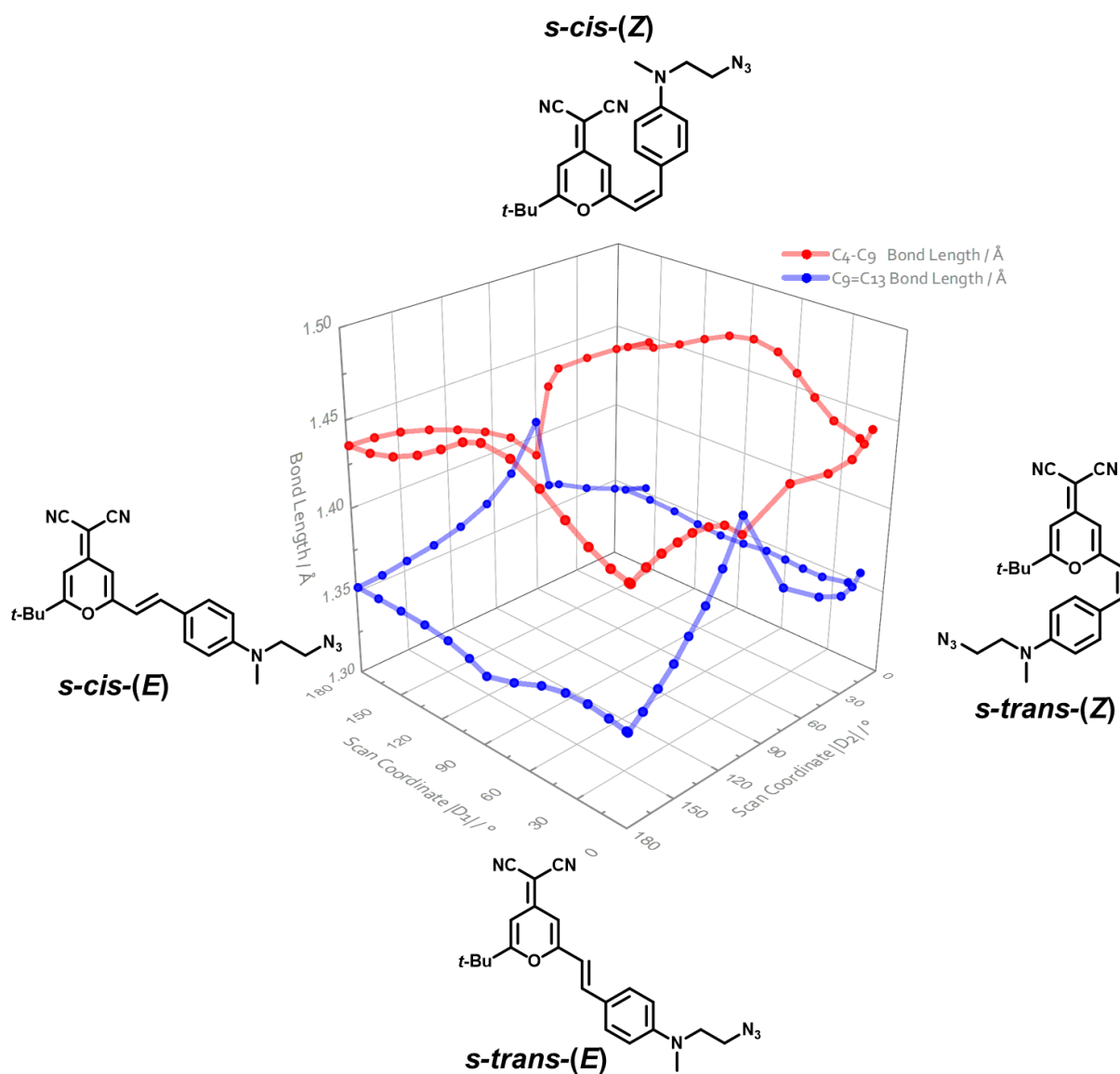
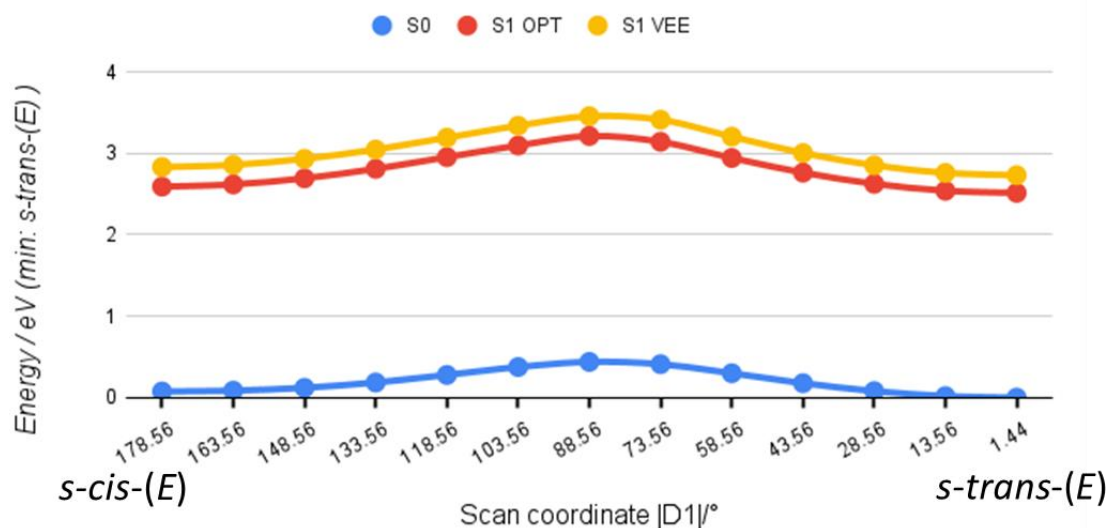




**Figure S12.** C<sub>4</sub>-C<sub>9</sub> single bond dihedral D1 scan between *s-cis* and *s-trans* conformers of the ground states energy ( $S_0$ ), relaxed excited state energy ( $S_1$  opt), and  $S_0 \rightarrow S_1$  vertical excitation energies ( $S_1$  VEE) calculated at the PBE0/def2-SVP level with IEFPCM model of THF solvent.

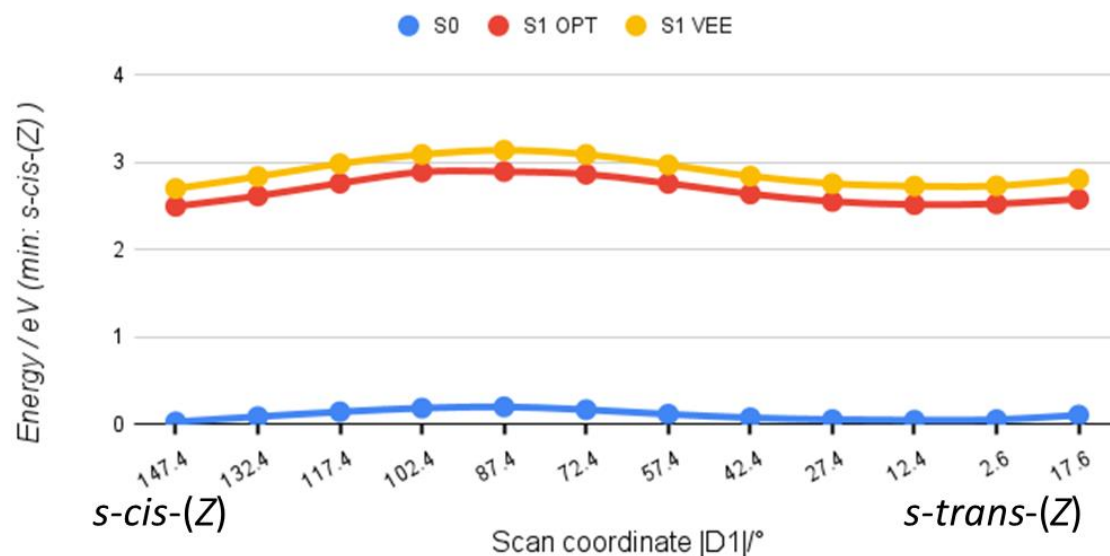
### Dihedral D1 scan optimization from optimized *s-cis*-(E)

PBE0/def2-SVP DFT/TDDFT



### Dihedral D1 scan optimization from optimized *s-cis*-(Z)

PBE0/def2SVP DFT/TDDFT



### 3. Cartesian coordinates of conical intersections

**Table S7.** CI-1 *s-cis* type

Optimized Geometry:  $D_1 = 171.664780^\circ$   $D_2 = -78.582787^\circ$

$D_{C-C} = 1.39874 \text{ \AA}$

$D_{C-C} = 1.46450 \text{ \AA}$

$E(S_0) = -1292.8949705457$  a. u.  $\langle S^2 \rangle = 0.1986$

$E(S_1) = -1292.8934745913$  a. u.  $\langle S^2 \rangle = 0.1421$

$E_{\text{gap}}(S_0/S_1) = 0.0014959544$  a. u. 0.04 eV

C	0.6356678	-0.63559532	1.38684916	N	8.13875484	4.07203007	3.95549035
C	1.5110631	-1.32766545	0.61327189	N	7.5050621	5.09260321	3.71603775
O	2.49175406	-2.07581162	1.16255069	N	7.008986	6.07331991	3.41495252
C	2.69305801	-2.05970097	2.51205945	H	-0.15129089	-0.06150969	0.91506886
C	1.85937834	-1.35196066	3.35392952	H	2.10031819	-1.37013066	4.4126277
C	0.73869061	-0.64821392	2.81805658	H	4.16499615	-3.48904395	2.2010119
C	-0.16259339	-0.01503781	3.66069436	H	0.50027561	-0.58298916	-2.59410954
C	1.55536652	-1.36884046	-0.89383656	H	-0.55646545	-0.88451159	-1.21146715
C	3.72581482	-2.86723757	2.99994588	H	0.52359593	0.53167152	-1.22520137
C	0.43604133	-0.52423352	-1.50342929	H	2.97394371	-0.82899398	-2.43484116
C	2.92008257	-0.81174511	-1.34169018	H	3.74753737	-1.40964985	-0.94972014
C	1.41410768	-2.82848811	-1.35784602	H	3.05344939	0.22418962	-1.01193523
C	4.24257803	-2.89080691	4.37034512	H	2.21000743	-3.45905018	-0.95145822
C	5.13421631	-1.86414552	4.78188896	H	0.44813445	-3.25051212	-1.05981529
C	5.49331284	-1.68174076	6.14194059	H	1.47643638	-2.86496592	-2.45015645
C	6.42494535	-0.74331927	6.55448437	H	3.64500928	-3.4476223	5.0849967
C	7.09105778	0.10008202	5.65066433	H	5.02619886	-2.31342578	6.89483738
C	6.72638702	-0.04094121	4.30386019	H	6.63830519	-0.68119425	7.61716938
C	5.79007339	-0.97608489	3.88899326	H	7.18358755	0.58164227	3.53964806
N	8.10451317	0.99321198	6.07851028	H	5.58619022	-1.02395046	2.81898975
C	8.55032635	2.02411342	5.17979002	H	9.47557545	2.45527339	5.5791173
C	8.15621948	1.30978549	7.48473024	H	8.82013226	1.58381271	4.21317101
C	7.54743624	3.1530962	4.94420242	H	7.20717382	1.70284355	7.88930845
C	-0.04333416	-0.07192465	5.07628202	H	8.42442799	0.42417338	8.07434654
N	0.04491945	-0.13354023	6.23319054	H	8.93602943	2.05845857	7.65229511
C	-1.26465833	0.69754976	3.11557174	H	6.5996809	2.74496675	4.57041311
N	-2.15173411	1.26643169	2.62456322	H	7.33984041	3.68294597	5.88402367

**Table S8.** CI-2 *s-trans* typeOptimized Geometry:  $D_1 = 18.876789^\circ$   $D_2 = -87.396843^\circ$  $D_{C-C} = 1.39486 \text{ \AA}$  $D_{C=C} = 1.45635 \text{ \AA}$  $E(S_0) = -1292.8945194677$  a. u.  $\langle S^2 \rangle = 0.1771$  $E(S_1) = -1292.8934989218$  a. u.  $\langle S^2 \rangle = 0.1360$  $E_{\text{gap}}(S_0/S_1) = 0.0010205459$  a. u. 0.03 eV

C	0.27079824	-1.07720625	1.48285675	N	8.59030533	2.13576984	1.51913226
C	1.41102612	-0.48953256	1.92357552	N	7.98227072	3.00523686	0.90496492
O	2.08921957	-0.98115432	2.98199463	N	7.49088478	3.79010344	0.2418187
C	1.74327576	-2.17015195	3.53505325	H	-0.27489105	-0.63631231	0.65815347
C	0.64282352	-2.87386179	3.062433	H	0.40417621	-3.83337879	3.510952
C	-0.20275667	-2.2979219	2.07621527	H	2.31094575	-3.61578417	4.93746233
C	-1.40452898	-2.90780687	1.71869969	H	1.80862224	2.24382114	-0.13729842
C	2.12672377	0.69320363	1.3197962	H	1.03777027	0.72000873	-0.58087397
C	2.47670507	-2.568748	4.65166903	H	0.32219145	1.74837995	0.6829654
C	1.26498902	1.38190007	0.26206341	H	3.07331586	2.5166924	1.9782306
C	2.50470781	1.69408822	2.42416668	H	3.12324142	1.22500229	3.19401169
C	3.41457915	0.14895043	0.66771805	H	1.61388314	2.11715937	2.9011066
C	3.27135658	-1.66042411	5.46741056	H	4.06445599	-0.32759866	1.40873349
C	4.59626198	-1.25424242	5.3086915	H	3.18510532	-0.57901883	-0.11880878
C	5.13921165	-0.25795725	6.17418337	H	3.9663341	0.97766995	0.21136408
C	6.40694332	0.25811893	6.01025724	H	2.63830709	-1.08449721	6.14547062
C	7.25814056	-0.18993704	4.98526812	H	4.51454306	0.12002107	6.98023653
C	6.76493835	-1.21712744	4.15531731	H	6.73737049	1.03709304	6.69038868
C	5.49314356	-1.73029149	4.3025732	H	7.40565634	-1.6293081	3.37992883
N	8.55726624	0.33176693	4.79600668	H	5.16651964	-2.51854467	3.62693238
C	8.92586994	0.69990146	3.44377327	H	9.98933983	0.96437818	3.43146873
C	9.06684208	1.21447086	5.81912613	H	8.81460381	-0.15798298	2.77343917
C	8.110075	1.86390889	2.88298178	H	8.53916359	2.18212914	5.89703465
C	-1.82292283	-4.11933708	2.32747531	H	9.0029583	0.72123504	6.79418802
N	-2.13437867	-5.10978937	2.85320354	H	10.12159634	1.42292976	5.61528158
C	-2.25490522	-2.30861688	0.75415939	H	7.04563189	1.59372842	2.87457037
N	-2.927001	-1.78035545	-0.03549787	H	8.2278738	2.75683379	3.51234365

## 2.3 APPENDIX: THEORETICAL TECHNIQUES

### 2.3.1 Choice of the functionals and basis sets

The theoretical studies on the **DCM-azide** started from the DFT and TDDFT calculations. From the XRD analysis, we assume that the *s-trans-(E)* isomer corresponds to its most stable isomer. Moreover, the steady-state and time-resolved fluorescence results demonstrated that the *s-trans-(E)* isomer can be considered to represent the main contributing component to the fluorescence. Therefore, the absorption and emission energy calculations were focused on this particular isomer. Computations with polarizable continuum model (PCM) for THF, and three DFT functionals (PBE0, CAM-B3LYP and  $\omega$ B97X-D), were adopted to explore the **DCM-azide** properties. 6-311G+(d,p) Pople basis set was used for the calculations in this part.

The reasons to select these three functionals are the experience on the previous studies on similar DCM analogs and the application of long-range-corrected functionals to model the charge transfer D-A character of chemical structures.<sup>120</sup>

The PBE0 is a global hybrid generalized gradient approximations (GGA) functional, mixing the 75% Perdew-Burke-Ernzerhof (PBE) exchange energy and 25% Hartree-Fock (HF) exchange energy, along with the full PBE correlation energy:

$$E_{xc}^{PBE0} = 75\% E_x^{PBE} + 25\% E_x^{HF} + E_c^{PBE} \quad x = \text{exchange} \quad c = \text{correlation}$$

Both CAM-B3LYP and  $\omega$ B97X-D are range-separated hybrid functionals and they are generally considered as good functionals for excitation energy calculations. CAM-B3LYP is a Coulomb attenuated method (CAM) version of the B3LYP functional, while  $\omega$ B97X-D is a range-separated version of Becke's 97 (B97) functional with dispersion correction. CAM-B3LYP includes 19% HF exchange at the short range and 65% HF exchange at long range, whereas the HF exchange at short and long ranges for  $\omega$ B97X-D is comprised between 22% and 100%, respectively. Both CAM-B3LYP and  $\omega$ B97X-D have error functions describing the intermediate region with a default range separation parameter  $\omega = 0.33$  and 0.2, respectively.

In the previous work of Casimiro *et al.*, Pople basis set 6-311+G(d,p) has been chosen.<sup>3</sup> Here, the first trial and the theoretical data to use were obtained at 6-311++G(d,p) level. However, given that it is meaningless in most cases to add diffuse functions on the H-atoms, the heavier calculation jobs concerning the  $S_0$  potential energy surface (PES) scans were performed decreasing the basis set down to 6-311+G(d,p). For a higher demanding excited state optimization, due to the limitation of the node wall time, the Karlsruhe def2 basis set was applied. Both Karlsruhe "def2" and Pople basis sets are split valence basis sets, therefore, the def2-SVP level should provide similar precision as 6-31G+(d,p) but at lower cost.

All calculations in this section took the solvent into consideration. As the previous work by Casimiro *et al.* demonstrated,<sup>3</sup> THF represents an ideal solvent for the photoisomerization conversion yield and the fluorescence properties. The default integral equation formalism variant polarizable continuum model (IEFPCM) was used consistently.

### 2.3.2 Calculations of absorption and emission energies, solvent effects

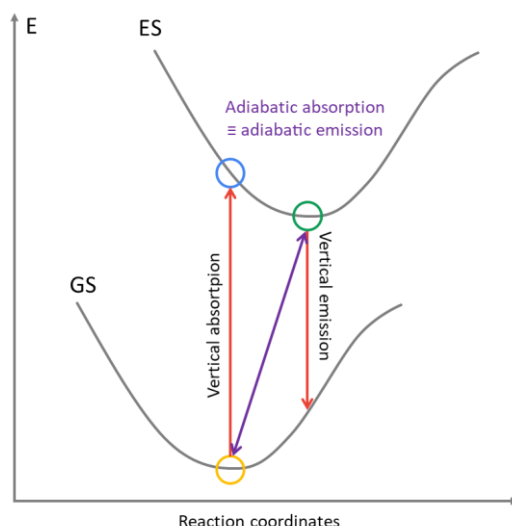


**Figure 41:** Illustration of the electronic transitions between the ground state (GS) and an excited state (ES), involving the vertical absorption and emission transitions, as well as the adiabatic absorption / emission.

The calculations of absorption and emission energies involve the transition between electronic states and vibration states. Taking all the factors into account is not possible in practice, especially regarding the vibrational analysis of excited states. To simplify the calculations, only the electron potential energy surface (PES) is taken into consideration. **Figure 41** shows the basic model of electronic transitions occurring on the different PES, namely the ground state (GS) and an excited state (ES).

Generally, the vertical absorption, the vertical emission and the adiabatic energy difference are the most interesting values for the calculations of the excitation energies. The vertical absorption means the electron absorbs the photon and gets excited from the GS to the ES, while the geometrical features remain that of the GS. Therefore, the calculations include the geometry optimization of the molecule in the GS and the excitation energy from the GS to the target ES on the basis of the optimized GS geometry. The vertical emission is a reversed process, occurring from the optimized geometry of the ES. The adiabatic absorption considers the starting point as the GS minimum, and the final state as the ES minimum (relaxed). The energy is yielded by the energy difference of these two minima.

However, when we add the solvent together with the solute, the case becomes more complicated. In the polarizable continuum, the solvent and the GS solute polarization are mutually equilibrated. On the other side, the ES also contains the mutual equilibrated polarizations. As shown in the **Figure 42**, under the circumstance of the vertical excitation, the solute charge distribution evolves rapidly, but at the same time the solvent molecule remains immobile. The "nonequilibrium" state is subsequently generated. From the "nonequilibrium" state to the re-equilibrated solute-solvent state, there will be a rearrangement step, higher polar solvents inducing a larger rearrangement process. The "nonequilibrium" solvation can be properly described within the PCM work frame: during the vertical excitation process, the solvent degrees of freedom and charges are kept frozen.

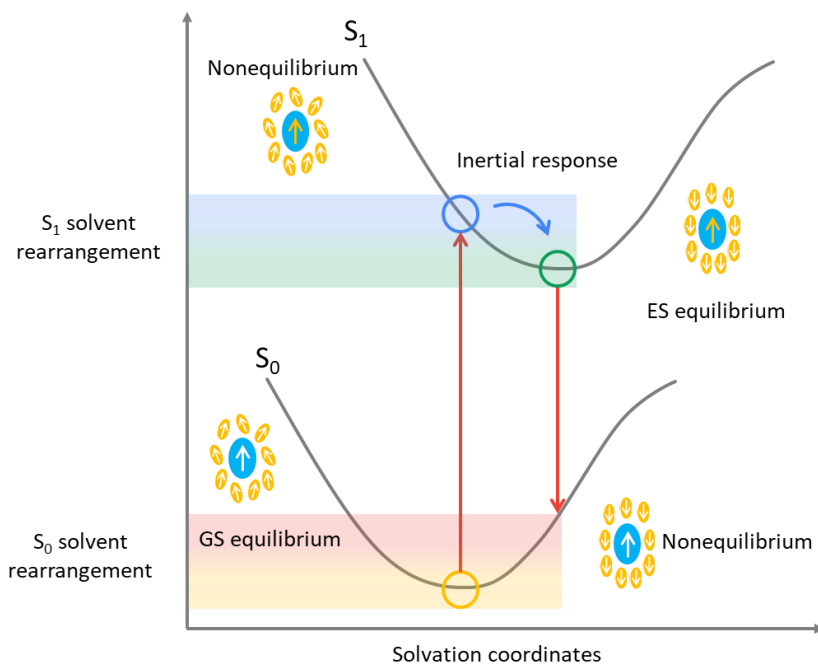


**Figure 42:** Illustration of the different steps involved in the formation and relaxation of excited states in a polar solvent.<sup>121</sup>

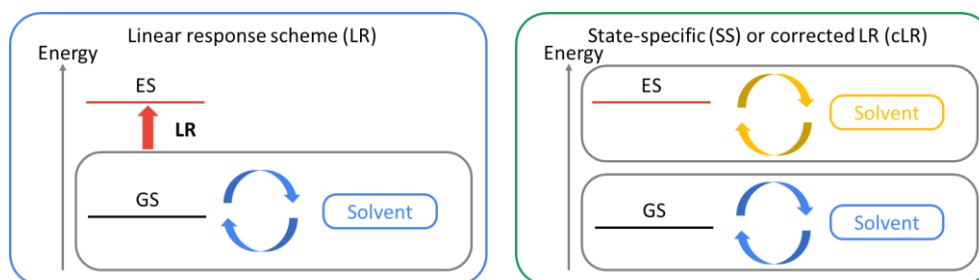


**Figure 43:** Basic solvent treatments, using the LR, SS and cLR solvent models.

In practice, PCM provides an environmental model to calculate solvated absorption and emission spectra by TDDFT. There exist several PCM approaches to describe the solvent polarization induced by the solute electronic transition. The simplest one is called the linear response (LR) model. The transition densities are exclusively used to determine the changes of the PCM charges located on the surface of the cavity. The others, the corrected linear response (cLR) model and the state-specific method (SS, or external iteration in some situations) treat the actual density of the excited states to obtain the surface charges in a perturbative way.

As shown in the **Figure 43**, in a SS or cLR method, the calculated energies should fulfill the following equations:

$$E^{\text{Vert-abs}} = E^{\text{ES}}(R^{\text{GS}}, \text{noneq}) - E^{\text{GS}}(R^{\text{GS}}, \text{eq})$$

$$E^{\text{Vert-fl}} = E^{\text{ES}}(R^{\text{ES}}, \text{eq}) - E^{\text{GS}}(R^{\text{GS}}, \text{noneq})$$

$$E^{\text{adiabatic}} = E^{\text{ES}}(R^{\text{ES}}, \text{eq}) - E^{\text{GS}}(R^{\text{GS}}, \text{eq})$$

where,  $R$  represents the optimized geometry of the corresponding state;  $E$  represents the energy; “Vert-abs” refers to vertical (absorption) transition energy; “Vert-fl” refers to vertical (fluorescence, de-excitation) transition energy; “eq” refers to “equilibrium”; “noneq” refers to “non-equilibrium”.

It is worthy to note that, although theoretically the state-specific method should provide the most precise excitation energy, the time cost is non-negligible. In addition, depending on the molecular systems

themselves, the functionals, basis sets and some offset factors, the results are not always of higher quality. From our side, we have carefully examined LR, cLR and the SS solvent models.

As the reference, the experimental spectra of **DCM-azide** in THF show band maxima at 459 nm (absorption) and 576 nm (fluorescence). The calculated results with different procedures are listed in the **Table 1**.

**Table 1:** Absorption and emission transition energies of *s-trans-(E)* form of **DCM-azide**, calculated by TDDFT with the 6-311G++(d,p) basis set in THF (IEFPCM), using the default Linear Response equilibrium (LR), corrected Linear-Response (cLR) and State-Specific (SS) solvation models, together with experimental data recorded for the *E*-form in THF solution.

	Calc. values						Exp. data	
	PBE0		CAM-B3LYP		$\omega$ B97-XD		(eV)	(nm)
	(eV)	(nm)	(eV)	(nm)	(eV)	(nm)		
<b>Abs. LR</b>	2.68	463	3.06	405	3.15	394		
<b>Abs. cLR</b>	2.71	457	3.11	402	3.31	386	2.70	459
<b>Abs. SS</b>	2.42	512	2.85	436	2.98	416		
<b>Em. LR</b>	2.38	521	2.44	509	2.45	507		
<b>Em. cLR</b>	2.60	478	2.71	457	2.74	452	2.15	576
<b>Em. SS</b>	2.42	528	2.56	485	2.56	482		
<b>Stokes shift LR</b>	2404 cm <sup>-1</sup>		5045 cm <sup>-1</sup>		5657 cm <sup>-1</sup>			
<b>Stokes shift cLR</b>	947 cm <sup>-1</sup>		3236 cm <sup>-1</sup>		4609 cm <sup>-1</sup>		4425 cm <sup>-1</sup>	
<b>Stokes shift SS</b>	607 cm <sup>-1</sup>		2350 cm <sup>-1</sup>		3336 cm <sup>-1</sup>			

### 2.3.3 Principles of Spin-Flip TDDFT (SF-TDDFT)

To describe the location of CI points or CI seams, multi-referential methods like complete active space second-order or n-electron valence state perturbation theory (CASPT2 or NEVPT2) for the state-averaged complete active space self-consistent field (SA-CASSCF) are commonly applied. However, when it is desirable to determine the MECI geometries, it is not always possible to use multi-reference approaches. **DCM-azide** contains 54 atoms, it is therefore rather tremendous to treat the active space within limited computational power. Here we consider more efficient calculations with TDDFT methods to locate the MECI between  $S_0$  and  $S_1$  PESs.

The conventional linear-response TDDFT (LR-TDDFT) is a computationally cheap method, providing good excitation energies for most scenarios. LR-TDDFT solves the excitation  $\Omega$  and transition amplitudes  $X$  and  $Y$  by the non-Hermitian matrix equation

$$\begin{bmatrix} A & B \\ B^* & A^* \end{bmatrix} [XY] = \Omega \begin{bmatrix} 1 & 0 \\ 0 & -1 \end{bmatrix} [XY]$$

in which, the coupling matrices  $A$  and  $B$  are

$$\begin{aligned} A_{ia,jb}^{TDDFT} &= (\epsilon_a - \epsilon_i)\delta_{ab}\delta_{ij} + \langle ib|aj \rangle - C_{HF}\langle ib|ja \rangle + \langle ib|f^{xc}|aj \rangle \\ B_{ia,jb}^{TDDFT} &= \langle ij|ab \rangle - C_{HF}\langle ij|ab \rangle + \langle ij|f^{xc}|ab \rangle \end{aligned}$$

The  $i, j$  labels represent occupied orbitals and  $a, b$  represent the virtual ones.  $C_{HF}$  represents the fraction of Hatree-Fock exchanged included in the hybrid exchange-correlation functional implemented, e.g., B3LYP, PBE0, M06-2X, etc.

However, LR-TDDFT have difficulties in describing the CIs. The closed-shell ground state  $S_0$  used as single reference in LR-TDDFT brings a lot of troubles in such cases, such as the underestimation of response states, the too rapid change in the PES in the vicinity, resulting in wrong energy values.

**SF-TDDFT with a collinear kernel.**<sup>122-124</sup> The spin-flip TDDFT (SF-TDDFT) is a simple extension of LR-TDDFT and a remedy to localize the CIs. As shown in **Figure 44**, SF-TDDFT chooses an open-shell triplet state with 2 unpaired  $\alpha$ -electrons  $\alpha\alpha$  ( $M_S = +1$ ) and the target states are generated by single  $\alpha \rightarrow \beta$  spin-flipped excitations. The target states (*e. g.*  $S_0$  ground state and  $S_1$  lowest excited state) are treated on the same footing as the response states. As a result, the SF-TDDFT is able to consider contributions from doubly excited configuration, whereas the LR-TDDFT cannot.

The electronic correlations from that state and the CI pointing excited state are not matching, not alone some DFT instability problems in singlet profiles. In the formulation of SF-TDDFT, the excitation difference is from the  $\alpha \rightarrow \beta$  spin-flipped excitations, which require the equation orbitals  $i, j \dots$  to be  $\alpha$  spin orbitals and  $a, b \dots$  to be  $\beta$  spin orbitals. Then the matrix  $B$  is set to 0

$$A_{ia,jb}^{SF-TDDFT} = (\epsilon_a - \epsilon_i)\delta_{ab}\delta_{ij} - C_{HF}\langle ib|ja \rangle$$

$$B_{ia,jb}^{SF-TDDFT} = 0$$

Here, the collinear exchange-correlation functional is assumed, *i.e.*,  $\langle ij|f^{xc}|ab \rangle = 0$ . The treatment results a Hermitian matrix equation  $AX = \Omega X$ . The framework of collinear SF-TDDFT required matrix  $B = 0$  is also known as the Tamm-Dancoff approximation, which can be called to deploy as modular pair in several quantum chemistry softwares.

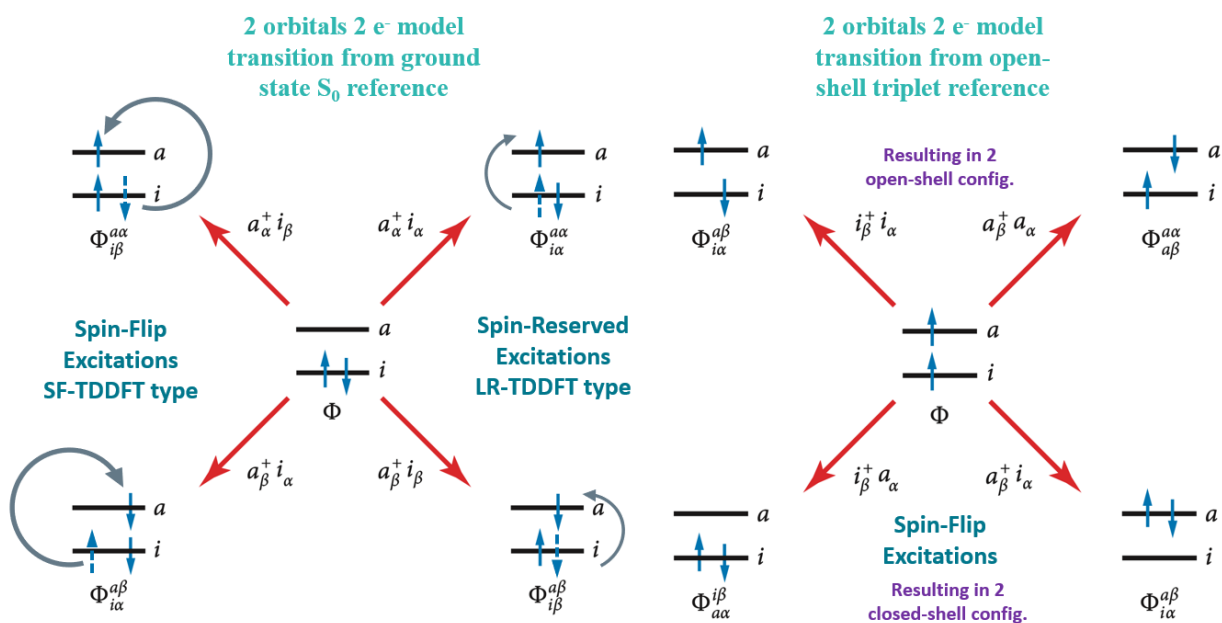


**Figure 44:** The two orbital models of LR-TDDFT (left) and SF-TDDFT (right) excitations, starting from different reference states.<sup>123</sup>

**Penalty-constrained (PC) optimization algorithm.**<sup>125</sup> The PC optimization following the objective function  $f$  between states  $i$  and  $j$  is expressed as

$$f(R, \sigma) = \overline{E_{ij}}(R) + \sigma \left( \frac{[E_i(R) - E_j(R)]^2}{E_i(R) - E_j(R) + \alpha} \right) \quad E_i(R) \geq E_j(R)$$

where the first term  $\overline{E_{ij}}(R)$  refers to the average potential energy of the two states, and the second term is the penalty term resulted as the product of the Lagrange multiplier  $\sigma$ . State  $i$  is taken as the higher



state.  $\alpha$  functions are the smoothing parameter to circumvent the singularities, effectively differentiating the equation and the adjacent CI regions.

The convergence criteria are composed with the change of  $f$ , the parallel and perpendicular components of the gradient of  $f$  from the  $n^{th}$  step to the  $(n + 1)^{th}$  step. The objective function  $f$  is minimized with a fixed Lagrange multiplier  $\sigma$ , and its gradients are minimized simultaneously. The penalty function is performed in an iterative pattern with increasing values of  $\sigma$  until the energy difference between the two states becomes less than the convergence tolerance. In theory, the PC optimization algorithm only treat the gradient difference factor  $\mathbf{g}$  in the *branching space* ( $\mathbf{g-h}$  plane) description of the PESs, it is not related to the interstate coupling vector  $\mathbf{h}$ .

The validation of PC optimization has been proved to be qualitatively acceptable in the SF-TDDFT compared to other algorithms or multi-referential methods, usually performing as the lowest cost among all if the studied system is well fitted with the protocol.

In addition to the data in the paper, we have also calculated the four isomers and conformers of **DCM-azide** at  $S_1$  state, which were optimized at SF-PBE0/6-31G(d) level *in vacuo* to compare with the CIs. The results are shown in the **Table 2**.

**Table 2:** The four isomers and conformers optimized at SF-PBE0/6-31G(d) *in vacuo* compared with two CIs obtained.

	Energy (a.u.)	$\Delta E$ of $S_1$		D1 (°)	D2 (°)	$\langle \hat{S}^2 \rangle$
		(eV)	(kcal mol <sup>-1</sup> )			
<i>s-trans-(E)</i>	-1292.9122938979 ( $S_1$ )	–	–	0.12	179.41	0.3946
<i>s-cis-(E)</i>	-1292.9122938979 ( $S_1$ )	0.058	1.329	-179.32	179.74	0.2317
<i>s-trans-(Z)</i>	-1292.9016183698 ( $S_1$ )	0.290	6.699	4.66	18.63	0.4996
<i>s-cis-(Z)</i>	-1292.9090506581 ( $S_1$ )	0.088	2.035	-171.35	23.92	0.1443
CI-1 ( <i>s-cis</i> )	-1292.8934745913 ( $S_1$ )	0.511	11.794	171.66	-78.58	0.1421
CI-2 ( <i>s-trans</i> )	-1292.8934989218 ( $S_1$ )	0.512	11.809	18.88	-87.40	0.1360

## 2.4 CONCLUSIONS AND PERSPECTIVES

This Chapter is a photophysical and theoretical investigation of the photoswitchable fluorophore candidate, **DCM-azide**, expected to play the role of the “fast photoswitchable unit” in the full system for fluorescence hysteresis applications. Unlike the other photochromic diarylethene candidate, DAE, for which the photoisomerization mechanisms are well studied by means of multi-referential methods, we tried here to describe and rationalize the first levels of the photoisomerization mechanism of the DCM series, which remains relatively unexplored.

As we demonstrated in the paper, there are two CIs existing at **DCM-azide** PES, located on each side of isomers. According to the previous studies of  $E \leftrightarrow Z$  isomerization, there could be a CI seam between the two MECI founded by SF-TDDFT method.<sup>126</sup> The two through-CI pathways are thought to be competitive to each other. If we would like to investigate more on the rate, the non-adiabatic dynamics simulation using *ab initio* multiple spawning (AIMS) is good way to answer the population-based rates.<sup>127</sup> Beyond the through-CI relaxation pathways, the solvent effect is another important issue to discuss. In the context, we did not find the solution to the problem with current the PCM model and its variants. Handling the THF as the explicit solvent and using quantum mechanical/molecular mechanical (QM/MM) setups may resolve the problem.<sup>128, 129</sup> The theoretical investigations on DCM molecules can be enriched in the future as the computation cost will be lower for the molecules of this dimension.

Their fluorescence properties and interchromophoric interactions will be investigated into the next Chapters, especially in multichromophoric systems where resonance energy transfer (RET) can occur. The better understanding related to the DCM photoisomerization was necessary to unravel the complex processes encountered in larger structures and more sophisticated environments.

# Chapter III



## 3 CHAPTER III – SYNTHESIS AND INVESTIGATION OF MULTI-DCM SYSTEMS

---

### 3.1 INTRODUCTION

In the previous studies, the series of 1,3,7-DAE fluorescent photoswitchable multichromophores, and the mixed DAE-DCMs were synthesized and characterized by Dr S. Maisonneuve *et al.* at PPSM. Considering the complexity of RET in the multi-DAE systems, we decided to prepare a series of multi-DCM derivatives (1,2,3-DCM), investigate their photophysical, photochemical and structural properties, in the perspective of further multichromophoric functionalizations (**Chapter IV**). Indeed, in a fluorescence hysteresis system, a bright and fast photoisomerizable part like DCM is welcomed. The general objective of the **Chapter III** consists in the synthesis, photophysical and theoretical studies of multi-DCMs compounds, in order to define the proper design for the multichromophoric DAE-DCM systems to be synthesized and investigated.

This chapter introduces the synthetic strategies to obtain the desired dendritic linkers and cyclodextrin scaffold to hold multichromophores. In order to synthesize the desired number of DCMs, the literature will be reviewed. The molecular dynamics protocols and analysis methodologies are discussed for modeling the multi-DCM.

One manuscript to be submitted to *Chem. Eur. J.* covering **DCM-azide**, **2DCM**, **3DCM** series investigations describes the fluorophore-fluorophore interactions among the synthesized multi-DCMs with absorption, fluorescence, and anisotropy spectroscopies. The molecular dynamics simulation accompanied statistical analyses on **2DCM** reveal the intramolecular FRET efficiencies, which are in accordance with the experimental observations.

A complete set of data regarding the **4DCM** and **14DCM** of the higher level multi-DCM synthesis in the appendix are described in detail.

## 3.2 STRATEGIES TO DESIGN MULTI-DCM COMPOUNDS

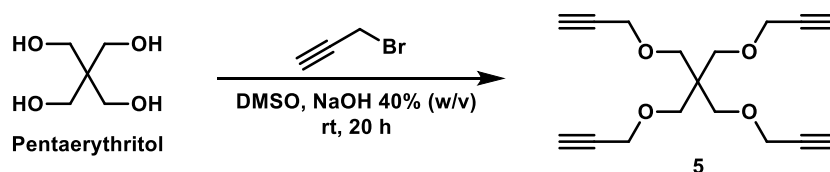
Regarding the scalability to accommodate enough chromophoric units, we have focused on the pentaerythritol dendritic linker and the  $\beta$ -cyclodextrin platform. The synthesized multivalent platforms should allow the covalent attachment of DCM units *via* CuAAC reaction. This is to say that the dendritic linkers or the  $\beta$ -cyclodextrin is required to have either an alkyne terminal or an azido function. Based on these, the CuAAC reaction is able to deliver the final compound with selectively pure 1,4-triazole species. The functionalization and the multichromophoric synthesis will obey these prerequisites.

### 3.2.1 Pentaerythritol scaffold

Pentaerythritol is a tetrahydric alcohol as a white crystalline odorless solid synthesized in the end of the 19<sup>th</sup> century.<sup>130</sup> In the industrialization era, it is a component involved in many compounds and intermediates appearing in the medicinal or even military manufacturing.<sup>131, 132</sup> As the multifunctional compounds are essential to the organic and medicinal chemistry, the pentaerythritol is a versatile building block for the polyfunctionalized compounds because of the presence of the neopentane core and one hydroxy group on each terminal function. It is a common precursor in manufacturing esters of  $C(CH_2OX)_4$ . For example, pentaerythritol tetranitrate (PETN) was produced at large amount for the use of explosives during the second world war. Later, it was used for vasodilation pharmaceutical applications, like nitroglycerin.<sup>133</sup> In the modern industrial field, the most famous representative is pentaerythritol tetraacrylate (PETA), which is used in epoxy resin chemistry and photopolymer coatings.<sup>134, 135</sup>

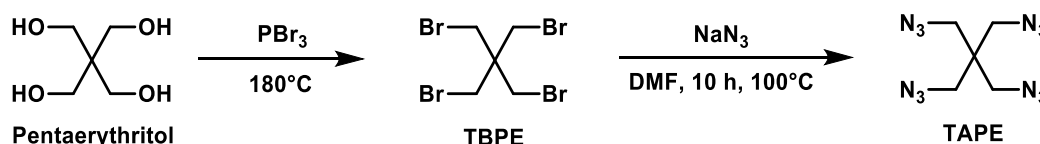
In practical laboratory synthesis, the pentaerythritol allows the attachment of four identical or different groups to construct highly branched molecular structures. It features the great expandability for combinatorial chemical libraries for oligonucleotides and peptides, providing additional functionalities by introducing additional groups.

**Tetra-branching motifs.** The examples talked above are all based in the tetravalent pentaerythritol derivatives. In practice of realizing CuAAC reaction, it is convenient to synthesize tetra-alkynes with four propargyl groups, *i.e.*, compound **5**<sup>136</sup> in **Scheme 4**.



**Scheme 4:** Synthetic route to obtain tetra-branching linker **5**.<sup>136</sup>

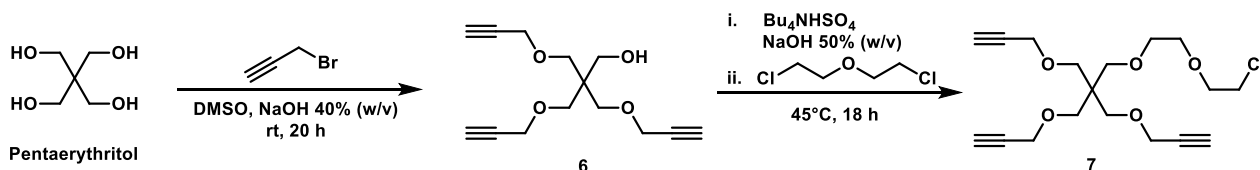
Pentaerythritol tetrabromide is also accessible from the halogenation exchange of pentaerythritol or directly commercially available. This tetra-branching branching bromide can be transformed into tetraazidopentaerythritol (TAPE). However, TAPE is a potentially explosive and sensitive species, which requires a Kevlar covered laboratory. We do not consider it at first for safety reasons.<sup>137</sup>



**Scheme 5:** Synthetic route to obtain TAPE (explosive).<sup>137</sup>

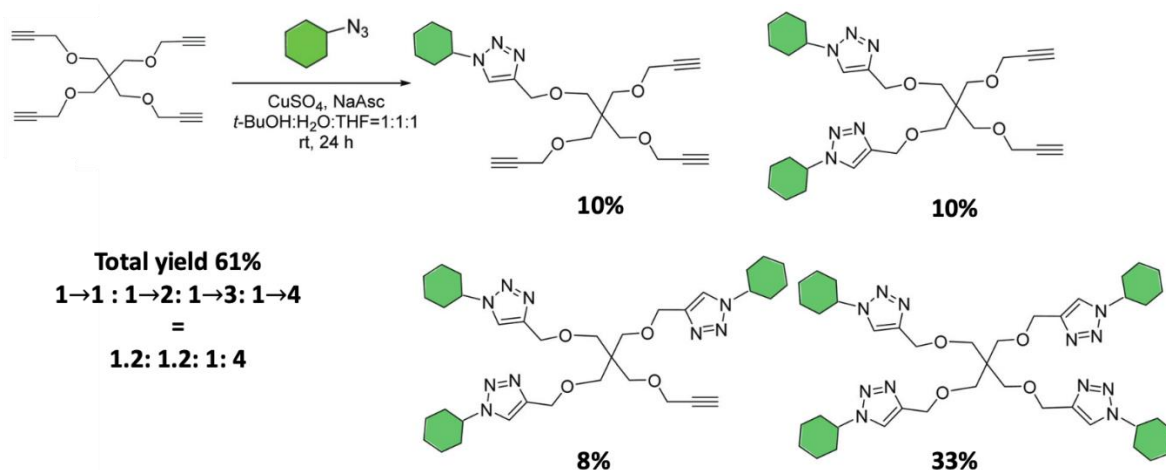
**Tri-branching motifs.** These motives are widely described in the literatures. The tri-functionalized amide, ester, ether derivatives are reported.<sup>138</sup> By protection-deprotection strategies, one can easily preserve one hydroxyl group on the pentaerythritol to be further functionalized according to special demands, *e.g.* as a dendron focal point to join bigger dendritic systems. The strategy we used in the first stage of

pentaerythritol propargylation is a typical tri-functionalized branching scheme shown in **Scheme 6**. We decided to introduce a PEG chain with a chloro-tail on the fourth hydroxyl group.<sup>139</sup> The chloride can be later converted into the azide for the synthesis of bigger derivatives. In this regard, the **3DCM** we have synthesized after retains the capability to form greater dendritic generations.



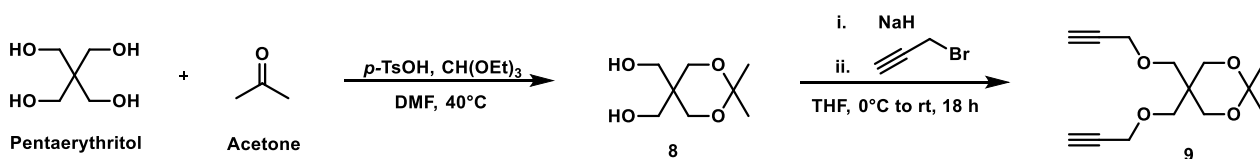
**Scheme 6:** Synthetic route to obtain tri-branching linker **7**.

**Di-branching motifs.** This category is the rare case of the pentaerythritol class. Since pentaerythritol contains four equivalent hydroxyl groups, the selective protection strategy is required to obtain the di-branching motifs. As shown in **Scheme 7**, a one-step synthesis of mono-, bi-, tri- and tetra-branching products was reported through the click reaction.<sup>140</sup> However, it is usually difficult to control the selectivity.



**Scheme 7:** Separately distributed CuAAC compounds from pentaerythritol branching alkyne realized by Chen *et al.*<sup>140</sup>

We decided to employ 1,2-isopropylidene ketal to lock the diols,<sup>141</sup> and the compound can be further propargylated for CuAAC shown in **Scheme 8**. The deprotected di-branching motif introduces building blocks on the same structure.



**Scheme 8:** Synthesis of di-branching pentaerythritol derivative **9**.

### 3.2.2 $\beta$ -Cyclodextrin scaffold

Cyclodextrins (CDs) are probably the most famous family of host molecules in the scientific and industrial fields. They are cyclic oligomers of glucose linked by  $\alpha$ -1,4 glycosidic bond, corresponding to the cyclodextrin containing 6, 7 or 8 units of glucose, denoted as  $\alpha$ ,  $\beta$  and  $\gamma$ -CD, respectively. As shown in **Figure 45**, these three CDs all feature a toroidal truncated-cone topology, where  $\alpha$ -1,4 glucose units fit into chair conformation, orientating the hydroxyl groups to the outer space. The wider diameter side (secondary alcohols) of the toroidal truncated cone have the double of the number of hydroxyl groups than the narrower side (primary alcohols). Because of C-H3 and C-H5 pointing inside of the cavity, the inner nanometric cavity is hydrophobic and the outer region is hydrophilic, enabling the encapsulation of

organic molecules into aqueous solutions. This feature makes it prevalent in the host-guest system construction, drug delivery related to pharmaceutical or biomedical applications.<sup>142</sup>

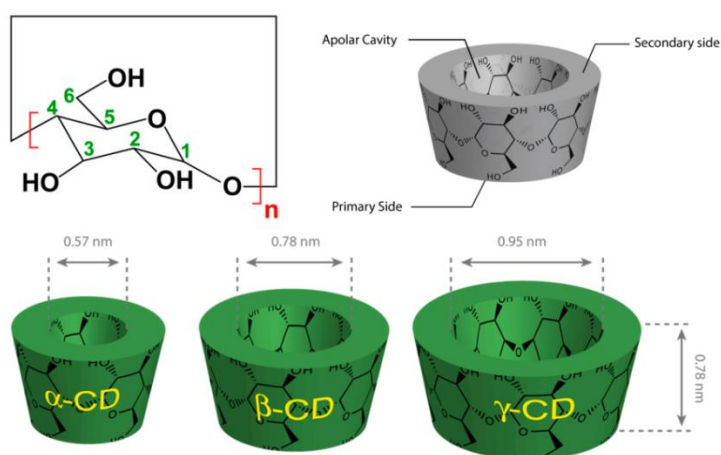


**Figure 45:** Functional structural scheme of  $\alpha$ -CD ( $n = 6$ ),  $\beta$ -CD ( $n = 7$ ) and  $\gamma$ -CD ( $n=8$ ). Bottom: Geometric dimensions of cyclodextrins.<sup>143</sup>

Among the three variants,  $\beta$ -CD is the most widely described in literatures due to its low cost and suitable cavity size for different applications. Here, we also focus on the functionalization of  $\beta$ -CD as the multivalent scaffold for linking several dyes into multichromophoric structures. It should be pointed out that the multivalent CDs also involve a large number of covalently-linked CDs such as dimers or oligomers.<sup>144</sup> This PhD thesis lays the emphasis on the functionalization of single CDs.

According to the reported classification method, the functionalizations can be divided into four face-selective CD-scaffolded glycocluster categories: primary face-anchored *jellyfish-type* glycoclusters, secondary face-anchored *skirt-type* glycoclusters, dual-face substituted *bouquet-type* glycoclusters and hyperbranched *star-type* CD glycoconjugates.<sup>145</sup>

By direct functionalizations of the primary alcohols, secondary alcohols or both of them, the former three types can be easily categorized. The last *star-type* CD glycoconjugates require the preparation of dendronized branches which enables the total structure to sustain the symmetrical star-type arrangement surrounding the cyclooligosaccharide core while increasing the valency as well. The prepared branches often occupy the dendron linkers starting from pentaerythritol scaffolds mentioned in last section.

The classification is based on the intrinsic reactivities of three hydroxyl groups on the 2, 3, 6-position. The OH-6 on the primary face is the most nucleophilic. The OH-2 on the secondary face is the most acidic hydroxyl group, which can form reactive oxyanions. The OH-3 on the secondary face is the most inaccessible one, which is the least reactive position.<sup>142</sup>

**Jellyfish-type glycoclusters.** The primary face-anchored *jellyfish-type* glycoclusters (**Figure 46**) are the most common multivalent CDs described in the literatures. The *jellyfish-type* CDs retain the entrance for the proper guest molecules to the internal cavity, favored to drug delivery designs that require strong peripheral chemical supports. Generally speaking, the *jellyfish-type* CDs are functionalized on the primary alcohol sides, which have 7 hydroxyl groups in the case of  $\beta$ -CD. The selective substitution of primary hydroxyl groups is easily and efficiently accessed by the halogenation. The per-6-substituted or heptakis-6-substituted  $\beta$ -CD derivatives are the most common ones, including the sulfur nucleophile coupling, the amide-coupling and CuAAC.<sup>79, 92, 93, 145-151</sup> The CuAAC is an efficient route to connect the azido  $\beta$ -CD and corresponding alkynes. For the azide preparation, once the halogenated  $\beta$ -CD is obtained, it is easy to prepare the azido  $\beta$ -CD by azidation with the sodium azide.<sup>152</sup> The secondary hydroxyl side is often modified to increase or decrease the solubility in certain solvents, usually with methoxy or acetyl groups.



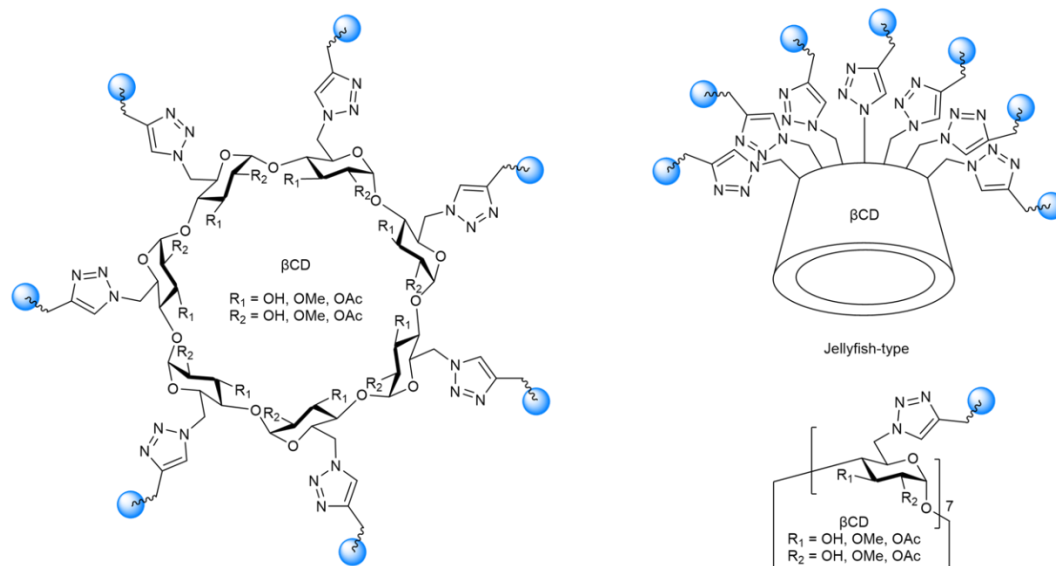


**Figure 46:** General structure of jellyfish-type  $\beta$ -CD with CuAAC functionalization.

To start with per-(6-azido)- $\beta$ -CDs, several CuAAC reactions have been reported successfully by our group and other research groups. The yields of the reaction are in the range of 62% to 92% using different copper sources, solvent pairs, or secondary alcohol substituents.<sup>92, 93, 153</sup> The DCM<sub>7</sub>- $\beta$ -CD reported by Jiao *et al.*<sup>151</sup> is a good example of multi-DCM synthesis in **Figure 47**. The compound further shows its potentials for host-guest assembly in a hierarchy construction. However, in order to further increase the multivalency of the system, different protocols need to be developed beyond the seven slots provided.

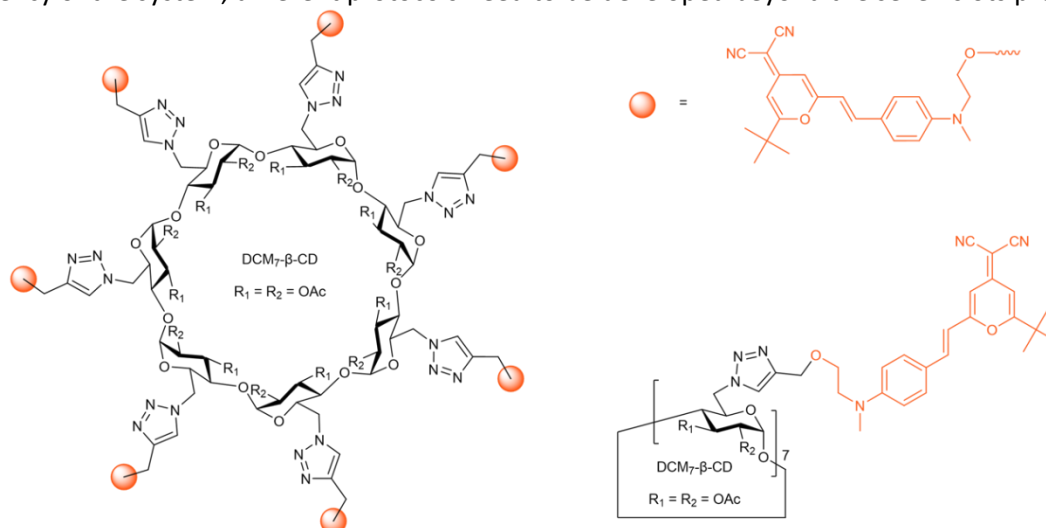
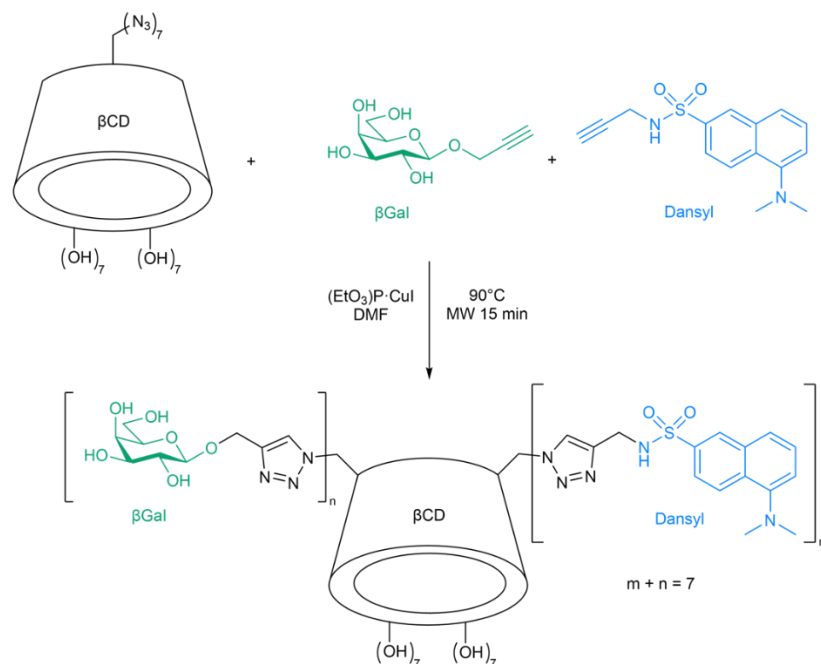


**Figure 47:** Structure of the hepta-DCM appended  $\beta$ -CD reported by Jiao *et al.*<sup>151</sup>

Apart from homogenous glycoclusters, there are examples of heterogeneous glycoclusters. In the case of CuAAC, Santoyo-Gonzalez group reported that per-(6-azido)- $\beta$ -CD reacted with  $\beta$ Gal and dansyl reactants and generated a mixture (**Scheme 9**).<sup>150</sup> However, the (m,n) ratio is not controllable.



**Scheme 9:** Synthesis of fluorescence labeled multivalent  $\beta$ -CD conjugates *via* CuAAC as a case of heterogeneous heptavalent glycoclusters. The resulting products are in the mixture form.<sup>150</sup>

**Skirt-type glycoclusters.** On the other side, the *skirt-type* glycoclusters are functionalized at the face of secondary hydroxyl groups. In principle, the reactivities of OH-2 and OH-3 are different, thus the selective functionalizations are both possible. The functionalizations of hydroxyl groups require prior protection of the primary hydroxyl groups. Usually, due to the weak reactivity of OH-3, the functionalization on the secondary face possesses seven slots on the OH-2 positions. However, Ling *et al.*<sup>154</sup> reported 14-substituted  $\beta$ -CDs (**Figure 48**).

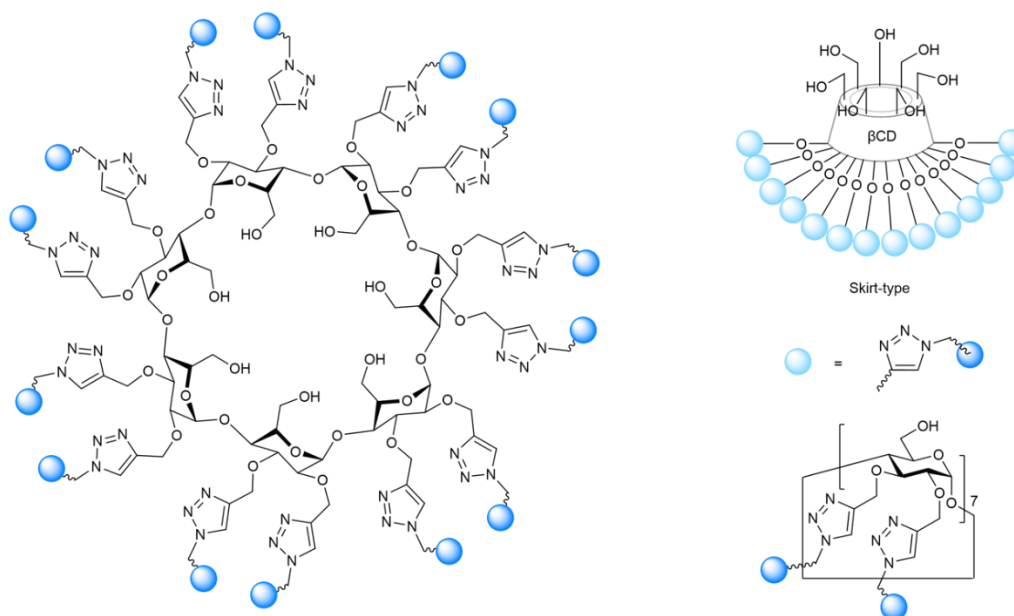
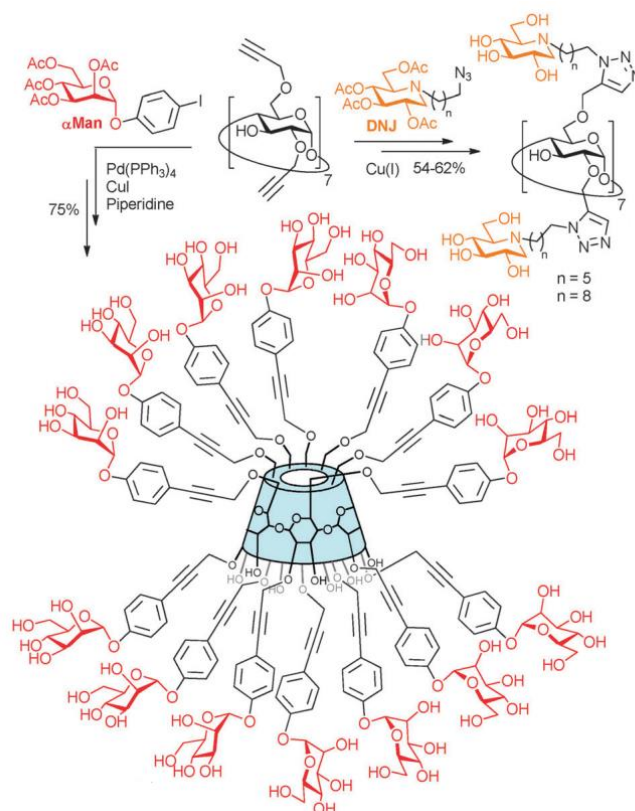


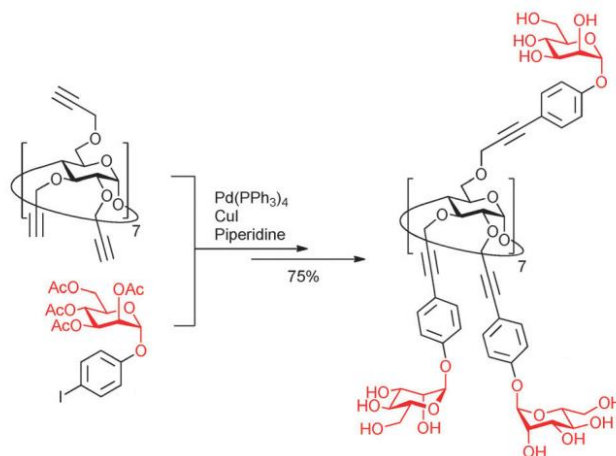
**Figure 48:** The general structure of *skirt-type*  $\beta$ -CD with CuAAC functionalization.

**Bouquet-type glycoclusters.** The bouquet-type glycoclusters are functionalized on both the primary and secondary faces. However, due to the lower reactivity of the OH-3, the 14-valent  $\beta$ -CDs are more commonly reported. In the framework of CuAAC applications, Compain *et al.* reported one bouquet-type  $\beta$ -CD clicked with iminosugars with a yield of 44% (**Scheme 10**).<sup>155</sup> Later, the same group reported the same  $\beta$ -CD clicked with a long chain sugar with a yield of 83% under the same conditions.<sup>156</sup> 21-Valent bouquet-type glycoclusters are accessible in the report of Vargas-Berenguel group (**Scheme 11**).<sup>157</sup>

Although the result is based on the Sonogashira reaction, the scaffold was a 21-propargylated CD, which is capable of occurring the CuAAC reaction. In taking all the OH-positions on the  $\beta$ -CD scaffold into consideration, 21-valent glycoclusters can be seen as the limitation.

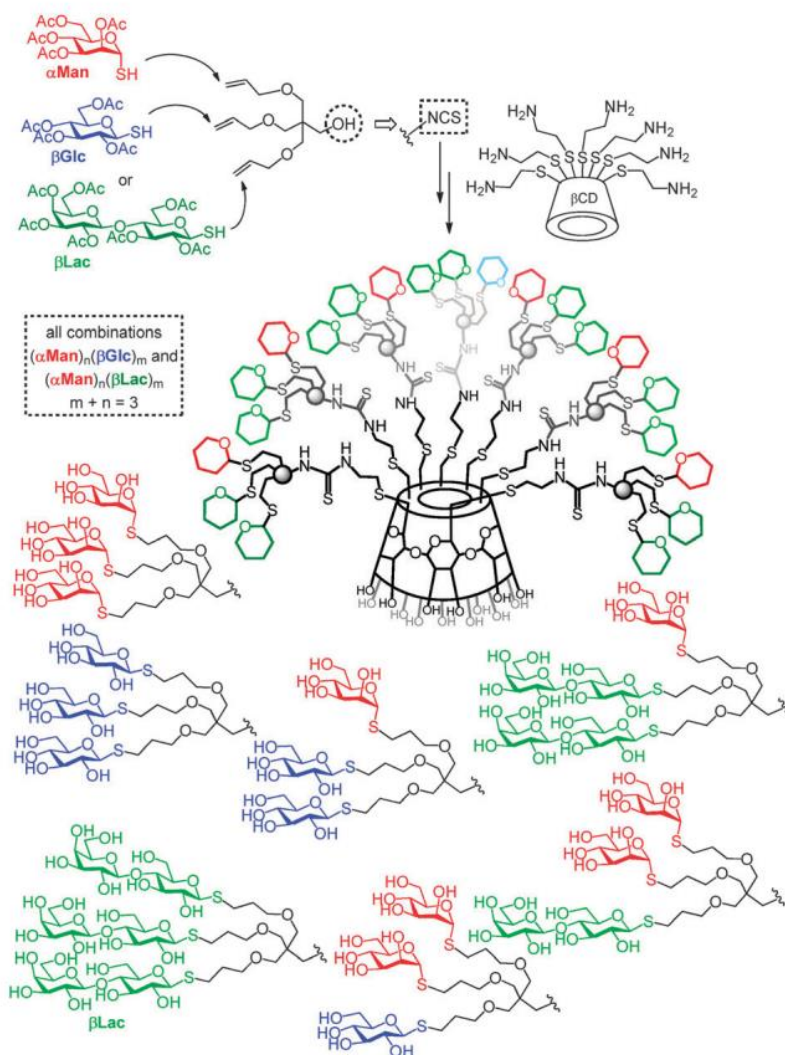


**Scheme 10:** Synthesis of *bouquet-type* 14-valent glycoclusters by Sonogashira<sup>155</sup> and CuAAC ligation chemistries.<sup>155</sup>



**Scheme 11:** Synthesis of the 21-valent *bouquet-type* glycocluster.<sup>156, 157</sup>

**Hyperbranched glycoclusters.** After digging all the potentials of the  $\beta$ -CD itself, the other way to increase the multi-valencies is to modify the branching units. Multiconjugation of CDs with dendronized branches allows increasing the total valency of the glycocluster. The reported hyperbranched CD glycoclusters are mostly based on the primary face functionalized CD (**Scheme 12**).<sup>158, 159 145, 160</sup>



**Scheme 12:** Synthesis and general structure of  $\beta$ -CD-scaffolded hyperbranched homo- and heteroglycoclusters by thiourea-forming reactions.<sup>158, 159 145, 160</sup>

The key point to construct the hyperbranched glycoclusters is to obtain a dendritic linker that connects the multiple functional units and possesses an interface to the readily CDs. The pentaerythritol mentioned in the last section plays a perfect role here in our frameworks. It can drive three "arms" of branched units and keep one alcohol for the conjugation interface. Many other groups use it as a hyperbranched amplifier for bioactive molecules.<sup>158, 159 145, 160</sup>

### 3.3 PRINCIPLES OF MOLECULAR DYNAMICS SIMULATIONS

#### 3.3.1 Classical molecular dynamics

The classical molecular dynamics (MD) simulation is a common computational technique employed in a large variety of theoretical studies. MD simulations are much favored to model biological molecules and materials for studies related to protein bindings, conformational changes, surfactant effects, surface reactivities, etc. In short, the computational approach allows the observation of molecular motions and their time evolution.

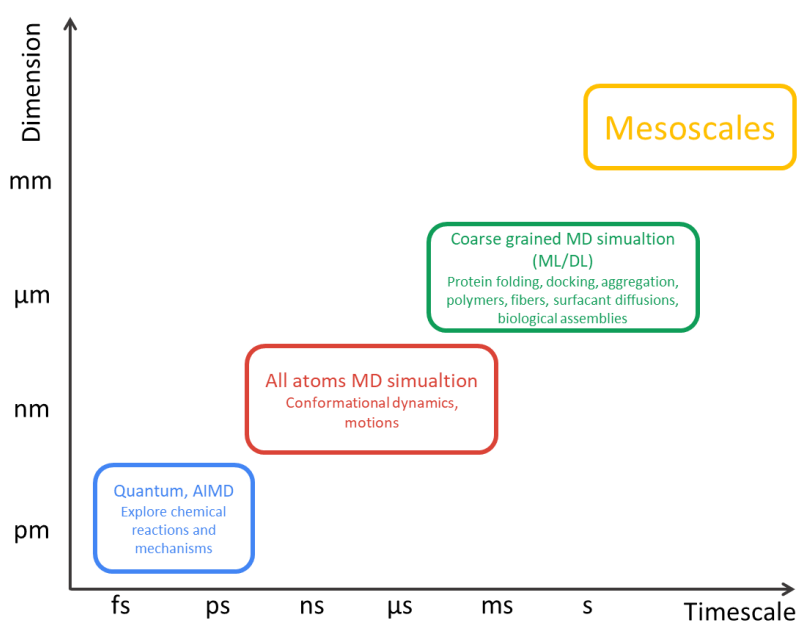


**Figure 49:** Computational molecular dynamics (MD) approaches, positioned along the dimension and the timescales of the system under investigation.

In **Figure 49**, the available computational approaches are listed and linked to their corresponding timescales and dimensional scales. The quantum chemical approaches and the *ab initio* molecular dynamics (AIMD), recently appeared and involving quantum chemistry, allow the observation of some chemical reactions during the total system motion, focusing on the chemical reaction processes, *e.g.*, chemical bond cleavage/generation. The dimension and the timescale cannot be too large, due to the computational power requested for such calculations.

The classical all atoms MD simulations are the most commonly used in studies related to conformational dynamics and motions of big molecules: DNA, RNA and proteins within a decent size. However, these systems usually require very long-time simulations or many times of simulations with different starting points. The data amount is growing exponentially in order to collect enough events. For studying the protein folding, docking, aggregation, or polymers, fibers, surfactant diffusions, biological assemblies, MD simulations derive coarse-grained simulations accelerated by machine learning or deep learning techniques to enhance the propagation for the timescales.<sup>161, 162</sup> Mesoscales are referring to the real life sized substances and materials over thousand nanometers. Traditional computational chemistry is not capable of resolving these materials, usually demanded in industrial fields. The computational methods need to address the chemical and physical mesophase formation, such as dissipative particle dynamics, lattice Boltzmann, etc.<sup>163, 164</sup>

The classical MD simulations are based on the Newton's equation of motions, in the framework of the classical mechanics. The results of MD simulations are the lists of atomic positions and the velocities as a

function of time. The method to describe the relationship between the energy and the corresponding conformation (atomic locations) is called force field. According to Born-Oppenheimer approximation in the quantum chemistry region with a great simplification on the calculations in electrons, the energy of one molecule can be approximately viewed as the function of all atoms positions which compose the whole molecule in the space. The energy of the molecule will change according to the conformational evolution. The force field is one way to describe it. However, the force field is sourced from empirical formula of the experiments. Compared to the *ab initio* quantum calculations, it is undoubtedly much rougher but saving much more computational time/cost. The force field generally contains the description of the following items:

$$\begin{aligned} E_{\text{total}} &= E_{\text{bonded}} + E_{\text{nonbonded}} \\ E_{\text{bonded}} &= E_{\text{bond}} + E_{\text{angle}} + E_{\text{dihedral}} \\ E_{\text{nonbonded}} &= E_{\text{electrostatic}} + E_{\text{vanderWaals}} + \dots \end{aligned}$$

The bonded part  $E_{\text{bonded}}$  includes the bond stretching, angle bending and the dihedral angle distorting the structure of the molecule in the force field, generally indicating the covalent bonds. Most force fields model them by quadratic energy functions, which do not allow bond cleavages except for the specific reactive force field ReaxFF.<sup>165</sup> The other nonbonded part  $E_{\text{nonbonded}}$  includes the electrostatic interactions, van der Waals forces, and the coupling corrections. Some additional corrections are also pre-included in most force field, *e.g.*, the mandatory planarity of aromatic rings to avoid undesirable torsions. The development of the force fields has been derived into various families to fit the most popular fields of research, *i.e.*, protein sciences and material sciences.

The multichromophoric systems studied in this dissertation are all organic molecules, therefore the general AMBER force field (GAFF) was used as the force field to study their conformational changes. AMBER force field has been developed by the Peter Kollman group<sup>166</sup> and is suitable for proteins, nucleic acids and large biological molecules. The GAFF extends the parameters for all organic molecules composed of C, N, O, H, S, P, F, Cl, Br and I, fitting the demands for pharmaceutical molecules. The functional form is expressed as:

$$\begin{aligned} E_{\text{pair}} &= \sum_{\text{bonds}} K_r (r - r_{eq})^2 + \sum_{\text{angles}} K_\theta (\theta - \theta_{eq})^2 + \sum_{\text{dihedrals}} \frac{V_n}{2} [1 + \cos(n\phi - \gamma)] \\ &+ \sum_{i < j} \left[ \frac{A_{ij}}{R_{ij}^{12}} - \frac{B_{ij}}{R_{ij}^6} + \frac{q_i q_j}{\epsilon R_{ij}} \right] \end{aligned}$$

The  $r_{eq}$  and  $\theta_{eq}$  are equilibrium structural parameters;  $K_r, K_\theta, V_n$  are the force constants;  $n$  is multiplicity and  $\gamma$  is the phase angle for torsional angle  $\phi$  parameters; the  $A, B, q$  characterize the non-bonded potentials. The constitution is effectively divided by the bonded and the unbonded part. The first term (summing over the bonds) expresses the energy between covalently bonded atoms. The second term (summing over the angles) expresses the energy related to the angles of covalently bonding atoms. The third term (summing over dihedrals) expresses the energy of bond torsions. The fourth term (double summing over  $i$  and  $j$ ) expresses the non-bonded energy between atom pairs.<sup>166, 167</sup>

The force field is complete for the molecular descriptions with the required parameters and generally applicable to organic chemical species. According to the benchmarks reviewed, GAFF can also provide similar performance on organic molecules to the more costly force fields.<sup>168, 169</sup> The MD simulation part described in this work were carried out with the GAFF and a restrained electrostatic potential charges calculation of a larger functional to improve the accuracy of the results.

Canonical ensemble (NVT, substance N, volume V, temperature T conserved) and isothermal-isobaric ensemble (NPT, substance N, pressure P, temperature T conserved) were applied gradually to the

systems. The equilibrium and the production states are generated by NPT ensemble to simulate the laboratory condition with open flask to the ambient temperature and pressure.

In the framework of this dissertation, the classical MD simulations were used to model the solvated multichromophoric systems (**2DCM**), linking the random conformational movement of the molecules and the variations of intramolecular FRET. Following the MD simulation trajectories, the time-dependent intramolecular FRET efficiency can be calculated, following the donor-acceptor pair distance and the orientation factors.

### 3.3.2 Trajectory based clustering analysis

MD trajectories qualitatively reveal the variations of geometries, which are the keys to understand the high or low intramolecular FRET efficiencies occurring between neighboring chromophores. However, to describe the composition of the conformations, we need some analytic tools to quantify and visualize the meaningful information from the MD data.

MD simulation generates huge amount of data, including over thousands of atoms moving simultaneously as a function of time. The challenge is to extract the molecular motions responsible for FRET processes, distinct from the vast range of “background noise”. The multivariant data are treated with either simplification on data or classification with features.

For the trajectories obtained by MD simulations, we first implemented the clustering analysis to visualize clusters of conformations. This analysis is supported by the VMD clustering plugin or the **gmx cluster** in GROMACS toolkit. Clustering analysis is the typical classification or grouping method to divide the original data into clusters with same qualities.

In practice, one of the most often used clustering algorithm applied to MD trajectories is based on the root mean square deviation (RMSD) analysis.<sup>170</sup> This method was implemented to compare the atomic displacements in a 3D geometry of two conformations. The RMSD by time evolution reflects the structural changes in a MD trajectory, as shown in the following equation:

$$RMSD(v, w) = \sqrt{\frac{1}{n} \sum_{i=1}^n ((v_{ix} - w_{ix})^2 + (v_{iy} - w_{iy})^2 + (v_{iz} - w_{iz})^2)}$$

The RMSD results are given in Å or nm. The toolkit will compare all the mutual RMSD of all snapshots sampled by time. A RMSD cut-off distance will be defined by the user to determine the cluster membership, *i.e.*, the grouping size defined to count the number of neighbors. By comparing the variance, the largest quantity of similar snapshots will be extracted and isolated from the next cluster, to identify the second largest group. By this mean, the energy minimum of the zone A, B, C, D, can be obtained. The largest group is not necessarily the global minimum. In practice, the trajectory snapshots are all aligned with one snapshot by RMSD algorithm at the beginning of the work.

### 3.3.3 Principal component analysis (PCA)

The amount of data generated by the MD trajectories is huge. Considering the atomic movements in the space, *e.g.*, **2DCM** in the MD trajectory, it is a 146-atoms molecule, and it then has  $146 \times 3 = 438$  dimensions in a 3D space. Then the movements are multiplied by the time with an interval of sampling steps, to constitute the trajectory data. Additionally, the **2DCM** molecule is surrounded by 1500 THF molecules, which are also free to move in time. Therefore, we need to reduce the dimensionality to analyze the data.



Principle component analysis (PCA) is one of the most important concepts in mathematical statistics. And it is the simplest multivariate technique to reduce the dimensionality of complicated sets of data. The PCA allows us to reduce the dimensions down to single digit level and provides the feature information as much as possible. **2DCM** was treated with PCA to extract the free energy landscapes (FEL) and better visualize all the composition of the conformations.

### 3.3.3.1 Principles of PCA

The main idea of PCA is to maximize the variance among the variables and project them down to the lower dimensionality, where you can concentrate the most useful information. It utilizes the orthogonal linear transformation to treat the set of data and projects into so-called “principal components” (PCs).

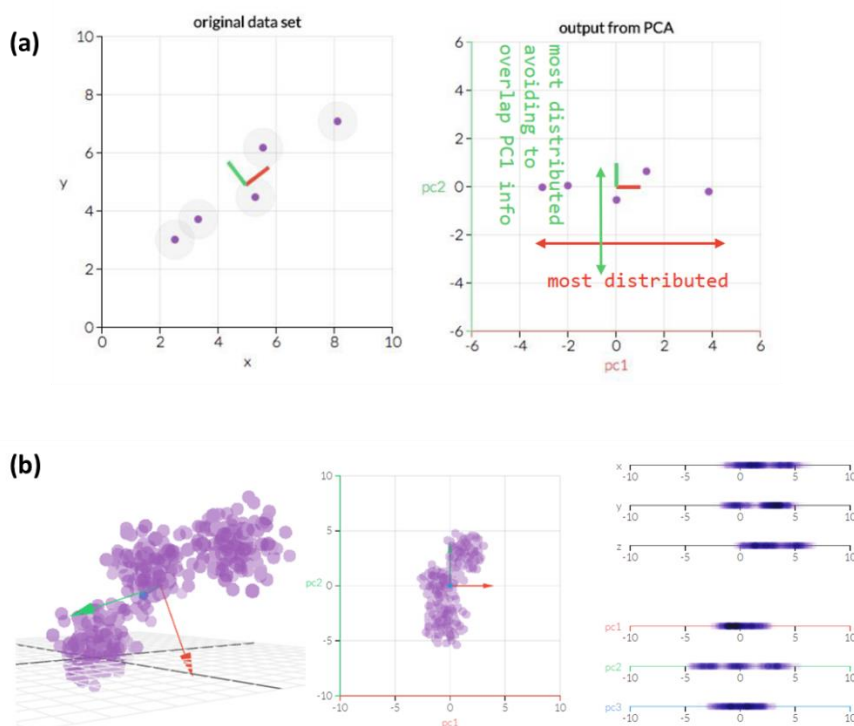


**Figure 50:** (a) Illustration of the treatment of PCA to the data points down to PC1 × PC2. (b) The dots in 3D space get PCA treatments down to the PC1, PC2 and PC3, respectively.<sup>171</sup>

As illustrated in **Figure 50**, the procedures to perform PCA are quite simple and clear:

1. Move the coordinate axis to the center of the data set and rotate the coordinate axis to maximize the variance of the data on the axis. The coordinate axis then is called PC1, the first principal component.
2. The second PC, PC2, is obtained by finding the axis which has the zero covariance with PC1, avoiding the data overlapping, and again maximizing the variance on this axis.
3. Repetition until PC<sub>n</sub>.

From the methodology we can see that PCA can preserve the features which contribute to the variance, and it is sensitive to data pretreatment.

### 3.3.3.2 Free energy landscape (FEL)

The free energy landscape analysis is the cornerstone to investigate proteins. In our case, it certainly facilitates the understanding of the structural flexible geometry of the **2DCM** molecules. The FEL analysis is drawn based on PCA as the data input from the equilibrium MD simulation. The FEL  $\Delta G(x)$  is expressed as

$$\Delta G(x) = -\kappa_B T \ln \frac{P(x)}{P(x_0)}$$

where  $k_B$  is the Boltzmann constant;  $T$  represents the temperature;  $P(x)$  is the probability distribution and  $x_0$  refers to some reference states. The FEL is related to the probability of the various states: the metastable states are distributed in low free energy regions while the barriers between the metastable state regions should account for the transition states.

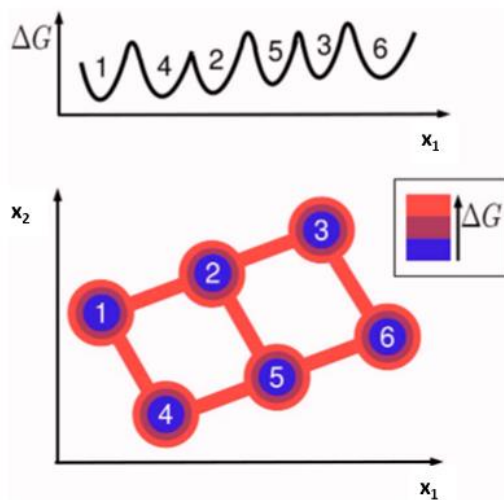


**Figure 51:** Schematic 1D and 2D representations of a FEL. The 2D scheme shows the pathway link relationships between metastable states which cannot be visualized with the 1D scheme.

As shown in **Figure 51**, when the FEL is plotted in a 2D scheme, the pathway link relationships can be seen by means of a simple network model. The 2D or 3D FEL is a useful indication on the conformational changes. In addition, the FEL is not only available for PCA, but also for other dimensionality reduction treatments, such as the Markov state model (MSM, see next section).

### 3.3.4 Markov state models (MSMs)

The MSM is a stochastic model used to solve probability related problems. For example, the “random walk” is a special case of Markov chain, which is the simplest MSM. MSM assumes that the future states depend only on the current state, not on the historic events. The history independent property is called Markov property (or Markovian). Therefore, such an assumption can be used to compute or rationalize the predictive and probabilistic modelling.

In the field of MD simulations, the MSMs are growing and become an increasingly powerful framework for analyzing the data and setting up the transition probabilities inside the metastable states in the field of computational biochemistry and biophysics. They are used to study protein folding, unfolding, and aggregations, in Alzheimer’s disease related fields, or the mechanisms against SARS-Cov-2, for instance.<sup>172-175</sup>

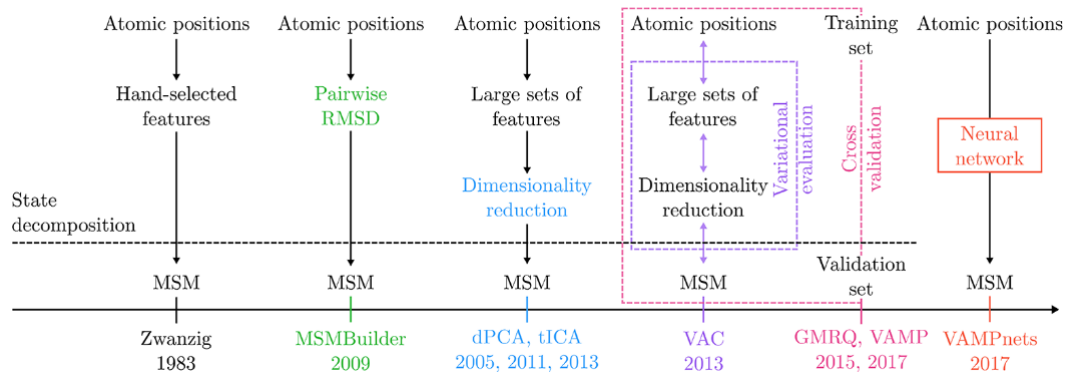


**Figure 52:** The chronological summary of major improvements to the MSM implementations in MD simulation fields.<sup>176</sup>

Starting from the emerging dimensionality reduction approaches, the MSM has entered the practical stage, especially with the time-lagged independent component analysis (tICA) as the dimensionality reduction. After that, the scoring system combined variational evaluation (VAC)<sup>177</sup>, and cross validation with training sets debuted as reliability improvement. Currently, with the rising influence of the deep learning and machine learning fields, the neural networks data training approaches are emerging as the next generation of analysis methods in this domain.<sup>178</sup>

For the **2DCM** molecular system, which is much simpler than the large protein structures, the mature tICA dimensionality reduced MSM provides satisfying results. In the frame of my PhD dissertation, MSM was implemented with the PyEMMA code package and the tICA integrated in the code package.<sup>179</sup>

tICA has been used as the dimensionality reduction method from 2013 in the implementation of MSM.<sup>180</sup> As a sub-category of the independent component analysis (ICA), tICA has been first introduced and evolved since 1994.<sup>172, 180-182</sup> It originally serves as a solution to the *blind source separation* problem, where the correlation matrix and the time-delayed correlation matrix are used to distinguish the superimposed signals. It computes the optimal linear projection for approximating the *slowest* relaxation processes, providing the eigenvalues and eigenfunctions. In MD simulation, tICA is used as a preprocessing step, as well as PCA, to reduce the size of the state space by projecting the dynamics onto a lower number of coordinate axes. Unlike maximizing the orthogonality in PCA, tICA maximizes the uncorrelated autocovariances by the assigned lag time  $\tau$ . The tICA projection results in finding the *slowest* process among the dynamics. For example, as shown in **Figure 53**, one set of data was generated by a stochastic process which would typically spend a long time in one of the two clusters before it jumps to another state. We are interested in the metastable states during the process. The PCA analyzed the data set coordinate vector in red and tICA is shown in black.

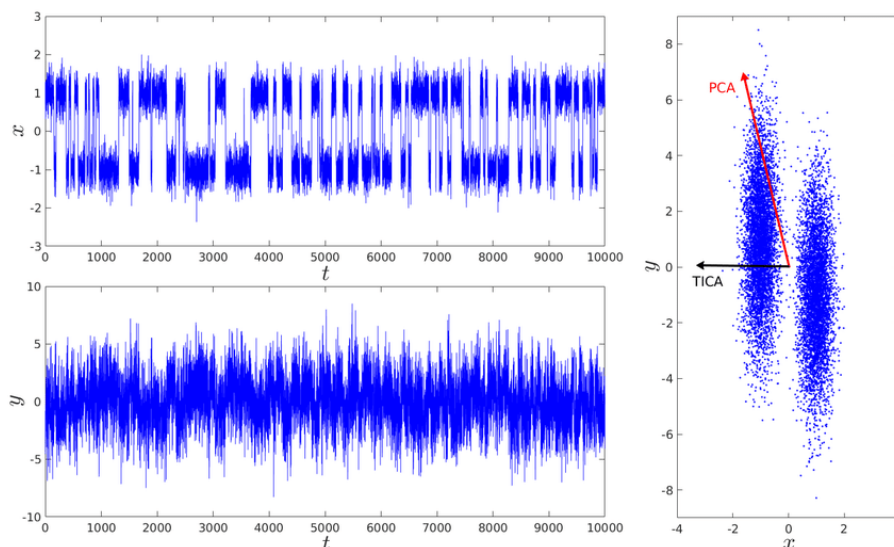


**Figure 53:** The difference between PCA and TICA. The top and bottom plot show the x- and y-component of the system, respectively, the plot on the right is the resulting main principal component vector and the main TICA coordinate.<sup>183</sup>

From **Figure 53**, we can clearly see that the PCA is along the direction of the maximal variance in the data extending from the (0,0) to the maximum (x,y)-coordinate. In this example, PCA is not very informative for resolving the rare events which may be critical. Oppositely, tICA successfully identifies the slow reaction coordinate. Taking the temporal information into account, the x-coordinate projection preserves the slow process while eliminating the fast stochastic noise. The identification of the slow processes in the MD data is important to provide the approximations to the eigenvalues and eigenfunctions of the Markov operators. In the following content, we plot the 2D FELs based on the tICA.

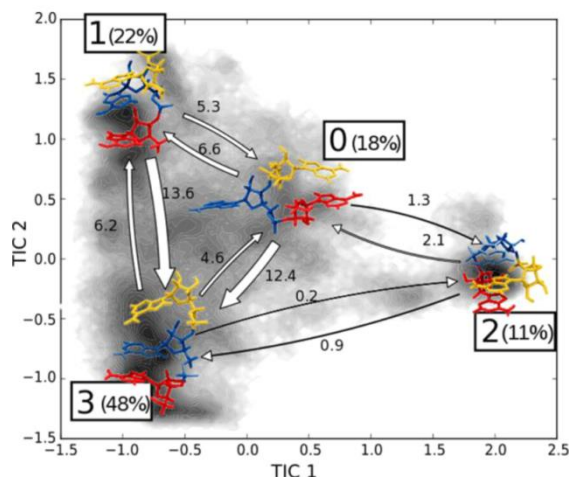


**Figure 54:** Schematic representation of four-state hidden MSM for adenine trinucleotide.<sup>184</sup> Nucleotides are colored according to their position in sequence (red, 1; blue, 2; yellow, 3). Percentages indicate the equilibrium population of each state; the widths of arrows are proportional to the transition rates between the states. Shading indicates the distribution of the simulation data projected on the plane defined by two leading tICA components. Figure reprinted by American Chemical Society.<sup>185</sup>

As shown in **Figure 54**, Pinamonti *et al.*<sup>184</sup> demonstrated the predictions on the kinetics of RNA oligonucleotides using MSM with tICA. The implementation shows the transition rates of well-distinguished states of the adenine trinucleotide and their morphologies in a highly visualized way.

In our research, the interactions between photochromes and fluorophores are important topics to investigate. Especially, the FRET requires the D-A pair distance and orientation factor parameters, which depends on the molecular geometries. By utilizing MSM with tICA, the good separation of molecular geometry types and the understanding of their transition rates among the different geometries are undoubtedly useful.

### 3.4 PAPER MANUSCRIPT #2 (CHEM. EUR. J.)

# Competitive photoisomerization and energy transfer processes in fluorescent multichromophoric systems

Yang Zhou,<sup>[a]</sup> Stéphane Maisonneuve,<sup>[a]</sup> François Maurel,<sup>\*[b]</sup> Juan Xie,<sup>\*[a]</sup> Rémi Métivier<sup>\*[a]</sup>

[a] Y. Zhou, S. Maisonneuve, J. Xie, R. Métivier  
ENS Paris-Saclay, Université Paris-Saclay  
CNRS, PPSM  
F-91190 Gif-sur-Yvette, France  
E-mail: joanne.xie@ens-paris-saclay.fr, remi.metivier@ens-paris-saclay.fr

[b] F. Maurel  
Université Paris Cité  
CNRS, ITODYS  
F-75013 Paris, France  
E-mail: maurel@u-paris.fr

Supporting information for this article is given via a link at the end of the document.

**Abstract:** Multichromophoric systems showing both fluorescence and photoisomerization are fascinating, with complex interchromophoric interactions. The experimental and theoretical study of a series of compounds, bearing a variable number of 4-dicyanomethylene-2-*tert*-butyl-6-(*p*-(*N*-(2-azidoethyl)-*N*-methyl)aminostyryl)-4H-pyran (DCM) units are reported. The photophysical properties of multi-DCM derivatives, namely **2DCM** and **3DCM**, were compared to the single model azido-functionalized **DCM**, in the *E* and *Z* isomers. The (*EE*)-**2DCM** and (*EEE*)-**3DCM** were synthesized via the click reaction. Steady-state spectroscopy and photokinetics experiments under UV or visible irradiation indicated the presence of intramolecular energy transfer processes among the DCM units. Homo- and hetero-energy transfer processes between adjacent chromophores were confirmed by fluorescence anisotropy and decays. Molecular dynamics simulations for **2DCM** were carried out and analyzed using a Markov state model, providing geometrical parameters (orientation and distance between chromophores) and energy transfer efficiency. This work contributes to a better understanding and rationalization of multiple energy transfer processes occurring within multichromophoric systems.

## Introduction

Multichromophoric molecules and assemblies are envisioned as a promising category of functional building blocks to be applied in light-harvesting materials, optoelectronic devices, adjustable polymers, or supramolecular systems.<sup>[1]</sup> Multichromophores containing a large number of chromophores enable specific features in a wide range of fields. For example, the multichromophores including photochromic moieties (multiphotochromic compounds) and fluorophores can exhibit photoswitchable colors, high-contrast fluorescence via resonance energy transfer (RET), and they can serve as multidimensional logic gates or induce multiple states supramolecular structural rearrangements.<sup>[1c, 2]</sup>

Besides applications involving structural changes or multi-logic gates, several reports highlight the use of photoisomerizable units, such as azobenzenes, in multichromophoric systems to enable non-linear optical features.<sup>[3]</sup> Some studies were reported about photoisomerizable chromophore-chromophore interactions, whereas most of them focus on the changes in the mechanical forces of films or crystalline solids, or the electronically or conjugationally influencing structures.<sup>[4]</sup> As far

as we know, photoisomerizable fluorophores included in large multichromophoric systems have not been explored to date.

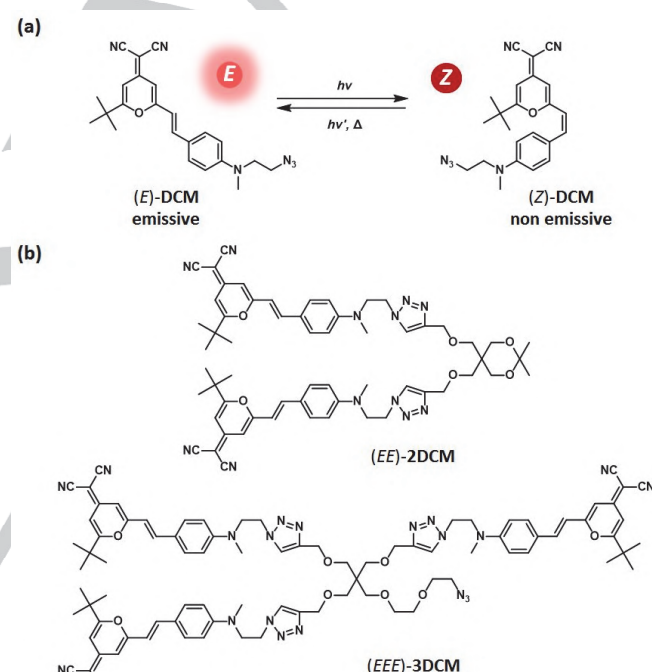


**Figure 1.** (a) *E-Z* photoisomerization reaction of **DCM** and (b) structures of **2DCM** and **3DCM** derivatives with each DCM unit being in the *E* form.

4-Dicyanomethylene-2-*tert*-butyl-6-(*p*-(*N*-(2-azidoethyl)-*N*-methyl)aminostyryl)-4H-pyran (DCM) derivatives represent one category of photoisomerizable fluorophores with a donor- $\pi$ -acceptor character, as previously reported by our group.<sup>[5]</sup> The double-bond isomerization can be induced by light, leading to the interconversion between the emissive *E*-form and the non-emissive *Z*-form. Several DCM analogues have been investigated,<sup>[5]</sup> demonstrating their efficiency, fatigue resistance, and ability to serve as brightly emissive molecular photoswitches. Since the DCM molecule shows both fluorescence and photoisomerization properties, we could expect interesting interactions by Förster resonance energy transfer (FRET) processes and following, novel optical features, when merged together in larger molecules. Therefore, we designed a series of DCM-based molecules, from the single model chromophore,



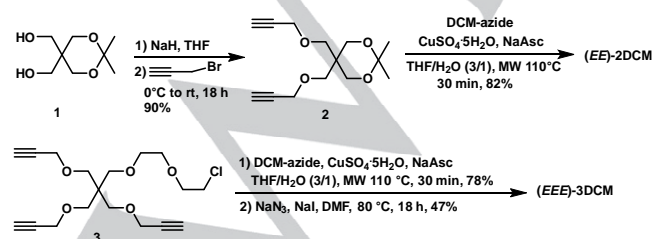
**DCM**, to more sophisticated structures, **2DCM** and **3DCM**, where two and three parent azido DCMs are connected together via a central flexible dendritic linker by the copper (I)-catalyzed alkyne-azide cycloaddition (CuAAC) reaction.<sup>[6]</sup> The corresponding chemical structures are shown in Figure 1, where all the DCM units are represented in the *E*-form. Such a design strategy offers the possibility to consider further functionalization with other molecular systems.

In this work, we report on the synthesis, photophysical and photochemical investigations of the **2DCM** and **3DCM** multichromophoric compounds, which are compared to the **DCM** model chromophore, by means of steady-state absorption spectroscopy, time-resolved fluorescence, fluorescence anisotropy, and photokinetics experiments. The photophysical properties of the series were investigated, and the comparison of their respective photokinetics under UV and visible irradiation could reveal the interchromophoric interactions existing among the DCM units. At the theoretical level, molecular dynamics (MD) simulations were performed on the **2DCM** molecule, which is a well-representative derivative to investigate both homo-FRET and hetero-FRET processes, followed by Markov state model (MSM) implementation to unravel the correlation between the molecular conformational changes and their impact on the FRET efficiencies.

## Results and Discussion

### Synthetic protocols and molecular structures

The design of functional dendritic architectures with well-defined structures is a very active and exciting field of research, and many multichromophoric systems have been synthesized with dendrimers or dendrons bearing large numbers of chromophores.<sup>[7]</sup> With the aim of gathering several independent DCM units, two dendritic linkers **2** and **3** with two and three propargyl groups respectively were firstly prepared (Scheme 1). Compound **2** was obtained after di-*O*-propargylation of isopropylidene acetal protected pentaerythritol **1**,<sup>[8]</sup> while **3** was synthesized according to the reported procedure.<sup>[9]</sup> CuAAC reaction of **2** with (*E*)-**DCM** under microwave irradiation led to **2DCM** as pure (*EE*)-isomer in 82% yield, by shielding the ambient light during the whole synthesis procedures. For the synthesis of **3DCM**, compound **3** was firstly reacted with (*E*)-**DCM** under microwave activation, followed by azidation with sodium azide in the presence of catalytic amount of sodium iodide in DMF at 80 °C. the (*EEE*)-**3DCM** was obtained in 37% total yield from **3**.



**Scheme 1.** Synthesis of (*EE*)-**2DCM** and (*EEE*)-**3DCM**.

(*E*)-**DCM** was an orange red crystal, whereas (*EE*)-**2DCM** and (*EEE*)-**3DCM** were obtained as red solids. The X-ray diffraction structure of **DCM** single crystals revealed its *s-trans*-(*E*) configuration, as already described in our previous studies.<sup>[5b]</sup> The *s-trans*-(*E*)-**DCM** is the most stable form among its four identified isomers and conformers, with a planar structure. However, the crystalline ability of (*EE*)-**2DCM** and (*EEE*)-**3DCM** is not good enough to allow single crystal X-ray diffraction analyses. When **2DCM** and **3DCM** are synthesized, we assume that the DCM units adopt preferentially the *s-trans*-(*E*) configuration, with high degrees of freedom between the DCM units allowed by the flexible central dendritic linker.

### Steady-state spectroscopy and photokinetic studies

According to our previous reports, THF was selected as the ideal solvent, since it allows the highest photoisomerization conversion of the DCM chromophore under irradiation, with significant emission properties.<sup>[5a]</sup> The absorption and fluorescence spectra of **DCM**, **2DCM** and **3DCM** in their *E* forms in THF are depicted in Figure 2. The absorption and fluorescence show that the three compounds have similar absorption and emission bands, with their maxima located at 457 nm and 588-590 nm, respectively. Table 1 presents their molar absorption coefficient ( $\epsilon$ ) at 457 nm, with increasing values in the sequential order **DCM** < **2DCM** < **3DCM**. However the  $\epsilon$  increments are not exactly proportional to the number of DCM units: it is only 1.8 times higher (2.6 times, resp.) higher for **2DCM** (**3DCM**, resp.) than for **DCM**. The deviation from linearity of  $\epsilon$  with the number of DCM units indicates that interchromophoric interactions between neighbouring chromophores exist in the multichromophoric systems. In addition, the fluorescence quantum yield ( $\Phi_F$ ) was measured at 0.25 for **DCM**, but slightly decreases to 0.21 for **2DCM** and **3DCM**. Again, the decrease of  $\Phi_F$  in diluted THF may be due to some level of intramolecular  $\pi$ - $\pi$  stacking between the DCM units within the **2DCM** and **3DCM**. It is worth noting that the DCM chromophores are only fluorescent in their *E* form, not in their *Z* form.<sup>[5]</sup> After irradiation at 485 nm (inducing the *E*→*Z* forward reaction of DCM) and 335 nm (to induce the *Z*→*E* backward reaction), photostationary states (PSS) were obtained for the three compounds, showing a decrease of the main absorption band at 457 nm and a clear isosbestic point at 391 nm (Figure 2), revealing that the DCM units can be considered as simple photoswitches, either in their *E* or *Z* forms. However, major differences on the PSS photoconversion levels reached at 485 nm and 335 nm were identified through their absorption spectra. The absorbance ratio of the two PSS at 485 nm and 335 nm,  $A_{PSS-485}/A_{PSS-335}$ , measured at 457 nm, is relatively low for **DCM** (0.75) which reflects its noticeable *E*→*Z* conversion under visible irradiation. Interestingly, the **2DCM** is less prone to be isomerized to the *Z*-form under 485 nm irradiation ( $A_{PSS-485}/A_{PSS-335} = 0.90$ ), whereas **3DCM** shows the lowest photoconversion ( $A_{PSS-485}/A_{PSS-335} = 0.96$ ). Obviously, the number of DCM units has a great impact on the *E*-*Z* interconversion by light.

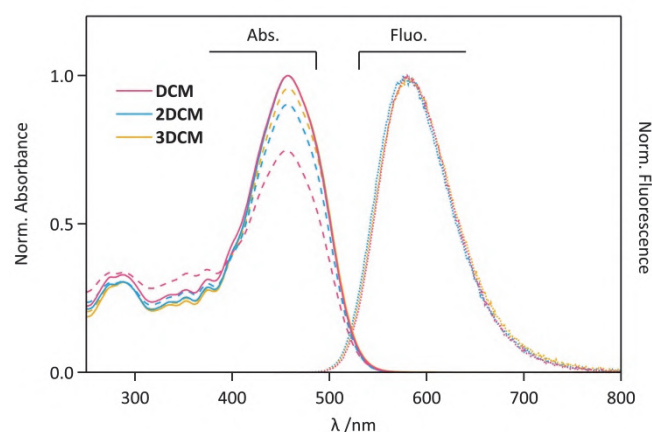


**Figure 2.** Absorption spectra after irradiation at 485 nm (dashed lines, PSS<sub>485</sub>) or 335 nm (full lines, PSS<sub>335</sub>) and emissionspectra before irradiation (dotted lines) of **DCM** (pink color) **2DCM** (blue color) and **3DCM** (orange color), in THF.

**Table 1.** Photophysical properties of **DCM**, **2DCM** and **3DCM** in THF: maximum absorption and emission wavelengths  $\lambda_{\text{abs}}$  and  $\lambda_{\text{em}}$ , fluorescence quantum yields  $\Phi_{\text{F}}$ , molar absorption coefficients at 457 nm  $\epsilon_{457\text{nm}}$ .

	$\lambda_{\text{abs}}/\text{nm}$	$\lambda_{\text{em}}/\text{nm}$	$\Phi_{\text{F}}^{[a]}$	$\epsilon_{457\text{nm}}/\text{L mol}^{-1} \text{cm}^{-1}$
<b>DCM</b>	457	590	$0.25 \pm 0.03$	$48700 \pm 600$
<b>2DCM</b>	457	588	$0.21 \pm 0.02$	$88400 \pm 1800$
<b>3DCM</b>	457	590	$0.21 \pm 0.02$	$128300 \pm 1800$

[a] Emission quantum yields  $\Phi_{\text{F}}$  were determined using Coumarine 153 in ethanol ( $\Phi_{\text{em}} = 0.54$ )<sup>[10]</sup> as the standard,  $\lambda_{\text{exc}} = 435 \text{ nm}$ .

To further investigate the photoisomerization properties, we carried out photokinetic experiments under similar irradiation conditions for **DCM**, **2DCM** and **3DCM**, starting from the fresh *E*-forms. Each compound was dissolved in THF solution, continuously probed by absorption spectra, and irradiated with visible light at 485 nm under vigorous stirring, which induced the *E*→*Z* photoisomerization of the DCM units to reach the PSS<sub>485</sub>. After 45 min, a subsequent irradiation at 335 nm was applied to trigger the reverse *Z*→*E* transformation to the PSS<sub>335</sub>. The absorbance was monitored at 457 nm and corresponding time-profiles are plotted in Figure 3. During the first sequence of irradiation at 485 nm, **3DCM** reaches the PSS equilibrium first (c.a. 10 min) and shows a limited decrease of absorbance ( $\Delta\text{Abs} < 0.06$ ), whereas **DCM** presents an opposite behaviour, with a large absorption change ( $\Delta\text{Abs} > 0.2$ ) but a slow photokinetics, the PSS equilibrium not being reached after 30 min of irradiation. **2DCM** exhibits intermediate properties, with a PSS reached in 20 min with an absorbance decrease of  $\Delta\text{Abs} \sim 0.1$ . During the second sequence of irradiation at 335 nm, the situation is similar, with a slow (resp. fast) photokinetics associated to large (resp. small) absorption changes for **DCM** (resp. **2DCM** and **3DCM**). This intriguing observation that the photoconversion rate and yield evolve in opposite ways, with a strong dependence on the number of DCM units in the molecules, could originate in the possible energy transfer processes that can act within chromophores in the **2DCM** and **3DCM** cases.

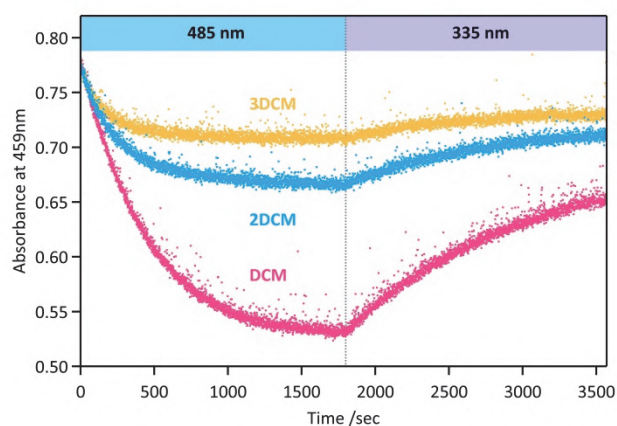


**Figure 3.** Absorbance at 459 nm of **DCM** (pink color), **2DCM** (blue color) and **3DCM** (orange color) in THF, as a function of irradiation time at 485 nm and 335 nm.

As a matter of fact, spectral overlaps exist between emission and absorption spectra of **DCM**, suggesting the possibility of intramolecular FRET between neighbouring chromophores in the case of **2DCM** and **3DCM** derivatives. More specifically, Figure 4 overlays the emission spectrum of (*E*)-**DCM** with the absorption spectra of (*E*)-**DCM** and (*Z*)-**DCM**, revealing a small but significant spectral overlap in both cases (highlighted in red in Figure 4). Therefore, two distinct energy transfer paths can be expected in **2DCM** and **3DCM**: homo-FRET processes between two (*E*)-**DCM** chromophores, and hetero-FRET processes between **DCM** units from the *E* form (donor) to the *Z* form (acceptor). As illustrated in Figure 4, when mutual orientations and interchromophoric distances are favorable, both processes can occur in the multichromophoric systems **2DCM** and **3DCM**. In the case of **3DCM**, the mixed model with two types of homo-FRET and hetero-FRET occurring simultaneously is also possible. Such intramolecular FRET pathways could explain the differences observed in conversion yields and rates for the three **DCM**-based compounds. Indeed, hetero-FRET may represent an efficient pathway leading to the deactivation of the *E* form and promoting the formation of *Z* form excited states, which in turn would decrease the *E*→*Z* reaction efficiency and favor the *Z*→*E* reaction. Therefore, hetero-FRET processes are expected to decrease the *E*→*Z* conversion yield under visible irradiation, but also increase the rate to reach the PSS equilibrium, through enhanced *Z*→*E* rates. This effect would be consistently higher in **3DCM**, where multiple FRET pathways are foreseen, compared to **2DCM**. In the case of **3DCM**, homo-FRET between identical **DCM** units in the *E* form (hopping mechanism), can increase the probability to find an energy transfer route from the *E* forms to the *Z* form (e.g. *E*→*E*→*Z* stepwise energy transfer sequence), thus indirectly promoting the excitation of the *Z* form.

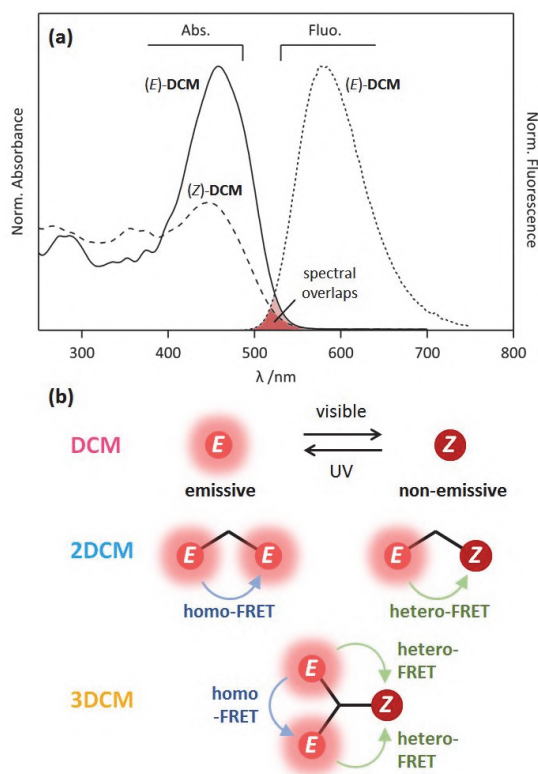


**Figure 4.** (a) Absorption spectra of (*E*)-DCM and (*Z*)-DCM, and emission spectrum of (*E*)-DCM. Spectral overlaps are highlighted in dark and light red colors. (b) Illustration of *E*↔*Z* photoisomerization of DCM and intramolecular energy transfer processes (homo-FRET and hetero-FRET) occurring in 2DCM and 3DCM.

### Fluorescence decays and anisotropy investigations

Fluorescence decay curves of the DCM, 2DCM and 3DCM were recorded by the time correlated single photon counting (TCSPC) method (Figure 5), with an excitation (resp. emission) wavelength at 400 nm (resp. 590 nm). The emission decays of the three compounds are not perfectly overlapping, with a more pronounced multiexponential character for 2DCM and 3DCM. The decay curves were fitted by a global analysis procedure using a bi-exponential function for the case of DCM, and a tri-exponential function for 2DCM and 3DCM, with satisfactory  $\chi^2_R < 1.2$ . According to our previous studies,<sup>[5]</sup> the emission arises only from the (*E*)-DCM units. Only two components  $\tau_1 = 0.25$  ns and  $\tau_2 = 0.84$  ns were identified for DCM can be ascribed to different conformers of the *E* form, namely the *s-trans*-(*E*)-DCM (longer decay-time  $\tau_2$ ) and *s-cis*-(*E*)-DCM (short decay-time  $\tau_1$ ).<sup>[5]</sup> An additional third component  $\tau_3 = 1.90$  ns was found for 2DCM and 3DCM, associated with small contributions to the whole decays ( $a_3 < 0.07$ ,  $f_3 < 0.18$ ), which can be ascribed to a certain proportion of DCM units interacting together, through intramolecular  $\pi$ - $\pi$  stacking for instance, as already suggested in the previous paragraphs. Such interactions may restrict nonradiative deactivation pathways of the DCM units, resulting in a longer decay time. After irradiation at 485 nm, the decay curve of DCM remained unaffected, whereas 2DCM and 3DCM showed slightly shortened fluorescence decays: the pre-exponential coefficient and the fraction of fluorescence intensity of the shortest decay-time  $\tau_1$  ( $a_1$ ,  $f_1$ ) increased, while those of  $\tau_2$  ( $a_2$ ,  $f_2$ ) decreased, and the proportion of the third decay

component  $\tau_3$  remained almost stable. For 2DCM and 3DCM, the changes in relative weights of  $\tau_1$  and  $\tau_2$ , corresponding to the *s-cis* and *s-trans* conformers of the (*E*)-DCM units, respectively, can be tentatively explained by the conformational redistribution of the chromophores following the relaxation process after excitation. Since constraints from the linkers exist for the DCM units in 2DCM and 3DCM, the *s-cis*↔*s-trans* interconversion after the photoreaction is probably hindered by the covalent connections, which could lead to higher proportions of *s-cis*-(*E*) species. Unfortunately, the homo-FRET and hetero-FRET could not be confirmed by time-resolved fluorescence because: (i) homo-FRET is basically not expected to affect the fluorescence decays of the (*E*)-DCM, and (ii) the (*Z*)-DCM being non emissive, the hetero-FRET from (*E*)-DCM to (*Z*)-DCM would induce a fluorescence quenching and a strong decrease of (*E*)-DCM lifetime, down to a level below the temporal resolution of our instrumental setup (~0.03 ns).

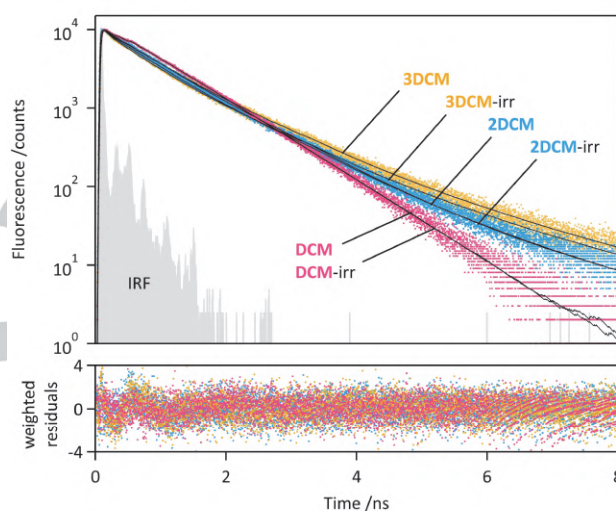


**Figure 5.** Fluorescence decay curves, instrumental response function (IRF, grey), bi-exponential (DCM) and tri-exponential (2DCM, 3DCM) curve fits (black), and weighted residuals of DCM (pink), 2DCM (blue) and 3DCM (orange) in THF, before and after irradiation at 485 nm (PSS<sub>485</sub>).  $\lambda_{exc} = 400$  nm,  $\lambda_{em} = 590$  nm.

**Table 2.** Time-resolved fluorescence parameters of DCM, 2DCM and 3DCM in THF, before and after irradiation at 485 nm.

	$\tau_1$ ( $a_1$ , $f_1$ )	$\tau_2$ ( $a_2$ , $f_2$ )	$\tau_3$ ( $a_3$ , $f_3$ )	Local $\chi^2_R$ [a]
DCM	0.25 (0.11, 0.04)	0.84 (0.89, 0.96)	–	1.02
DCM irr. <sup>[b]</sup>	0.25 (0.11, 0.03)	0.84 (0.89, 0.97)	–	1.01
2DCM	0.25 (0.23, 0.08)	0.84 (0.74, 0.84)	1.90 (0.03, 0.08)	1.12
2DCM irr. <sup>[b]</sup>	0.25 (0.32, 0.12)	0.84 (0.65, 0.78)	1.90 (0.04, 0.10)	1.07
3DCM	0.25 (0.27, 0.09)	0.84 (0.66, 0.73)	1.90 (0.07, 0.18)	1.12
3DCM irr. <sup>[b]</sup>	0.25 (0.39, 0.15)	0.84 (0.55, 0.69)	1.90 (0.06, 0.16)	1.13

[a] The global  $\chi^2_R$  corresponding to the global analysis of the full series of decay curves was calculated at 1.08. [b] Irradiated samples at  $\lambda_{irr} = 485$  nm.



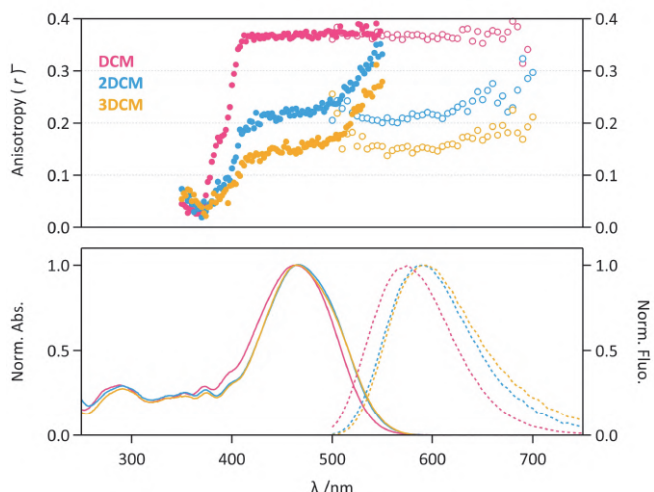


**Figure 6.** (Top) Fluorescence anisotropy of **DCM** (pink), **2DCM** (blue) and **3DCM** (orange) in propylene glycol at  $-45^{\circ}\text{C}$ , collected as a function of excitation wavelength (full circles) and emission wavelength (open circles). (Bottom) Absorption (full lines) and emission spectra (dotted lines) of **DCM** (pink), **2DCM** (blue) and **3DCM** (orange) in propylene glycol at  $-45^{\circ}\text{C}$ .

Steady-state fluorescence anisotropy being a relevant method to investigate the homo-FRET in multichromophoric assemblies,<sup>[11]</sup> it was measured for **DCM**, **2DCM** and **3DCM** derivatives in propylene glycol at  $-45^{\circ}\text{C}$  (Figure 6), which forms a vitrified medium and freezes the molecules to avoid rotation movements during the excitation timescale. The steady-state anisotropy ( $\bar{r}$ ) of **DCM** reaches a level as high as 0.36 for  $\lambda_{\text{exc}} > 410\text{ nm}$ , which is very close to the maximum theoretical limit of the single-photon excitation fluorescence anisotropy  $r_0 = 0.4$ . This high value reflects the almost colinear absorption and emission transition dipole moment of **DCM**: the angle  $\beta$  between these transition dipole moments was calculated to be  $\sim 15^{\circ}$  for **DCM**. At  $\lambda_{\text{exc}} < 410\text{ nm}$ , the anisotropy decreases down to almost zero at  $360\text{ nm}$ , which is consistent with transition dipole moments of higher excited states. **2DCM** and **3DCM** show a steady-state anisotropy plateau value of 0.22 and 0.18 in the range  $430\text{ nm} < \lambda_{\text{exc}} < 500\text{ nm}$  (Figure 6). This depolarization compared to **DCM** clearly confirms that homo-FRET processes do occur in **2DCM** and **3DCM**, the latter being more depolarized in the same experimental condition. At longer excitation wavelength ( $\lambda_{\text{exc}} > 500\text{ nm}$ ), the steady-state anisotropy rises up to 0.35 and 0.30 for **2DCM** and **3DCM**, respectively, due to the so-called Weber's red-edge effect: excitation in the low-energy region of the  $S_0 \rightarrow S_1$  electronic transition selects the **DCM** chromophores which are less prone to  $E \rightarrow E$  homo-FRET, and as a result, leads to an increase of the  $\bar{r}$  value. Therefore, steady-state anisotropy provides evidences of homo-FRET within **DCM** units in **2DCM** and **3DCM**, and we can assume that the higher depolarization of **3DCM** emission is related to larger homo-FRET efficiencies, due to more favorable orientation arrangements of the chromophores and/or shorter interchromophoric distances. The transition dipole moment orientations of the **DCM** units within multichromophoric architecture, and inter-**DCM** distance parameters are critical parameters influencing the efficiency of homo-FRET and hetero-FRET in these systems. However, direct and dynamic measurements of such structural parameters are out of reach by conventional experimental techniques. For this reason, we decided to perform MD simulations to characterize the geometrical parameters and their influence on the FRET efficiencies.

## Modelling of the FRET parameters of 2DCM

To examine the geometrical parameters of the **DCM-DCM** interaction and their effect on the homo-FRET and hetero-FRET efficiencies, we selected **2DCM** as the simplest molecule to be studied by MD simulations. Two models can be prepared, representing the typical FRET patterns in dendritic multichromophoric **DCM**-based molecules. The first model is the (*EZ*)-**2DCM** configuration, where we assign the (*E*)-**DCM** as the donor and the other (*Z*)-**DCM** as the acceptor in the frame of the  $E \rightarrow Z$  hetero-FRET. Besides, the (*EE*)-**2DCM** represents a good model to investigate the  $E \rightarrow E$  homo-FRET (the donor and acceptor chromophores are chosen arbitrarily).

Due to the large size of the studied systems, the initial structures for MD simulations were optimized using the mixed ONIOM method. The **DCM** units were calculated using PBE0 functional and the 6-311G+(d,p) basis set while the bridge connecting the **DCM** unit was treated using the semi-empirical PM6 method (see details in Figure S1). The optimized geometries have been built and converged in an unfolded conformation for both (*EZ*)-**2DCM** and (*EE*)-**2DCM** structures, as shown in Figure 7 and Figure S1. They were packed with 1500 THF molecule by Packmol (Figure S2),<sup>[12]</sup> and MD simulations were performed with the GROMACS software package version 2020<sup>[13]</sup> using general AMBER force field (GAFF)<sup>[14]</sup> from AmberTools.<sup>[15]</sup> All the simulations for (*EZ*)-**2DCM** and (*EE*)-**2DCM** were performed in a sequence involving the energy minimization, the equilibrium isothermal-isobaric (constant particle number, pressure and temperature, NPT) ensemble, and the production NPT ensemble for 200 ns, which was validated by comparison with longer trajectories (Figure S5 and Table S1).

**MD simulations and FRET efficiency trajectories.** A first observation to the MD trajectories showed us that the **DCM** unit keep their *E* or *Z* isomeric state over the whole simulation, but could flip sometimes from *s-cis* to *s-trans* and vice versa (Figure S3). The instantaneous values  $R_{DA}(t)$  of the distance between the donor-acceptor pair and orientation factor  $\kappa^2(t)$  were generated by the MD software toolkit from the trajectories. In this MD section, even though energy transfer processes involve the donor species in the excited state, we assume that the ground state geometry of the multichromophoric systems can be used to estimate the FRET efficiency  $E_{\text{FRET}}$ , by the equation (1):

$$E_{\text{FRET}} = \frac{1}{1 + (R_{DA}/R_0)^6} \quad (1)$$

where  $R_0$  is the Förster radius of the donor-acceptor pair, calculated by the equation (2):

$$R_0^6 = \frac{9000 \times \ln(10) \times \kappa^2 \times \Phi_D^0}{128 \times \pi^5 \times N_A \times n^4} \times J(\lambda) \quad (2)$$

where  $n$  is the refractive index of THF,  $\Phi_D^0$  is the fluorescence quantum yield of the **DCM** chromophore in absence of energy transfer,  $J(\lambda)$  refers to the absorption and emission spectral overlap integral,  $N_A$  is the Avogadro constant. The initial geometries of (*EZ*)-**2DCM** and (*EE*)-**2DCM** are depicted in Figure 7 and Figure S1. The  $R_{DA}$  was derived from the distance between atoms closest to the mass centers of each **DCM** fragment, and the transition dipole moment vectors of the (*E*)-**DCM** and (*Z*)-**DCM** fragments at their first excited states were calculated by TDDFT. The  $\kappa^2(t)$  was then calculated through the equation (3):

$$\kappa^2 = (\sin \theta_D \sin \theta_A \cos \phi - 2 \cos \theta_D \cos \theta_A)^2 \quad (3)$$

where  $\theta_D$ ,  $\theta_A$ , and  $\phi$  are defined in Figure 7.

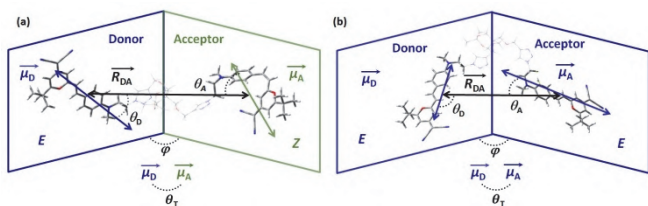


**Figure 7.** (a) *(EZ)*-2DCM and (b) *(EE)*-2DCM, optimized by the ONIOM method, and used as initial structures for the MD simulations.  $\vec{\mu}_D$  refers the donor transition dipole moment vector,  $\vec{\mu}_A$  to the acceptor transition dipole moment,  $\theta_T$  is the angle between the two vectors,  $\vec{R}_{DA}$  is the vector defined between the two mass centers of the DCM units,  $\theta_D$  and  $\theta_A$  are the angles between  $\vec{R}_{DA}$  and  $\vec{\mu}_D$ ,  $\vec{R}_{DA}$  and  $\vec{\mu}_A$ , respectively, and  $\varphi$  is the dihedral angle between the  $(\vec{R}_{DA}, \vec{\mu}_D)$  plane and the  $(\vec{R}_{DA}, \vec{\mu}_A)$  plane.

The *(Z)*-DCM molar absorption coefficient was determined from the *(Z)*-DCM conversion rate  $\alpha_Z$ , by a well-established method in our group.<sup>[5]</sup> From the **DCM** spectra shown in Figure 4a, the spectral overlap integrals  $J(\lambda)$  were then calculated for *(EZ)*-2DCM and *(EE)*-2DCM to be  $1.03 \times 10^{13} \text{ nm}^4 \text{ M}^{-1} \text{ cm}^{-1}$  and  $5.90 \times 10^{13} \text{ nm}^4 \text{ M}^{-1} \text{ cm}^{-1}$ , respectively. The instantaneous  $E_{\text{FRET}}(t)$  can be derived from the instantaneous orientational factor  $\kappa^2(t)$  and the interchromophoric distance  $R_{\text{DA}}(t)$  (corresponding histograms and average values in Figure S4). The 200 ns trajectory of  $E_{\text{FRET}}(t)$  for *(EZ)*-2DCM is shown in Figure 8a, together with the histogram of  $E_{\text{FRET}}$ . As a result, the  $E_{\text{FRET}}$  values calculated for the *(EZ)*-2DCM span from 0% to 100%, with an average level of 63.4%, showing that a very wide variety of geometries are

visited during the MD simulation, associated to very different FRET efficiencies. The highest probability (largest number of frames) corresponds to  $E_{\text{FRET}}$  in the 80-100% range, but the statistical distribution has a very flat behaviour, with a large contribution of events where  $E_{\text{FRET}} < 10\%$ . These extreme regions indicate the great conformational variability of the molecule, at the origin of the large dispersion of  $\kappa^2$  and/or  $R_{\text{DA}}$  values. Figure 8b,d corresponds to enlarged areas of the  $E_{\text{FRET}}$  trajectory, their corresponding  $R_{\text{DA}}$  and  $\kappa^2$  being plotted in Figure 8c,e, respectively. During some specific time-periods (58.0-58.5 ns, 183-190 ns), the  $R_{\text{DA}}$  values are below 1.3 nm, pushing the FRET efficiency up to nearly 100%, except for some extremely unfavorable orientations. For  $R_{\text{DA}} < 1$  nm, the conformations of *(EZ)*-2DCM are mostly in a folded geometry, as exemplified for the geometry #3 in Figure 8f, with  $\kappa^2$  close to 1 (two transition dipole moment almost parallel to each other). When the interchromophoric distance is in the interval  $1.5 < R_{\text{DA}} < 2$  nm, *i.e.* 58.5-61.0 ns in Figure 8b-c, the  $\kappa^2$  starts to control the  $E_{\text{FRET}}$  level, the higher the  $\kappa^2$ , the higher the  $E_{\text{FRET}}$ . The geometry #1 displayed in Figure 8f presents a folded structure, but an unfavored orientation of the DCM units ( $\kappa^2 \sim 0$ ) leading to an absence of hetero-FRET. When the  $R_{\text{DA}}$  becomes higher than 1.5 nm, the  $\kappa^2$  fully dominates the FRET efficiency shape: the  $E_{\text{FRET}}$  trajectory synchronizes the  $\kappa^2$  one in Figure 8b-c, showing identical trends (two tendency dashed lines in the range 59.2-60.7 ns, where  $R_{\text{DA}} \geq 2$ ).

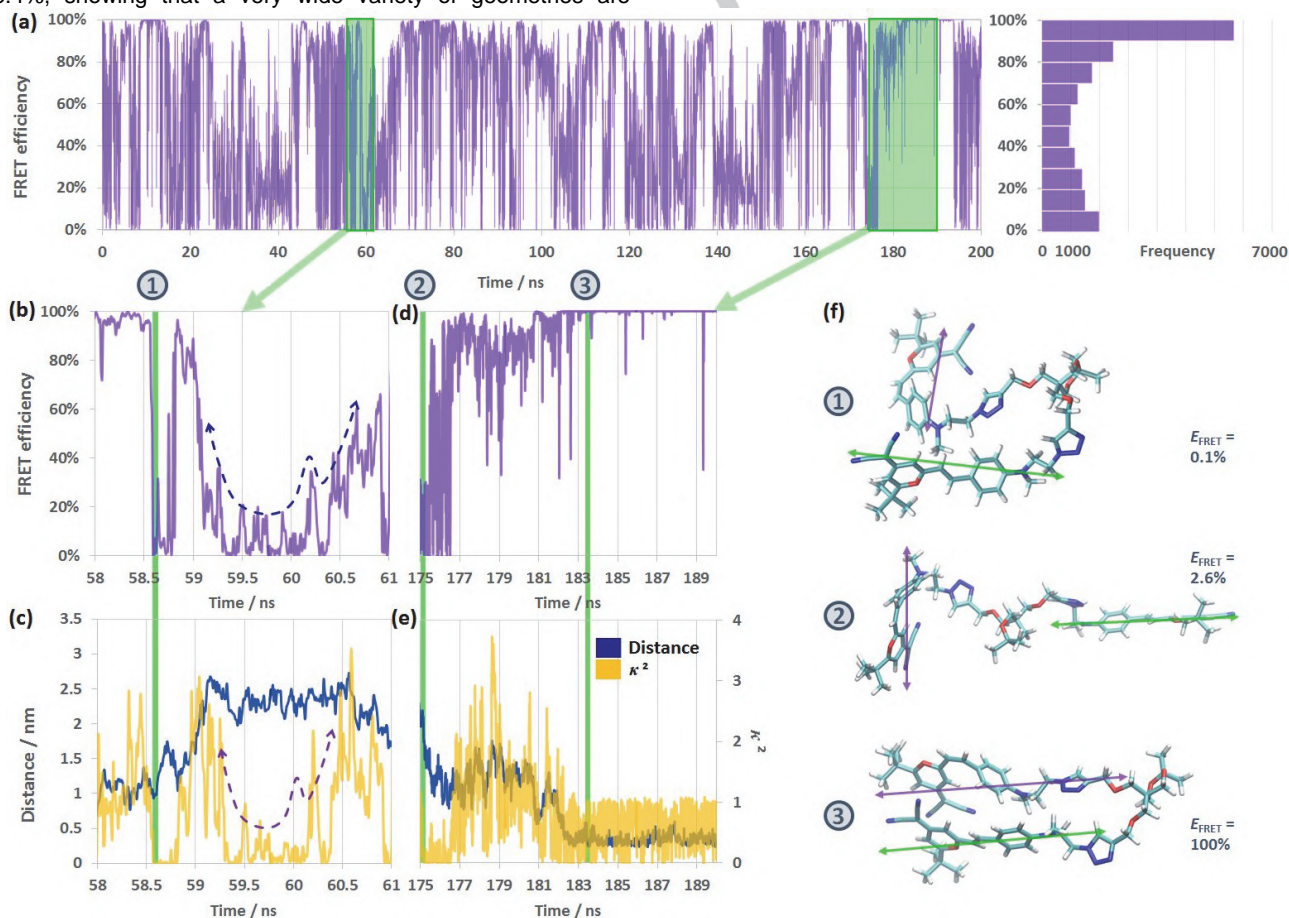


**Figure 8.** (a) MD trajectory of *(EZ)*-2DCM hetero-FRET efficiency  $E_{\text{FRET}}(t)$  during 200 ns, and corresponding histogram of  $E_{\text{FRET}}$  distribution. (b, d) Enlarged areas of the  $E_{\text{FRET}}(t)$  trajectory in the time intervals 58-61 ns and 175-190 ns. (c, e) Enlarged areas of the  $R_{\text{DA}}(t)$  (navy blue) and  $\kappa^2(t)$  (yellow) trajectories corresponding to (b, d), respectively. (f) Three selected typical geometries of *(EZ)*-2DCM, indicated by green vertical bars in (b-e), with green and violet arrows representing the transition dipole moments of the donor (*E*)-DCM and the acceptor (*Z*)-DCM units, respectively. Their corresponding FRET efficiencies are marked in the insets.



The unfolded conformation #2 shown in Figure 8f highlights the typical situations where both large DCM-DCM distance and almost perpendicular orientation prevent the FRET process.

In the case of (*EE*)-2DCM, the MD simulation provides similar trajectories (see Figure S6), with even higher levels of homo-FRET efficiency throughout the whole trajectory length, resulting in an average  $E_{\text{FRET}}$  value as high as 87.8%. In a first approach, the larger homo-FRET efficiency compared to hetero-FRET efficiency is essentially due to the higher spectral overlap,  $J(\lambda)$  being almost six times larger (*vide supra*). From the histogram shown in the Figure S6, most frames contribute to  $E_{\text{FRET}}$  over 90%. The enlarged areas of the (*EE*)-2DCM trajectory highlight that the orientations and distances of the DCM fragments are rarely unfavorable to the homo-FRET. Several examples of conformations have been selected in Figure S6, and even the unfolded form can reach an  $E_{\text{FRET}}$  value of 55% since the transition dipole moments are favorably parallel.

Concerning the interchromophoric distance between the DCM units,  $R_{\text{DA}}$ , the Table 3 lists three categories, counting the situations (frames) where  $R_{\text{DA}} \leq 1$ ,  $1 < R_{\text{DA}} < 2$  and  $R_{\text{DA}} \geq 2$ . It provides a synthetic picture of conformations in the two trajectories. The  $R_{\text{DA}} \leq 1$  region of (*EZ*)-2DCM reaches 91.5% average  $E_{\text{FRET}}$  and reaches 98.5% in the case of (*EE*)-2DCM. This region can be viewed as mostly dominated by the interchromophoric distance, since even unparallel orientations are still favorable to FRET processes. In the intermediate  $1 < R_{\text{DA}} < 2$  region, the average  $E_{\text{FRET}}$  of (*EZ*)-2DCM decreases substantially (64.7%) whereas it remains at a high value in the case of (*EE*)-2DCM (92.3%). When  $R_{\text{DA}} \geq 2$ , the average  $E_{\text{FRET}}$  drops down in both cases (23.2% and 61.5% respectively), and the  $\kappa^2$  starts to control the  $E_{\text{FRET}}$  level, as described previously.

Therefore, the MD simulations confirm that hetero-FRET and homo-FRET processes can take place within chromophores of (*EZ*)-2DCM and (*EE*)-2DCM, and the trajectory-based instantaneous FRET analysis reveals that the completely folded conformation is the most favorable to FRET, which can reach almost 100%. Based on the above statements, we further continued statistical implementations on the MD simulation data to identify the most representative geometries using the principal component analysis (PCA) method (Figures S7-8). More interestingly, connections between the main conformations found by PCA of (*EZ*)-2DCM and (*EE*)-2DCM, can be revealed by the Markov State Model (MSM) method, as detailed below.

**Table 3.** Average energy transfer efficiency value ( $E_{\text{FRET}}$ ) classified as a function of the interchromophoric distance ( $R_{\text{DA}}$ ), extracted from (*EZ*)-2DCM and (*EE*)-2DCM MD simulation trajectories.

	average $E_{\text{FRET}}$		
	$R_{\text{DA}} \leq 1$	$1 < R_{\text{DA}} < 2$	$R_{\text{DA}} \geq 2$
( <i>EZ</i> )-2DCM	91.5%	64.7%	23.2%
( <i>EE</i> )-2DCM	98.5%	92.3%	61.5%

**Markov State Models (MSMs) of 2DCM.** To further rationalize the conformational changes occurring during the trajectories produced by MD simulations, we built the MSM for both trajectories, corresponding to (*EZ*)-2DCM and (*EE*)-2DCM. The MSM reveals the important intermediate states from the MD

simulation data and their mutual relationships. The analysis was carried out using the PyEMMA package.<sup>[16]</sup> The MD trajectories were taken into a time-lagged independent component analysis (tICA), and featurized by the software. The tICA maximizes the autocorrelation of the linearly transformed coordinates by a lag time  $\tau$ , finding a maximally slow reaction in the MD simulation corresponding to the lag time of the input parameter as the first independent component (IC). This method allows to identify all conformational components even with insufficient sampling. A lag time of 1 ns was selected for each trajectory (for time lags longer than 1 ns, the timescale curves level off, for both (*EZ*)-2DCM and (*EE*)-2DCM, as shown in Figure S9). Furthermore, the Chapman-Kolmogorov tests for the two MSMs show that the lag time  $\tau = 1$  ns model accurately predicts the behaviors at longer timescales. The resulting 2D and 3D free energy landscapes (FELs) of (*EZ*)-2DCM and (*EE*)-2DCM configurations along their first and second independent components are shown in Figure 9. The principal component analysis (PCA) was carried out, as shown in the Figures S7-8. The 200 ns trajectories for both 2DCMs have rather low cosine contents of the first two principal components (PCs): (*EZ*)-PC1 = 0.03, (*EZ*)-PC2 = 0.06, (*EE*)-PC1 = 0.16, (*EE*)-PC2 < 0.01, which indicates an acceptable sampling of this duration.

The MSMs were obtained with 200 microstates using  $\kappa$ -means clustering method and further lumped into 6 metastable states using the Perron cluster analysis (PCCA+) method, respectively. These metastable states were clustered to extract the major conformations of (*EZ*)-2DCM and (*EE*)-2DCM, as depicted in Figure 9a,c with several colors. The locations of the representative conformations from the metastable states are marked on the 3D FELs. The MSMs with transition pathways and pathway percentages on 2D FELs are displayed in Figure 9b,d.

In the (*EZ*)-2DCM MSM (Figure 9a-b), the main transition pathway starts from the unfolded form *EZ*-A, transits through the completely folded *EZ*-3 and *EZ*-4, and finally ends with the more compact rolled *EZ*-B, with a total pathway percentage of 75%. Another pathway, counting for 21%, omits the *EZ*-3, getting twisted conformations directly (*EZ*-2) and then converges into *EZ*-4 and *EZ*-B. We can clearly observe that this is a process which continuously shrinks the interchromophoric distance. The *EZ*-A unfolded types generally correspond to  $R_{\text{DA}} > 2$ , whereas the most compact *EZ*-1 and *EZ*-B have  $R_{\text{DA}} < 1$ , as visualized in the last section, and the intermediates have geometries with  $1 < R_{\text{DA}} < 2$  frames. Consequently, the average FRET efficiency increases along the pathways. The other minor routes with lower fluxes follow the same pattern as well, with decreasing  $R_{\text{DA}}$  from the unfolded conformations, thus improving the  $E_{\text{FRET}}$  along the path.

On the (*EE*)-2DCM side (Figure 9c-d), the situation is different. The unfolded forms *EE*-3 are the most probable intermediates during the process, and the MSM indicates a “folded conformations” → “unfolded conformations” → “single folded conformations” chain. The single folded conformations (*EE*-2 or *EE*-4) converge into the *EE*-B, for about 83% of the pathway flux. The pathways are based on the shift of the single folded and folded conformations *via* the unfolded conformations. Besides, other paths omitting the unfolded *EE*-3, directly through *EE*-2 and *EE*-4, can occur as well. In addition, 8% pathway flux is induced by the rolled folded types from the starting *EE*-A.

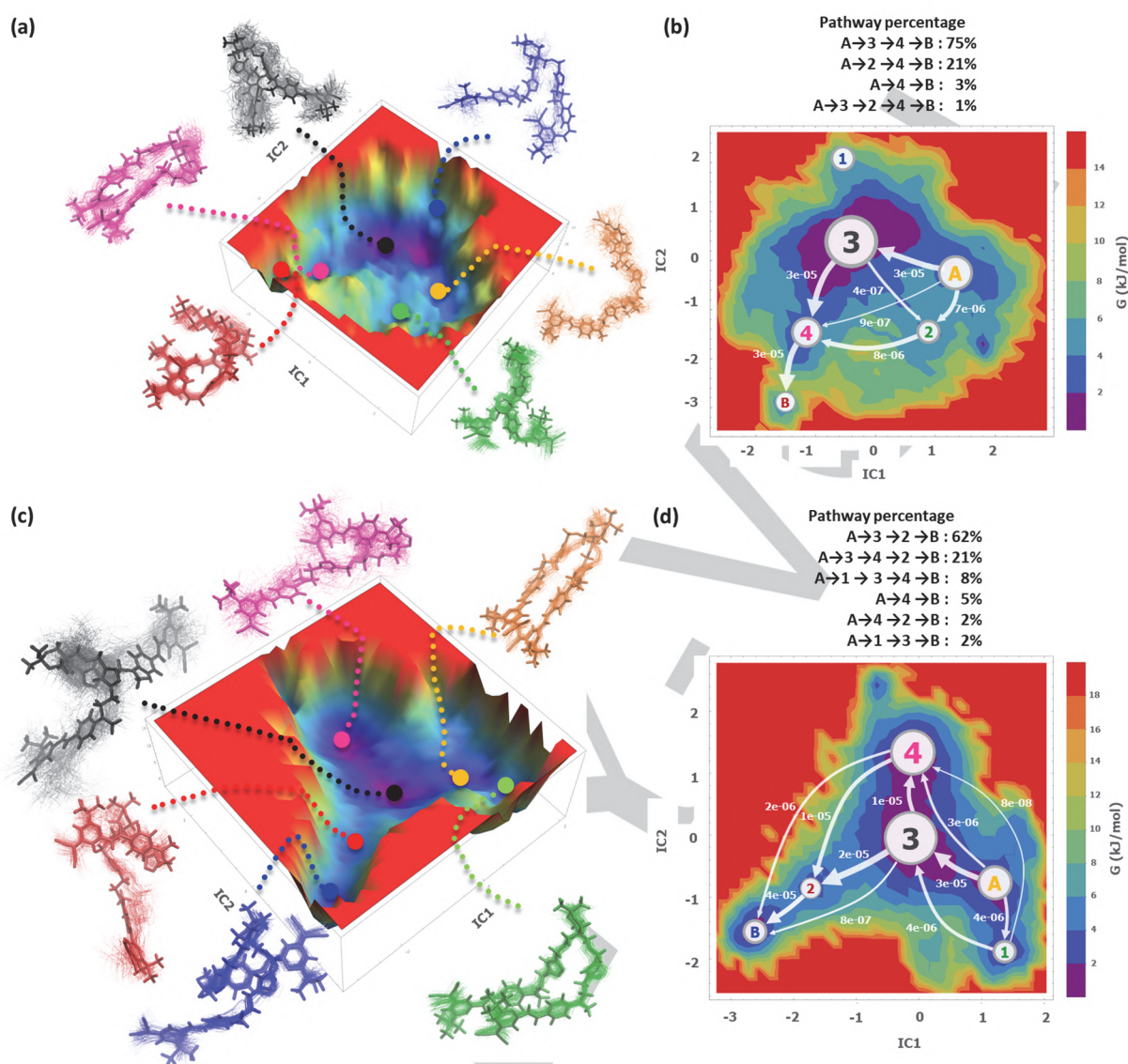


**Figure 9.** (a) tICA based on 200 ns MD trajectories of **(EZ)-2DCM** and (b) its tICA-FEL visualized MSM. (c) tICA based on 200 ns MD trajectories of **(EE)-2DCM** and (d) its tICA-FEL visualized MSM. The  $k$ -means clustering method generated 200 microstates that are lumped into 6 metastable states by the PCCA+ algorithm. The metastable states trajectories are clustered to extract the major conformations in six colors, which correspond to the labels in the transition pathway maps. The size of the labels and the arrows in (b, d) correspond to their proportional coarse-grained fluxes. The percentages of transition pathways are listed above each MSM in (b) and (d).

We explored the MD simulation trajectories with both MSM (tICA) methods (and PCA, see Figures S7-8), extracting the pathways along the typical conformations of **2DCM**. The representative conformations in the FELs can be categorized according to their  $R_{DA}$ , which are in turn related to the FRET efficiencies. In the case of **(EZ)-2DCM**, the evolution process from the unfolded forms to the completely/rolled folded conformations results in nearly 70% enhancement of the FRET efficiency. **(EE)-2DCM** undergoes an increase of FRET efficiency by 30% as long as its  $R_{DA}$  starts to shrink. Connected to the fluxes and pathway percentages of MSMs, the conformational fluctuation causing FRET efficiency variations in THF solution can be deduced.

## Conclusion

We have synthesized and characterized a series of DCM-based molecules, namely **DCM**, **2DCM** and **3DCM**, to serve as first specimens and models of photoisomerizable multichromophoric assemblies, and to investigate their behaviors under irradiation. Although possessing very similar absorption and emission spectral features, lower photoconversion yields and faster photokinetics were observed for **2DCM** and **3DCM** compared to **DCM**, which originate from intramolecular energy transfer processes. The homo-FRET was demonstrated to occur. By means of steady-state fluorescence anisotropy, an increasing depolarization of the emission was observed for **2DCM** and **3DCM**, demonstrating the occurrence of homo-FRET within the systems. Although time-resolved fluorescence cannot determine precisely the hetero-FRET, we selected the **2DCM** molecule as

a model to carry out MD simulations in two different states, (*EZ*)-2DCM and (*EE*)-2DCM. Thanks to the MD simulations, we could rationalize the connections between the FRET efficiency, the interchromophoric distances, orientation factors, explaining the reasons of the FRET fluctuations in time. Statistically, higher efficiencies FRET were identified for homo-FRET (87.8% average) than for hetero-FRET (63.4% average). The MSMs methodology and the statistics based on FELs, related to the MD simulations data, provided the main transition pathways among the structural conformations. In summary, we elucidated the strong FRET dependence on the molecular conformational changes. We can conclude that the photoisomerizable multichromophoric molecular architectures based on DCM chromophores are prone to be strongly affected by intramolecular energy transfer processes (homo- and hetero-FRET), with tuneable properties under irradiations. The future designs on multi-DCM systems should take into account the structural and geometrical factors (distances, orientations) to achieve desired performances.

## Experimental Section

**Materials.** The synthetic protocols of DCM, 2DCM and 3DCM are given in the Supporting Information. All commercially available compounds and solvents are purchased from Sigma-Aldrich affiliated to Merck KGaA, Carlo Erba Reagents, TCI chemicals and Acros Organics affiliated to Thermo Fisher Scientific without further purifications. <sup>1</sup>H-, <sup>13</sup>C, COSY, HSQC NMR data were acquired by JEOL ECS-400 spectrometer with a broadband probe. Spectroscopic measurements were performed with spectroscopic grade solvents from Carlo Erba Reagents and Sigma-Aldrich affiliated to Merck KGaA.

**Steady-state spectroscopy.** Absorption spectra at room temperature were recorded using Agilent Cary-4000 or Cary-5000 UV spectrometers. Fluorescence emission and anisotropy data were measured with Horiba Jobin-Yvon Fluorolog-3 spectrofluorometer equipped with polarizers in excitation and emission. Quartz cuvettes with a 1 cm path length were used. Fluorescence emission quantum yields were determined using Courmarine 153 in ethanol ( $\Phi_{em} = 0.544$ ) as the reference. Steady-state anisotropy was recorded by means of the  $I_{VV}$ ,  $I_{VH}$ ,  $I_{HV}$  and  $I_{HH}$  measurements (*V*, vertical; *H*, horizontal) of the sample at -45 °C in propylene glycol, after calibration of the polarizers with a Ludox scattering suspension.

**Photoisomerization studies.** Irradiation experiments were performed at room temperature, with a Hamamatsu Hg-Xe lamp LC8 (Lightningcure 200 W) excitation source. The desired wavelengths were selected using appropriate Semrock interferential filters at 335 nm and 485 nm. The incident lamp power was measured by means of an Ophir PD300-UV photodiode, subtracting the residual NIR contribution from the total value. Photoisomerization kinetics were determined using a home-made setup allowing the collection of absorption spectra at high rates under continuous irradiation. A Xenon lamp (75 W) was used as a probe light source placed at 90° with respect to the irradiation beam. Spectra were recorded every 0.2 seconds, with a spectrometer coupled with a CCD (Roper Scientific and Princeton Instruments, respectively).

**Time-resolved fluorescence spectroscopy.** Fluorescence decay curves were obtained by the time-correlated single-photon counting (TCSPC) method. The setup is composed of a titanium sapphire Ti:Sa oscillator (Spectra Physics, Mai Tai) emitting pulses of 100 fs duration for the fundamental laser beam, at 80 MHz frequency. The repetition rate is reduced down to 4 MHz by a pulse picker which implements an acousto-optic modulator. Non-linear SHG crystals generate the desired

wavelength (GWU Lasertechnik, UHG-23-PSK), then the beam is directed to the sample solution after adjusting the excitation power with an intensity attenuator filter wheel. Fluorescence photons are detected at 90° through a polarizer at the magic angle and a monochromator, by means of a micro-channels plate photomultiplier (MCP-PMT R3809U-50, Hamamatsu), connected to a TCSPC module (SPC-630, Becker & Hickl). Fluorescence decays were finally processed with the help of the global non-linear least-squares minimization method including reconvolution analysis (Globals, Laboratory for Fluorescence Dynamics at the University of California, Irvine).

**Quantum chemical geometry optimizations.** The DCM and DCM units in the 2DCM and 3DCM were optimized by density functional theory (DFT) by using Gaussian 16 software package.<sup>[17]</sup> The 2DCMs were optimized by the ONIOM strategy in Gaussian 16, partitioning DCM units into DFT and the dendritic linker part into PM6 semi-empirical functional. PBE0 was used for all DCM and DCM units at 6-311G+(d,p) basis set level. IEFPCM solvent model of THF is used. The optimized geometries were taken into the MD simulation input set-ups.

**Molecular Dynamics (MD) simulations.** The MD simulation inputs were based on the geometries optimized in quantum chemistry level. The electrostatic potentials of 2DCMs were calculated at B3LYP/def2-SVP level of theory by following the restrained electrostatic potential (RESP) procedure. Each configuration of 2DCM was encapsulated with 1500 THF molecules by Packmol program,<sup>[12]</sup> setting the mutual distance tolerance limit at 2 Å, and modelled by AmberTools<sup>[15]</sup> with general AMBER force field (GAFF).<sup>[14]</sup> The MD simulation was carried out using GROMACS software package version 2020. 2<sup>[13]</sup> trajectories of (*EE*) and (*EZ*) configured 2DCM were obtained. All trajectories were written every 5 ps for analysis. The production ensembles use the leapfrog integrator with the step size of 2 fs, a reference temperature at 298 K, a reference pressure at 1 bar.

**Molecular Dynamics (MD) analyses.** The 2DCM trajectories were pretreated by GROMACS toolkit (principal components analysis, PCA). The covariance matrix and following eigenvalues, eigenvectors were generated and calculated by GROMACS toolkit or PyEMMA. The all-trajectory clustering was realized in VMD.<sup>[18]</sup> The MSM was obtained from the MD simulation data by analyzing with program PyEMMA.<sup>[16]</sup> The MD simulation data of 2DCM coordinates was estimated by computing a time-lagged independent component analysis (tICA). The Markov State Model (MSM) was validated by the methods provided from PyEMMA, including the implied timescale test and Chapman-Kolmogorov test (Figure S10). The free energy landscapes (FELs) were drawn in Wolfram Mathematica. After getting the probability density P(x), we apply the equation below to calculate the Gibbs free energy with Boltzmann constant  $k_B$ .

## Acknowledgements

We gratefully thank Arnaud Brosseau for his help in running the time-resolved fluorescence instrument. Funding from the Agence Nationale de la Recherche (ANR-17-CE07-0056-01) is acknowledged.

**Keywords:** Fluorescence • Photoisomerization • Energy transfer • Multichromophoric systems • Molecular Dynamics

- [1] a) D. Chen, Y. Kusakabe, Y. Ren, D. Sun, P. Rajamalli, Y. Wada, K. Suzuki, H. Kaji, E. Zysman-Colman, *J. Org. Chem.* **2021**, *86*, 11531-11544; b) H. Lee, Y. H. Jeong, J. H. Kim, I. Kim, E. Lee, W. D. Jang, *J. Am. Chem. Soc.* **2015**, *137*, 12394-12399; c) O. Kulyk, L. Rocard, L. Maggini, D. Bonifazi, *Chem. Soc. Rev.* **2020**, *49*, 8400-8424; d) R. Dabirian, V. Palermo, A. Liscio, E. Schwartz, M. B. Otten, C. E. Finlayson,



- E. Treossi, R. H. Friend, G. Calestani, K. Mullen, R. J. Nolte, A. E. Rowan, P. Samori, *J. Am. Chem. Soc.* **2009**, *131*, 7055-7063; e) U. Hahn, M. Gorka, F. Vögtle, V. Vicinelli, P. Ceroni, M. Maestri, V. Balzani, *Angew. Chem. Int. Ed.* **2002**, *41*, 3595-3598; f) F. Laquai, Y. S. Park, J. J. Kim, T. Basche, *Macromol. Rapid Commun.* **2009**, *30*, 1203-1231; g) A. Fermi, P. Ceroni, M. Roy, M. Gingras, G. Bergamini, *Chem. Eur. J.* **2014**, *20*, 10661-10668; h) F. Khan, A. Ekbote, S. M. Mobin, R. Misra, *J. Org. Chem.* **2021**, *86*, 1560-1574.
- [2] a) H.-h. Liu, Y. Chen, *J. Mater. Chem.* **2011**, *21*, 1246-1249; b) A. Galanti, V. Diez-Cabanes, J. Santoro, M. Valasek, A. Minoia, M. Mayor, J. Cornil, P. Samori, *J. Am. Chem. Soc.* **2018**, *140*, 16062-16070; c) M. Baroncini, S. d'Agostino, G. Bergamini, P. Ceroni, A. Comotti, P. Sozzani, I. Bassanetti, F. Grepioni, T. M. Hernandez, S. Silvi, M. Venturi, A. Credi, *Nat. Chem.* **2015**, *7*, 634-640.
- [3] a) M. Schulze, M. Utecht, T. Moldt, D. Przyrembel, C. Gahl, M. Weinelt, P. Saalfrank, P. Tegeder, *Phys. Chem. Chem. Phys.* **2015**, *17*, 18079-18086; b) F. Terenziani, G. D'Avino, A. Painelli, *ChemPhysChem* **2007**, *8*, 2433-2444; c) T. Jaunet-Lahary, A. Chantzis, K. J. Chen, A. D. Laurent, D. Jacquemin, *J. Phys. Chem. C* **2014**, *118*, 28831-28841.
- [4] a) J. Bahrenburg, C. M. Sievers, J. B. Schonborn, B. Hartke, F. Renth, F. Temps, C. Nather, F. D. Sonnichsen, *Photochem. Photobiol. Sci.* **2013**, *12*, 511-518; b) S. Sun, S. Liang, W.-C. Xu, G. Xu, S. Wu, *Polym. Chem.* **2019**, *10*, 4389-4401; c) J. E. Koskela, V. Liljestrom, J. Lim, E. E. Simanek, R. H. Ras, A. Priimagi, M. A. Kostianen, *J. Am. Chem. Soc.* **2014**, *136*, 6850-6853.
- [5] a) L. Casimiro, S. Maisonneuve, P. Retailleau, S. Silvi, J. Xie, R. Métivier, *Chem. Eur. J.* **2020**, *26*, 14341-14350; b) Y. Zhou, S. Maisonneuve, L. Casimiro, P. Retailleau, J. Xie, F. Maurel, R. Metivier, *Phys. Chem. Chem. Phys.* **2022**, *24*, 6282-6289.
- [6] a) H. C. Kolb, M. G. Finn, K. B. Sharpless, *Angew. Chem. Int. Ed.* **2001**, *40*, 2004-2021; b) C. W. Tornøe, C. Christensen, M. Meldal, *J. Org. Chem.* **2002**, *67*, 3057-3064.
- [7] D. Astruc, E. Boisselier, C. Ornelas, *Chem. Rev.* **2010**, *110*, 1857-1959.
- [8] M. Murguía, S. Vaillard, R. Grau, *Synthesis* **2004**, *2001*, 1093-1097.
- [9] R. Ribeiro-Viana, M. Sanchez-Navarro, J. Luczkowiak, J. R. Koeppel, R. Delgado, J. Rojo, B. G. Davis, *Nat. Commun.* **2012**, *3*, 1303.
- [10] K. Rurack, M. Spieles, *Anal. Chem.* **2011**, *83*, 1232-1242.
- [11] a) M. N. Berberan-Santos, P. Chopinet, A. Fedorov, L. Jullien, B. Valeur, *Journal of the American Chemical Society* **1999**, *121*, 2526-2533; b) K. Seintis, D. Agathangelou, D. Cvejn, N. Almonasy, F. Bures, V. Giannetas, M. Fakis, *Phys. Chem. Chem. Phys.* **2017**, *19*, 16485-16497; c) Y. Teijeiro-Gonzalez, A. Crnjar, A. J. Beavil, R. L. Beavil, J. Nedbal, A. Le Marois, C. Molteni, K. Suhling, *Biophys J* **2021**, *120*, 254-269.
- [12] L. Martinez, R. Andrade, E. G. Birgin, J. M. Martinez, *J. Comput. Chem.* **2009**, *30*, 2157-2164.
- [13] a) H. J. C. Berendsen, D. van der Spoel, R. van Drunen, *Comput. Phys. Commun.* **1995**, *91*, 43-56; b) E. Lindahl, B. Hess, D. van der Spoel, *J. Mol. Model.* **2001**, *7*, 306-317; c) D. Van Der Spoel, E. Lindahl, B. Hess, G. Groenhof, A. E. Mark, H. J. Berendsen, *J. Comput. Chem.* **2005**, *26*, 1701-1718; d) M. J. Abraham, T. Murtola, R. Schulz, S. Páll, J. C. Smith, B. Hess, E. Lindahl, *SoftwareX* **2015**, *1-2*, 19-25.
- [14] a) J. Wang, R. M. Wolf, J. W. Caldwell, P. A. Kollman, D. A. Case, *J. Comput. Chem.* **2004**, *25*, 1157-1174; b) J. Wang, W. Wang, P. A. Kollman, D. A. Case, *J. Mol. Graph. Model.* **2006**, *25*, 247-260.
- [15] D. A. Case, H. M. Aktulga, K. Belfon, I. Y. Ben-Shalom, S. R. Brozell, D. S. Cerutti, T. E. Cheatham, G. A. C. III, V. W. D. Cruzeiro, T. A. Darden, R. E. Duke, G. Giambasu, M. K. Gilson, H. Gohlke, A. W. Goetz, R. Harris, S. Izadi, S. A. Izmailov, C. Jin, K. Kasavajhala, M. C. Kaymak, E. King, A. Kovalenko, T. Kurtzman, T. S. Lee, S. LeGrand, P. Li, C. Lin, J. Liu, T. Luchko, R. Luo, M. Machado, V. Man, M. Manathunga, K. M. Merz, Y. Miao, O. Mikhailovskii, G. Monard, H. Nguyen, K. A. O'Hearn, A. Onufriev, F. Pan, S. Pantano, R. Qi, A. Rahnamoun, D. R. Roe, A. Roitberg, C. Sagui, S. Schott-Verdugo, J. Shen, C. L. Simmerling, N. R. Skrynnikov, J. Smith, J. Swails, R. C. Walker, J. Wang, H. Wei, R. M. Wolf, X. Wu, Y. Xue, D. M. York, S. Zhao, P. A. Kollman, *Amber 2021*, University of California, San Francisco, **2021**.
- [16] M. K. Scherer, B. Trendelkamp-Schroer, F. Paul, G. Perez-Hernandez, M. Hoffmann, N. Plattner, C. Wehmeyer, J. H. Prinz, F. Noe, *J. Chem. Theory Comput.* **2015**, *11*, 5525-5542.
- [17] M. J. Frisch, G. W. Trucks, H. B. Schlegel, G. E. Scuseria, M. A. Robb, J. R. Cheeseman, G. Scalmani, V. Barone, G. A. Petersson, H. Nakatsuji, X. Li, M. Caricato, A. V. Marenich, J. Bloino, B. G. Janesko, R. Gomperts, B. Mennucci, H. P. Hratchian, J. V. Ortiz, A. F. Izmaylov, J. L. Sonnenberg, D. Williams-Young, F. Ding, F. Lipparini, F. Egidi, J. Goings, B. Peng, A. Petrone, T. Henderson, D. Ranasinghe, V. G. Zakrzewski, J. Gao, N. Rega, G. Zheng, W. Liang, M. Hada, M. Ehara, K. Toyota, R. Fukuda, J. Hasegawa, M. Ishida, T. Nakajima, Y. Honda, O. Kitao, H. Nakai, T. Vreven, K. Throssell, J. A. M. Jr., J. E. Peralta, F. Ogliaro, M. J. Bearpark, J. J. Heyd, E. N. Brothers, K. N. Kudin, V. N. Staroverov, T. A. Keith, R. Kobayashi, J. Normand, K. Raghavachari, A. P. Rendell, J. C. Burant, S. S. Iyengar, J. Tomasi, M. Cossi, J. M. Millam, M. Klene, C. Adamo, R. Cammi, J. W. Ochterski, R. L. Martin, K. Morokuma, O. Farkas, J. B. Foresman, D. J. Fox, *Gaussian 16, revision B.01*, Gaussian, Inc., Wallingford CT, **2016**.
- [18] W. Humphrey, A. Dalke, K. Schulten, *J. Mol. Graph.* **1996**, *14*, 33-38.

## Supporting Information

---

# Competitive photoisomerization and energy transfer processes in fluorescent multichromophoric systems

Yang Zhou,<sup>[a]</sup> Stéphane Maisonneuve,<sup>[a]</sup> François Maurel,<sup>\*[b]</sup> Juan Xie,<sup>\*[a]</sup> Rémi Métivier<sup>\*[a]</sup>

[a] ENS Paris-Saclay, Université Paris-Saclay, CNRS, PPSM, F-91190 Gif-sur-Yvette, France

[b] Université Paris Cité, CNRS, ITODYS, F-75006 Paris, France

\* Corresponding authors. Email: maurel@univ-paris-diderot.fr, joanne.xie@ens-paris-saclay.fr, remi.metivier@ens-paris-saclay.fr

<b>1. GENERAL EXPERIMENTAL</b> .....	<b>2</b>
<b>2. SYNTHETIC PROCEDURES</b> .....	<b>3</b>
SYNTHESIS OF COMPOUND 2 .....	3
SYNTHESIS OF COMPOUND ( <i>EE</i> )-2DCM .....	3
SYNTHESIS OF COMPOUND 4 .....	4
SYNTHESIS OF COMPOUND ( <i>EEE</i> )-3DCM .....	5
<b>3. MOLECULAR DYNAMICS (MD) SIMULATIONS</b> .....	<b>6</b>
OPTIMIZED GEOMETRIES OF ( <i>EZ</i> )-2DCM AND ( <i>EE</i> )-2DCM .....	6
SOLVENT CUBIC BOX WITH ( <i>EZ</i> )-2DCM .....	7
MD DATA ANALYSIS FOR ( <i>EZ</i> )-2DCM AND ( <i>EE</i> )-2DCM.....	8
MD TRAJECTORIES AND RELATED DATA ANALYSES .....	10
FREE-ENERGY LANDSCAPE (FEL) BASED ON PRINCIPAL COMPONENTS ANALYSIS (PCA).....	12
IMPLIED TIMESCALES FOR THE MARKOV MODEL OF ( <i>EZ</i> )-2DCM AND (B) ( <i>EE</i> )-2DCM .....	14
CHAPMAN-KOLMOGOROV TEST CURVES OF ( <i>EZ</i> )-2DCM AND (B) ( <i>EE</i> )-2DCM .....	14
<b>4. NMR SPECTRA</b> .....	<b>15</b>
NMR SPECTRA OF COMPOUND 2 IN CDCl <sub>3</sub> .....	15
NMR SPECTRA OF COMPOUND ( <i>EE</i> )-2DCM IN CDCl <sub>3</sub> .....	16
NMR SPECTRA OF COMPOUND 4 IN CDCl <sub>3</sub> .....	17
NMR SPECTRA OF COMPOUND ( <i>EEE</i> )-3DCM IN CDCl <sub>3</sub> .....	18

## 1. General experimental

**Commercially available solvents and reagents** were used without further purification. The reactions carried out under anhydrous conditions were performed under argon. DMF and THF were previously dried through alumina or molecular sieves cartridge using a solvent purification system from MBRAUN SPS-800. Reactions were monitored by TLC on Silica Gel 60F-254 plates with detection by UV (254 nm or 365 nm) or by spraying with 10% H<sub>2</sub>SO<sub>4</sub> in EtOH and heating about 30 s at 400-600 °C.

**Column chromatography purifications** were performed on silica gel or with a CombiFlash® Rf+ purification system using RediSep® RF or RF Gold normal phase silica columns with UV-Vis detection.

**Microwave reactions** were realized in a reactor of 30 mL sealed with a septum using a Monowave 300 microwave synthesis reactor from Anton Paar GmbH.

**<sup>1</sup>H and <sup>13</sup>C-NMR spectra** were recorded on a JEOL ECS-400 spectrometer (399.78 MHz for <sup>1</sup>H, and 100.53 MHz for <sup>13</sup>C) equipped with an auto-tunable broad band probe. Chemical shifts (δ) are reported in part per million (ppm) relative to the residual solvent pic or Si(CH<sub>3</sub>)<sub>4</sub>.<sup>1,2</sup> Coupling constants are reported in Hertz (Hz), and the attribution of the signals is given with the following abbreviations: s (singlet), d (doublet), t (triplet), q (quartet), m (multiplet), br (broad).

**HRMS** (ESI) spectrum was recorded on a Q-TOF mass spectrometer by the "Fédération de Recherche" ICOA/CBM (FR2708) platform. The adducts are described as in the specific literature.<sup>3</sup>

---

<sup>1</sup> H. E. Gottlieb, V. Kotlyar, A. Nudelman ; *J. Org. Chem.* **1997**, *62*, 7512-7515.

<sup>2</sup> G. R. Fulmer, A. J. M. Miller, N. H. Sherden, H. E. Gottlieb, A. Nudelman, B. M. Stoltz, J. E. Bercaw, K. I. Goldberg ; *Organometallics* **2010**, *29*, 2176-2179.

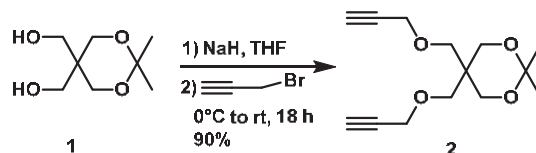
<sup>3</sup> H. Tong, D. Bell, K. Tabei, M.M. Siegel ; *J. Am. Soc. Mass Spectrom.* **1999**, *10*, 1174-1187.



## 2. Synthetic procedures

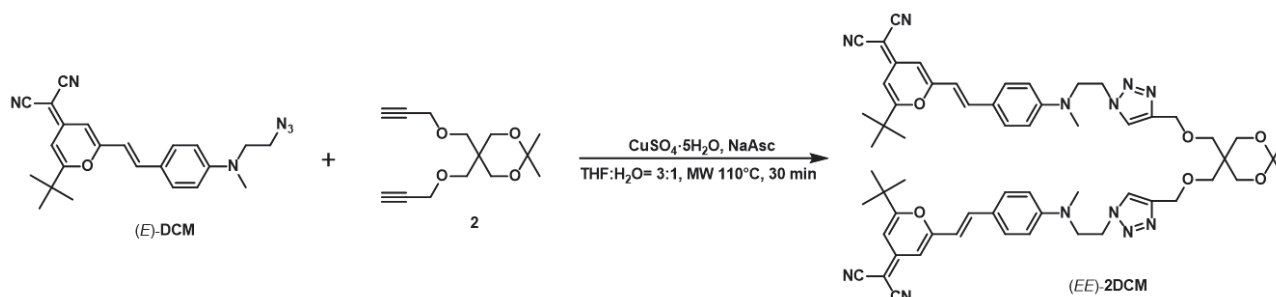
### Synthesis of compound 2

#### 2,2-Dimethyl-5,5-bis((prop-2-yn-1-yloxy)methyl)-1,3-dioxane (2)



To a solution of compound **1**<sup>4,5</sup> (114 mg, 0.65 mmol) in THF (10 mL), sodium hydride (60% dispersion in mineral oil, 2.4 equiv.) was added in portions under argon at 0°C. After addition, the reaction mixture was stirred for 30 min, propargyl bromide (80% in toluene, 6 equiv.) was added dropwise to the reaction mixture which was then stirred at room temperature for 18 h. Saturated NH<sub>4</sub>Cl aq. was added to quench the reaction and the reaction mixture was extracted by ethyl acetate (20 mL) for 3 times. The organic layer layers were combined and washed with brine, dried over anhydrous MgSO<sub>4</sub>, filtered and concentrated. The crude product was purified by CombiFlash® chromatography with an eluent of petroleum ether and ethyl acetate (8:1) to afford **2** as a transparent liquid (147 mg, 90%). <sup>1</sup>H NMR (400 MHz, CDCl<sub>3</sub>): δ (ppm) = 4.14 (d, *J* = 2.3 Hz, 4H, CH<sub>2</sub>), 3.75 (s, 4H, CH<sub>2</sub>), 3.53 (s, 4H, CH<sub>2</sub>), 2.43 (t, *J* = 2.5 Hz, 2H, C≡CH), 1.41 (s, 6H, CH<sub>3</sub>). <sup>13</sup>C NMR (100 MHz, CDCl<sub>3</sub>): δ (ppm) = 98.27, 79.85 (C<sub>q</sub>); 74.46 (C≡CH), 69.29, 62.66, 58.77, 38.87 (CH<sub>2</sub>); 23.83 (CH<sub>3</sub>). *m/z* [M+Na]<sup>+</sup> calcd. for [C<sub>14</sub>H<sub>20</sub>NaO<sub>4</sub>]<sup>+</sup>: 275.1254; found 275.1254.

### Synthesis of compound (EE) 2DCM



Compound **2** (33 mg, 0.13 mmol), (*E*)-DCM<sup>6</sup> (2.2 equiv.), CuSO<sub>4</sub>·5H<sub>2</sub>O (0.4 equiv.) and sodium ascorbate (0.8 equiv.) were added together in a mixed solvent THF/H<sub>2</sub>O (4 mL, 3:1, v/v) to a microwave reactor tube (glass, 30 mL). The reaction mixture was kept irradiated with microwave, holding at 110°C for 30 minutes. After the reaction mixture returned to room temperature, it was poured into 0.1 M EDTA aqueous solution. The mixture was extracted with ethyl acetate (30 mL) for 3 times. The organic layers were combined and washed with brine, dried over anhydrous MgSO<sub>4</sub> and filtered. After evaporation of the solvent, the crude product was purified by

<sup>4</sup> C. M. Murguía, S. E. Vaillard, R. J. Grau, *Synthesis* **2001**, 7, 1093-1097.

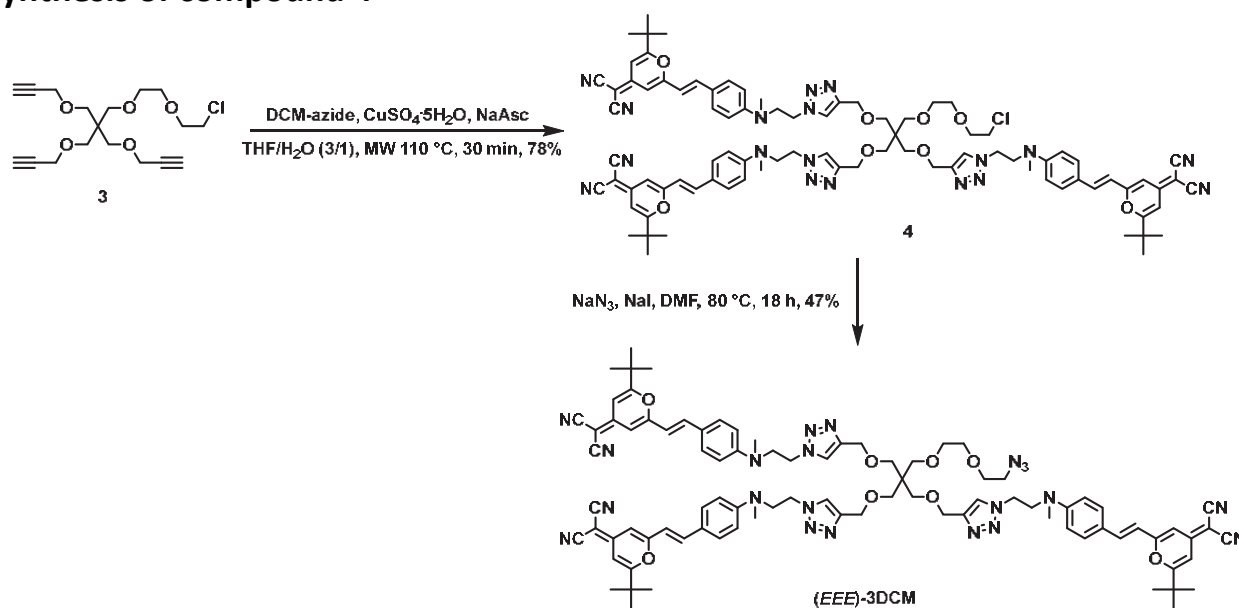
<sup>5</sup> V. Percec, P. Leowanawat, H.-J. Sun, O. Kulikov, C. D. Nusbaum, T. M. Tran, A. Bertin, D. A. Wilson, M. Peterca, S. Zhang, N. P. Kamat, K. Vargo, D. Moock, E. D. Johnston, D. A. Hammer, D. J. Pochan, Y. Chen, Y. M. Chabre, T. C. Shiao, M. Bergeron-Brlek, S. André, R. Roy, H.-J. Gabius, P. A. Heiney, *J. Am. Chem. Soc.* **2013**, 135, 9055-9077.

<sup>6</sup> K. Ouhenia-Ouadahi, R. Métivier, S. Maisonneuve, A. Jacquart, J. Xie, A. Léaustic, P. Yu, K. Nakatani, *Photochem. Photobiol. Sci.*, **2012**, 11, 1705-1714.

CombiFlash® chromatography with dichloromethane and ethanol as eluent (gradient, 100:0 to 90:10, v/v) to afford (*EE*)-**2DCM** as red powder (113 mg, 82%).

<sup>1</sup>H NMR (400 MHz, CDCl<sub>3</sub>): δ (ppm) = 7.50 (s, 2H, triazole-*H*), 7.43-7.41 (m, 4H), 7.33 (s, 1H), 7.29 (s, 1H), 6.63 (d, *J* = 8.8 Hz, 4H, CH<sub>Ar</sub>), 6.62-6.60 (m, 2H, CH=), 6.53-6.49 (m, 4H, CH=), 4.60 (t, *J* = 6.2 Hz, 4H, CH<sub>2</sub>), 4.56 (s, 4H, CH<sub>2</sub>), 3.94 (t, *J* = 6.0 Hz, 4H, CH<sub>2</sub>), 3.66 (s, 4H, CH<sub>2</sub>), 3.43 (s, 4H, CH<sub>2</sub>), 2.88 (s, 6H, NCH<sub>3</sub>), 1.37 (s, 18H, *t*-Bu), 1.36 (s, 6H, CH<sub>3</sub>). <sup>13</sup>C NMR (100 MHz, CDCl<sub>3</sub>): δ (ppm) = 172.08, 160.02, 156.91, 149.89, 145.52 (C<sub>q</sub>); 137.98, 129.97, 123.55 (CH<sub>Ar</sub>); 115.82, 115.71 (C<sub>q</sub>); 114.02 (CH<sub>Ar</sub>); 112.10, 105.95, 102.58 (CH=); 98.37 (C<sub>q</sub>); 69.65, 64.96, 62.91 (CH<sub>2</sub>); 58.32 (C<sub>q</sub>); 52.56, 47.69 (CH<sub>2</sub>); 38.89 (CH<sub>3</sub>), 36.83 (C<sub>q</sub>, *t*-Bu); 28.28, 23.88 (CH<sub>3</sub>). HRMS (ESI-HRMS): *m/z* [M+H]<sup>+</sup> calcd. for [C<sub>60</sub>H<sub>69</sub>N<sub>12</sub>O<sub>6</sub>]<sup>+</sup>: 1053.5458; found 1053.5454.

## Synthesis of compound 4



Compound **3**<sup>7</sup> (50 mg, 0.14 mmol), (*E*)-**DCM** (3.3 equiv.), CuSO<sub>4</sub>·5H<sub>2</sub>O (0.4 equiv.) and sodium ascorbate (0.8 equiv.) were added together in a mixed solvent THF/H<sub>2</sub>O (4 mL, 3:1, v/v) to a microwave reactor tube. The reaction mixture was kept irradiated with microwave, holding at 110 °C for 30 minutes. After the reaction mixture returned to room temperature, it was poured into 0.1 M EDTA solution. The mixture was extracted with ethyl acetate (30 mL) for 3 times. The organic layers were combined and washed with brine, dried over anhydrous MgSO<sub>4</sub> and filtered,. After evaporation of the solvent, the crude product was purified by CombiFlash® chromatography with dichloromethane and ethanol as eluent (gradient, 100:0 to 90:10, v/v) to afford compound **4** as a red powder (170 mg, 78%).

<sup>1</sup>H NMR (400 MHz, CDCl<sub>3</sub>): δ (ppm) = 7.53 (s, 3H, triazole-*H*), 7.43-7.41 (m, 6H), 7.32-7.27 (m, 3H), 6.63 (d, *J* = 8.8 Hz, 6H, CH=), 6.59-6.58 (m, 3H, CH=), 6.54-6.50 (m, 6H, CH=), 4.60 (t, *J* = 6.2 Hz, 6H, CH<sub>2</sub>), 4.52 (s, 6H, CH<sub>2</sub>), 3.93 (t, *J* = 5.6 Hz, 6H, CH<sub>2</sub>), 3.70 (t, *J* = 6.0 Hz, 2H, CH<sub>2</sub>), 3.58 (t, *J* = 5.6 Hz, 4H, CH<sub>2</sub>), 3.49 (m, 2H, CH<sub>2</sub>), 3.41-3.38 (m, 8H, CH<sub>2</sub>), 2.87 (s, 9H, NCH<sub>3</sub>), 1.37 (s, 27H, *t*-Bu). <sup>13</sup>C NMR (100 MHz, CDCl<sub>3</sub>): δ (ppm) = 172.11, 160.05, 156.92, 149.92, 145.66 (C<sub>q</sub>); 137.99, 129.98, 123.64, 123.53 (CH<sub>Ar</sub>); 115.87, 115.72 (C<sub>q</sub>); 113.95, 112.12, 105.93, 102.57 (CH=); 71.36, 71.05, 70.51, 69.29, 64.96 (CH<sub>2</sub>); 58.22 (C<sub>q</sub>); 52.71, 47.56 (CH<sub>2</sub>); 45.37 (C<sub>q</sub>), 43.25 (CH<sub>2</sub>), 38.82 (NMe), 36.79 (C<sub>q</sub>),

<sup>7</sup> R. Ribeiro-Viana, M. Sánchez-Navarro, J. Luczkowiak, J. R. Koeppe, R. Delgado, J. Rojo, B. G. Davis, *Nat. Commun.*, **2012**, 3, 1-9.

28.28 (CH<sub>3</sub>, *t*-Bu). HRMS (ESI-HRMS): *m/z* [M+H]<sup>+</sup> calcd. for [C<sub>87</sub>H<sub>98</sub>N<sub>18</sub>O<sub>8</sub>Cl]<sup>+</sup>: 1557.7498, 1558.7532; found 1557.7498, 1558.7529.

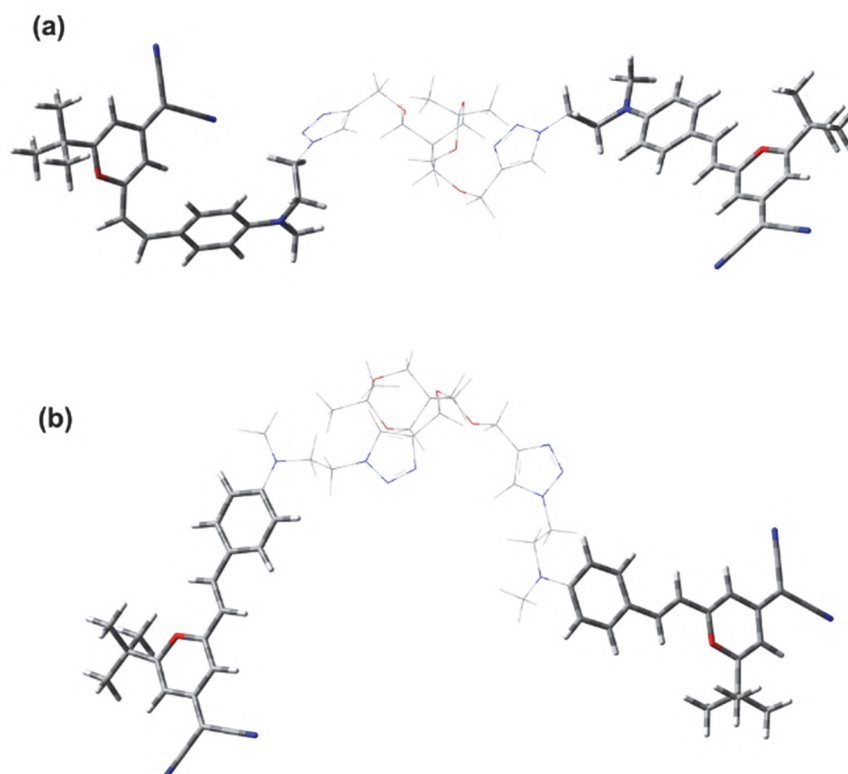
### Synthesis of compound (*EEE*) **3DCM**

To a solution of compound **4** (136 mg, 87 μmol) in DMF (5 mL), NaI (0.1 equiv.) and NaN<sub>3</sub> (8 equiv.) were added. The reaction mixture was heated up to 80°C and stirred for 18 hours. After completion of the reaction, the mixture was concentrated and the residue was diluted in EtOAc (20 mL), washed successively with water and brine, dried over MgSO<sub>4</sub>, filtered, concentrated and purified by CombiFlash® chromatography with dichloromethane and ethanol (gradient, 100:0 to 90:10, v/v) to yield (*EEE*)-**3DCM** as a red solid (64 mg, 47%).

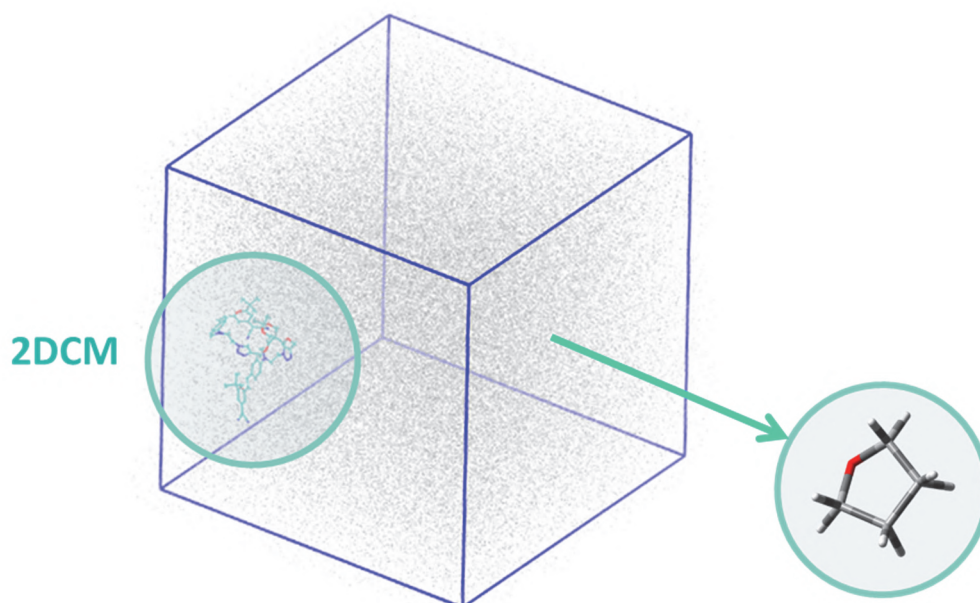
<sup>1</sup>H NMR (400 MHz, CDCl<sub>3</sub>): δ (ppm) = 7.54 (s, 3H, triazole-*H*), 7.41 (d, *J* = 8.7 Hz, 6H, CH<sub>Ar</sub>), 7.32-7.27 (m, 3H), 6.64 (d, *J* = 9.2 Hz, 6H, CH=), 6.58-6.57 (m, 3H, CH=), 6.53-6.49 (m, 6H, CH=), 4.60 (t, *J* = 6.0 Hz, 6H, CH<sub>2</sub>), 4.52 (s, 6H, CH<sub>2</sub>), 3.93 (t, *J* = 6.0 Hz, 6H, CH<sub>2</sub>), 3.64-3.61 (m, 2H, CH<sub>2</sub>), 3.58-3.56 (m, 2H, CH<sub>2</sub>), 3.52-3.49 (m, 2H, CH<sub>2</sub>), 3.42-3.39 (m, 8H, CH<sub>2</sub>), 3.33 (t, *J* = 5.2 Hz, 2H, CH<sub>2</sub>), 2.87 (s, 9H, NCH<sub>3</sub>), 1.37 (s, 27H, *t*-Bu). <sup>13</sup>C NMR (100 MHz, CDCl<sub>3</sub>): δ = 172.07, 160.04, 156.88, 149.90, 145.61 (C<sub>q</sub>); 138.01, 129.95, 123.60, 123.42 (CH=); 115.84, 115.72 (C<sub>q</sub>); 113.88, 112.07, 105.85, 102.48 (CH=); 71.05, 70.55, 70.08, 69.91, 69.25, 64.91, 58.02 (C<sub>q</sub>); 52.65, 50.82, 47.51, 45.33 (C<sub>q</sub>); 38.76 (NMe), 36.73 (C<sub>q</sub>), 29.79 (CH<sub>2</sub>), 28.22 (CH<sub>3</sub>, *t*-Bu) ppm. HRMS (ESI-HRMS): *m/z* [M+H]<sup>+</sup> calcd. for [C<sub>87</sub>H<sub>98</sub>N<sub>21</sub>O<sub>8</sub>]<sup>+</sup>: 1564.7902, 1565.7936; found 1564.7915.

### 3. Molecular Dynamics (MD) Simulations

#### Optimized geometries of (*EZ*)-2DCM and (*EE*)-2DCM



**Figure S1.** ONIOM optimized initial geometries of (a) (*EZ*)-2DCM and (b) (*EE*)-2DCM at the {PBE0/6-311G+(d,p):PM6} IEFPCM:THF level. The molecular fragments represented in the tube mode (resp. wire mode) were optimized at the DFT level (resp. PM6 level).

**Solvent cubic box with (EZ)-2DCM**

**Figure S2.** Packmol encapsulated (EZ)-2DCM with 1500 THF molecules in a cubic box.

Explicit THF molecules were encapsulated with unknown density together with the 2DCMs. The cubic box after the energy minimization was still not similar to the volume observed in the equilibrium state. The cubic box starts simultaneously to compress with the NPT ensemble to the THF density with the constant  $\tau_p = 0.2$  ps and 1 bar reference pressure. Finally, we obtain a cubic box with proper density around  $0.889 \text{ kg L}^{-1}$  at 298K.

To describe the electrostatic interactions, periodic boundary conditions (PBC) were imposed, a Verlet cut-off of  $12 \text{ \AA}$  was considered and the Particle Mesh Ewald (PME) coulomb type was used. For each box, NPT ensembles were run for more than 5 ns with the time step of 2 fs. The production runs are taken after the NPT equilibriums during a total time of 200 ns.

## MD data analysis for (EZ)-2DCM and (EE)-2DCM

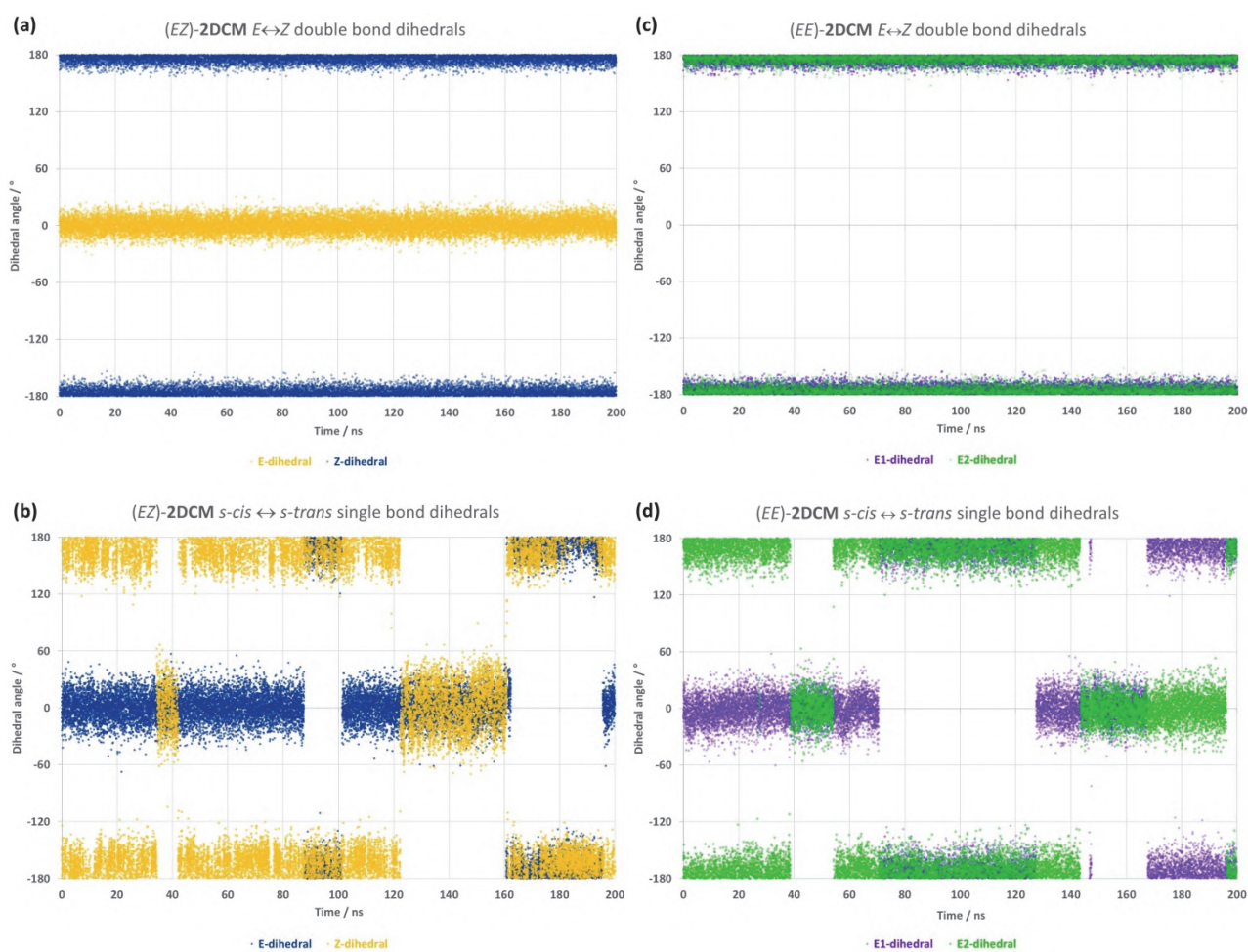


**Figure S3.** (a, c) MD trajectories of dihedral angles of central C=C double bond controlling the  $E \leftrightarrow Z$  photoisomerization of each DCM unit and (b, d) MD trajectories of dihedral angles of the C-C single bond controlling the  $s\text{-cis} \leftrightarrow s\text{-trans}$  interconversion of each DCM unit, for (a, b) (EZ)-2DCM and (c, d) (EE)-2DCM.





**Figure S4.** (a) 200 ns (EZ)-2DCM  $R_{DA}$  histogram and fitted norm density. (b) 200 ns (EZ)-2DCM  $\kappa^2$  histogram and fitted norm density. (c) 200 ns (EE)-2DCM  $R_{DA}$  histogram and fitted norm density. (d) 200 ns (EE)-2DCM  $\kappa^2$  histogram and fitted norm density.

## MD trajectories and related data analyses

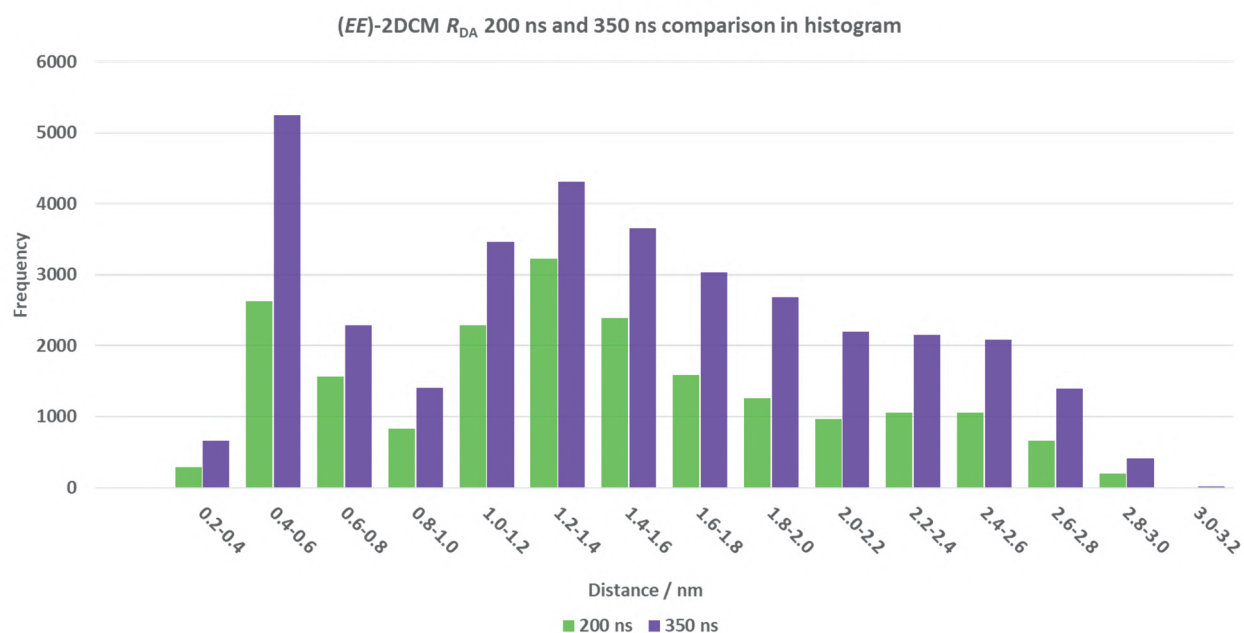
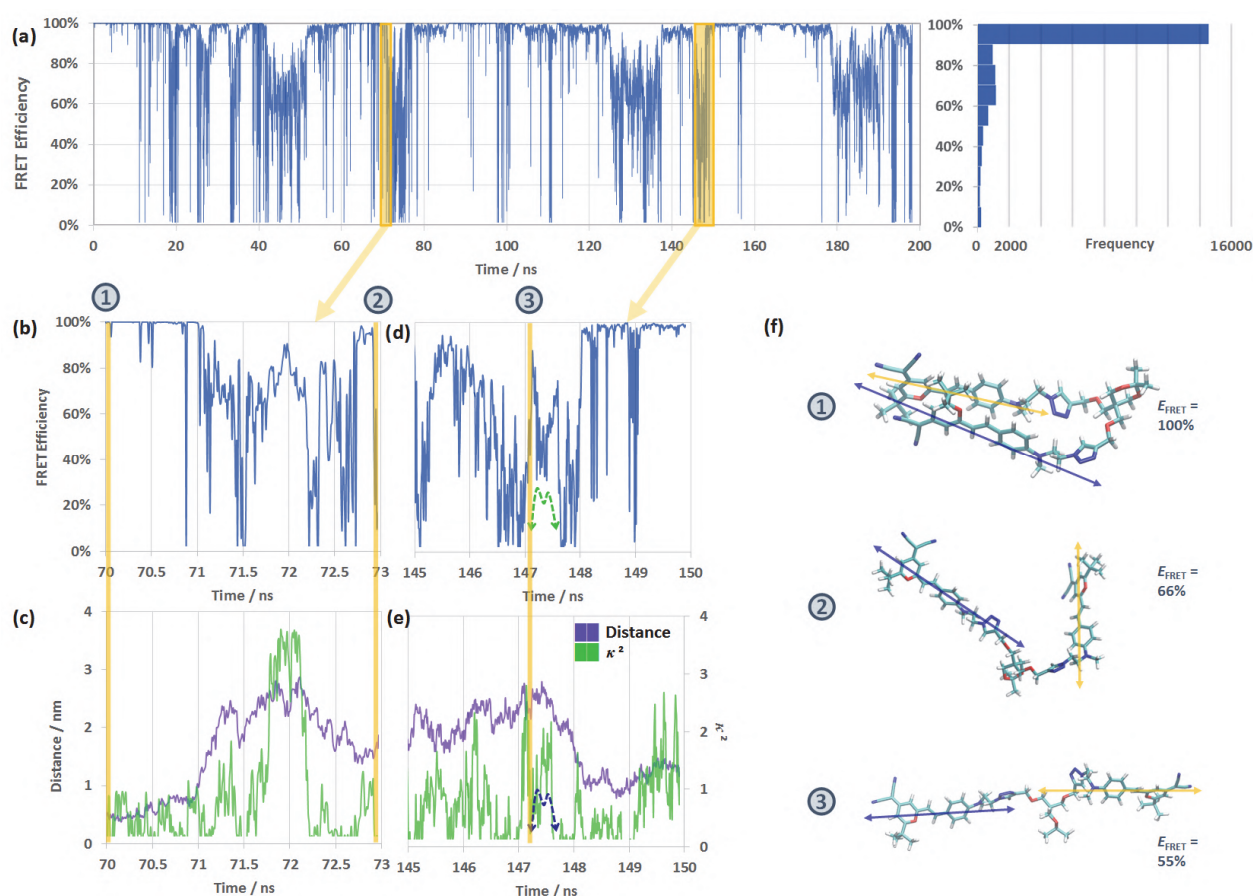


**Figure S5.** Comparison of  $R_{DA}$  histograms of (EE)-2DCM recorded from 200 ns and 350 ns trajectories, respectively.

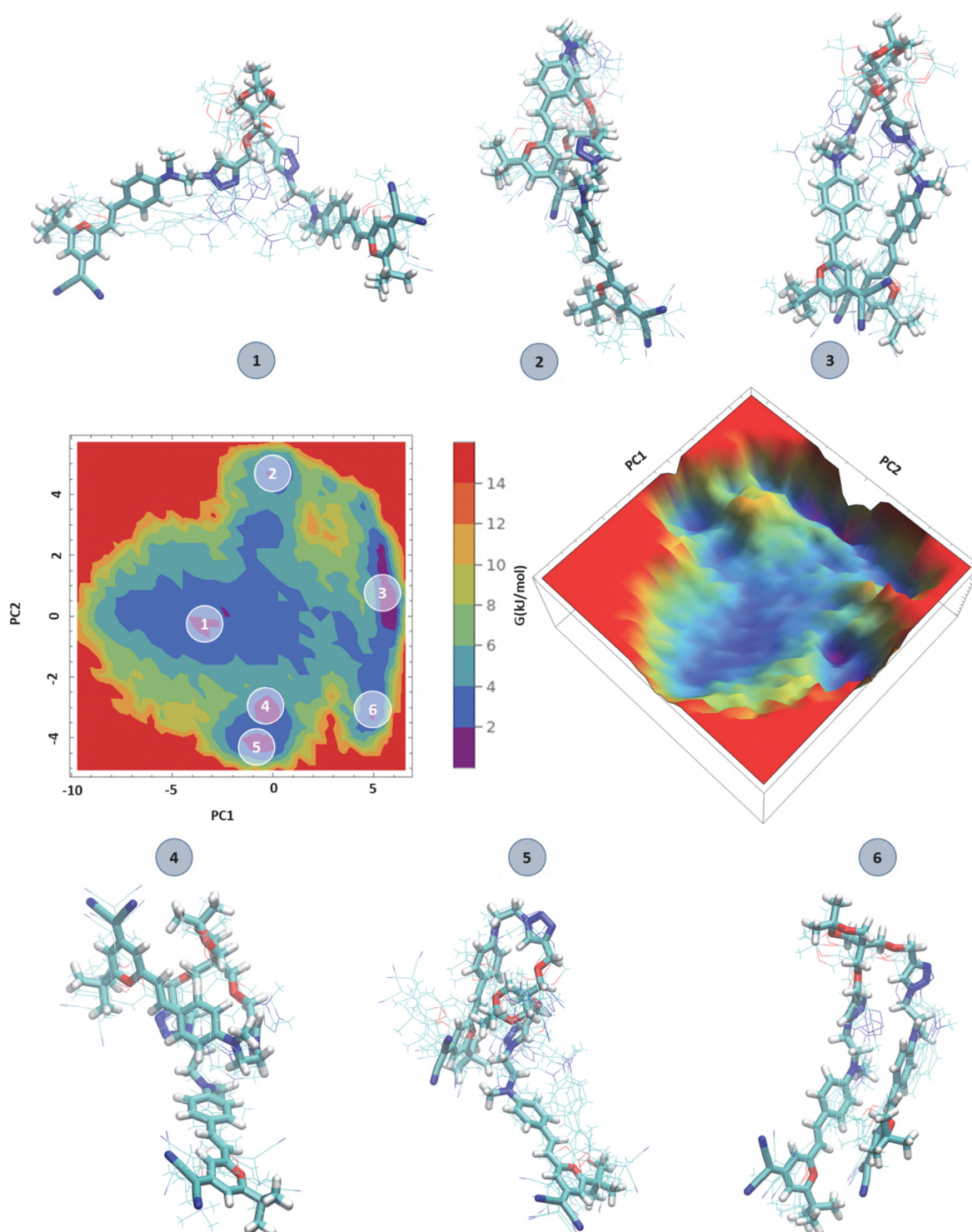
**Table S1.** Time-duration of MD simulations and corresponding average parameters.

Configuration	Time duration	Avg. $R_{DA}$	Avg. $\kappa^2$	Avg. $E_{FRET}$
(EE)-2DCM	200 ns	1.407 nm	1.043	87.8%
(EE)-2DCM	350 ns	1.446 nm	1.019	85.7%
(EZ)-2DCM	100 ns	1.476 nm	0.740	61.4%
(EZ)-2DCM	200 ns	1.446 nm	0.814	63.4%
(EZ)-2DCM	300 ns	1.451 nm	0.820	64.0%
(EZ)-2DCM	450 ns	1.404 nm	0.761	65.6%
(EZ)-2DCM	600 ns	1.448 nm	0.795	64.6%
(EZ)-2DCM	750 ns	1.437 nm	0.786	64.7%
(EZ)-2DCM	900 ns	1.392 nm	0.775	66.5%





**Figure S6.** (a) MD trajectory of (EE)-2DCM homo-FRET efficiency  $E_{\text{FRET}}(t)$  during 200 ns, and corresponding histogram of  $E_{\text{FRET}}$  distribution. (b, d) Enlarged areas of the  $E_{\text{FRET}}(t)$  trajectory in the time intervals 70-73 ns and 145-150 ns. (c, e) Enlarged areas of the  $R_{\text{DA}}(t)$  (violet) and  $\kappa^2(t)$  (green) trajectories corresponding to (b, d), respectively. (f) Three selected typical geometries of (EE)-2DCM, indicated by yellow vertical bars in (b-e), with violet and yellow arrows representing the transition dipole moments of the donor (E)-DCM and the acceptor (E)-DCM units, respectively. Their corresponding FRET efficiencies are marked in the insets.

**Free-energy landscape (FEL) based on principal components analysis (PCA)**

**Figure S7.** Free-energy landscape (FEL) based on principal components analysis (PCA) of a 200 ns trajectory of *(E,E)*-2DCM. The represented geometries correspond to each energy valley.

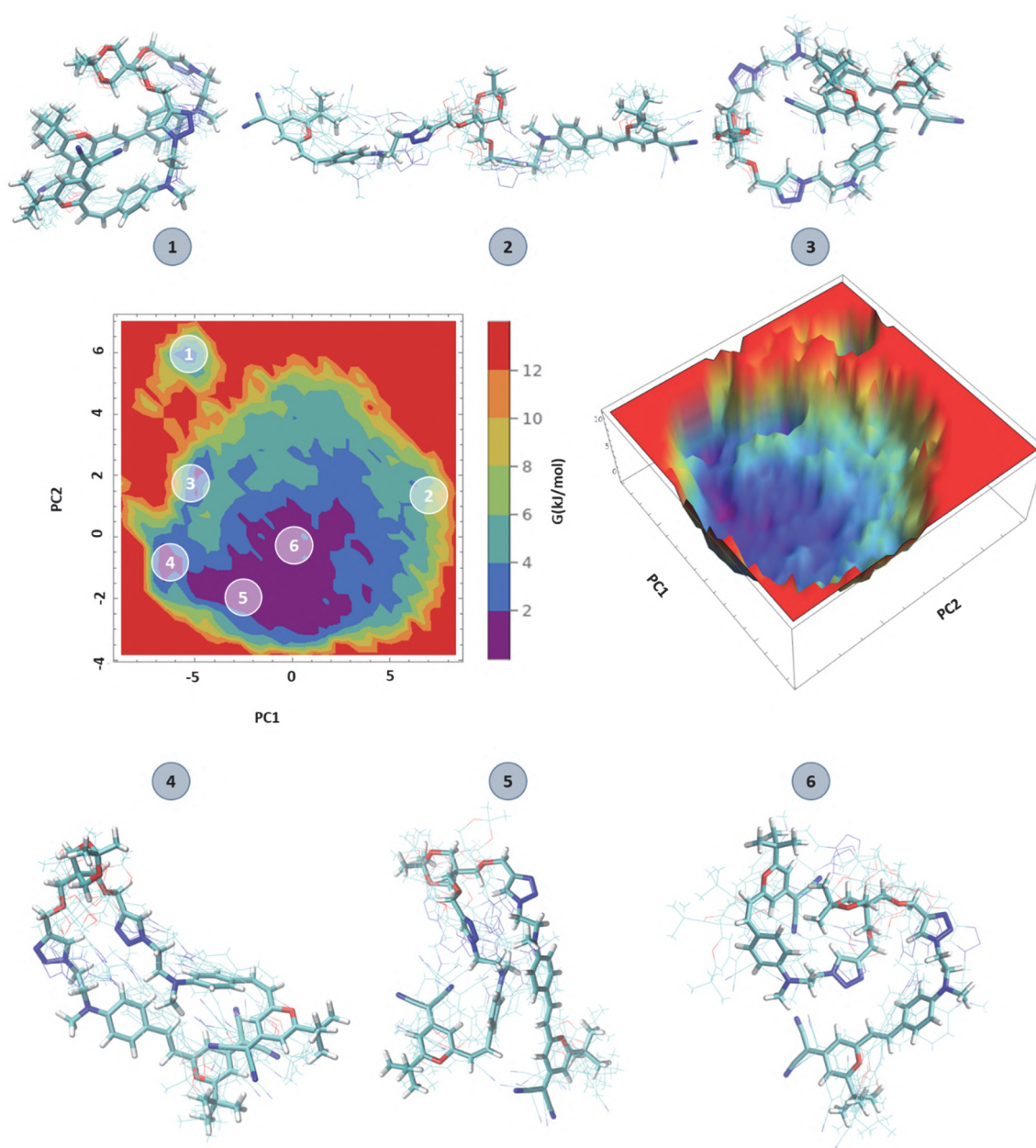


**Figure S8.** Free-energy landscape (FEL) based on principal components analysis (PCA) of a 200 ns trajectory of (EZ)-2DCM. The represented geometries correspond to each energy valley.

## Implied timescales for the Markov model of (a) (EZ)-2DCM and (b) (EE)-2DCM

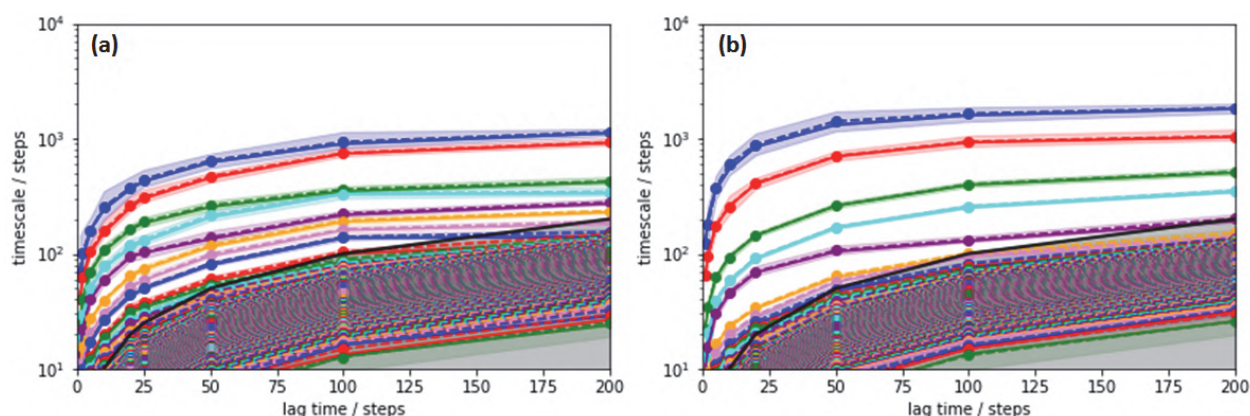


**Figure S9.** Implied timescales for the Markov model of (a) (EZ)-2DCM and (b) (EE)-2DCM. The error bars are 95% confidence intervals estimated using the reversible transition matrix sampling algorithm. The unit of steps has the reduction formula: 100 steps = 1 ns.

## Chapman-Kolmogorov test curves of (a) (EZ)-2DCM and (b) (EE)-2DCM

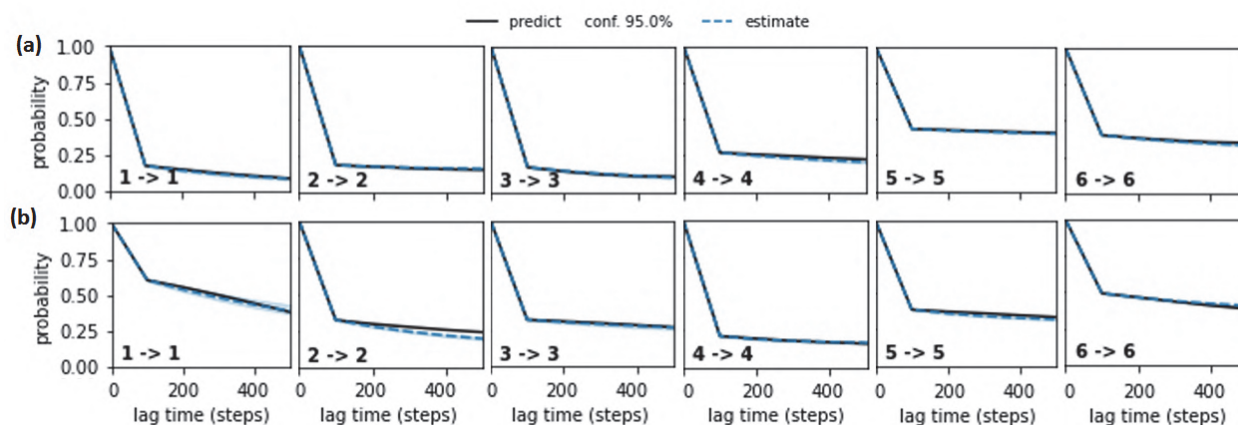


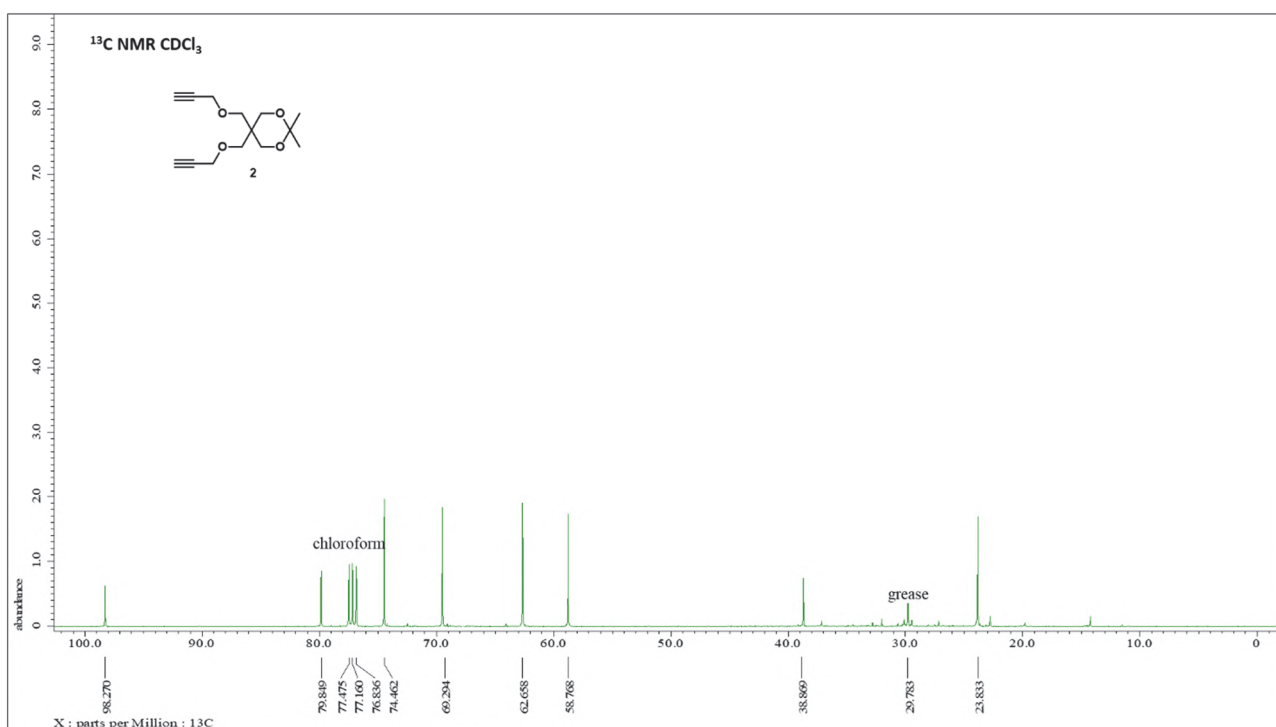
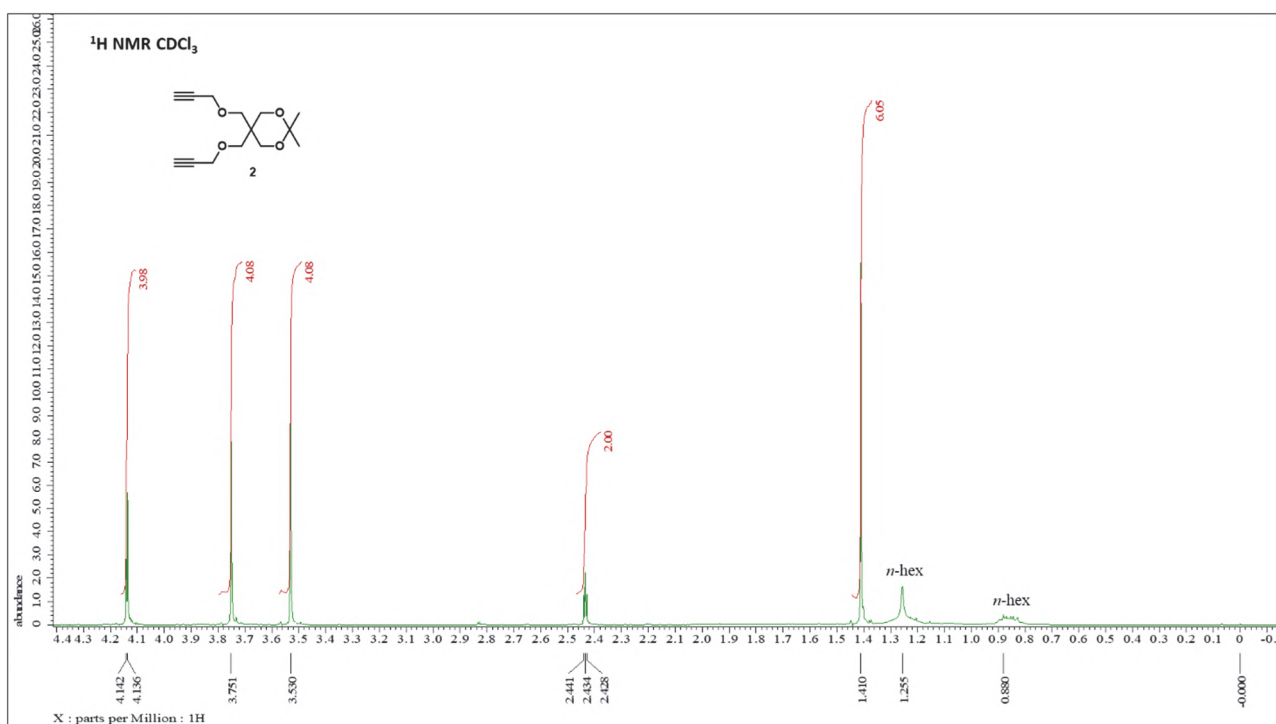
**Figure S10.** The Chapman-Kolmogorov test curves obtained by 6 macrostates of (a) (EZ)-2DCM and (b) (EE)-2DCM. Where “ $i - i$ ” represents the coincidence degree between the predicted probability of the MSM and the simulation probability in  $i^{th}$  macrostate. The unit of steps has the reduction formula: 100 steps = 1 ns.



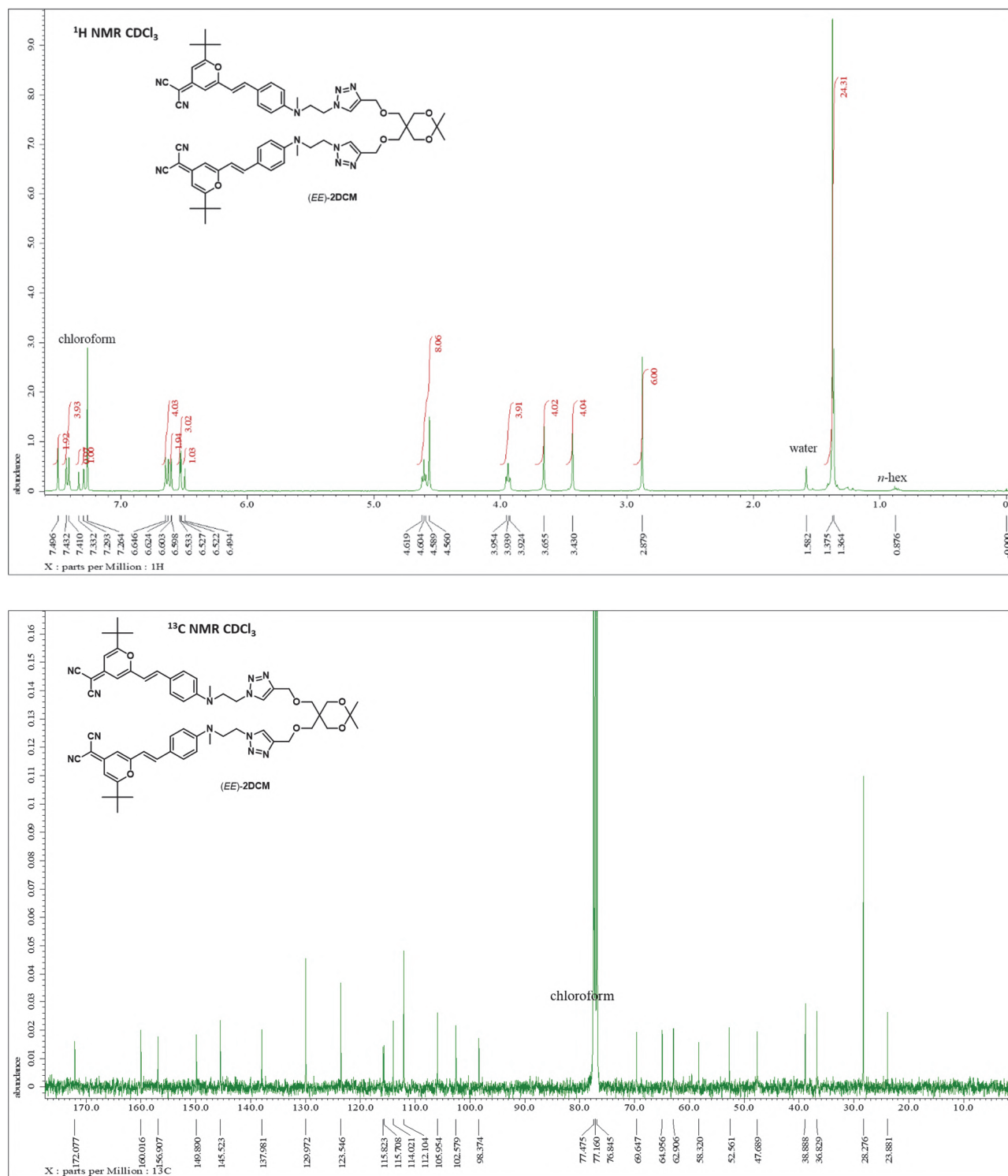
## 4. NMR spectra

### NMR spectra of compound **2** in CDCl<sub>3</sub>

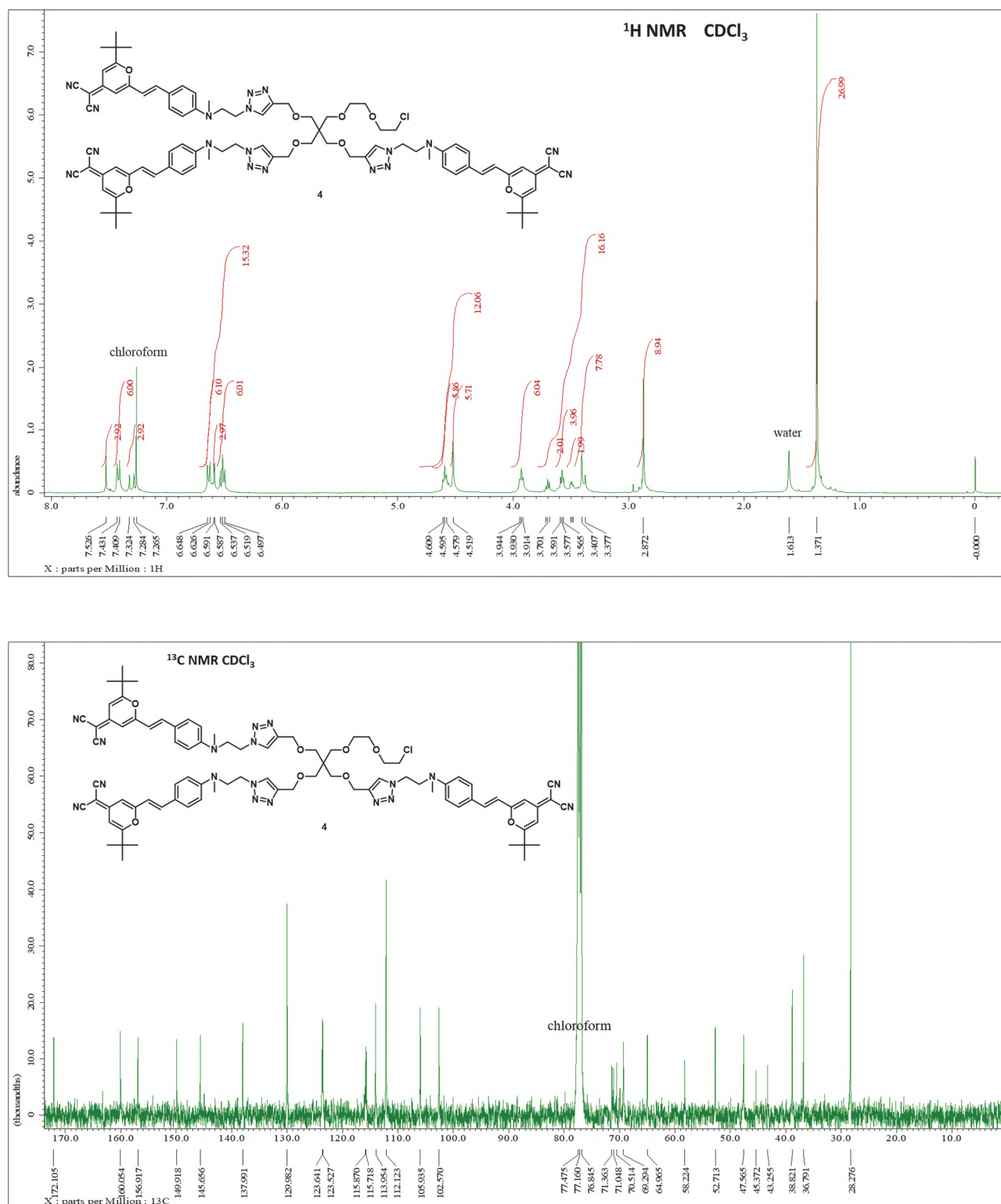
2,2-Dimethyl-5,5-bis((prop-2-yn-1-yloxy)methyl)-1,3-dioxane (**2**)



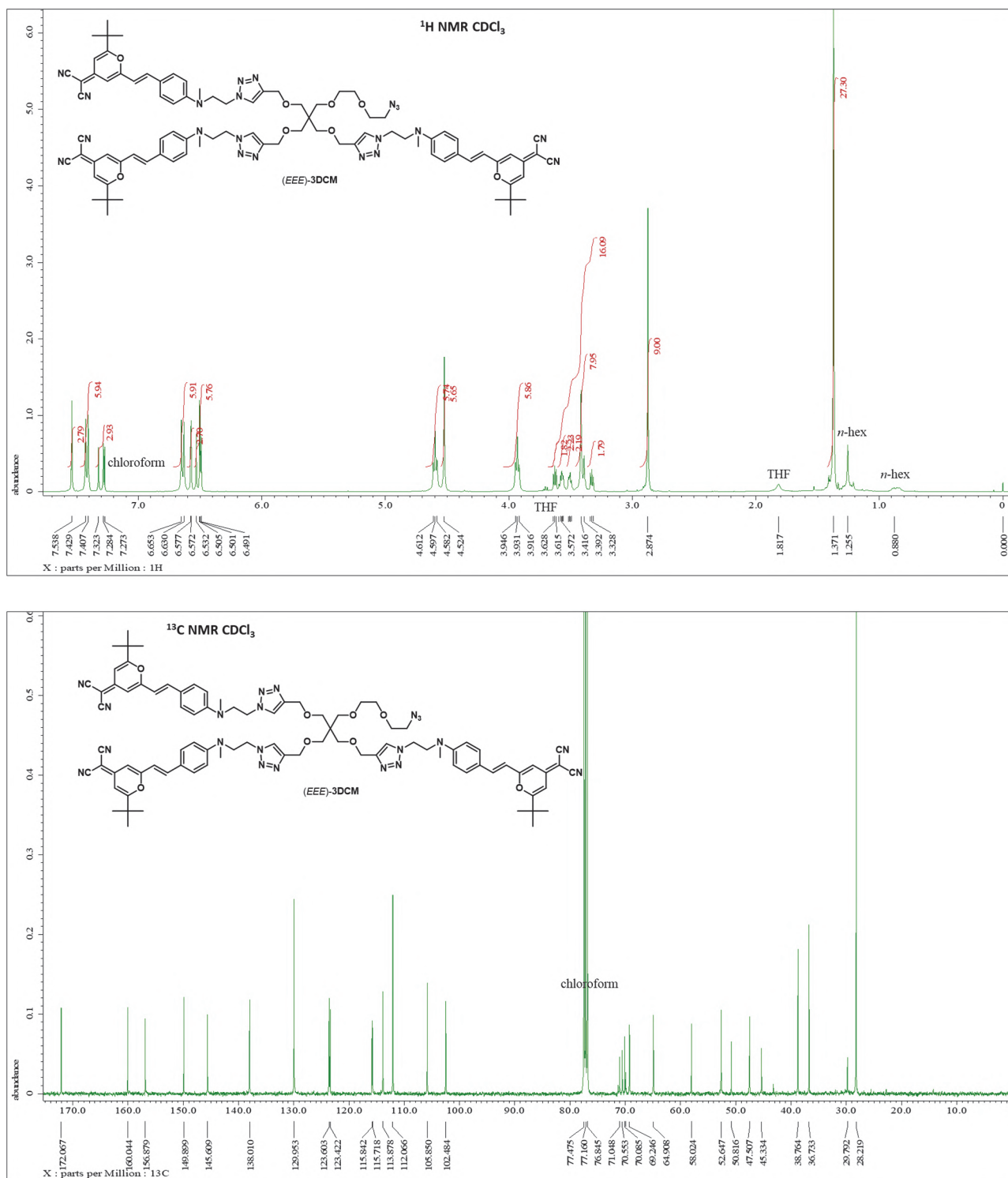
**Figure S11.** <sup>1</sup>H (top) and <sup>13</sup>C (bottom) NMR spectra of compound **2** recorded in CDCl<sub>3</sub> respectively at 400 MHz and 100 MHz.

NMR spectra of compound (*EE*)-2DCM in CDCl<sub>3</sub>

**Figure S12.** <sup>1</sup>H (top) and <sup>13</sup>C (bottom) NMR spectra of compound (*EE*)-2DCM recorded in CDCl<sub>3</sub> respectively at 400 MHz and 100 MHz.

NMR spectra of compound 4 in CDCl<sub>3</sub>

**Figure S13.** <sup>1</sup>H (top) and <sup>13</sup>C (bottom) NMR spectra of compound 4 recorded in CDCl<sub>3</sub> respectively at 400 MHz and 100 MHz.

NMR spectra of compound (*EEE*)-3DCM in CDCl<sub>3</sub>

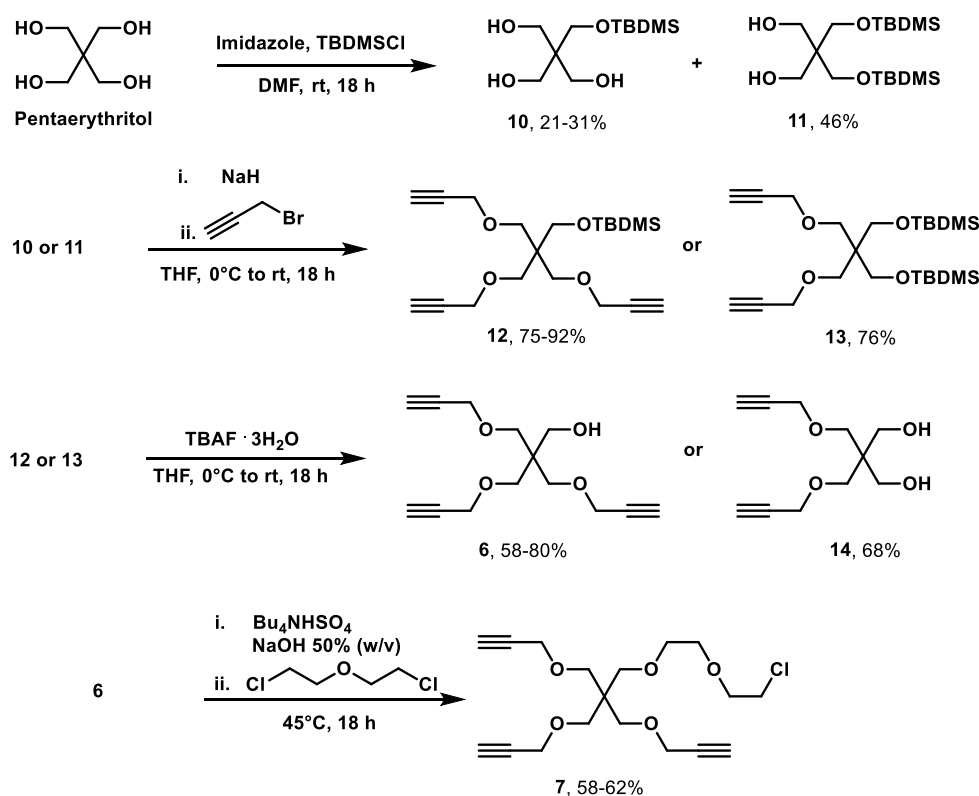
**Figure S14.** <sup>1</sup>H (top) and <sup>13</sup>C (bottom) NMR spectra of compound (*EEE*)-3DCM recorded in CDCl<sub>3</sub> respectively at 400 MHz and 100 MHz.



## 3.5 SYNTHESIS DETAILS OF MULTI-DCM COMPOUNDS

### 3.5.1 Preparation of dendritic linkers

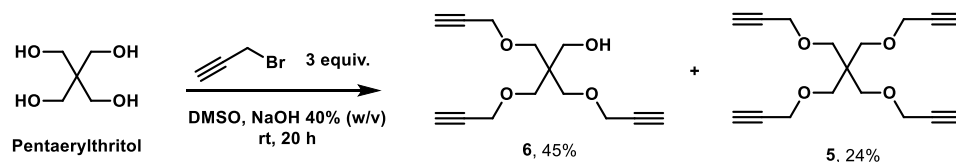
The tri-branching dendritic linker was firstly targeted. Initially, we tried monosilylation with *tert*-butyldimethylsilyl ether (TBDMS) according to the reported method.<sup>139</sup> As a result, we have obtained the mixture of **10** and **11** (**Scheme 13**). The TBDMS protected diol and triol were further propargylated into **L3** and **13**, respectively. The TBDMS groups were removed with tetrabutylammonium fluoride (TBAF) to result **6** and **14**. The **6** alcohol was functionalized with bis(2-chloroethyl) ether. The total yields of **14** and **7** are 24% and 14%, respectively.



**Scheme 13:** Initial route to prepare the di-branching and tri-branched dendritic linkers **14** and **7**, respectively.

Generally, the whole scheme works well from the pentaerythritol according to the reported methods. However, the first step was greatly restricting the amount of following compounds and the total yields. In addition, a purification problem occurred to the **14** follow-ups.

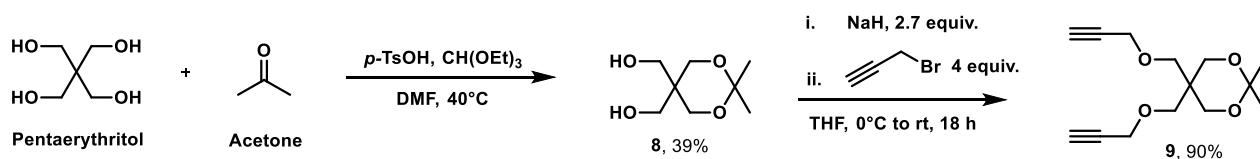
To improve the synthesis, we changed the synthetic method to another reported protocol to obtain **L5** directly, accompanying the *tetra-O*-propargylated compound **5** (**Scheme 14**).<sup>136</sup>



**Scheme 14:** Preparation of tri-*O*-propargyl and tetra-*O*-propargyl dendritic linkers **6** and **5**, respectively.

The synthesis of **6** according to the **Scheme 14** reached 45% yield, which is comparable to the yield of 23% obtained by the first method (**Scheme 13**). In addition, we obtained **6** just by one step. With the addition of 9 equivalent propargyl bromide to the pentaerythritol, no improvement of the yield of **6** was observed. In fact, we obtained the same ratio (about 2:1) of **6** and **5**.

We have also tried the synthesis of di-*O*-propargyl compound **9** through the protection of the diol as the isopropylidene acetal, followed by *O*-propargylation (**Scheme 15**).

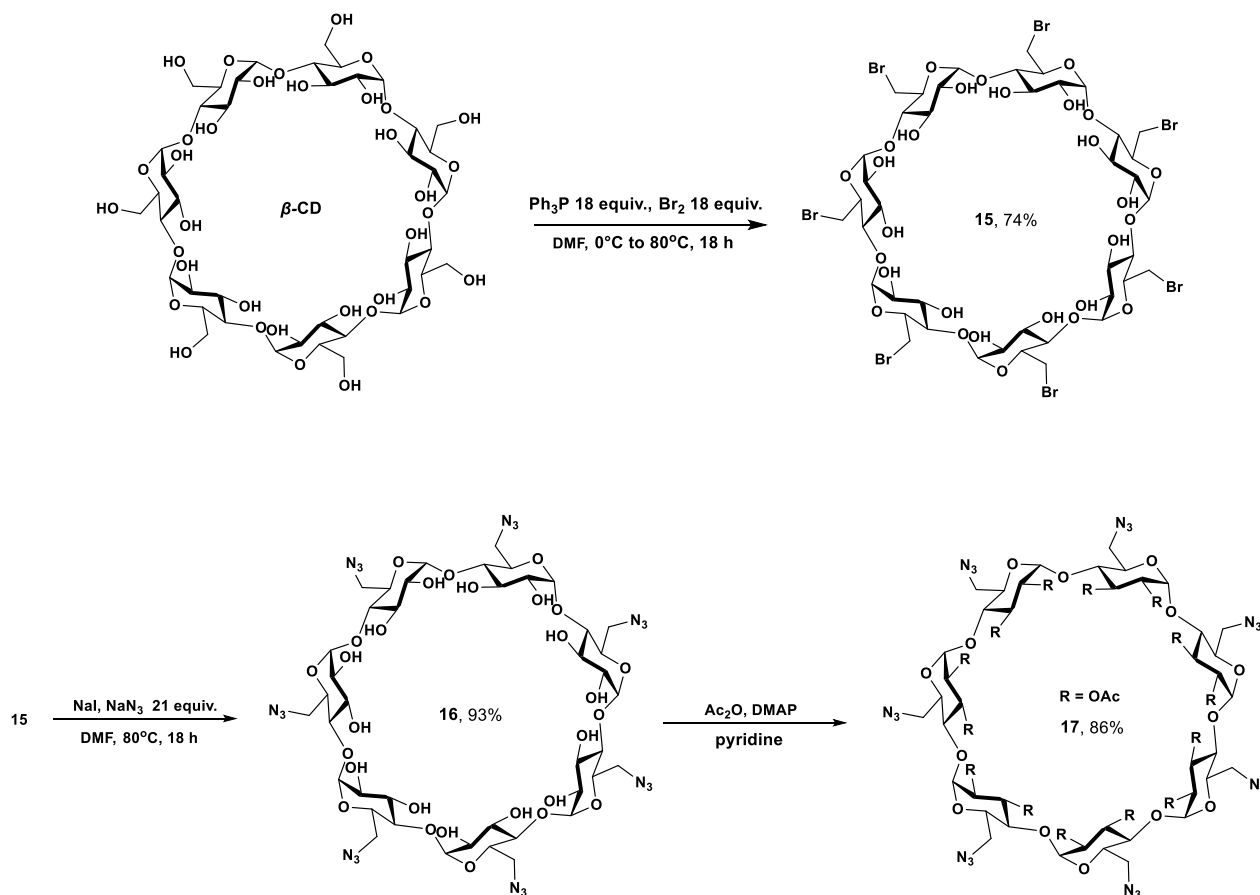


**Scheme 15:** Preparation of di-*O*-propargyl dendritic linkers **9**.

In summary, we have synthesized di-, tri- and tetra-*O*-propargylated linkers **9**, **7** and **5**, respectively.

### 3.5.2 Preparation of $\beta$ -CDs

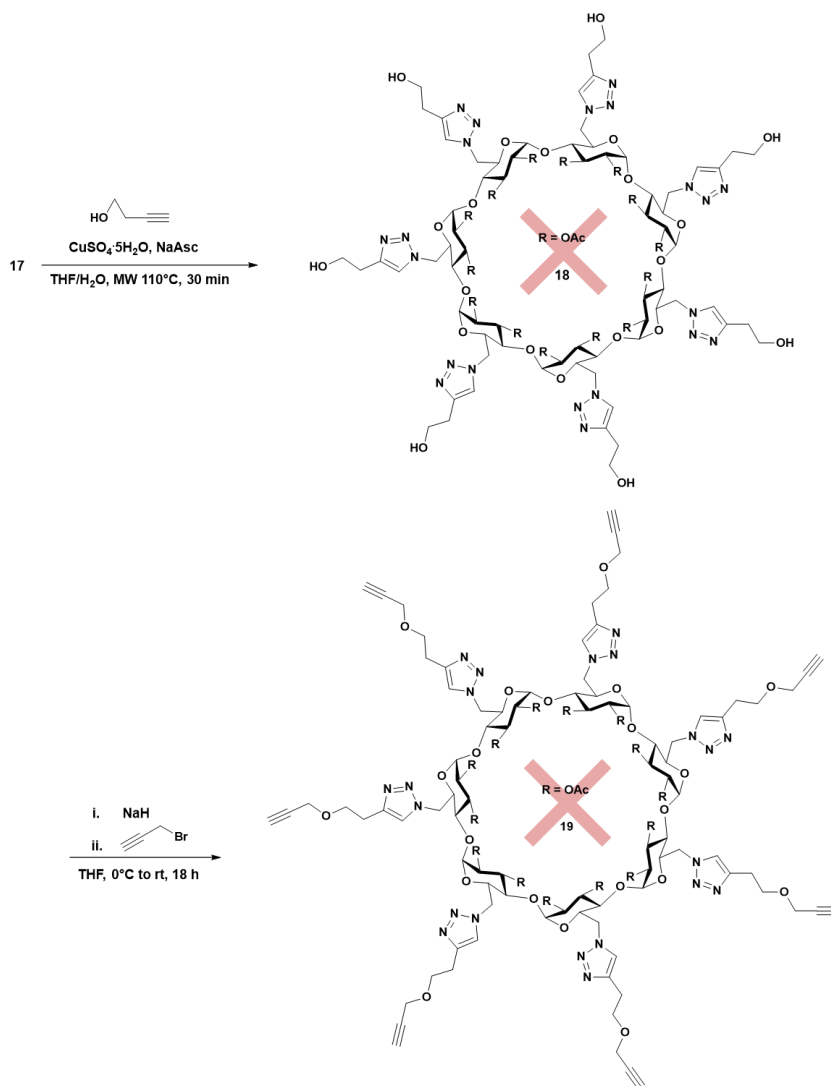
To obtain more valencies, the  $\beta$ -CD as platform has been explored. As the chromophore units will be functionalized as azido forms of higher multivalent molecules, the propargylated  $\beta$ -CDs are required. As the first trial, a *jellyfish-type* seven-unit propargylated  $\beta$ -CD was proposed with the elongation by the "click reaction" approach. We firstly synthesized the per-6-bromo- and per-6-azido- $\beta$ -CD **15** and **16** (**Scheme 16**). **25** was prepared by action of triphenylphosphine and bromine on the  $\beta$ -CD which was converted to the azido-CD **16** by nucleophilic substitution with sodium azide (**Scheme 16**). Compound **16** was then protected with acetyl groups **17** to facilitate the purification and solubility in organic solvents.<sup>152, 186-188</sup>



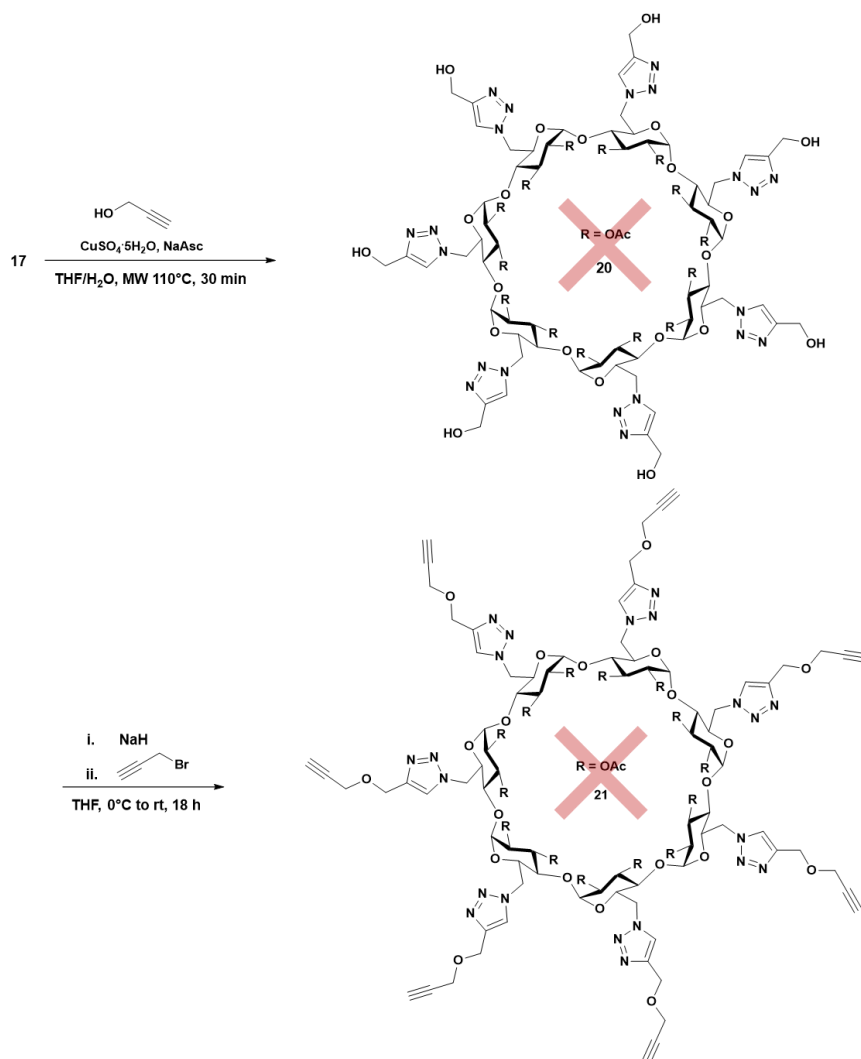
**Scheme 16:** Preparation of the per-6-azido  $\beta$ -CD **17**.

In order to obtain *O*-propargyl-functionalized CD on the primary face, we decided to realize the click reaction of the azido-CD **17** with propargyl or homopropargyl alcohol to prepare **18** or **20**, respectively, then introduce the propargyl functions through the *O*-alkylation reaction (**Scheme 13**). However, the **18** and **20** cannot be isolated by organic extractions. After washing with EDTA, **18** and **20** were dried and

processed to the *O*-propargylation reaction. Unfortunately, we didn't find **19** and **21** in the final reaction mixtures after purifications (**Scheme 18**).

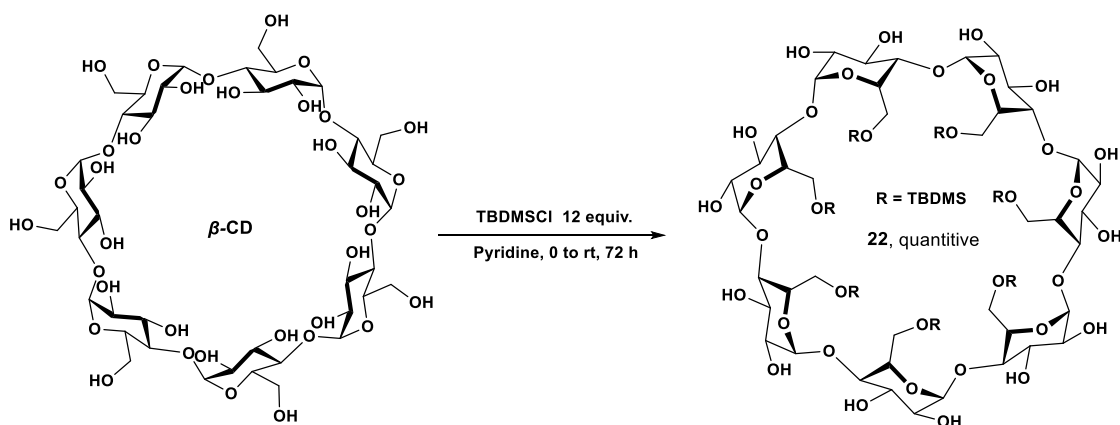


**Scheme 17:** Tentative synthesis of **18** and **19**.



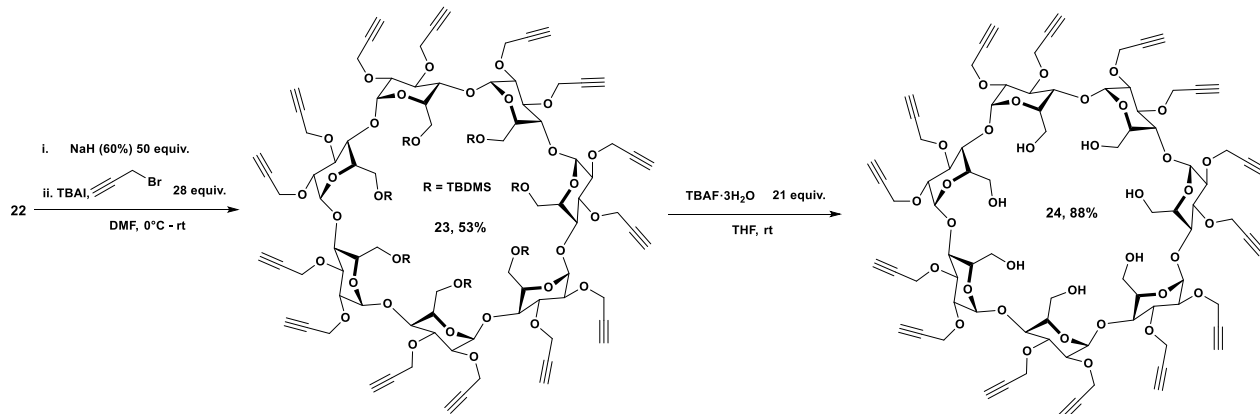
**Scheme 18:** Tentative synthesis of **20** and **21**.

Then we decided to prepare per-2,3-*O*-propargyl  $\beta$ -CD by using a reported method.<sup>154</sup> The synthesis starts from the  $\beta$ -CD by using TBDMSCl to protect the primary hydroxyl groups (**Scheme 19**).<sup>149</sup>



**Scheme 19:** Preparation of the TBDMS-protected  $\beta$ -CD **22**.

The TBDMS protection resulted in per-6-*O*-TBDMS- $\beta$ -CD with a quantitative yield as a white transparent solid **22**. **22** then reacted with 28 equivalents propargyl bromide (2 equiv. propargyl bromide/OH) to obtain the 14-*O*-propargylated  $\beta$ -CD **23** in 53% yield (**Scheme 20**). After desilylation with TBAF in THF, the final target **24** has been isolated in 88% yield as a pale-yellow powder.



**Scheme 20:** Preparation of  $\beta$ -CD **24** with all *O*-propargyl groups on the secondary face.

### 3.5.3 Preparation of multi-DCMs

The azido DCM (**DCM-azide**), and propargyl DCM (**DCM-*o*-alkyne**) used in this PhD work were prepared previously by Dr. S. Maisonneuve. We have prepared pentaerythritol derived linkers, CD-based scaffolds, and the final targets (**Figure 55**) by the “click reaction”.

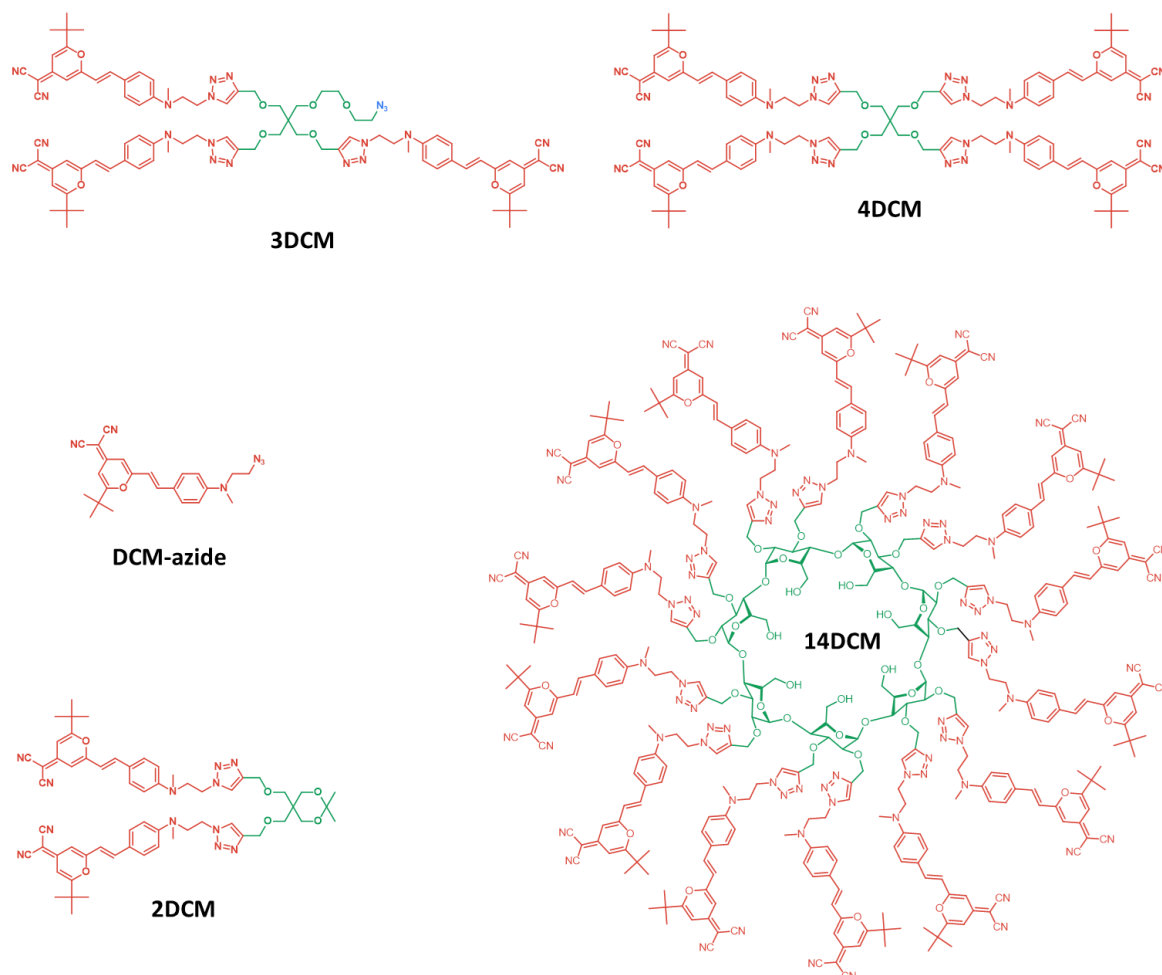
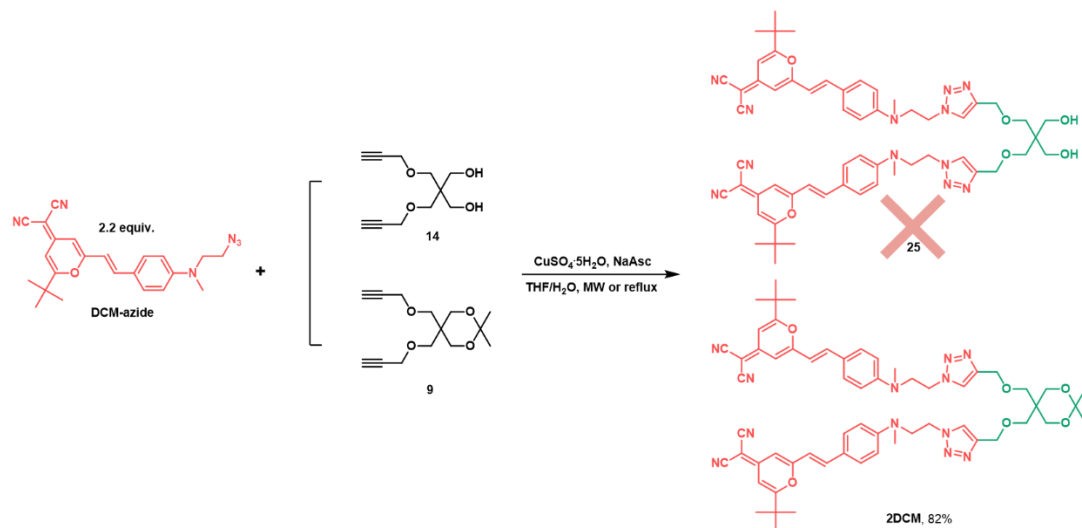


**Figure 55:** Structure of target DCM series.

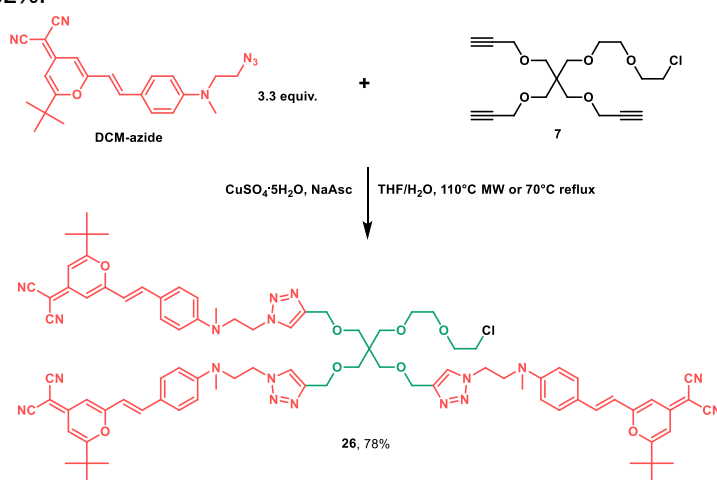
The full multi-DCM series of compounds is composed of **DCM-azide**, **2DCM**, **3DCM**, **4DCM** and **14DCM**. The spectroscopic studies were focused on the **DCM-azide**, **2DCM** and **3DCM**.

The same general procedures have been applied to the **2DCM**, **4DCM**, **14DCM** and the first step of **3DCM**. The azide and corresponding alkyne are added by ratio (1 equiv. azide function/alkyne function), and the catalyst set of copper (II) sulfate and sodium ascorbate is always maintained at a 1:2 ratio. The reactions are either available in heated solution for a long time (over 12 hours reflux) or in microwave reaction lasting for at least 30 minutes. The resulted mixtures are treated with EDTA aqueous solution to dissociate the copper chelation. After extraction with organic solvent, final products have been obtained after column chromatography.



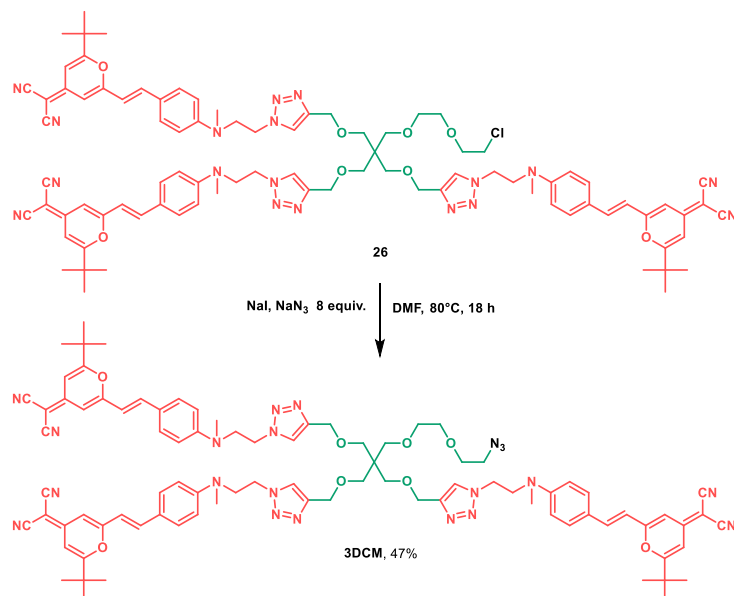
**Scheme 21:** Tentative synthesis of compound **25** and synthesis of **2DCM**.

We have explored two ways of synthesizing the model compound **2DCM**. Unfortunately, the click reaction of **DCM-azide** with compound **14** (**Scheme 13**) led to impure compound **25** which is difficult for purification (**Scheme 21**). Reaction with compound **9** was carried out successfully to obtain the target **2DCM** with a yield of 82%.



**Scheme 22:** Synthesis of trichromphoric compound **26**.

The same strategy was applied to the tri-branching linker compound **7**. We have obtained compound **26** in 78% yield (**Scheme 22**). The azido **3DCM** was prepared by azidation of compound **25** (**Scheme 23**). This transformation aims at eliminating potential influence from halogen atoms in the spectroscopy measurements. **3DCM** is also considered to be the dendron unit for further elongation, such as *hyperbranched-type* compound.



**Scheme 23:** Azidation to yield **3DCM**.

The **DCM-azide**, **2DCM** and **3DCM** have an increasingly deep color along with the growing number of DCM units, as shown in **Figure 56**.

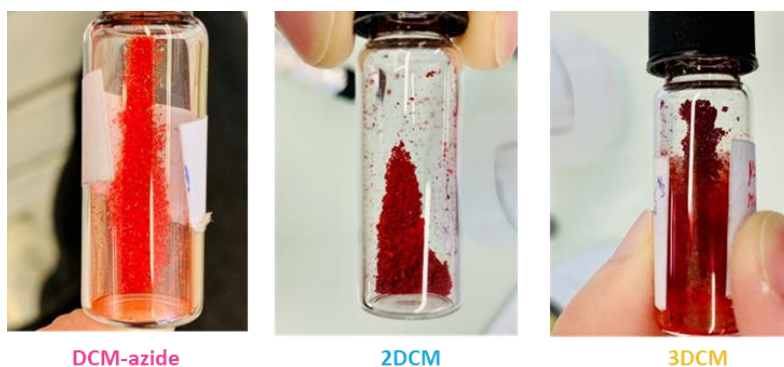
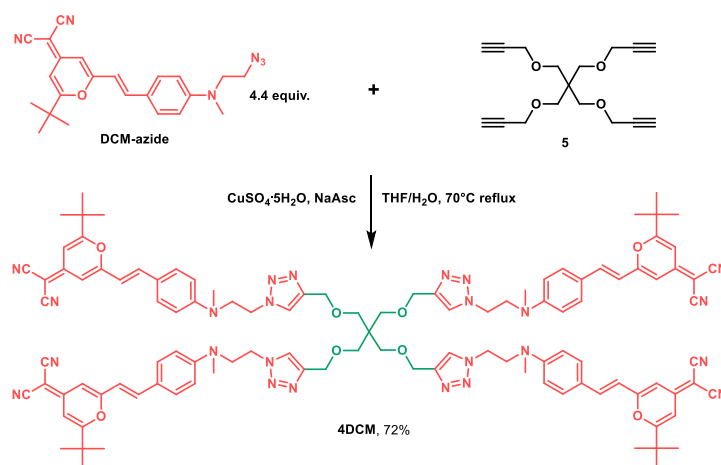


**Figure 56:** Colors of the solid powder compounds **DCM-azide**, **2DCM** and **3DCM**.

The tetrachromophoric **4DCM** was obtained with the linker **5** in a yield of 72% (**Scheme 24**).

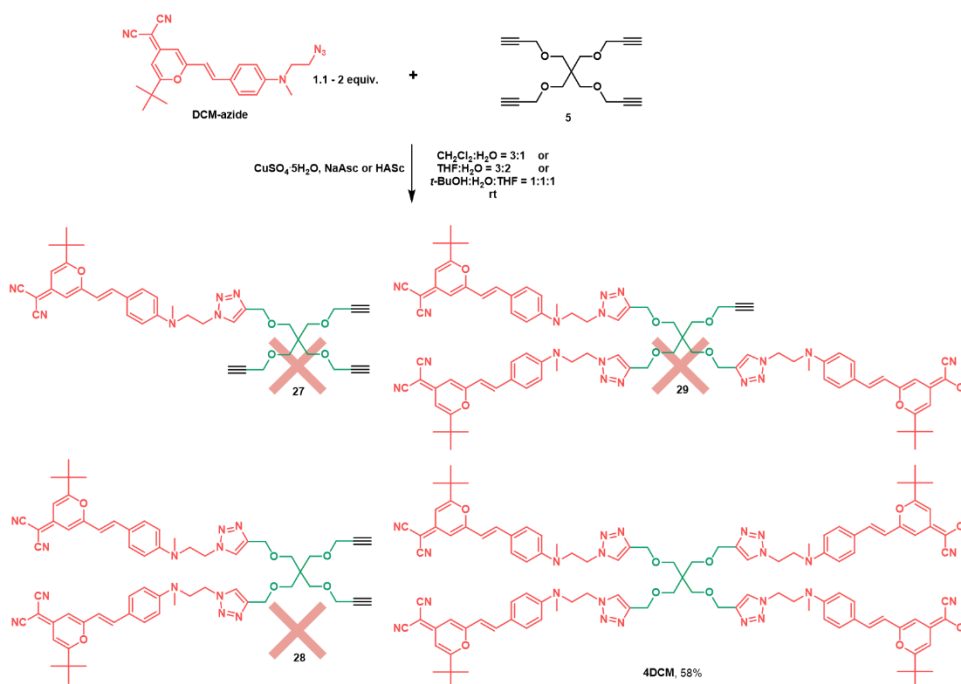


**Scheme 24:** Synthesis of tetrachromophoric **4DCM**.

We have tried to obtain one, two or three DCM simultaneously by varying the ratio of **DCM-azide** to **5** in a one-pot reaction (**Scheme 25**), as some authors reported the synthesis of different ratios of click product



by using similar reaction conditions.<sup>140</sup> However, in our case, the **4DCM** is always the major isolated product (See **Table 3**). It is consistent with the fact that the CuAAC reaction is a self-catalytic process. In spite of the trials of all solvent pairs, the reactants themselves are speculated to be one of the reasons to dominate the reaction equilibrium. The products cannot be controlled by the reactant ratio, which were expected to be equivalently uncontrollable to other moieties to introduce on the scaffold. Therefore, the synthesis trials were stopped.

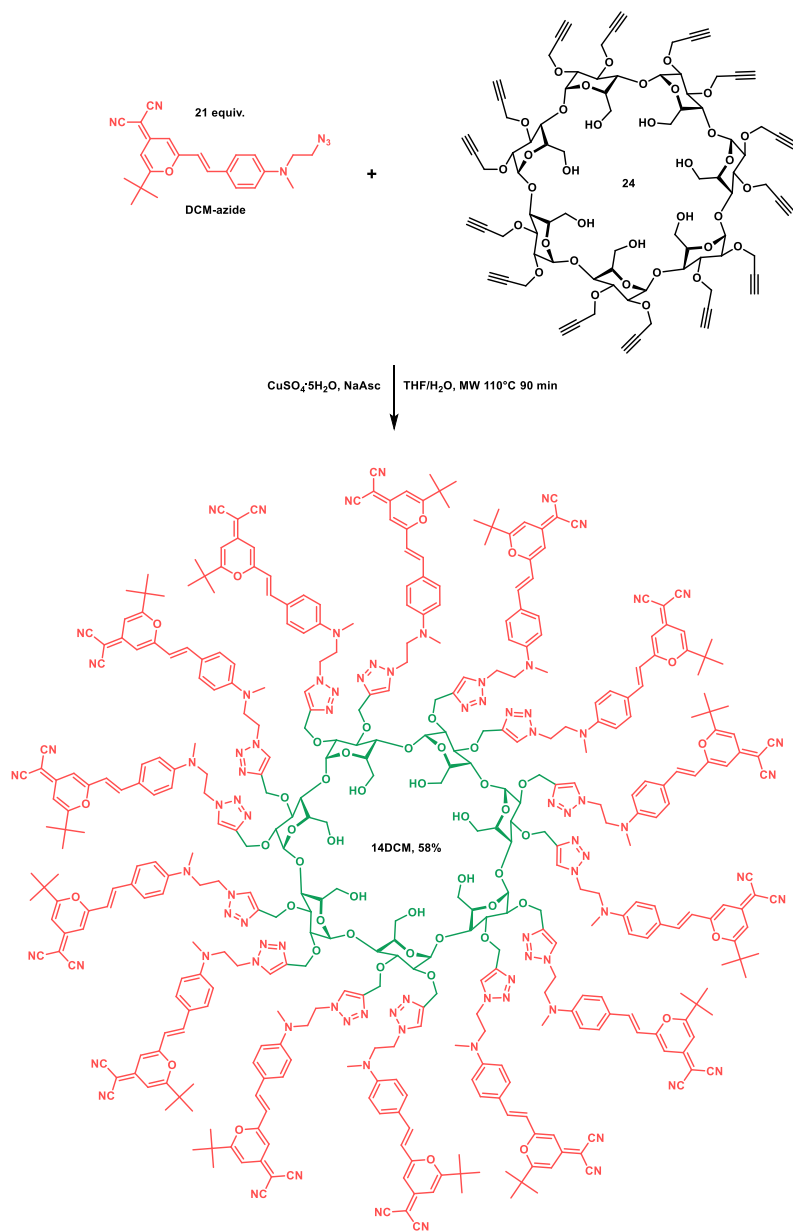


**Scheme 25:** Click reaction of DCM-azide with compound 5.

**Table 3.** The synthesis trials of **Scheme 25**.

Entry	Equiv. (DCM-azide:linker 5)	Catalyst	Solvent	Time	4DCM	27	28	29
1	2 :1	$\text{CuSO}_4 \cdot 5\text{H}_2\text{O}$ NaAsc	$\text{CH}_2\text{Cl}_2 : \text{H}_2\text{O} = 3:1$ 4 mL	60 h	Major	x	x	x
2	1.1 :1	$\text{CuSO}_4 \cdot 5\text{H}_2\text{O}$ HAsc	$\text{THF} : \text{H}_2\text{O} = 3:2$ 5 mL	24 h	Major	x	x	x
3	1.1 :1	$\text{CuSO}_4 \cdot 5\text{H}_2\text{O}$ HAsc	$t\text{-BuOH} : \text{H}_2\text{O} : \text{THF} = 1 : 1 : 1$ 6mL	24 h	Major	Trace	x	x

The 14-valent **14DCM** was synthesized from  $\beta$ -CD **24** (**Scheme 26**). To reach the full reaction, the ratio of the catalyst and the reactant **DCM-azide** was set to **DCM-azide**:  $\text{CuSO}_4 \cdot 5\text{H}_2\text{O}$ : NaAsc: **24** = 21: 7: 14: 1. After 90 min microwave irradiation or 4-day reflux, pure **14DCM** can be obtained in 58% yield.



Scheme 26: Synthesis of 14-valent 14DCM.



# Chapter IV



## 4 CHAPTER IV – MULTI-DAE/DCM SYSTEMS, TOWARDS FLUORESCENCE HYSTERESIS

### 4.1 THE DIFFERENT TYPES OF FLUORESCENCE HYSTERESIS

In the first chapter of this manuscript, we gave a general description of the hysteresis phenomenon and presented some previous results concerning what our group has named the “*photoswitchable fluorescence hysteresis effect*”, which also gave the name to the current ANR project SWIST (**SW**itchable **hy**Steresis **effec**T).

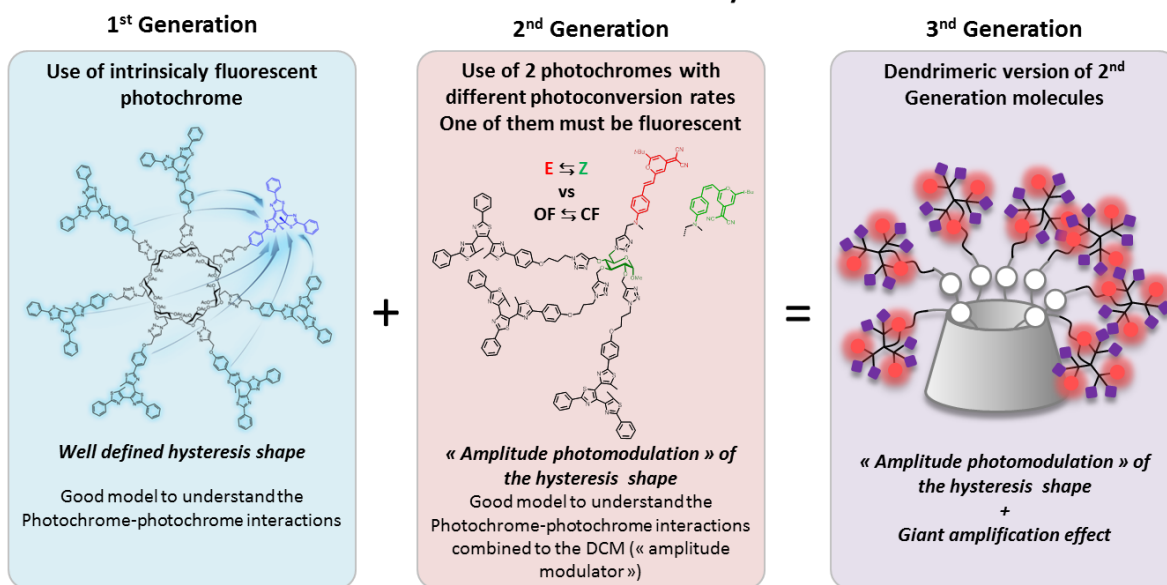
Since the first observation of this complex phenomenon in the middle of the year 2012, the involved processes of the fluorescence hysteresis is nowadays more understood by the group, but still unpublished yet. The different molecular systems led now to a classification by type of hysteresis.

The first generation corresponds to molecular systems involving multiple intramolecular FRET between intrinsically fluorescent photochromic units. This type of hysteresis has the advantage to have a well-defined hysteresis shape and can be obtained with weakly fluorescent photochromic units. The previous research work of the group, based on molecular systems containing multiple fluorescent DAE, demonstrated the structure-property relationship by using a statistical approach for the quantification of the FRET.

The second generation of hysteresis, discovered concomitantly by the group, utilizes two types of photoresponsive units where it is required that at least one of them is fluorescent to ensure the FRET. In such a type of molecular systems, the importance to involve species with a significant difference of photokinetic rates of the photoreactions was demonstrated (ex: *E/Z* photoisomerization of DCM vs OF/CF photocyclization of DAE). This is the key point to realize a fluorescence photomodulation involving a competition between processes (FRET vs photokinetic rates). The consequence of this research work based on a covalent association of DAE and DCM units led the group to reconsider the photoisomerization of the DCM and the possibilities of new molecular architectures (see previous chapters).

The third generation of hysteresis was imagined and represents the convergence of the two concepts developed by the group: the *photoswitchable fluorescence hysteresis effect* combined to a *giant amplification effect*.<sup>33</sup> In other terms, we aim to use appropriately the intermolecular fluorescence quenching of the *giant amplification effect* combined to the intramolecular non-linear fluorescence quenching observed in the *photoswitchable fluorescence hysteresis effect*.

## Fluorescent Photoswitchable Hysteresis



Stéphane MAISONNEUVE

**Figure 57:** Presentation of the three generations of *photoswitchable fluorescence hysteresis effects* proposed by the group in this long-term project during the last decade.<sup>79</sup>

## 4.2 TOWARDS A NEW TYPE OF HYSTERESIS EFFECT

### 4.2.1 Molecular architectures

The molecular architectures presented in this chapter were designed in order to achieve the third generation of hysteresis effect. For this purpose, we have imagined some molecular architectures able to realize the second type of hysteresis with the previously described fluorescent and photoisomerizable DCM unit and a new DAE unit. Compared to the DAE used in the previously described hysteresis, this new DAE unit was designed by Dr P. Yu (ICMMO laboratory, Univ. Paris-Saclay) and synthesized by N. Baggi, by adding a nitro group in order to make it non fluorescent and decrease its photochromic quantum yields while retaining suitable spectral features (for FRET purpose). This new DAE unit is described in the next paragraph **4.2.2** (Page 145). The expected impact on the hysteresis is to enlarge the gap between the forward and the backward pathways, in addition to an increased brightness of the system.

As we have demonstrated in the previous chapter, the multi-DCMs cause the lower conversion yield of  $E \leftrightarrow Z$  photoisomerization than the single DCM unit, accompanied with faster kinetics. The effect can be ascribed to the homo-FRET ( $E/E$ ) and hetero-FRET ( $E/Z$ ) within neighboring DCM dyes. Consequently, it is not proper to lay the plural DCMs together. This is the reason of the design of the dendron **YN-3c** which is also an ideal model compound to understand the dendrimeric versions **YN-12c**, **YN-42c**. (See **Figure 58**)

The synthetic strategy of the combined DCM-DAE multichromophoric architectures is based on the CuAAC reaction to assemble the units into a whole. The new DAE molecule **DAE-azide**, prepared by N. Baggi in his PhD work (ICMMO, Université Paris-Saclay), exhibits two colors, yellow (open form OF) and green (close form CF) in a THF solution and are spectrally compatible with the DCM, allowing spectral overlap between the DCM emission and the DAE absorption (in CF only). According to the concept of *photoswitchable fluorescence hysteresis effect* and the previous investigations made by Dr. S. Maisonneuve in the PPSM laboratory, our target is to install more DAE units than DCM ones in the multichromophoric system.



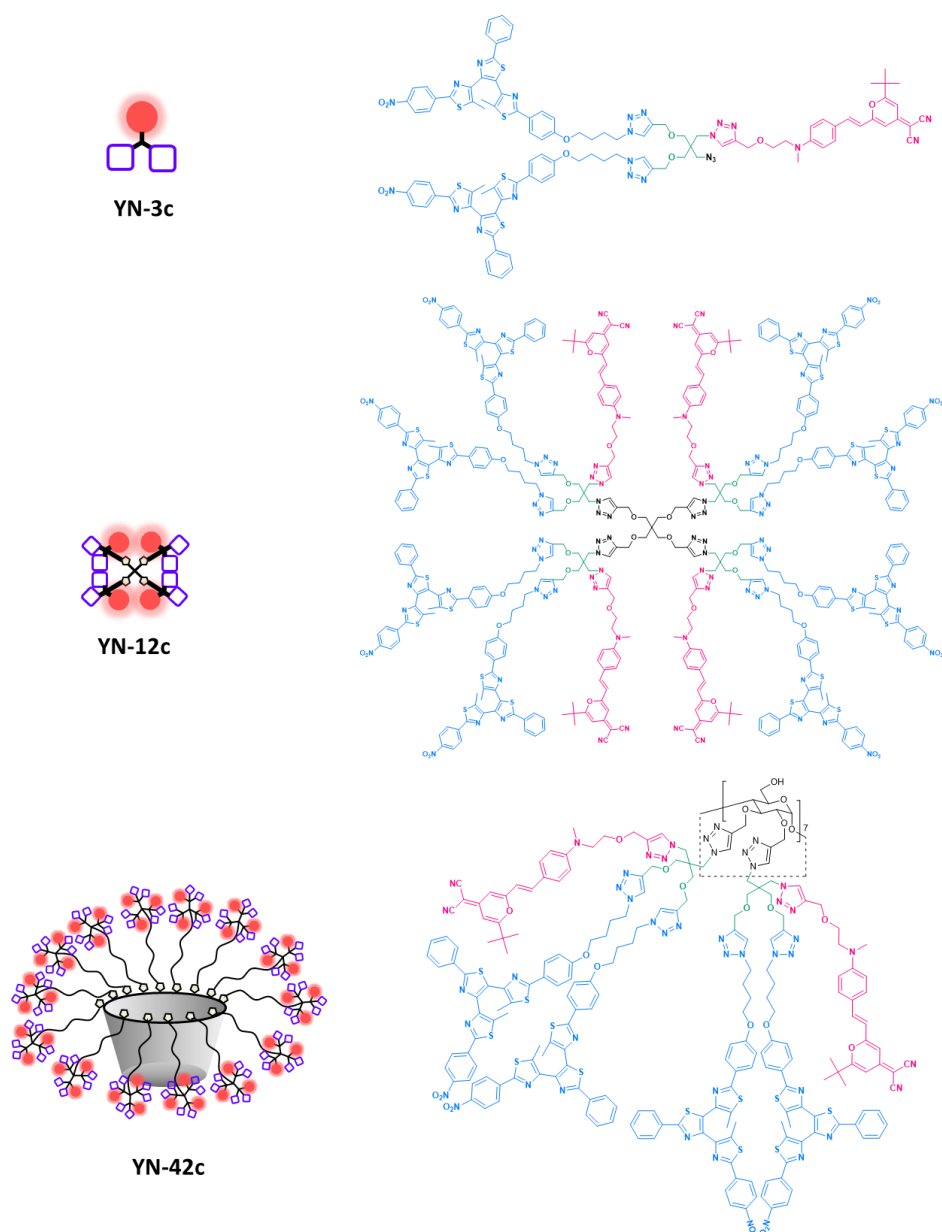
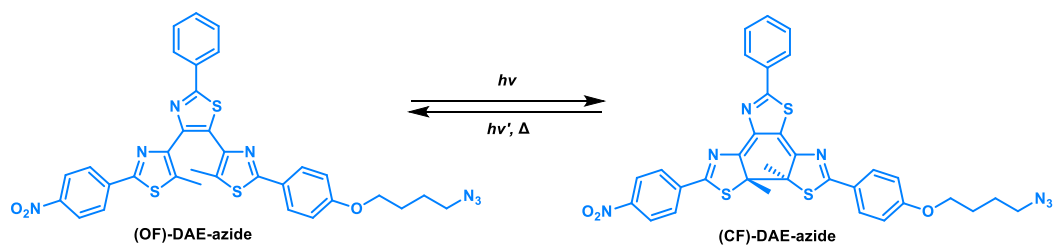


**Figure 58:** Chemical structures of **YN** series.

## 4.2.2 Spectroscopic and theoretical description of the new DAE

### 4.2.2.1 Spectroscopic studies

The DAE used in this work was provided by N. Baggi, PhD student at ICMMO laboratory (Univ. Paris-Saclay) under the supervision of Dr P. Yu and Dr A. Léaustic. The molecule was denoted by its internal laboratory number as **DAE-azide** and shown in the **Scheme 27** in open form and closed form, respectively.



**Scheme 27:** The photoisomerization scheme of **DAE-azide** between open form **(OF)-DAE-azide** and closed form **(CF)-DAE-azide**.

Thanks to Dr Régis Guillot from ICMMO laboratory, the X-ray structure of **DAE-azide** was obtained from a single crystal and shown in **Figure 59**. The crystal structure indicates that **(OF)-DAE-azide** is in a “parallel” form in the crystal, which is considered as the inactive form for the OF $\leftrightarrow$ CF isomerization according to the reported literature.<sup>32, 189-191</sup>

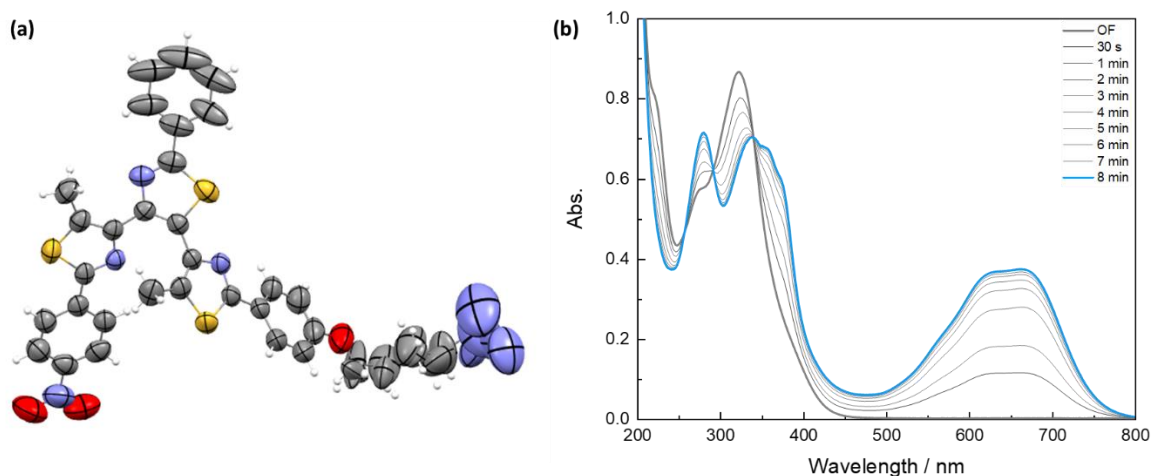


**Figure 59:** (a) XRD structure of **(OF)-DAE-azide** (ORTEP representation). (b) The UV-vis absorption spectra of **DAE-azide** under irradiation upon 320 nm until photostationary state in THF.

The UV-vis absorption spectrum of **(OF)-DAE-azide** in THF shows a maximum at 322 nm. After irradiation at 320 nm, the main absorption band of **(OF)-DAE-azide** decreases and a broad band rise in the red region with a maximum around 625-665 nm, leading to a colored solution. The presence of several isosbestic points in the UV and the visible regions suggest that the system obeys to a classical OF $\leftrightarrow$ CF photochromic transformation. These observations are representative of the typical photochromism phenomenon for DAE, with a OF $\rightarrow$ CF cyclization reaction under UV irradiation. The quantum yields of DAE OF $\leftrightarrow$ CF isomerizations were measured on the synthetic precursor of **DAE-azide**, **DAE-nitro** (**Figure 60**), which was originally designed for pursuing a countertrend low efficient isomerization performance. The demand was raised for pairing the DCM *E* $\leftrightarrow$ *Z* isomerization to create the isomerization speed contrast. According to the test from N. Baggi in PPSM, the nitro group greatly suppressed the OF $\rightarrow$ CF quantum yield at 4% and 0.4% of the backward reaction. In addition, the modification of the *ortho*-nitro group on the phenyl ring eliminates the fluorescence, where the analog with phenyl group used by Dr S. Maisonneuve was fluorescent in **Figure 57**.<sup>79</sup>

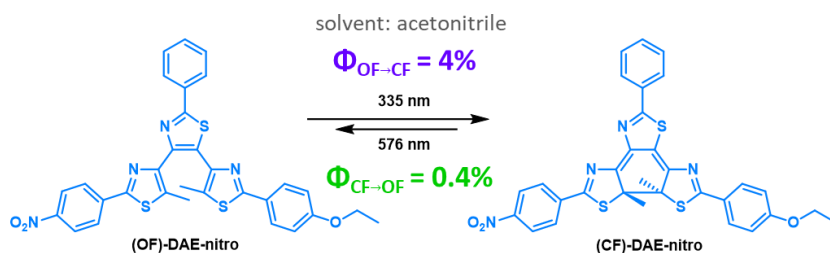


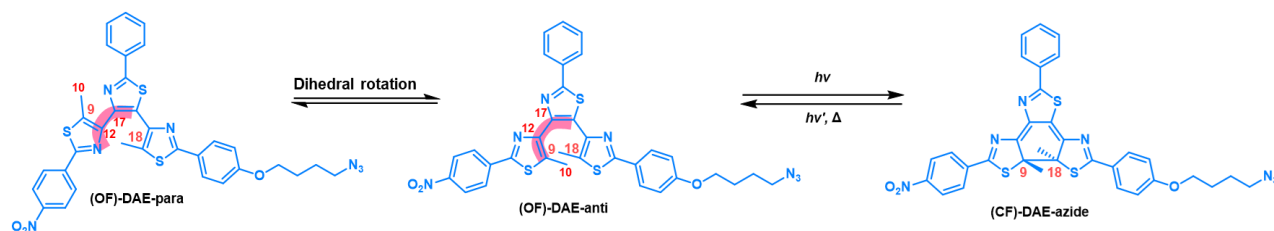
**Figure 60:** Chemical structures and isomerization quantum yields of **DAE-nitro** isomers.

In PPSM laboratory, we essentially studied the **DAE-azide** molecule theoretically with DFT and TDDFT methods.

#### 4.2.2.2 Theoretical studies

According to the reported literature, the parallel conformers of DAE in the OF are inactive for the photochromic reaction.<sup>32, 189-191</sup> The two carbon atoms connected to the methyl groups are called

“reactive carbons” in the DAE molecules as shown in **Scheme 28**. The measured distance of the two carbon atoms ( $C_9$  and  $C_{18}$ ),  $d(C-C')$ , of **(OF)-DAE-para** from the XRD structure is 4.68 Å, which is considered too far away for photocyclization reaction to occur. The common  $d(C-C')$  for photochemical reaction is under 4 Å.<sup>192</sup>



**Scheme 28:** The interconversion and isomerization relationships among the **DAE-azide** species. The reference parameters include the  $C_{10}-C_9-C_{12}-C_{17}$  dihedral angle,  $d(C-C')$  ( $C_9-C_{18}$  distance).

We have firstly optimized the geometries of **(CF)-DAE-azide**, **(OF)-DAE-para** and **(OF)-DAE-anti** with three DFT functionals at the level of def2-SVP Karlsruhe “def2” basis sets, taking the IEFPCM:THF as the solvent model. The PBE0 and CAM-B3LYP functionals both provided satisfying results in estimating the  $d(C-C')$  and the dihedral angle of **(OF)-DAE-para** with respect to the XRD structure (See **Table 4**). The  $d(C-C')$  of PBE0 and CAM-B3LYP estimations are both 4.64 Å, just having a 0.04 Å difference to the XRD result. The difference of the XRD  $C_{10}-C_9-C_{12}-C_{17}$  dihedral angle and the PBE0 result is less than 1°, which is the best of the three functionals (See **Table 4**). We set the PBE0/def2-SVP with IEFPCM:THF as the level for geometry optimization related calculations due to the much less time cost of PBE0 functional.

**Table 4:** Comparison of the DFT geometry optimizations with the XRD data for **DAE-azide**.

	<b>(CF)-DAE-azide</b>			<b>(OF)-DAE-anti</b>			<b>(OF)-DAE-para</b>			<b>XRD</b>
	<b>PBE0</b>	<b>CAM-B3LYP</b>	<b>ωB97X-D</b>	<b>PBE0</b>	<b>CAM-B3LYP</b>	<b>ωB97X-D</b>	<b>PBE0</b>	<b>CAM-B3LYP</b>	<b>ωB97X-D</b>	
<b><math>d(C-C')</math> (Å)</b>	<b>1.53</b>	<b>1.54</b>	<b>1.54</b>	<b>3.54</b>	<b>3.57</b>	<b>3.45</b>	<b>4.64</b>	<b>4.64</b>	<b>4.47</b>	<b>4.68</b>
<b>Dihedral (°)</b>	<b>9.51</b>	<b>8.48</b>	<b>8.39</b>	<b>48.77</b>	<b>50.20</b>	<b>49.13</b>	<b>154.67</b>	<b>153.72</b>	<b>149.04</b>	<b>155.26</b>

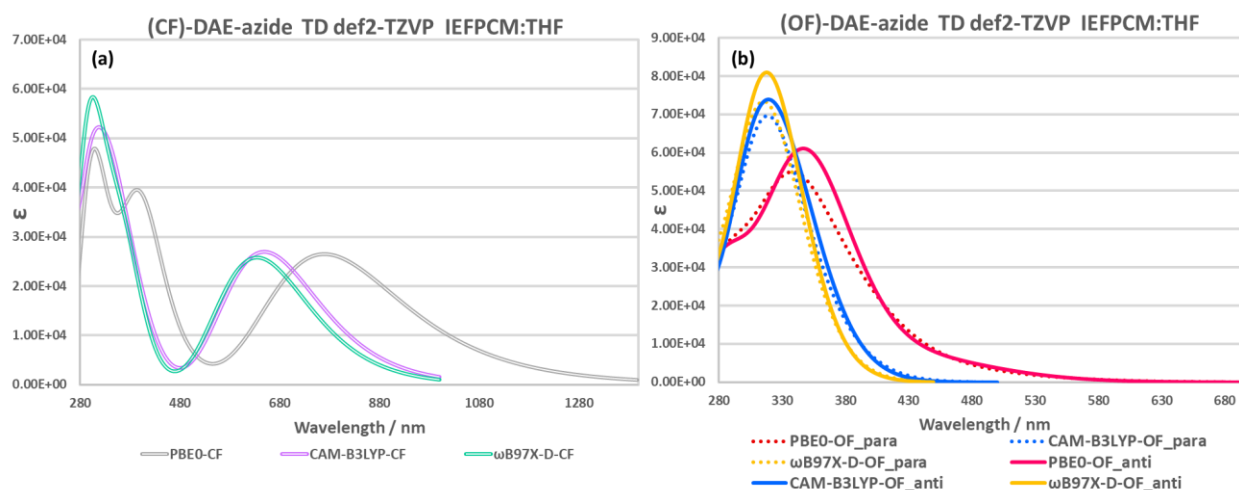


**Figure 61:** Calculated absorption spectra calculated by TDDFT of (a) **(CF)-DAE-azide**; (b) **(OF)-DAE-azide** of PBE0, CAM-B3LYP and  $\omega$ B97X-D, respectively. All calculations were based on def2-TZVP basis set and IEFPCM:THF solvent model. Number of calculated transitions = 30.

The TDDFT calculations were carried out based on the PBE0/def2-SVP optimized geometries, using an improved basis set up to def2-TZVP level. As a commonly known for charge transfer type chemical structures, CAM-B3LYP performs the best to estimate the electronic transitions of such molecules. CAM-B3LYP provided absorption wavelengths of the first electronic transition at 318 nm for **(OF)-DAE-azide**, and 650 nm for **(CF)-DAE-azide**, which are closed to the corresponding experimental values 322 nm and 625-665 nm range, respectively.  $\omega$ B97X-D shifts to 632 nm compared to CAM-B3LYP in the **(CF)-DAE-azide**

absorption. PBE0 systematically underestimates the transition energies on both OF and CF structures, especially giving 780 nm as the first transition energy in **(CF)-DAE-azide** situation.

We have performed a screening of the possible geometries of the open form in order to investigate the relationships among the three structures at the PBE0/def2-SVP IEFPCM:THF level, by scanning the dihedral angle around the C-C bond connecting the central thiazole ring to the other thiazole ring of one side-arm of DAE on both directions (See **Figure 62**). **(OF)-DAE-para** is the lowest energy form in the scan coordinate energy profile, whereas **(OF)-DAE-anti** has a slightly higher energy at  $\Delta E = 0.02$  eV, meaning that both conformers must be populated at room temperature. The results are consistent with the crystalline form of **(OF)-DAE-azide** showing a parallel arrangement. There are non-negligible energy barriers existing between **(OF)-DAE-para** and **(OF)-DAE-anti** along this torsion.

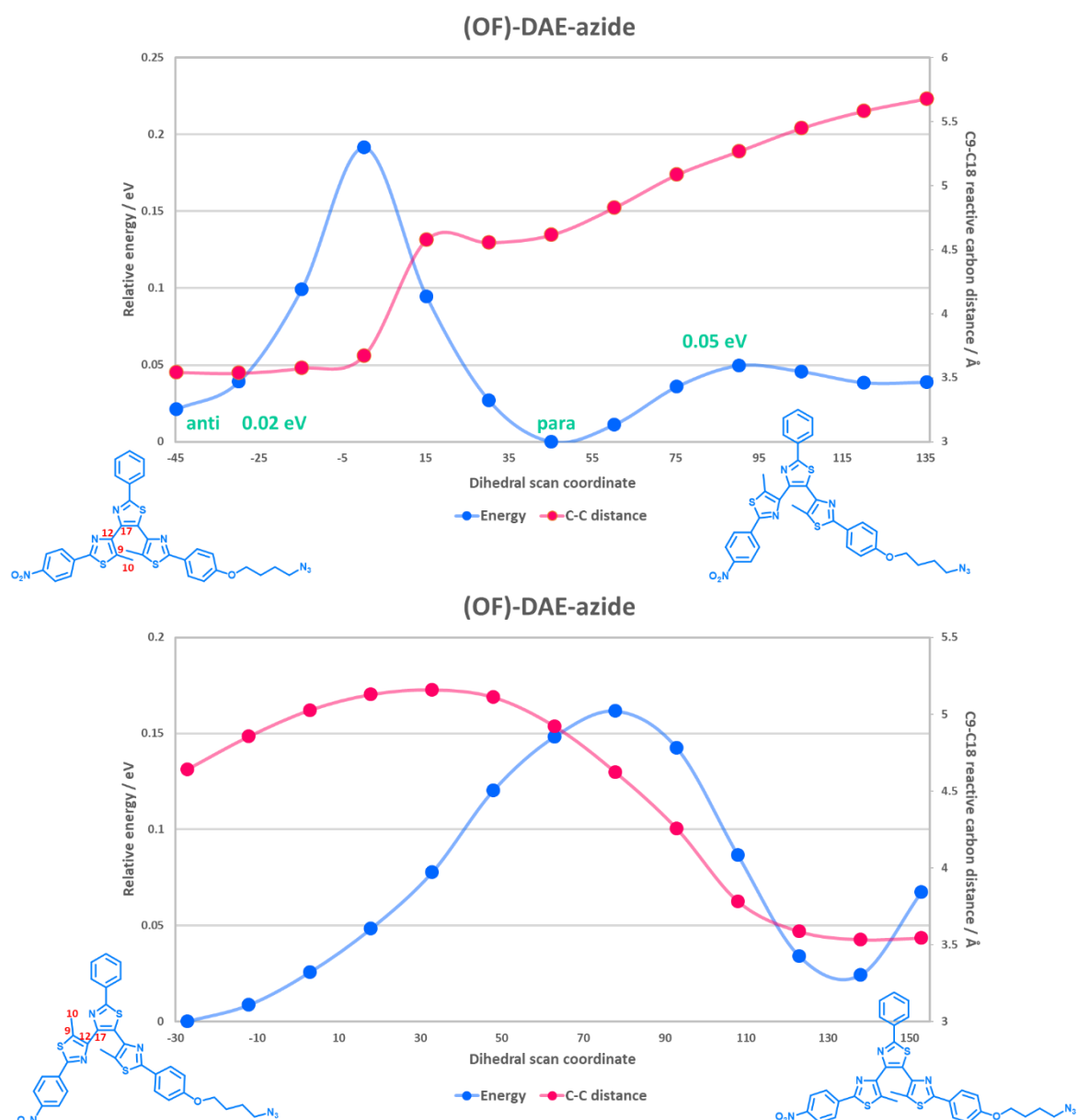


**Figure 62:** **(OF)-DAE-azide** geometry scan results obtained by rotating the C-C dihedral angle ( $C_{10}-C_9-C_{12}-C_{17}$ ). Relative energy in blue and  $d(C-C')$  vs. dihedral angle in red.

Through the DFT/TDDFT calculations, we have a basic theoretical verdict on the main forms of **NB105** DAE molecule. The estimations are reliable, compared to the reported literature and the experimental results.

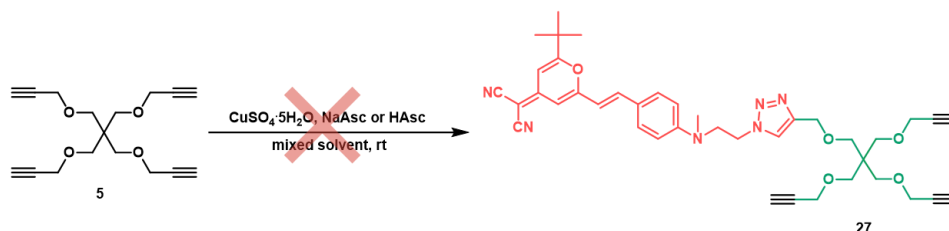
The calculated structures were used as starting inputs for the MD simulations presented in the following section 4.5.

## 4.3 SYNTHESIS OF THE DENDRITIC STRUCTURES FOR HYSTERESIS EFFECT

### 4.3.1 Synthesis of the azido-dendron

In the case studies of  $\beta$ -CD mentioned in the paragraph 3.2.2 (Page 90), the one-pot CuAAC reaction with both DCM and DAE will result in a blend mixture, which is difficult to isolate in a pure product. Consequently, the numbers of DCM and DAE cannot be properly controlled. We have decided to synthesize a trichromophoric unit, containing only one DCM moiety and two DAE moieties, with a CuAAC capable azido functional group in order to have an important versatility for future linkages. After that, the trichromophoric unit can be transformed into bigger systems with dendritic linkers or  $\beta$ -CDs.

In the paragraph 3.2.4 (Page 135), we have already shown that the CuAAC reaction is a self-catalytic process in the synthesis of multi-DCMs. It turns hard to obtain the non-fully occupied DCM compounds from the linker **5** even with a small amount of DCM in **Scheme 29**. It is also unpredictable when introducing the second chromophore to ensure the one alkyne to be preserved on the dendritic linker.



**Scheme 29:** Tentative synthesis of mono-DCM-functionalized **27**.

To circumvent the situation, a dissymmetric dendritic linker is required. For matching the azido and propargyl functions for the CuAAC reaction, the target compounds can be prepared from the two photoswitchable chromophores, **DCM-*o*-propargyl** and **DAE-azide**, as shown in **Figure 63** in their *E*-form and *OF*-form, respectively.

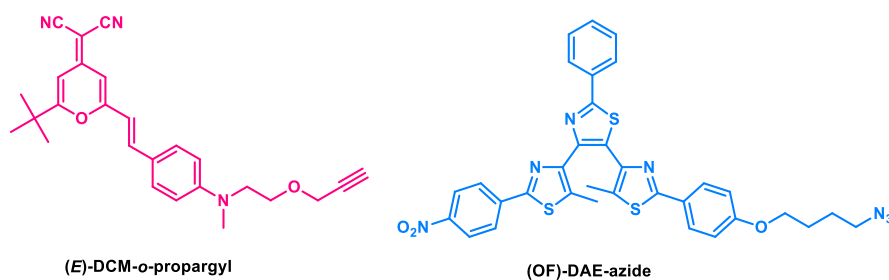
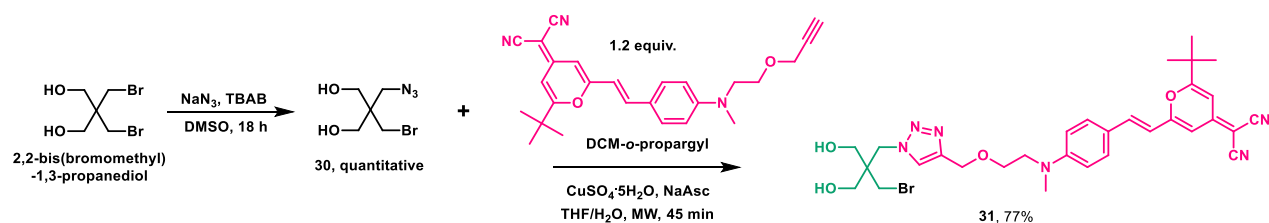


**Figure 63:** Structure of **(E)-DCM-*o*-paropargyl** and **(OF)-DAE-azide**.

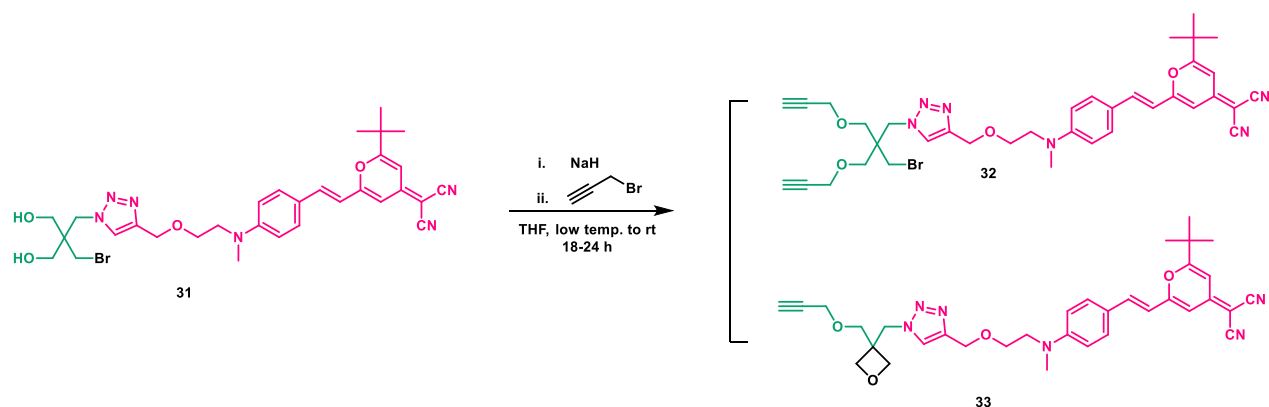
The trichromophoric unit **YN-3c** was designed from commercially available 2,2-*bis*(bromomethyl)-1,3-propanediol which has two bromo groups compared to pentaerythritol (**Scheme 30**). They can be converted to azido group one by one according to the literature.<sup>193</sup> According to this method, we can convert one bromo group into azido function so as to react with **DCM-*o*-propargyl**.



**Scheme 30:** Synthesis of DCM contained compound **31**.

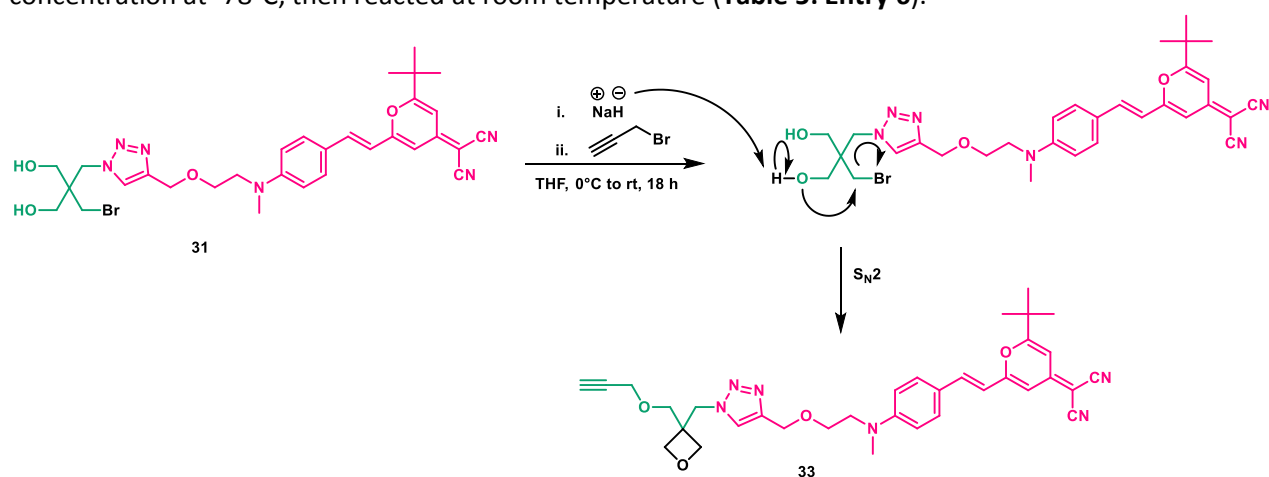
As shown in **Scheme 30**, the target linker **30** was obtained quantitatively by reacting 1 equivalent sodium azide with 2,2-*bis*(bromomethyl)-1,3-propanediol in DMSO. The mono-azide **30** then reacted with **DCM-*o*-propargyl** to obtain **31** in 77% yield.

However, the subsequent *O*-propargylation of **31** led to a mixture of the desired compound **32** and the mono-*O*-propargylated oxetane side product **33** (**Scheme 31**).



**Scheme 31:** Synthesis of target compound **32** and byproduct **33**.

The formation of **33** can be explained by an intramolecular  $S_N2$  reaction, after deprotonation of **31** by NaH (**Scheme 32**). The side product **33** is the major fraction in the presence of excess NaH. The optimization of the reaction condition was then realized for this important intermediate for the whole synthesis. The yield of **32** varies from 0 to 54% under different reaction conditions (See **Table 5**). The best yield was obtained by adding simultaneously 2.5 equivalent NaH and 20 equivalent propargyl bromide to **E1** under higher concentration at  $-78^\circ\text{C}$ , then reacted at room temperature (**Table 5: Entry 6**).



**Scheme 32:** Proposed mechanism for the formation of **33**.

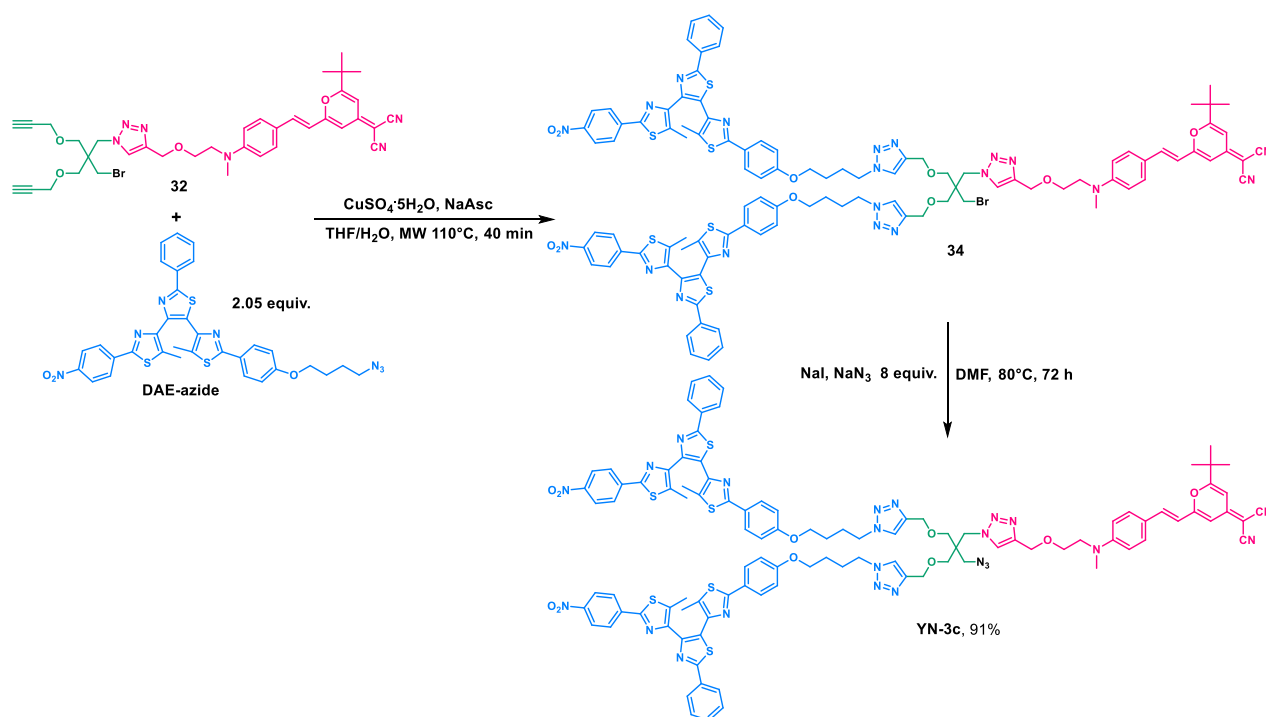
**Table 5:** Optimization of synthesis of **32**.

Entry	Molar ratio		Condition	<b>32</b>
<b>31</b>	NaH	Propargyl bromide	THF Temperature	Yield

1	1 (200 mg)	4	8	Approx. 10 mL	0°C 30 min then rt 18 h	6%
2	1 (159 mg)	2.5	4	Approx. 10 mL	0°C 30 min then rt 18 h	14%
3	1 (97 mg)	2.5	10	Approx. 10 mL	0°C 30 min then rt 18 h	25%
4	1 (269 mg)	2.5	20	Approx. 10 mL	0°C 30 min then rt 18 h	32%
5	1 (125 mg)	2.5	40	Approx. 5 mL	-78°C 3 h then rt 24 h	0%
6	1 (123 mg)	2.5	20	Approx. 5 mL	-78°C 5 min to rt 24 h	54%

### 4.3.2 Synthesis of the trichromophoric dendron

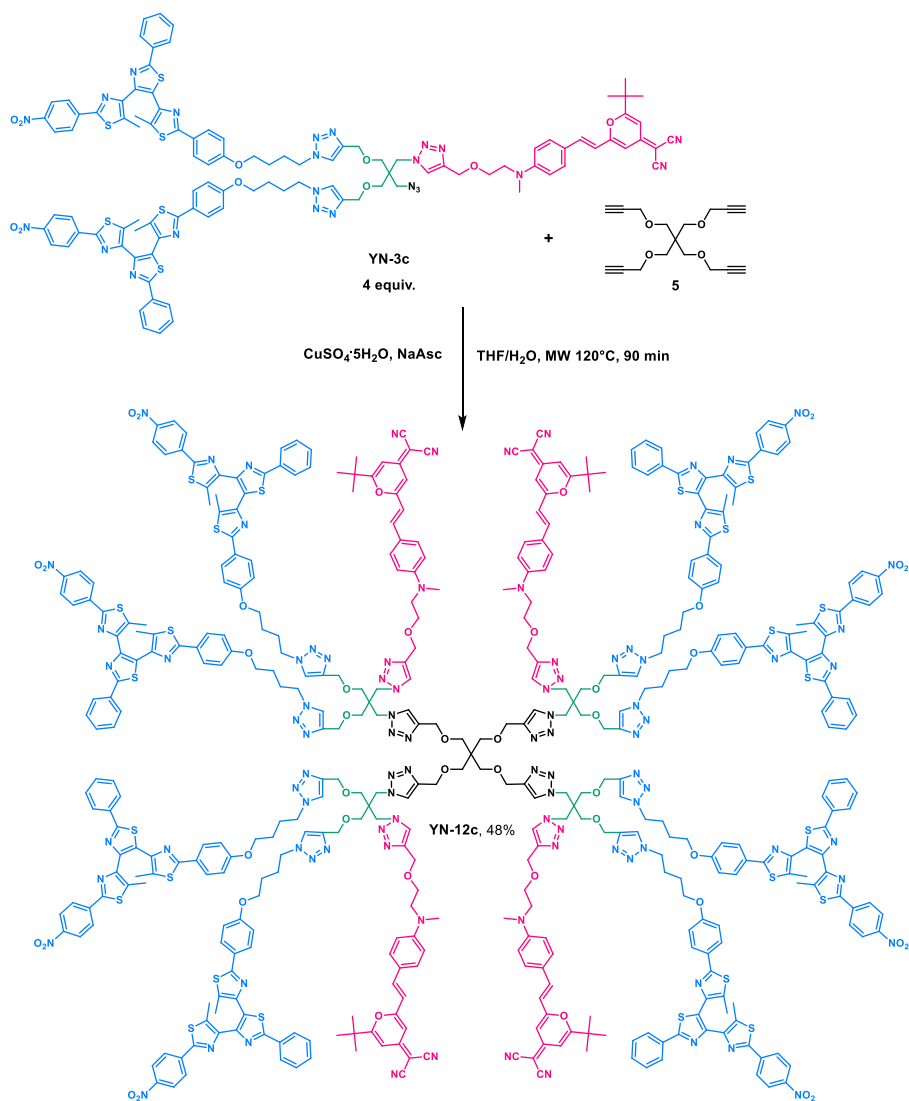
**Scheme 33** presents the CuAAC reaction between **32** and **DAE-azide** (in a molar ratio of 1:2.05) yielding **34** in 77% yield. To avoid the heavy-atom effect from the bromide, **34** was further transformed into the azido derivative **YN-3c** in 91% yield. Compound **YN-3c** has been fully characterized by NMR and HRMS and will then be investigated for the fluorescence hysteresis effect.



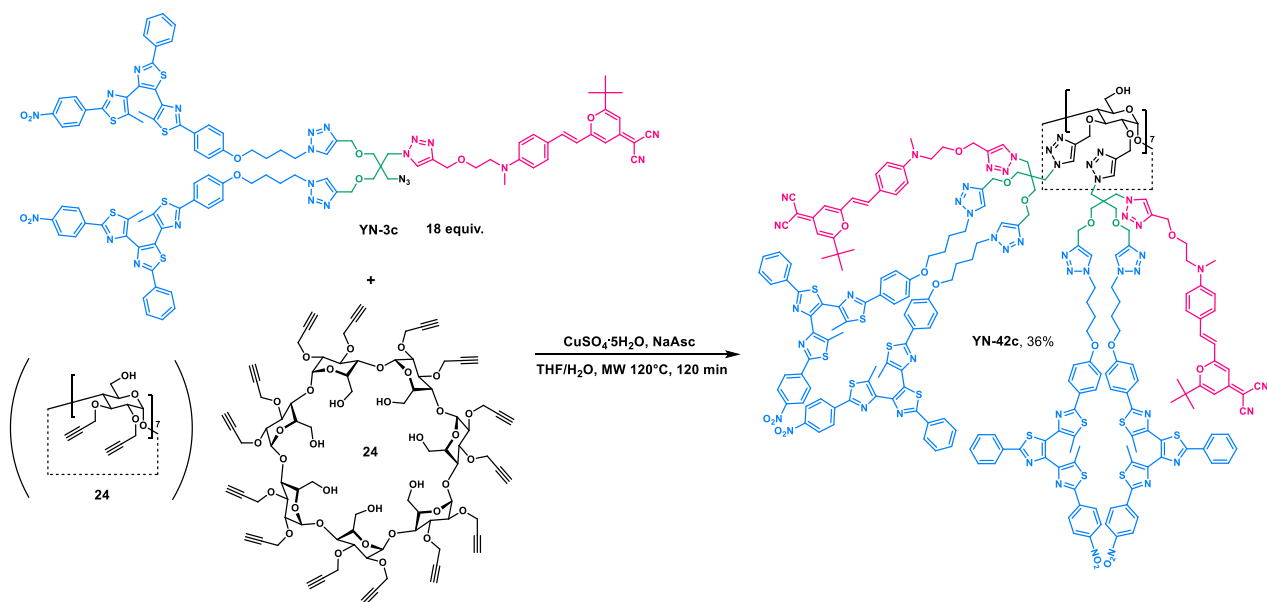
### 4.3.3 Synthesis of the dendritic architectures

We then try to prepare the dendritic compounds **YN-12c** and **YN-42c** by the click reaction between the azide-functionalized dendron **YN-3c** and the tetra-propargyl linker **5** (**Scheme 34**) or the propargylated  $\beta$ -CD **24** (**Scheme 35**).





Scheme 34: Synthesis of YN-12c.



Scheme 35: Synthesis of YN-42c.

During the synthesis of YN-12c and YN-42c, which contain respectively four and fourteen YN-3c units, CuAAC reactions between YN-3c and compound 5 or compound 24 resulted in red pellets poorly soluble

in organic solvents. Washing with a large amount of a 0.1 M EDTA solution, the usual work up for washing the organic layer, was not efficient for dissolving the reaction mixture. Only the **YN-3c** residues were found in the concentrated organic extraction, as shown on  $^1\text{H}$  NMR. The remained red pellets and precipitates were supposed to be some copper complexes due to the presence of the multiple triazole moieties. In addition of the work up with an EDTA solution, we tried the QuadraPure<sup>®</sup> resin in organic solvent, known to form strong chelates with metal ions and used for this purpose. The best way was finally to realize a sonication of the precipitates over 30 minutes in a mixture of ammonium solution and dichloromethane. The solids of target compounds were then dissolved mostly in the organic layer. After that, the water layers were combined and extracted with dichloromethane several times. The concentrated solutions were purified with CombiFlash<sup>®</sup> purifier over silica column chromatography equipped with UV-vis absorption detection.

To ensure a high purity for the spectroscopic measurements of these final compounds, a particular attention was dedicated to the optimization of the purification conditions. The **Figure 64** below reports the respective chromatograms corresponding to the purification of the compounds **YN-12c (a)** and **YN-42c (b)**. Firstly, the gradient of solvent pair was set to elute excessive **YN-3c** first with a mixture of petroleum ether and dichloromethane, then switched to 100% of dichloromethane followed by the mixed dichloromethane and methanol with an increasing polarity. The run was monitored at 458 and 280 nm, where 458 nm is the maximum absorption of DCM molecule. The remaining **YN-3c** can be seen in the **Figure 64 (b)** at around 5 minutes of elution, while another well-resolved peak appears after 20 minutes. The corresponding fraction latter was expected to be the compound containing 42 chromophoric units. No other peak was observed until 45 minutes of elution.

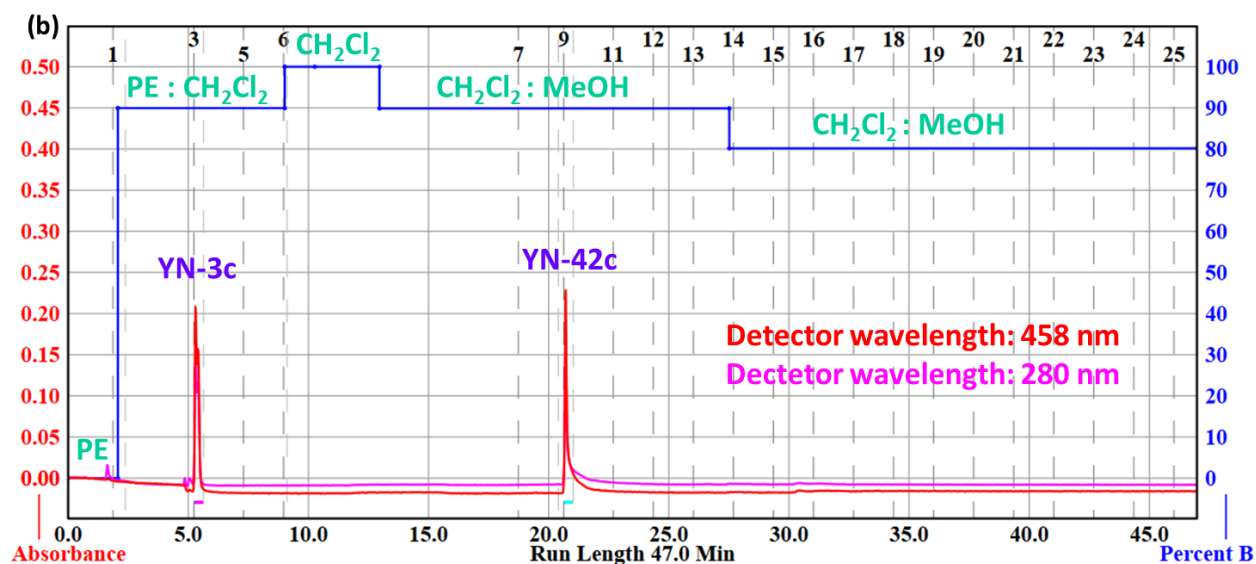
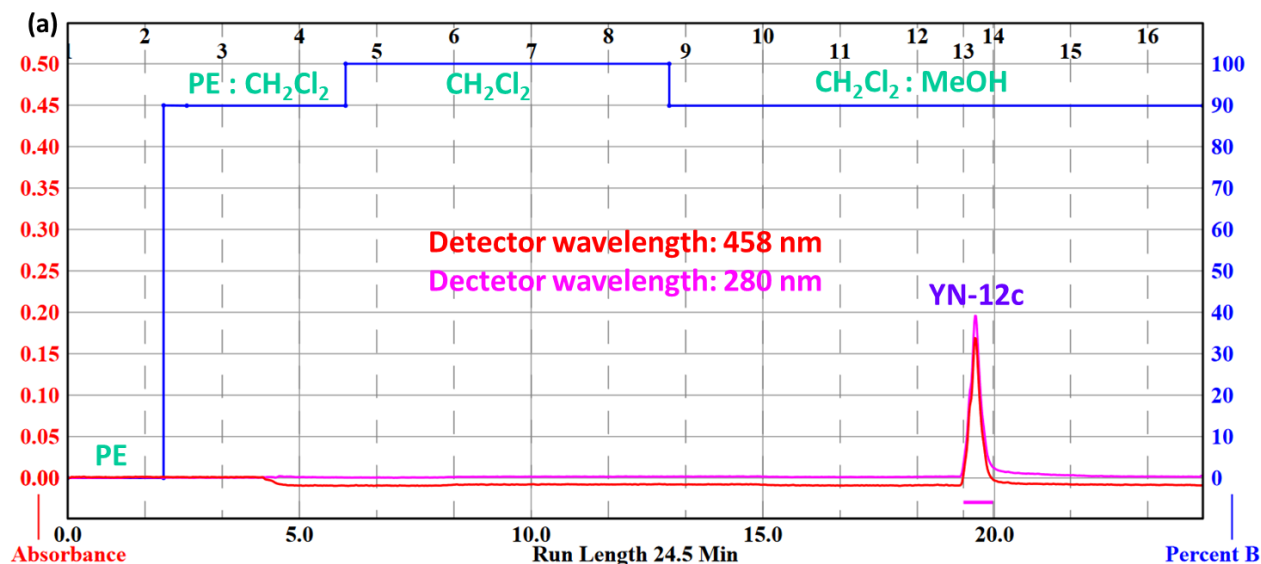


Figure 64: Column chromatograms of (a) YN-12c and (b) YN-42c.

Despite the attention paid to the purification, the validation of the molecular structure is still pending. Indeed, the NMR, the mass spectroscopy and the elemental analysis never confirmed these molecular architectures to date.

However, maybe due to the molecular size and other unknown reasons, the NMR and the mass spectroscopic determinations (already tried several times by both MALDI and ESI methods) for the two target compounds cannot be well characterized. The characterization of the two target compounds will be continued in future. The speculated YN-12c and YN-42c, paired with YN-3c, were nevertheless tested to evaluate the photoswitchable fluorescence hysteresis effect in the spectroscopic part (Paragraph 4.4.3.2), which supports the synthesis results as indirect evidence.

## 4.4 FLUORESCENCE HYSTERESIS MEASUREMENTS

### 4.4.1 Prerequisites for fluorescence hysteresis measurements

#### 4.4.1.1 Experimental measurement prerequisites

Before describing the experimental results of the fluorescence hysteresis, some prerequisites on the experimental conditions are required for a better understanding of this complex phenomenon. The **Figure 65** below represents a schematic illustration of the concept, the scenario and the expected properties.

#### The Fluorescence Hysteresis : Concept, Scenario & Properties

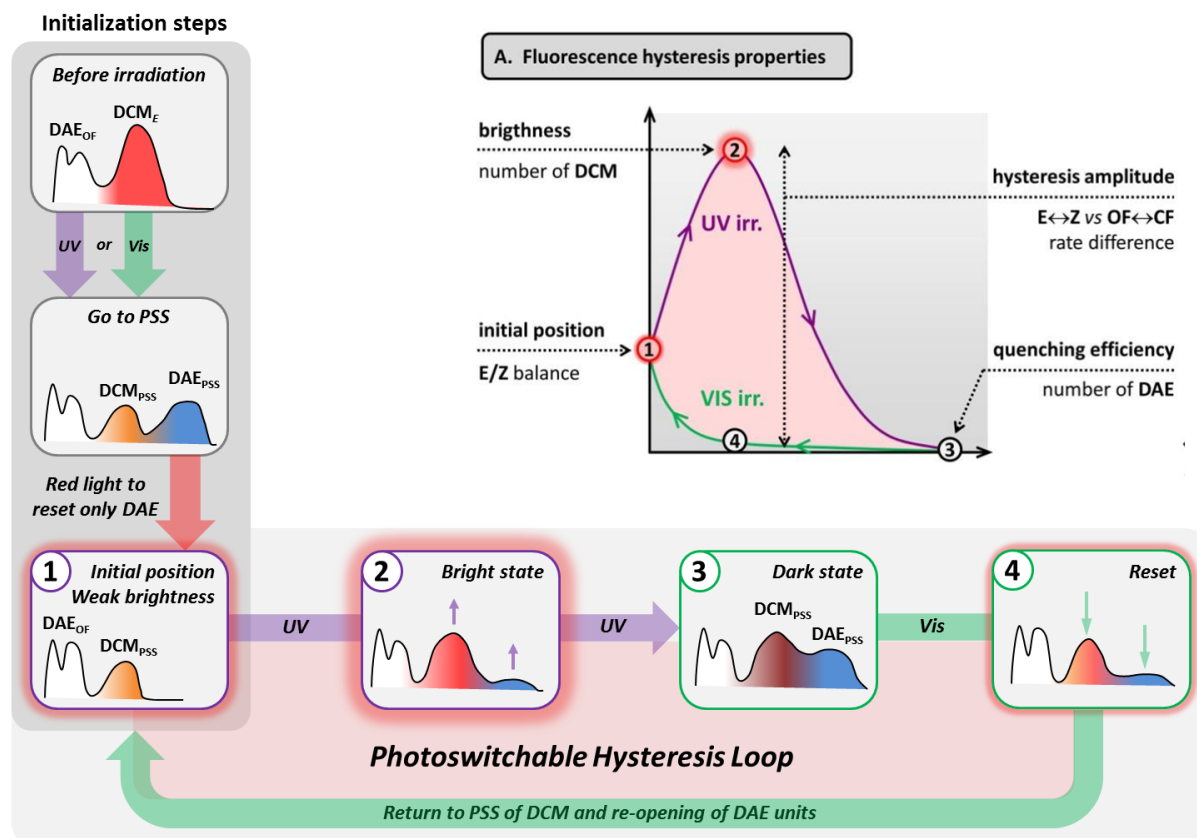


**Figure 65:** The fluorescence hysteresis outlines: an implementation with DCM and DAE molecules (shown in UV-vis absorption forms) at bottom is corresponding to the theoretical illustration on the top-right (state 1-4). DCM represents the faster  $E \leftrightarrow Z$  isomerization, and DAE represents the  $OF \leftrightarrow CF$  slow isomerization process. The preparation steps are pretreatments on the optical pure samples. The fluorescence hysteresis loop undergoes the competitive isomerizations from DAE and DCM molecules and their FRET interactions.

Before realizing the fluorescence hysteresis loop upon light irradiation, the system must be placed at an equilibrium state which is called the *initial position*. The *initial position* (1) corresponds to the  $E/Z$  balance of the population of DCM moieties in the sample, and where all the DAE units are under their open forms. To reach this state, a first series of illuminations must be realized. Before the first irradiation, we can naturally imagine that all the molecules contained in the sample are composed of DAE under their open forms, and DCM under its  $E$ -isomers. Whatever, if the sample has already been accidentally illuminated, the first irradiation consists in shining the sample by UV or visible light to reach the PSS for DCM units. In the case where the employed wavelength induces a photoconversion of the DAE in the closed form, *i.e.*, UV light at 335 nm, a second illumination is required in the red (*circa* 630 nm), where only the DAE under its closed form can absorb light, in order to recover a total population of open forms.

Once the *initial position* is reached, the illumination sequence can start. From the stage (1), an illumination by UV light reached to the stage (3). During this illumination, the composition of the different involved species in the sample change. Both DCM and DAE units are reaching to a new PSS, called PSS<sub>UV</sub>. The intermediate stage (2) which corresponds to the bright state of the system results from the increasing population of the *E*-isomers of DCM (faster process) and in the meantime a low photoconversion of the DAE under the closed form (lower process). These two competitive photoreactions are also in competition with the multiple FRET processes between the different species. This explains the sudden decrease of the fluorescence to the *dark state*, due to the major FRET process involving the *E*-DCM (donor) and the *CF*-DAE (acceptor).

Then, once the stage (3) is reached, a second illumination by visible light can be realized in order to return to the *initial position* (1). To successfully implement the *reset* step (4), the choice of the wavelength is crucial. By this, the chosen wavelength must be the same as the one chosen for the *initialization* step to ensure to reach the same distribution of species as the *initial position* (1). Upon the visible illumination, the proportion of *E*-isomer species will diminish to increase the proportion *Z*-isomers (faster process), and in the meantime, the total re-opening of the DAE units is on-going in competition with the FRET process. In one hand, it is to be noticed that the visible illumination induces the re-opening of the DAE units, but this re-opening can be also strongly pushed by the excitation of the DCM units which induce a FRET from the DCM (donor) to *CF*-DAE (acceptor). In the other hand, the photoconversion yield of the DAE cycloreversion is in this case much slower than the cyclization (precursor **DAE-nitro**  $\Phi_{OF \rightarrow CF} = 4\%$ ,  $\Phi_{CF \rightarrow OF} = 0.4\%$ ). All in all, the system must significantly decrease its population of quenchers (*CF*-DAE) in order to recover the *initial position* (1).

#### 4.4.1.2 Previous experiment considerations

In this section, we will briefly mention the previous results of *photoswitchable fluorescent hysteresis effect* obtained from the tetrachromophoric sugar (3DAE/1DCM) to introduce the importance of the data processing.<sup>79</sup>

**Figure 66** presents a series of 5 measurements realized with 5 different couples of illuminations where the same wavelength was used for the forward illumination (UV at 335 nm, in blue), and where only the wavelength for the backward photoreaction has been changed (Visible light, in red). The plotted results represent the normalized fluorescence taken at the maximum of emission as a function of the apparent molar absorption coefficient (normalised at isosbestic point) taken at different absorption wavelengths. On the left column, the absorption at 610 nm represents only the absorption of the *CF*-DAE units, while the right column represents the absorption at 462 nm of both the *CF*-DAE units and all the DCM units (*E* and *Z*). The comparison of the two columns shows that in the right one, the hysteresis gaps are larger than in the left one and offers the possibility to observe the fluorescence photomodulation thanks to the contribution of the DCM in the absorption band at 462 nm; the *initial position* is modulated thanks to the *E/Z* balance of DCM units. In other words, these plots finally demonstrate, first, the importance of the normalization of the data as a crucial parameter in obtaining the photoswitchable fluorescence hysteresis, and second, the importance of the choice of the irradiation and observation wavelengths.

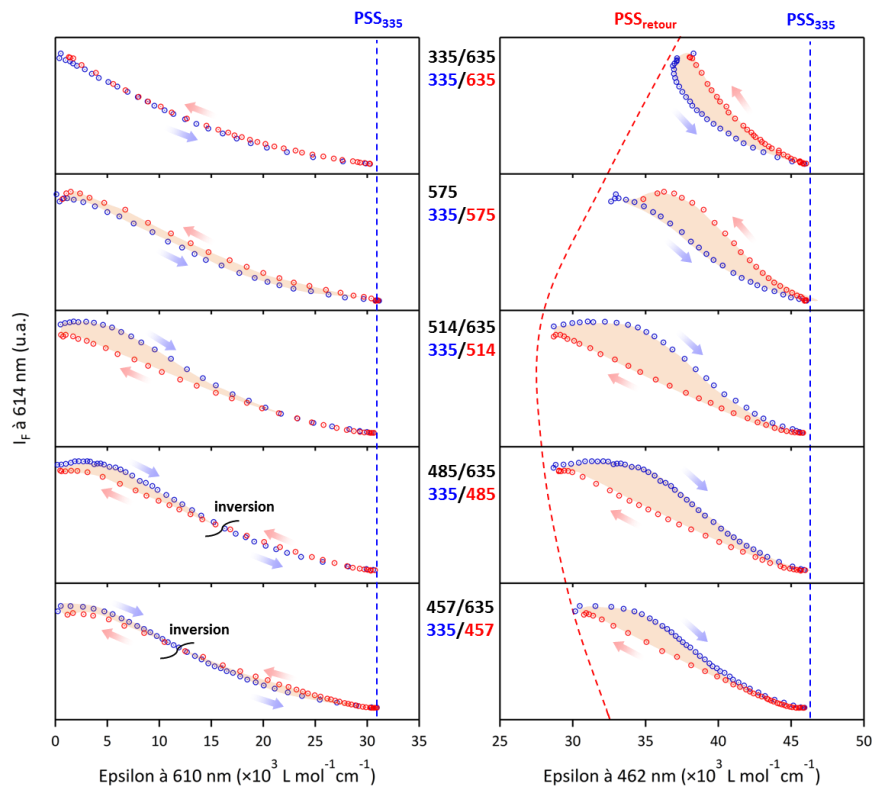


**Figure 66.** Comparison of the influence of the irradiation wavelength pairs on the shape of fluorescence hysteresis loops obtained after a plot of the normalized fluorescence intensity vs. the molar absorption coefficients. The initialization wavelength couples are represented in black, the forward irradiation in blue, and the backward irradiation in red.

## 4.4.2 Steady-state measurements

### 4.4.2.1 Photophysical properties

The **Figure 67 (a)** shows the UV-vis absorption spectra of **YN-3c** recorded in THF between 2 states corresponding to the PSS<sub>485</sub> and PSS<sub>335</sub>. The DCM characteristic absorption band is located at 468 nm, which shows a slight bathochromic shift compared to **DCM-azide** ( $\lambda_{\text{abs}} = 459$  nm). The OF-DAE absorption maximum is at 324 nm (**OF-NB105**  $\lambda_{\text{max}} = 322$  nm), and the CF-DAE characteristic band is around 625-675 nm (**CF-NB105**  $\lambda_{\text{abs}} = 625-665$  nm). The two **DAE** moieties contribute to a broad absorption band in the red region. Generally, the trichromophoric compound **YN-3c** preserves the photophysical properties of the three DCM/DAE chromophores. The normalized fluorescence spectrum obtained after excitation at 435 nm is shown in the **Figure 67 (a)** for illustrating the spectral overlap area of the CF-DAE and the DCM emission. The fluorescence almost covers the whole absorption band of the CF-DAE units, which is an important prerequisite favoring the FRET processes.

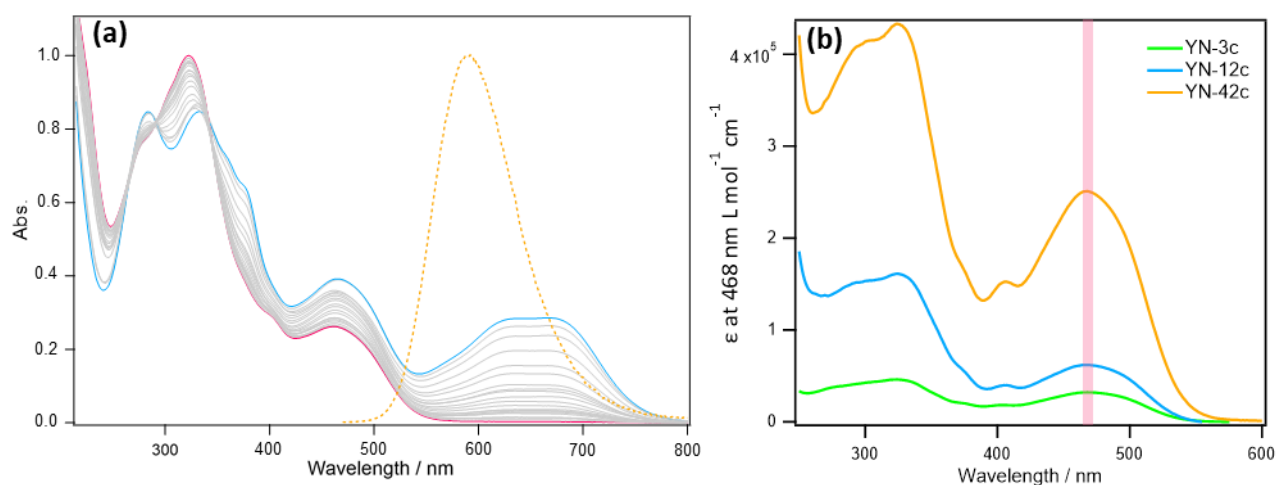


**Figure 67:** (a) Normalized UV-Vis absorption spectra of **YN-3c** between 335 (blue) and 485 nm (magenta) photostationary states and fluorescence of DCM-azide (yellow dash). (b) Absorption spectra of **YN-3c**, **YN-12c**, **YN-42c** normalized by their molar extinction coefficient at 468 nm, respectively. The red bar indicates 468 nm, contributed by DCM units. All spectra were measured in THF.

We also measured the UV-vis absorption spectra of **YN-12c** and **YN-42c**, and they share the same shape of spectrum as **YN-3c** shown in **Figure 67 (b)**, possessing the identical DCM band and DAE absorption band. The determination of the molar absorption coefficient at 468 nm shows that **YN-12c** and **YN-42c** are respectively 1.9 folds (62000 L mol<sup>-1</sup>cm<sup>-1</sup>) and 7.8 folds (251000 L mol<sup>-1</sup>cm<sup>-1</sup>) to **YN-3c** (32100 L mol<sup>-1</sup>cm<sup>-1</sup>). The molar absorption coefficients data are for reference only in the current stage due to the incomplete characterization described in the synthetic part. However, it is to be noticed that in an ideal case, where all chromophores can be considered as independent, the multichromophores are expected to be equally proportional to the sum of the chromophoric units taken alone. In the present case, the deviation from linearity suggests that **YN-12c** and **YN-42c** are effectively made of several fragments of **YN-3c** linked together, with a limited (but observable) degree of interaction between the assemblies of chromophores (such as  $\pi$ - $\pi$  interactions for instance).



#### 4.4.2.2 Demonstration of the photoswitchable fluorescence hysteresis behavior of YN-3c

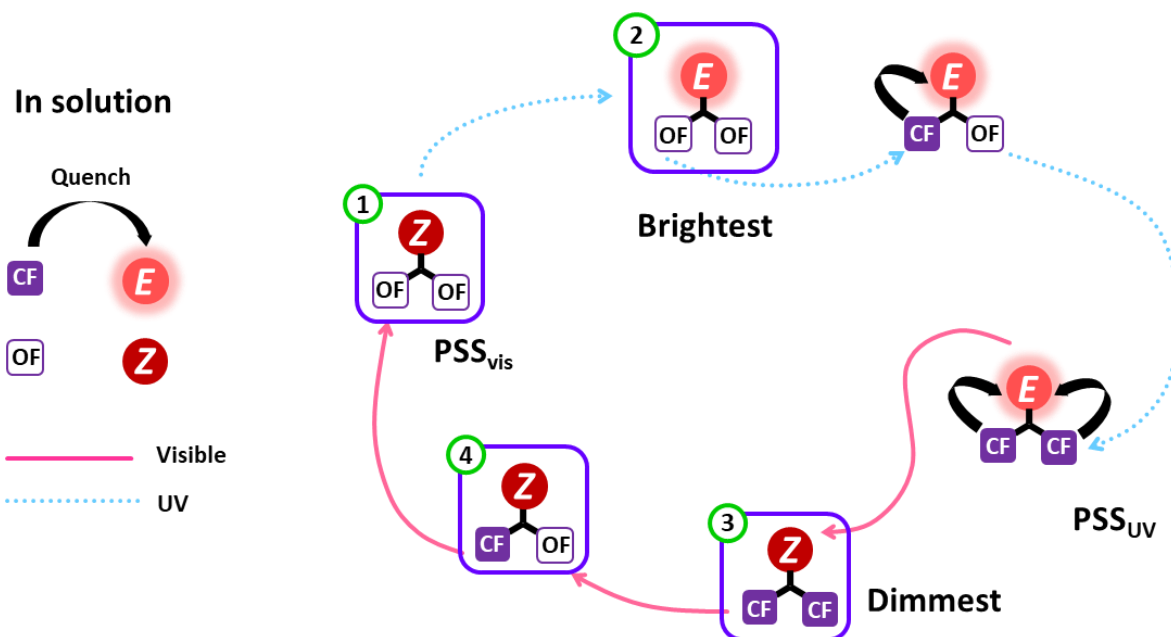


**Figure 68:** Illustration of the photoswitchable fluorescence hysteresis mechanism in the case of **YN-3c**.

If we transplant the photoswitchable fluorescence hysteresis illustration in a **YN-3c** form, we obtain the **Figure 68**. In solution, there are 4 species existing in all the process: the CF-DAE, OF-DAE, (*E*)-DCM, and (*Z*)-DCM. We prepare the solution in a pre-irradiated  $PSS_{vis}$  state **1**. Currently, there is no fluorescence quencher CF-DAE species in the solution, while due to the conversion yield of DCM, (*E*)-DCM and (*Z*)-DCM are both present as a mixture. When UV irradiation starts, the *Z*→*E* isomerization quickly happens, and the state **2**, which is the brightest state with fluorescent (*E*)-DCM and without quencher CF-DAEs, is expected to appear transiently. In the following step, OF→CF isomerization proceeds, converting DAE units into their closed forms, which quench the fluorescence from the (*E*)-DCM by FRET processes. The (*E*)-DCM keeps still under UV irradiation during the whole process and reaches  $PSS_{UV}$  state **3**. Switching to the backward reaction with visible light irradiation, *E*→*Z* isomerization has a faster equilibrium to convert (*E*)-DCM species into (*Z*)-DCM species, while the CF-DAEs are still quenching the fluorescence of the remaining (*E*)-DCMs. The state **4** is the dimmest stage of the loop. Then the visible light initiates the CF→OF isomerization (which proceeds with a lower photochromic quantum yield) and the OF-DAE will release the fluorescence from the remaining (*E*)-DCM species in solution. The fluorescence will rise until the process back to  $PSS_{vis}$  state **1**.

As demonstrated in the introduction, the fluorescence hysteresis can be plotted in the form of fluorescence at a certain wavelength vs. absorption at another certain wavelength to visualize and enhance the observed effect. We have tested the response of **YN-3c** firstly by steady-state spectroscopies in order to visualize its capability to realize a photoswitchable fluorescence hysteresis effect with only two DAE units compared to the tetrachromophoric sugar (mentioned as previous results in the section 1.5.3.3). All the measurements were carried out in argon degassed THF solution to prevent any possible photo-degradation; it has been demonstrated in a previous work that DCM units could be sensitive to air in presence of light.<sup>79</sup>

To initiate the fluorescence hysteresis shape (**Figure 68**), the **YN-3c** was first irradiated till  $PSS_{485}$  to convert partially the (*E*)-DCM to the (*Z*)-DCM while keeping the DAE in the open form. The initial state actually contains a mixture of (*E*)-DCM, (*Z*)-DCM and pure OF-DAE. The UV irradiation at 335 nm triggered the hysteresis shape. By taking the advantage of faster *E*↔*Z* photoisomerization, the (*Z*)-DCM in the solution system was converted to emissive (*E*)-DCM immediately, and the fluorescence intensity started to rise. After that, the OF↔CF isomerization process started to be visible by fluorescence quenching. The

UV irradiation transformed DAE units into closed forms to allow efficient FRET between the (*E*)-DCM and CF-DAE units, lowering down drastically the fluorescence intensity. Meanwhile, the absorption at 468 nm increased from PSS<sub>485</sub> referring to the UV-vis absorption spectra.

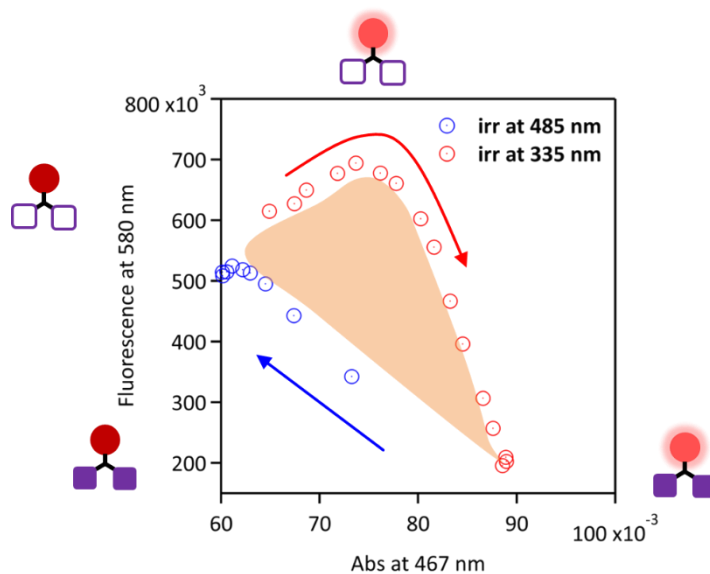


**Figure 69:** Fluorescence hysteresis shape plotted in the fluorescence (580 nm) vs. absorption (467 nm). Data obtained on **YN-3c** under irradiation of 485/335 nm. The dark red circle represents the (*Z*)-DCM; the bright red circle represents the (*E*)-DCM; the blank violet square represents the OF-DAE; the filled violet square represents the CF-DAE; The red arrow points to the forward reaction irradiated by UV 335 nm light source, and the blue arrow points to the backward reaction irradiated by visible 485 nm light source.

As shown in **Figure 69**, the PSS<sub>335</sub> state is an equilibrium state where the CF-DAE quenches the fluorescence of (*E*)-DCM, which was isomerized from the (*Z*)-DCM upon irradiation. When the **YN-3c** was irradiated at 485 nm visible light, the (*E*)-DCM quickly isomerizes into (*Z*)-DCM. Subsequently, the CF→OF isomerization contributes to decrease the number of fluorescence quenchers in the system. The intrinsic population of (*E*)-DCM of the sample started to increase the fluorescence intensity until PSS<sub>485</sub> as the full process of the backward reaction. So far, one fluorescence hysteresis shape has been completed. The missing data points in the beginning of backward reaction can be ascribed to the speed of isomerizing trichromophoric unit is very high and could not be observed under the steady-state condition. Besides, the test on **YN-3c** depicted a remarkable photoswitchable fluorescence hysteresis, which represents the minimal and fully functional unit bearing an azido group for further expansions.

#### 4.4.3 Dual photokinetics hysteresis measurement

##### 4.4.3.1 Setup description

The realization of the fluorescence hysteresis experiment by steady-state measurements described in the previous section is strongly time-consuming. Depending on the expected number of data points, a full acquisition can take 4 to 9 hours. Also, this method has several additional drawbacks: (i) we do not record absorption and fluorescence simultaneously, which can lead to changes in the sample state between the measurements, and (ii) only the fluorescence intensity is measured over very short period to prevent the photoconversion due to the light irradiation of the excitation beam of the fluorimeter.

Our idea was to extend the possibilities of an older setup, called “continuous photokinetics”, by adding a spectrofluorimeter to collect on a CCD camera simultaneously both absorption and emission spectra during the irradiation of the sample. Such a setup could be considered as a “dual photokinetics” hysteresis measurement. The implementation and the development of this equipment was one challenging task of the ANR SWIST project.

The “dual photokinetics” apparatus for measuring fluorescence and absorption simultaneously was built in the PPSM Laboratory by A. Brosseau and Dr R. Métivier, as shown in **Figure 70**. The beam is powered by one cw-Xenon lamp, split by one beam splitter into two beams. The excitation beam is the one passing through a pinhole and dichroic mirror to excite the sample and collect the fluorescence signal. The other one is directed through a neutral density filter and a diaphragm for measuring the absorption of the sample perpendicular to the excitation beam. The fluorescence and absorption signals are collected by a spectrograph (FERGIE, Princeton Instruments) through two optical fibers. Therefore, the simultaneous measurements of absorption and fluorescence can be implemented by receiving both signals on the same CCD camera (in two different regions of interests of the CCD).

The irradiation part is powered by one cw-Mercury-Xenon lamp, reflected by a prism in the total reflection mode, to cover the irradiation light onto the whole sample cuvette surface. The current setup is optimized for the fixed sample holder suitable for thin films, and the 2×6 mm path cuvettes when applying irradiation outside. The ordinary cuvettes cannot ensure the solution inside to be fully covered by the irradiation light.

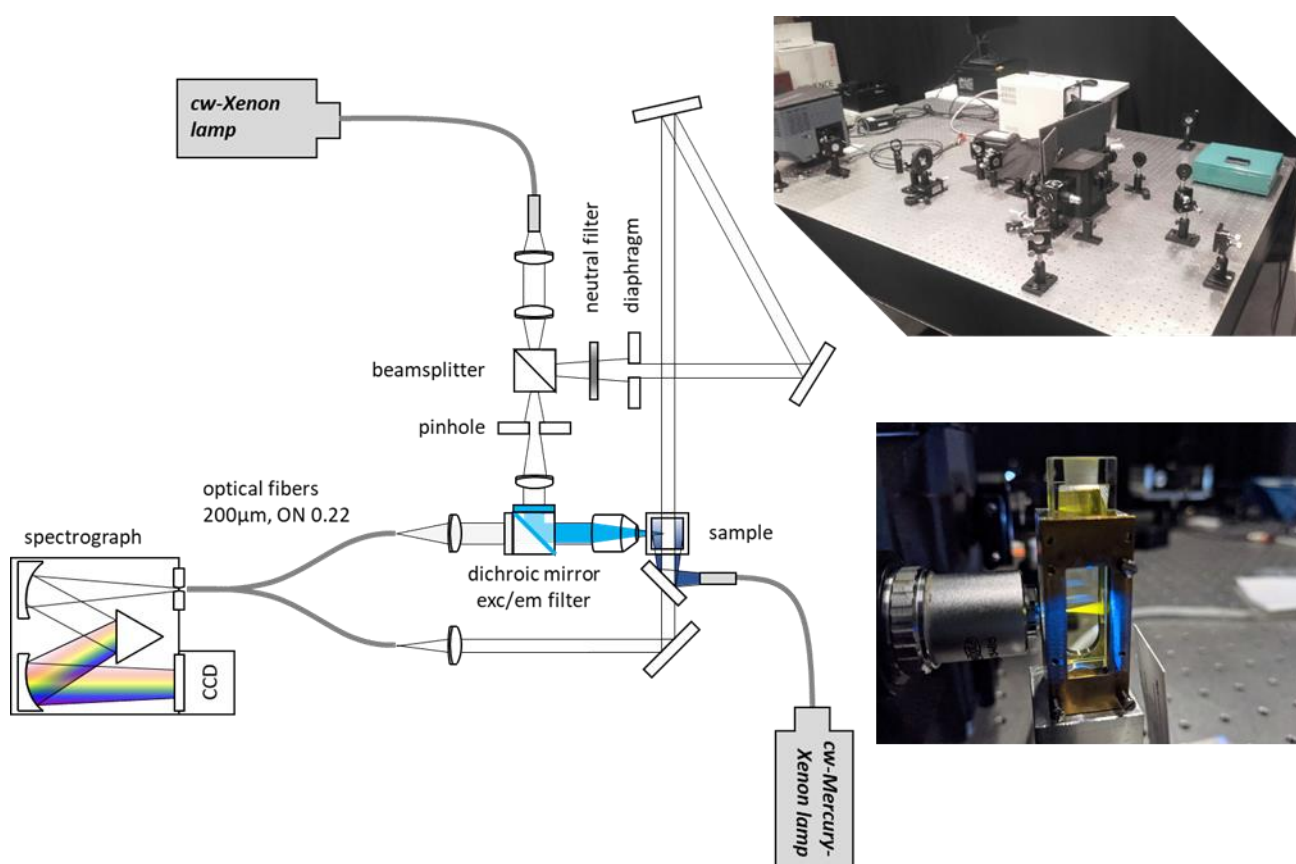


**Figure 70:** Illustration of the continuous photokinetics setup-II built in PPSM and one fluorescent test sample.

#### 4.4.3.2 Improvement of the setup with the multichromophoric compounds

The processed results of the multichromophoric molecules array are shown in the **Figure 71**. To obtain this series of graphs, the sample was previously illuminated at 485 nm in order to reach the initial position (*E/Z* balance + OF-DAE). Then, the forward photoreaction was firstly irradiated at 335 nm using a UV filter, and the backward photoreaction was carried out through a 514 nm filter.

The collected data points were extracted from the fluorescence and absorption raw of spectra, respectively at 590 nm, and at 468 nm. The raw absorption curves were then treated with exponential curve fitting to reduce the noise due to the background signal fluctuations.

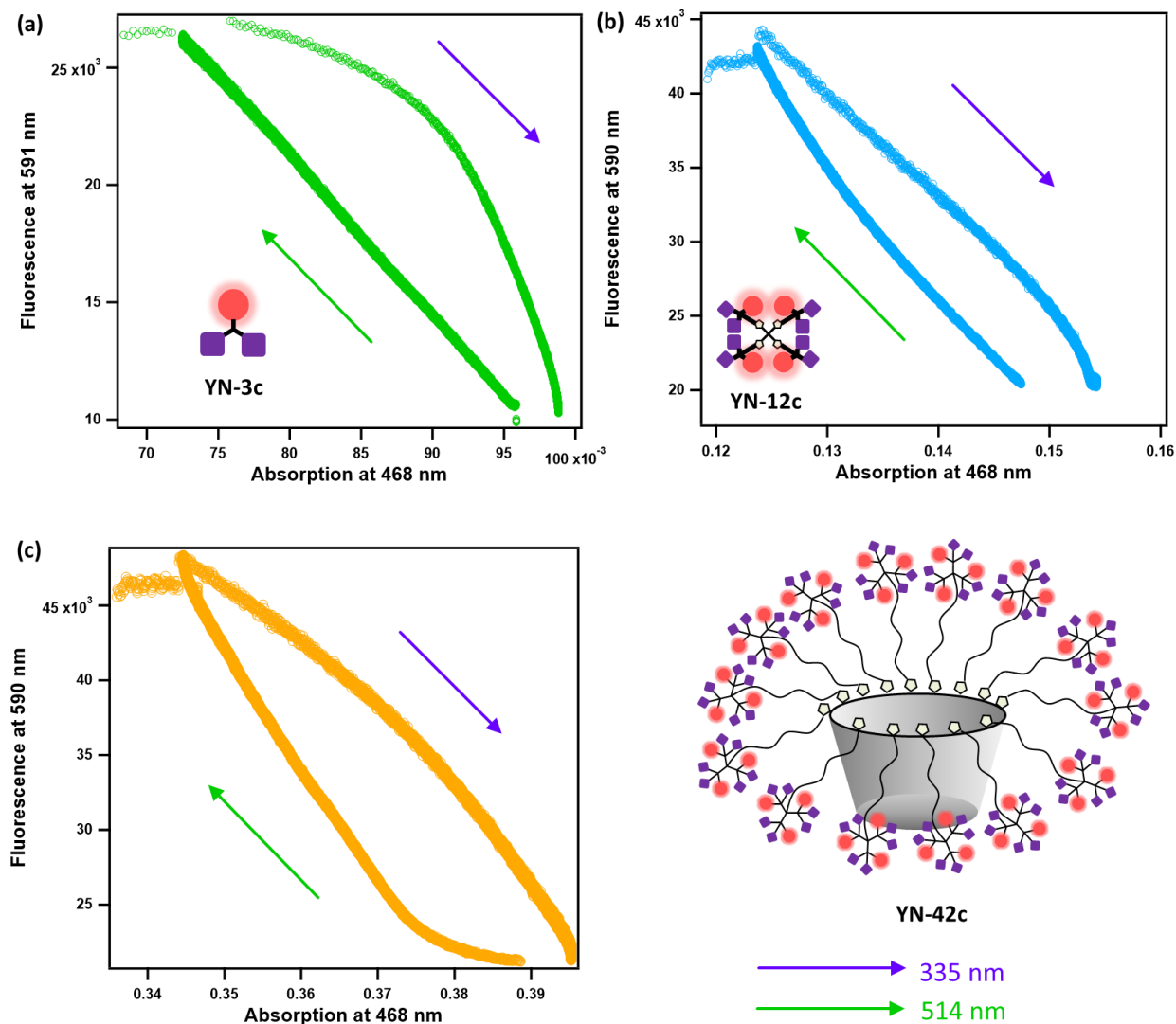


**Figure 71:** Preliminary fluorescence hysteresis obtained on the new photokinetic setup with a THF solution of compound (a) **YN-3c**, (b) **YN-12c**, (c) **YN-42c**. The violet arrow points to the forward reaction irradiated by 335 nm UV light, and the green arrow points to the backward reaction irradiated by 514 nm visible light.

It is important to note that preliminary tries were carried out with a 485 nm filter to cover the maximum absorption of the DCM band. We have then decided to abandon this way due to the important fluctuations identified as coming from the irradiation source which reflects on the 468 nm data sampling area, causing a huge deviation on the final data. Compared to the steady-state results shown in **Figure 69**, the first difference identified for **YN-3c** concerns the expected bright state **2** corresponding to the rise up stage of fluorescence intensity, which is missing under visible illumination at 485 nm (from the  $PSS_{485}$ , where (*Z*)-DCM isomerizes to (*E*)-DCM). This is attributed to the 480 nm excitation beam: the current “dual photokinetics” system actually suffers from the continuous excitation beam in the sampling area, keeping part of the molecules in solution influenced by the small area of excitation light (See **Figure 70**). This acts as a second source of irradiation, disturbing the expected hysteresis curve. In order to counterbalance the influence of the intrinsic excitation beam of the setup, the irradiation source has to be raised to a relatively high output power. Additionally, the power must be high enough to ensure reaching the proper  $PSS_{335}$ . In other words, the competition between the irradiations at 335 nm and at 480 nm led to an intermediate state located between the  $PSS_{335}$  and  $PSS_{480}$ , and will not end up with one confirmable termination.

Therefore, the “dual photokinetics” setup in the current stage can measure the fluorescence hysteresis with some limitations. With the **YN** array, the further tests for mutual improvements on this facility will be implemented. The key points to improve the data quality are listed below:

1. Reduce the excitation beam intensity.
2. Use specific sample holders allowing the irradiation and acceptable absorption data quality when applying stirring of the solution.
3. Raise the absorption signal quality to improve the light intensity passing through the optical fiber.

These preliminary results show a good practice on the new “dual photokinetics” setup, and very promising hysteresis shapes, changing along the increasing number of chromophores in the system. The **YN-3c** has a straight backward reaction line, and **YN-12c** starts to be curved. **YN-42c** has one even more curved backward reaction line until the PSS<sub>514</sub>. First, it could be considered as an indirect proof that the synthesis was successfully building up larger multichromophores by using the **YN-3c** dendron. In the featured backward reaction of **YN-42c** shown in **Figure 71 (c)**, we definitely observed that with the increment of chromophoric units in the system, the *E*→*Z* isomerization is faster, so that there is a drop down in absorption from 0.39 down to 0.38, accompanied with more *Z*-isomer generation. The CF→OF isomerization reduced the fluorescence quenching effect which is slower than the *E*→*Z* isomerization at the beginning, and then comes to the normal rate, showing the curve in the backward reaction. The forward reaction under UV irradiation is tough to draw conclusions. As mentioned, the competitive excitation beam and relatively high-power irradiation, compared to the visible range, will blur some details.

The studies on the “dual photokinetics” setup are preliminary explorations, however, it has already brought promising directions to improve the experimental instrument and the hysteresis data on the considered multichromophoric molecules.

## 4.5 MOLECULAR DYNAMICS SIMULATIONS ON DENDRON **YN-3c**

In addition of the measurements of the photoswitchable fluorescence hysteresis, it is necessary to know whether the mechanism of FRET is efficient in the simple building block **YN-3c**, based on simulation approaches. For this reason, we investigated not only the FRET efficiency values, but all the parameters which influence the FRET efficiency as well, by means of molecular dynamics (MD) simulations.

### 4.5.1 Trajectory-based analysis

In the MD simulation part that we have described in the **Chapter III**, we have implemented solid workflows and methodologies to support the spectroscopic studies and confirm the FRET mechanisms. Thanks to this experience, we decided to focus our attention on the trichromophoric unit **YN-3c**, where our purpose is the investigation of the intramolecular FRET efficiencies occurring within this structure. The trichromophoric unit **YN-3c** is designed by arranging one *E*-DCM unit as the donor and two DAE units as the acceptors. The closed form DAE (CF-DAE) is the only acceptor while there is no FRET existing between the open form DAE (OF-DAE) and the DCM. It is important to remind us that the **(OF)-DAE-azide** is not fluorescent, and cannot be considered as a donor. Therefore, we have built three configurations to study FRET efficiencies, CF-CF, CF-OF(anti), CF-OF(para), respectively (See **Figure 72**). The **(OF)-DAE-anti** and **(OF)-DAE-para** are calculated as the steric hindrance may be different within the D-A pair, when investigating whether there exist different FRET efficiencies compared to the double-donor CF-CF configuration.

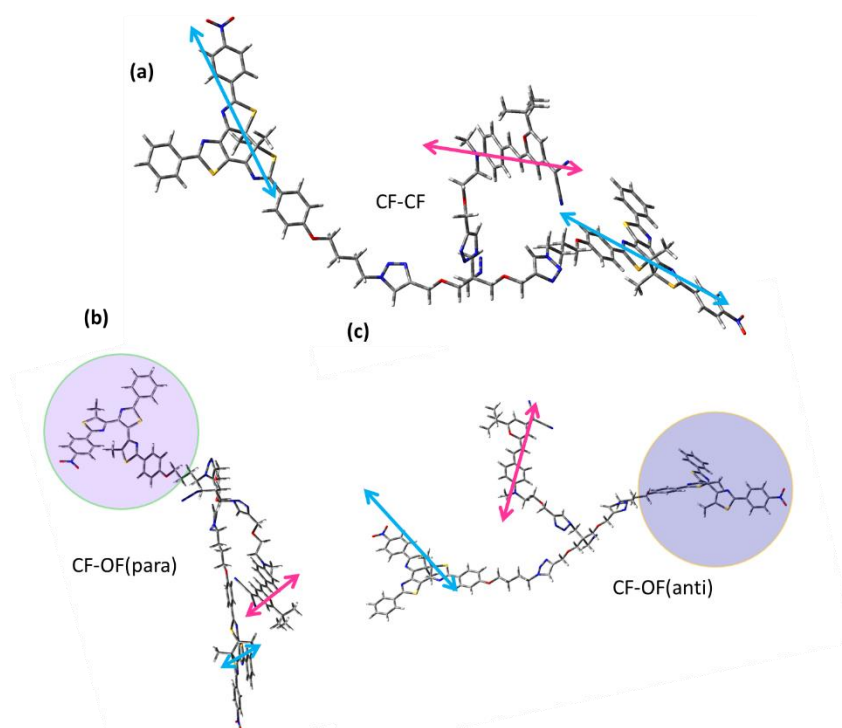


**Figure 72:** **YN-3c** configurations of (a) CF-CF (b) CF-OF(para) (c) CF-OF(anti) to be prepared for MD simulations. Blue arrows are the dipole moment vector illustrations of DAE units, and the magenta arrows are the dipole moment vector illustrations of DCM units.

The DCM and DAE moieties in **YN-3c** were taken from the DFT calculations in **Chapter II** and **4.2.2**. Each configuration was handled with RESP method elucidated in **Chapter III** and packed with 1500 THF molecules with Packmol.<sup>194</sup> The MD simulation procedures are identical to the **2DCM** simulation, including the energy minimization, the NPT (constant number, volume and temperature) ensemble equilibrium run and the NPT ensemble production run. Each production trajectory lasts for 325 ns.

The dipole moment vectors and mass centers were defined in the same way for the DCM and DAE moieties, as described in **Chapter III** to calculate the orientation factors  $\kappa^2$  and to read the D-A pair distance  $R_{DA}$ . The spectral overlap integral  $J(\lambda)$  was calculated to be  $1.557 \times 10^{15} \text{ nm}^4 \text{ M}^{-1} \text{ cm}^{-1}$ . Following, the instantaneous  $E_{\text{FRET}}(t)$  can be derived from the instantaneous orientation factor  $\kappa^2(t)$  and the interchromophoric distance  $R_{DA}(t)$ .

The **Figure 73** provides the full information about the CF-CF configuration **YN-3c** in MD simulation, including the  $E_{\text{FRET}}(t)$ ,  $R_{DA}(t)$ ,  $\kappa^2(t)$  and their respective histograms. As there are two acceptors (CF-DAE) in the configuration, each was calculated independently with the donor (*E*-DCM). The average FRET efficiencies for each D-A pair in **YN-3c** reach values as high as 94% and 93%, due to the two orders of magnitude higher  $J(\lambda)$  of **YN-3c** compared to the case of **2DCM** explained in **Chapter III**. In the histograms shown in **Figure 73 (b) (c)**, most of the data points of  $E_{\text{FRET}}(t)$  are located at values higher than 90%. At first, the MD simulation results indicate that the design of the molecule is successful. FRET is expected to occur quite efficiently with each pair of DCM and DAE.

The statistics of  $R_{DA}(t)$  shows that the D-A pairs are rarely far away from each other. The population in the region of 3-4 nm is low, due to the molecular design of the compact dendritic linker part. From the  $R_{DA}(t)$  trajectories shown in **Figure 73 (d)**, there are not many events either above 3 nm or under 1 nm. The population in the region 1-2 nm records the highest level in both D-A pairs, indicating that a sandwich-like A-D-A arrangement in the space is common. On the other side, the  $\kappa^2(t)$  seems to be less informative, but the values are dispersed over a large range of values, with larger populations in the interval 0-2, showing that the most favorable colinear geometry for FRET is not often reached.

To further analyze the results, we restricted the data of CF-CF **YN-3c** by selecting exclusively the situations where the FRET efficiency values ( $E_{\text{FRET}}(t)$ ) of one D-A pair is under 80% while leaving the other one free. The corresponding data were extracted with the criteria mentioned in the **Figure 74 (a) and (b)**. The remaining data points demonstrated that the same region of  $R_{\text{DA}}(t)$  distribution is found compared to the full data set in **Figure 74 (c) and (d)**, showing that the lower values of  $E_{\text{FRET}}(t)$  are not correlated to large distances in the D-A pairs. However, in **Figure Figure 74 (e) and (f)**, the  $\kappa^2(t)$  values corresponding to low FRET efficiencies  $E_{\text{FRET}}(t) < 80\%$  are almost all reaching the 0 level. Consequently, we can conclude that the  $R_{\text{DA}}$  is not the main geometrical parameter governing the total  $E_{\text{FRET}}$ , but rather the orientation factor  $\kappa^2(t)$ , for which the low  $E_{\text{FRET}}$  values are ascribed to the low values of  $\kappa^2$ . Therefore, the **YN-3c** design ensures that there is always one pair of DCM and DAE that can occur high FRET efficiently, even if the other one is transiently unfavored due to unfavorable mutual orientation of the D-A pair.

In **Figure 75**, we extracted the  $E_{\text{FRET}}(t)$  and  $\kappa^2(t)$  trajectories with the condition of  $\kappa^2 > 1$  for both D-A pairs. The corresponding  $E_{\text{FRET}}$  values are all approaching 100%, as expected. From both side of the screened results, the interchromophoric distance  $R_{\text{DA}}$  between the DCM and DAE units does not play an essential character in influencing the intramolecular FRET efficiencies, thanks to the compact dendritic linker design of **YN-3c** molecule.





**Figure 73:** Calculated trajectories obtained from MD simulation on **YN-3c** in the CF-CF configuration. **(a)** Calculated  $E_{\text{FRET}}(t)$  trajectories of the two DCM-DAE D-A pairs. **(b) (c)** Calculated histograms of the two sets of  $E_{\text{FRET}}(t)$ . **(d)** Calculated  $R_{\text{DA}}(t)$  trajectories of the two DCM-DAE D-A pairs (in nm). **(e) (f)** Calculated histograms of the two sets of  $R_{\text{DA}}(t)$  (in nm). **(g) (h)** Calculated histograms of the two sets of  $k^2(t)$ . **(i)** Calculated  $\kappa^2(t)$  trajectories of the two DCM-DAE D-A pairs.

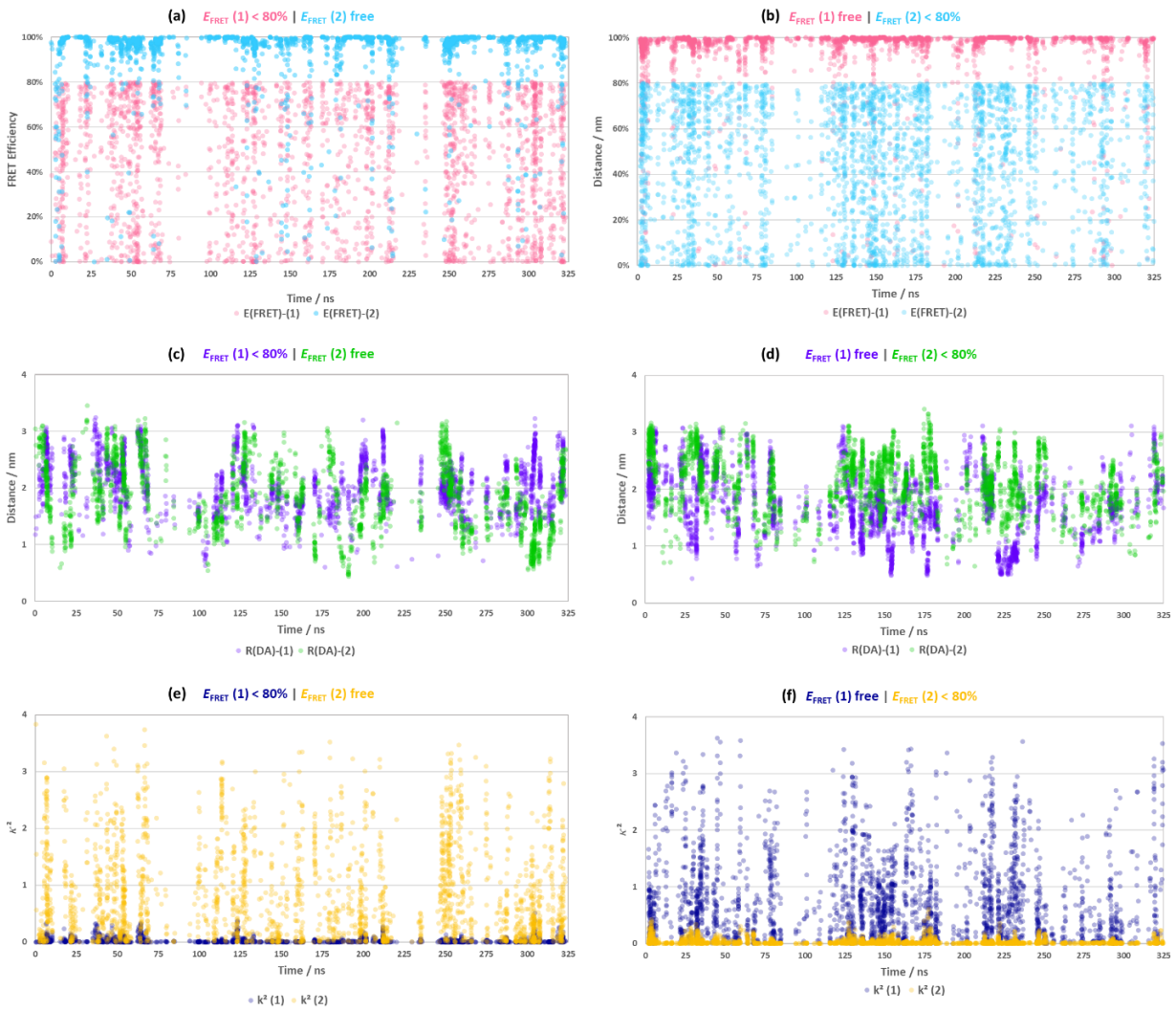


**Figure 74:** Calculated trajectories obtained from MD simulation on **YN-3c** in the CF-CF configuration, with restricted conditions on  $E_{\text{FRET}}(t)$ . **(a) (b)** Calculated  $E_{\text{FRET}}(t)$  trajectories of the two DCM-DAE D-A pairs when one side is below 80%. **(c) (d)** Calculated  $R_{\text{DA}}(t)$  trajectories of the two DCM-DAE D-A pairs when one side has a  $E_{\text{FRET}}(t)$  below 80%. **(e) (f)** Calculated  $\kappa^2(t)$  trajectories of the two DCM-DAE D-A pairs when one side has a  $E_{\text{FRET}}(t)$  below 80%.

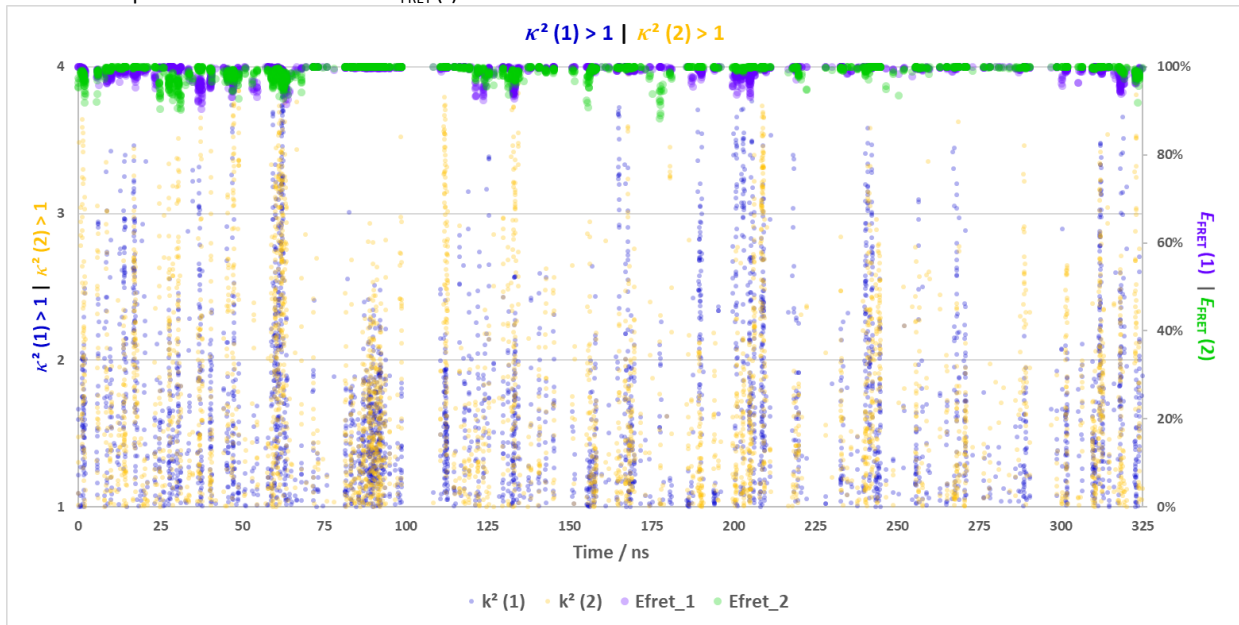


**Figure 75:** Calculated  $E_{\text{FRET}}(t)$  and  $\kappa^2(t)$  trajectories obtained from MD simulation when both side have  $\kappa^2(t)$  higher than 1.

In the other two MD simulations performed on the CF-OF-para and CF-OF-anti configurations of **YN-3c**, the **OF-DAE** moieties can be considered to play the role of inert species, just introducing additional steric hindrance between the *E*-DCM unit (donor) and the **CF-DAE** moiety (acceptor). CF-OF-anti reaches an average FRET efficiency at 92% and CF-OF-para reaches 91% during the 325 ns MD simulation trajectories for each, respectively. These figures are consistent with the independently calculated results of the CF-CF model, which demonstrate that the design of the **YN-3c** molecule is compact enough and flexible with several degrees of freedom, a favorable situation to let the intramolecular FRET to occur efficiently. We also extracted the trajectories, selecting exclusively the frames with the restriction criteria of  $E_{\text{FRET}}(t) < 80\%$ , as shown in the **Figure 76** for both CF-OF-para and CF-OF-anti configurations. As expected, the distance between the donor and acceptor of the D-A pair is not responsible for the lower FRET efficiency, but the  $\kappa^2$  values are all approaching the 0 level for both models. The conclusions are then identical to the CF-CF model: as shown by the simulations, the FRET efficiency is expected to be excellent in the **YN-3c** dendron, whatever the configuration (only one CF-DAE is enough to ensure the FRET), and the only situation which can transiently lead to lower FRET efficiency is related to the mutual orientation between the DCM and CF-DAE units.

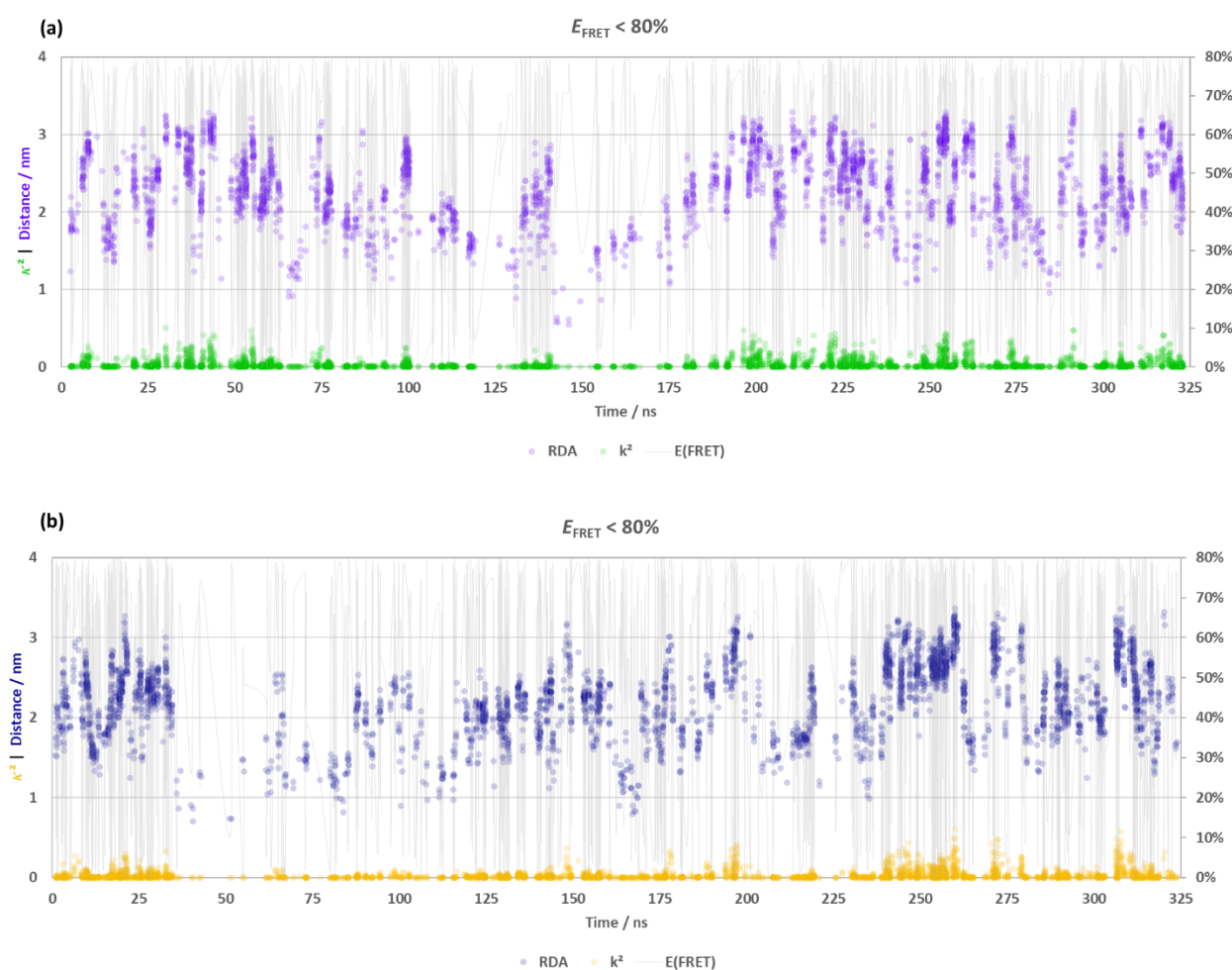


**Figure 76:** Calculated  $E_{\text{FRET}}(t)$ ,  $R_{\text{DA}}(t)$  and  $\kappa^2(t)$  trajectories obtained from MD simulation on **YN-3c** (a) in the CF-OF-para configuration and (b) in the CF-OF-anti configuration, with restricted condition on  $E_{\text{FRET}}(t) < 80\%$ .

To summarize the trajectory-based analysis of the MD simulations, the molecular design of **YN-3c** can ensure the effective intramolecular FRET to occur between the DCM and DAE moieties, at least over 90% efficiency thanks to the simulations. The D-A orientation factor  $\kappa^2$  controls the least FRET-efficient events primarily. In other words, we tried to reduce the influence of the interchromophoric distance  $R_{\text{DA}}$

parameter on the total efficiency from the molecular design level. The high intramolecular efficiencies provide a good foundation for the implementation of fluorescence hysteresis on **YN-3c** and its derivatives.

## 4.5.2 MSM analysis

Following the methodology described in **Chapter III**, we have implemented the MSM to the three configurations of **YN-3c**. The MSMs were all obtained with 200 microstates using *k*-means clustering method and further lumped into 6 metastable states using PCCA+ method each. The CF-CF, CF-OF(para), CF-OF(anti) are depicted in 2D FELs and 3D FELs in **Figure 77**, **Figure 78**, **Figure 79** respectively.

In the **Figure 77**, CF-CF configuration has the specific conformation of “well-folded” geometry shown in CF-CF(A) marked with orange color. The black CF-CF(3) metastable states cannot be precisely clustered into one shape, however, it can be seen as a little “chaotic” form of CF-CF(A), still keeping the three chromophores together. The magenta CF-CF(4) is similar but kicks one chromophore outside the group. The green CF-CF(B) represents the unfolded conformations. The “well-folded conformations” → “folded conformations” → “unfolded conformations” chain covers 96% of the transition pathway flux in 325 ns time duration.

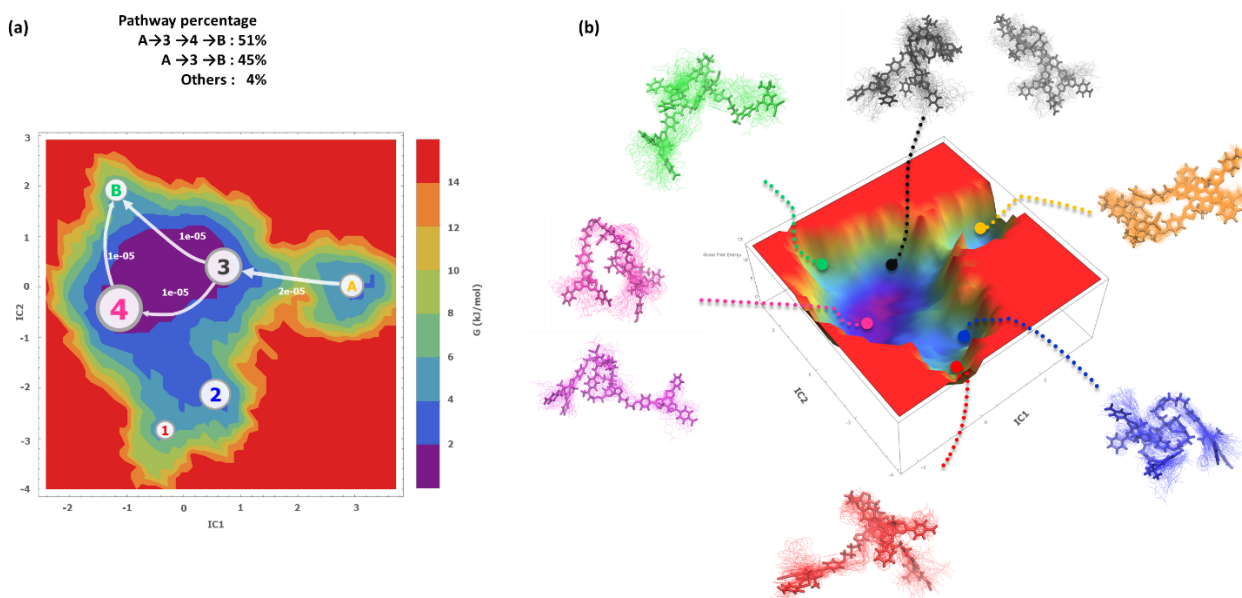


**Figure 77:** Free energy landscape of the **YN-3c** in the CF-CF configuration, corresponding tICA-FEL visualized MSM in 2D **(a)** and 3D **(b)**. The *k*-means clustering method generated 200 microstates that are lumped into 6 metastable states by PCCA+ algorithm. The metastable states trajectories are clustered to extract the major conformations in six colors, which are corresponding to the labels in the transition pathway maps. The size of the labels and the arrows in **(a)** correspond to their proportional coarse-grained fluxes. The percentages of transition pathways are listed above.

In the case of CF-OF(para), the situation is more complicated in the transition pathway flux routes as shown in **Figure 78**. The terminal green cluster CF-OF(para)(B) has a clear pattern of “trident” conformation. Even one cluster in red CF-OF(para)(1) has the similar form, indicating that the type of geometry has a wide range coverage on the free-energy landscape (FEL). All other clusters represent conformations which have more or less unfolded types. Especially the magenta CF-OF(para)(4) contributes to a large part of the transition pathway flux, showing a stretching conformation where two chromophores are in one side and the other one on the opposite side. The whole transitions can be seen as the stretching open forms gathering together.

On the other side, the CF-OF(anti) shown in **Figure 79** does not share the similar patterns of cluster conformations to the CF-OF(para), though both of them are considered to have one D-A pair and a steric hindrance. The resulted cluster conformations are more comparable to those of the CF-CF configuration.



It is reasonable to note that **OF-DAE-anti** moiety is more planar and more close to the completely planar **CF-DAE**. The starting orange clusters and ending green clusters are similar. The difference is that in CF-OF-anti, the molecule has more star-stretching conformations (CF-OF(anti-4)).

Due to the interchromophoric distance, the conclusion that **YN-3c** FRET efficiencies are mostly depending on the orientation factors of the D-A pair, which was already shown and discussed in the section 4.5.1. However, the MSM provides us the view that the conformations and transition pathways of each configuration are depending on every chromophore unit inside. The similar planar structures have the similar clusters in statistics, even though one of them is just used as steric hinderance. In addition, MSMs still indicate that for such structures, the structural shrinking and the expanding in conformations are the main transitions in simulations.

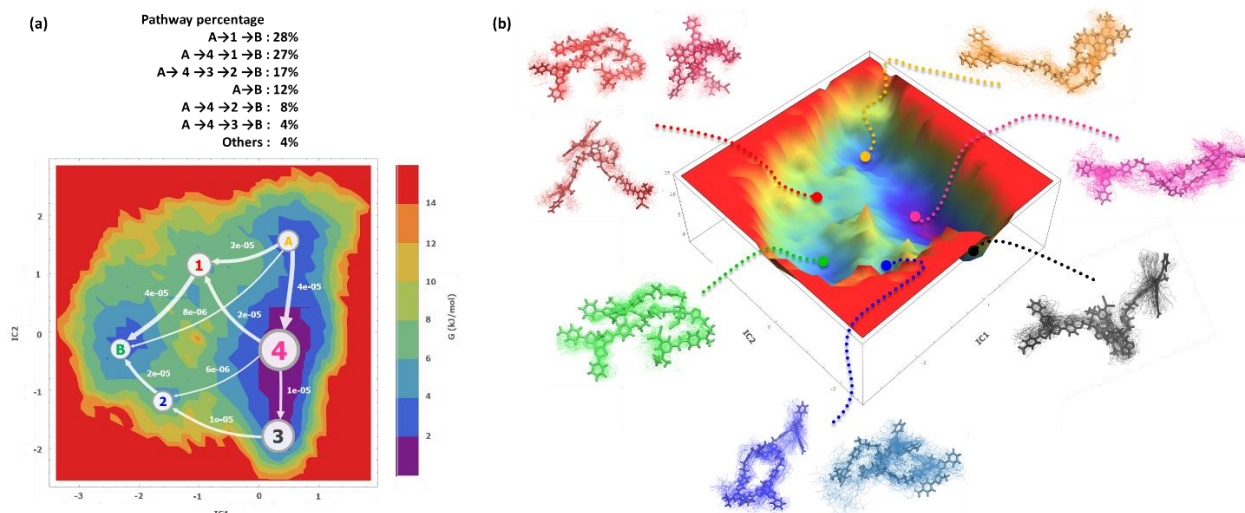


**Figure 78:** Free energy landscape of the **YN-3c** in the CF-OF(para) configuration, corresponding tICA-FEL visualized MSM in 2D **(a)** and 3D **(b)**. The *k*-means clustering method generated 200 microstates that are lumped into 6 metastable states by PCCA+ algorithm. The metastable states trajectories are clustered to extract the major conformations in six colors, which are corresponding to the labels in the transition pathway maps. The size of the labels and the arrows in **(a)** correspond to their proportional coarse-grained fluxes. The percentages of transition pathways are listed above.

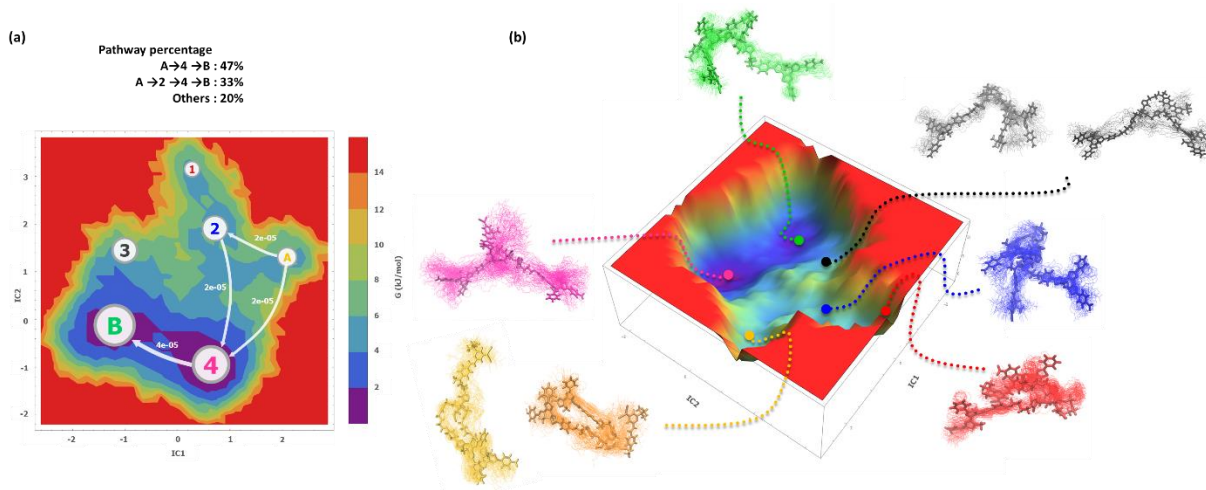


**Figure 79:** Free energy landscape of the **YN-3c** in the CF-OF(anti) configuration, corresponding tICA-FEL visualized MSM in 2D **(a)** and 3D **(b)**. The *k*-means clustering method generated 200 microstates that are lumped into 6 metastable states by PCCA+ algorithm. The metastable states trajectories are clustered to extract the major conformations in six colors, which are corresponding to the labels in the transition pathway maps. The size of the labels and the arrows in **(a)** correspond to their proportional coarse-grained fluxes. The percentages of transition pathways are listed above.

## 4.6 APPENDIX: MSM VALIDATIONS

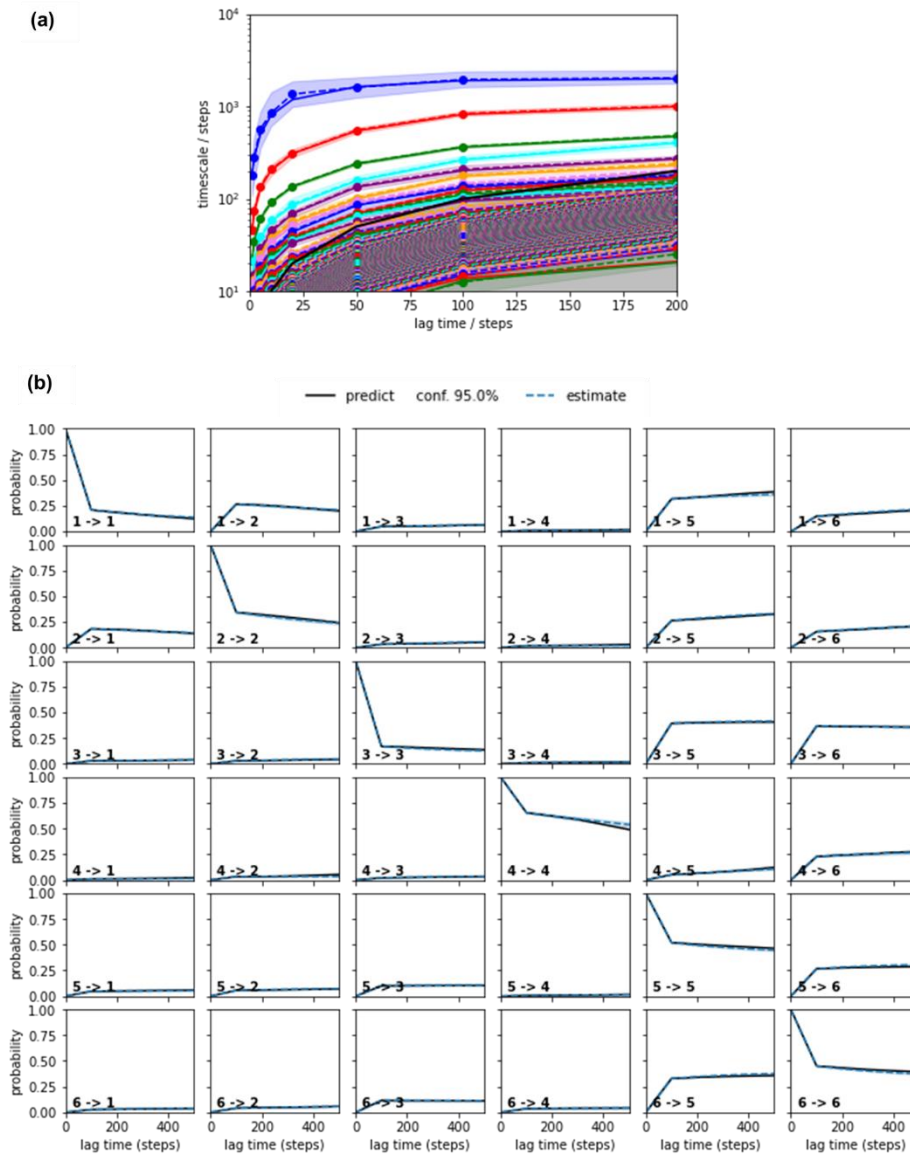


**Figure 80:** (a) Implied timescales for the MSM of CF-CF configuration **YN-3c**. The error bars are 95% confidence intervals estimated using the reversible transition matrix sampling algorithm. The unit of steps has the reduction formula: 100 steps = 1 ns. (b) The Chapman-Kolmogorov test curves obtained by 6 macrostates of CF-CF configuration.

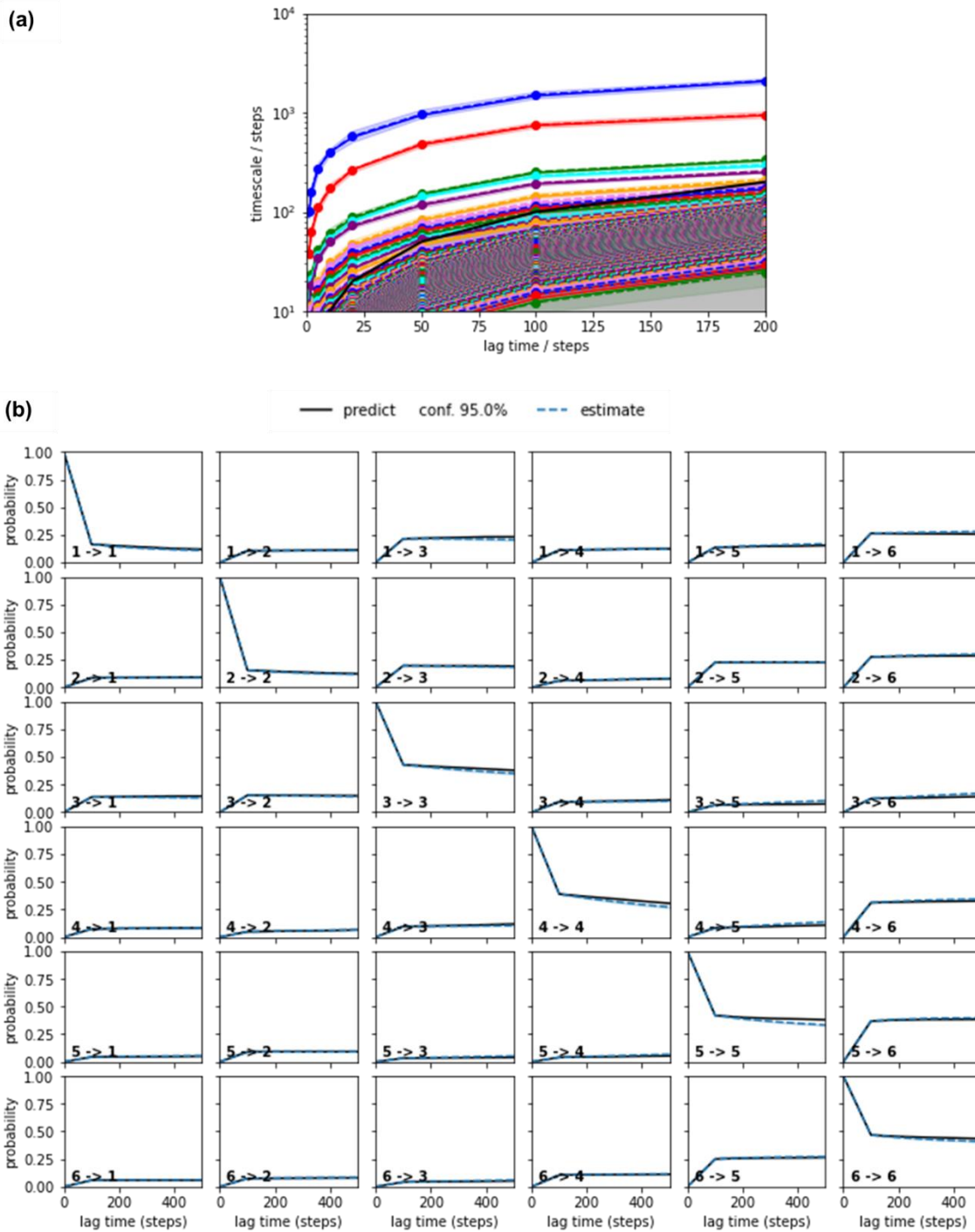


**Figure 81:** (a) Implied timescales for the MSM of CF-OF(para) configuration YN-3c. The error bars are 95% confidence intervals estimated using the reversible transition matrix sampling algorithm. The unit of steps has the reduction formula: 100 steps = 1 ns. (b) The Chapman-Kolmogorov test curves obtained by 6 macrostates of CF-CF configuration.



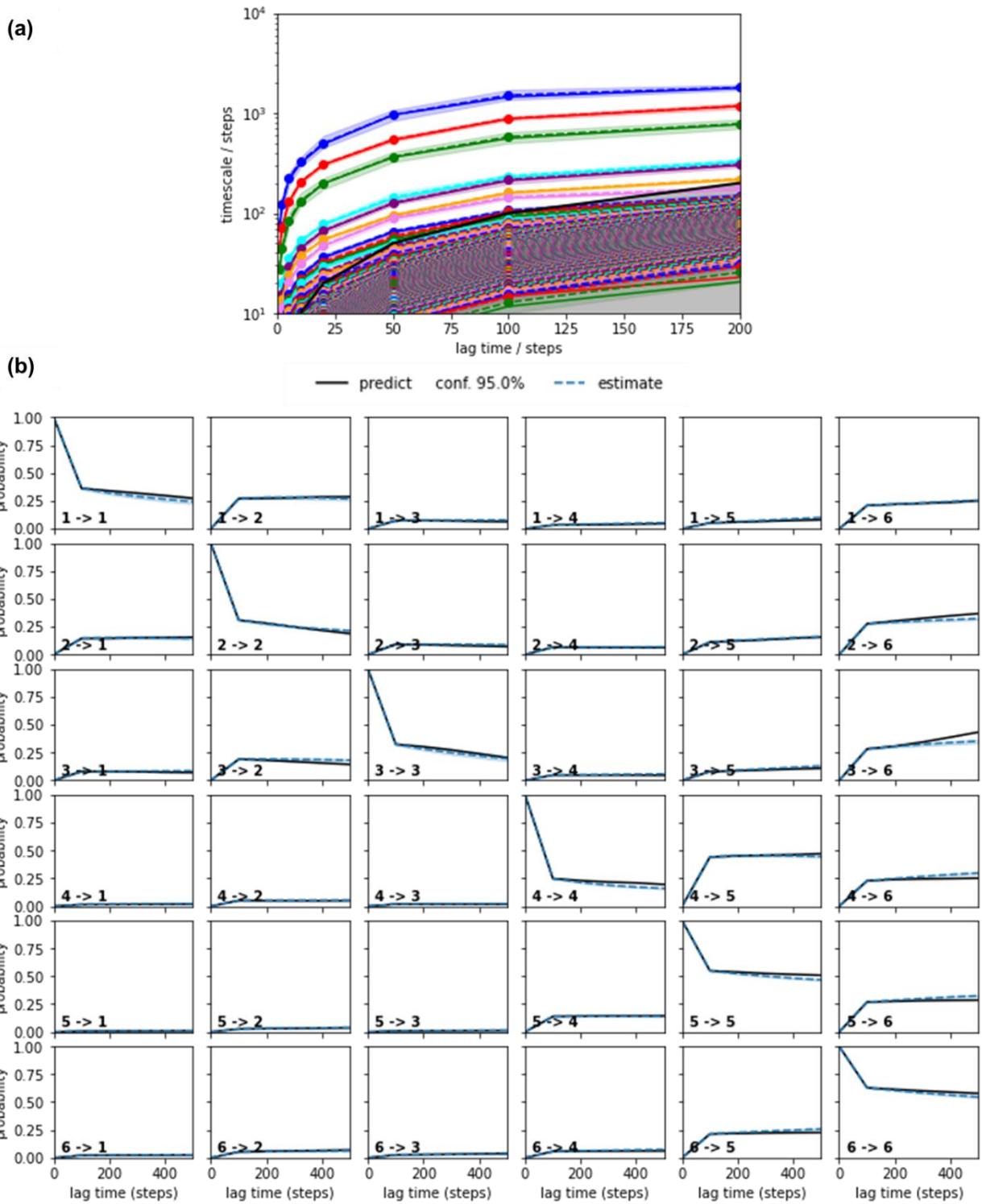


**Figure 82:** (a) Implied timescales for the MSM of CF-OF(para) configuration YN-3c. The error bars are 95% confidence intervals estimated using the reversible transition matrix sampling algorithm. The unit of steps has the reduction formula: 100 steps = 1 ns. (b) The Chapman-Kolmogorov test curves obtained by 6 macrostates of CF-CF configuration.

## 4.7 CONCLUSION AND PERSPECTIVES

In this chapter, after reviewing the different types of photoswitchable fluorescence hysteresis systems, we have firstly studied by DFT / TDDFT the **DAE-azide** molecule, provided by N. Baggi (Dr P. Yu's group, ICMMO, Univ. Paris-Saclay). The geometries and electronic transitions of the three forms of **DAE-azide** (parallel and anti-parallel open forms, closed form) have been calculated. Subsequently, the dissymmetric dendritic linker was designed and synthesized, including both **DAE-azide** and **DCM-o-propargyl**. After solving the synthetic problem (low yield) of a critical intermediate **32**, the desired compound **YN-3c** was successfully obtained with acceptable yield through the total steps (maximum 29%, 5 steps). **YN-3c** is well-confirmed with NMR and mass spectroscopy, therefore, it becomes the full-functional building blocks for the larger scale of multichromophoric systems. The following synthesis can find path dependence based on the success of 14 DCM. However, despite many attempts, the mass spectrometric characterization data are not available in the current stage for **YN-12c** and **YN-42c**. However, some indirect spectroscopic properties show that the correct target compounds **YN-12c** and **YN-42c** have been probably obtained, and could serve for the preliminary tests of photoswitchable fluorescence hysteresis.

To produce a photoswitchable fluorescence hysteresis effect, FRET processes and competitive photoisomerizations upon UV and visible irradiations of the molecular systems involving both DCM and DAE chromophores are expected to create several states to form a hysteresis loop. In other words, by controlling the irradiation parameters, we could in principle photoisomerize the DCM and DAE simultaneously but at different rates, leading to specific changes in fluorescence and absorption. Accordingly, the hysteresis measurements have been carried out on **YN-3c** by absorption and fluorescence steady-state spectroscopy, and on the full **YN** series (**YN-3c**, **YN-12c** and **YN-42c**) with a "dual photokinetics" instrument recently built in the laboratory, recording both signals simultaneously. The three derivatives could successfully display the targeted photoswitchable fluorescence hysteresis effect. Moreover, the extent of the photoswitchable fluorescence hysteresis was dependent on the number of chromophores: the **YN-42c** displayed a curved backward reaction under visible irradiation rather than a straight line for **YN-3c**.

The MD simulations on **YN-3c** revealed the intrinsic high FRET efficiencies of the basic building block designed for highly efficient energy transfer. As expected, the average intramolecular FRET efficiency between *E*-DCM and CF-DAE within the **YN-3c** multichromophore was calculated over 90%. Even when only one acceptor unit is present (only one CF-DAE), the FRET efficiency is still above 90% thanks to the other D-A pair. Given the good spectral overlap between **DCM-azide** and **DAE-azide**, and by analyzing the MD trajectories, we could conclude that the short interchromophoric distance, resulting from the compact molecular design, account for the general high FRET efficiencies. The few events with lower FRET efficiencies mostly come from specific geometries with randomly unfavorable arrangement of the D-A pair (orientation factor close to zero). The Markov state model (MSM) analyses could also provide the main geometries of **YN-3c** and tell that the transitions between them occur mostly between the unfolded conformations and the folded conformations. In summary, the MD simulation results strengthen the high performance of the **YN-3c** to induce fluorescence quenching by FRET processes. If it is installed in a compact linker or platform, the overall FRET efficiency of the resulting larger molecular structures is expected to be even higher.

As future improvements, the "dual photokinetics" setup is expected to be equipped with specific accessories to solve the limitations due to the excitation beam intensity, which currently interferes with the irradiation beam and prevents optimization of the hysteresis curve. As future perspectives, after optimization of the spectroscopic instrument, we plan to investigate the influence of many important parameters on the hysteresis shape: impact of the irradiation and excitation wavelengths and power, choice of the absorption and fluorescence signals, influence of the temperature, solvent or concentration, etc. The photoswitchable fluorescence hysteresis effect is a complex phenomenon which deserves a more complete rationalization to be fully understood and modeled.

For the future applications of the photoswitchable fluorescence hysteresis concept, bio-imaging, polymer embedding smart functionalities, and multi-logic gates are proposed. As we have shown that **YN-3c** is already a molecule allowing fluorescence hysteresis effects, its azido group provides an excellent capacity to be functionalize with other systems where you would like to use it *via* click reactions. Especially in the field of polymers, the total number of molecules can increase drastically, with scale up effects for the photoswitchable fluorescence hysteresis loop.

## GENERAL CONCLUSION AND PERSPECTIVES

This PhD thesis covers a variety of research techniques and scientific fields in organic synthesis, spectroscopy, quantum chemistry calculations and classical molecular dynamics simulations. Under the framework of the ANR-SWIST project, one photoswitchable fluorophore DCM and the DAE photochrome were investigated independently and jointly for developing new methodologies to implement the *photoswitchable fluorescence hysteresis* concept.

One of the research highlights of this thesis is the design and investigation of hierarchy structures from the DCM single molecule to the larger multichromophoric architectures. The spectroscopic and quantum chemistry studies on a DCM analog in **Chapter II** moved one more step forward our understanding of this molecule, which is of high interest in PPSM laboratory. Conical intersections and calculations on excitation energies are important issues in photochemistry which cannot be bypassed. Fortunately, we solved the problem at a low cost with a Spin-Flip TDDFT method which worked for the **DCM-azide** made of 54 atoms. The energy information from two CIs and their locations on the PES matches well the explanations on four isomers and conformers of the DCM fluorophore.

In the photochemistry field, further perspectives could be envisioned at the quantum chemistry level, such as *ab initio* molecular dynamics, which would be a powerful tool to learn and use, solving the population distributions of the relaxation pathways.

The next part (**Chapter III**) concerns the DCM-DCM interactions explored with proper dendrons and cyclodextrins for constructing the target compounds. In the synthesis part, this thesis started to explore one direction on enriching the dendritic linkers, and the other approach on azido or propargyl-functionalized  $\beta$ -CD so as to link with chromophores by employing CuAAC *click reaction*. The interest on multichromophores requires such platforms to install many or different kinds of chromophores together to carry out studies. The synthesis of dendrons and the 14-valent *O*-propargylated  $\beta$ -CD has been achieved successfully under microwave conditions. In the spectroscopy and simulation part, the DCM-DCM interactions are based on the proximity distance: the intramolecular FRET is competitive between the homo-FRET and hetero-FRET, which could be confirmed by absorption, emission and anisotropy spectroscopies, and simulation tools. Molecular dynamics accompanied with statistical analyses are other achievements in solving the FRET parameters. The comparison of the series **DCM**, **2DCM** and **3DCM** showed that homo- and hetero-FRET processes are extremely efficient, with consequences on their photoswitchable properties.

Due to the strong demands from biological sciences, such as proteins foldings/misfoldings, virus bindings, etc., the computational analysis models and tools are more accessible for all scientific fields. By means of these computational tools, the molecular designs could be smarter, especially the application scenario of FRET and multichromophoric systems. When chains are elongated, the molecular topological orientations are important parameters to know if the FRET system can reach high efficiencies.

The last part (**Chapter IV**) is related to our fluorescence hysteresis works on the basis of competitive photoisomerizations of mixed multichromophoric systems, involving several DAE and DCM units. The synthesis of another series of multi-DAE/DCM compounds, namely **YN-3c**, **YN-12c** and **YN-42c** was conducted. **YN-3c** was successfully characterized, whereas the larger multichromophoric counterparts were more challenging and require further confirmation by HRMS. The trichromophoric dendron **YN-3c** was studied by steady-state and “dual photokinetics” spectroscopy measurements, demonstrating the photoswitchable fluorescence hysteresis. However, the fluorescence hysteresis was difficult to elucidate with proper accuracy through every state of the hysteresis loop. In the next stage, we intend to optimize our instrumentation in order to investigate in more details the different parameters influencing the photoswitchable fluorescence hysteresis effect.

As the inspiration from the simulation side, long chain components could be promising alternative solution to accommodate a large number of chromophores and favor the emergence of new applications.

Sincerely, I hope you have enjoyed the thesis content from the design and understanding of photophysical processes in complex systems (by spectroscopy and calculation) to their roles in smart concepts and applications, such as photoswitchable fluorescence hysteresis. Many powerful techniques were involved to investigate this field. The fluorescence hysteresis effect is based on the competitive photoisomerizations: it has fundamental principles, and it also has the potential to enter into bulk materials. That requires progresses and efforts from synthetic, spectroscopic, and theoretical sides mutually.



# Experimental section





## 5 EXPERIMENTAL SECTION

### 5.1 GENERAL EXPERIMENTAL DETAILS

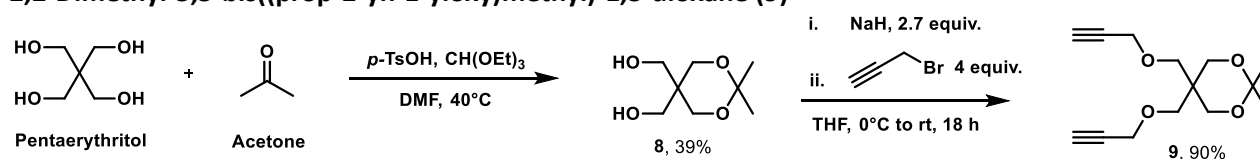
#### 5.1.1 Materials and characterizations

All commercially available compounds and solvents are purchased from Sigma-Aldrich affiliated to Merck KGaA, Carlo Erba Reagents, TCI chemicals and Acros Organics affiliated to Thermo Fisher Scientific without further purifications. THF, acetonitrile, DMF and  $\text{CH}_2\text{Cl}_2$  were previously dried through alumina or molecular sieves cartridge using a solvent purificator MBRAUN SPS-800. The reactions carried out under anhydrous conditions are performed under argon in glassware previously dried in an oven. Reactions were monitored by TLC on Silica Gel 60F-254 plates with detection by UV (254 nm or 365 nm) or by spraying with 10%  $\text{H}_2\text{SO}_4$  in EtOH and heating about 30 s at 400-600 °C. Column chromatography purification was performed on CombiFlash® Rf+ and RediSep® RF or RF Gold normal phase silica columns.  $^1\text{H}$  and  $^{13}\text{C}$ -NMR spectra were recorded on a JEOL ECS-400 spectrometer. with a broadband probe. The irradiation frequencies of  $^1\text{H}$  and  $^{13}\text{C}$  are respectively 399.78 MHz and 100.53 MHz. The chemical shift, denoted  $\delta$ , is expressed in parts per million (ppm) using as a reference the residual solvent signal or tetramethylsilane (TMS). The scalar coupling constants ( $J$ ) are given in Hertz (Hz). The abbreviations used are: (s) singlet, (d) doublet, (t) triplet, (m) massive. The assignment of the  $^1\text{H}$  and  $^{13}\text{C}$  signals was performed by comparison with spectroscopic data tables or near-structure compounds and using 2D sequences of the COSY, HMQC and HetCor type. The mention Cq indicates the quaternary carbons. The numbering of the different atoms does not necessarily follow the nomenclature rules recommended by IUPAC and is only used for the assignment of NMR spectra. HRMS (ESI) spectrum was recorded on a Q-TOF or a MALDI-Q-TOF maXis Bruker spectrometer, ESI-source, positive ionization by the "Fédération de Recherche" ICOA/CBM (FR2708) platform.

#### 5.1.2 Synthesis catalog

##### 5.1.2.1 2DCM

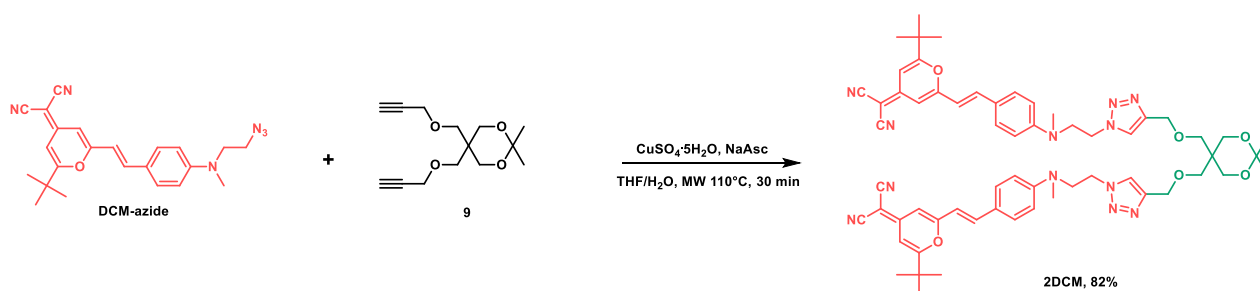
##### 2,2-Dimethyl-5,5-bis((prop-2-yn-1-yloxy)methyl)-1,3-dioxane (9)



Scheme 15: Preparation of di-*O*-propargyl dendritic linkers 9.

Compound 8 was prepared from pentaerythritol according to the reported method.<sup>141</sup> To a solution of compound 8 (114 mg, 0.65 mmol) in THF (10 mL), sodium hydride (60% dispersion in mineral oil, 2.4 equiv.) was added in portions under argon at  $0^\circ\text{C}$  ice bath. After addition, the reaction mixture was stirred for 30 min, propargyl bromide (80% in toluene, 6 equiv.) was added dropwise to the reaction mixture which was then stirred at room temperature for 18 h. Saturated  $\text{NH}_4\text{Cl}$  aq. was added to quench the reaction and the reaction mixture was extracted by ethyl acetate (20 mL) for 3 times. The organic layer was washed with brine, dried over anhydrous  $\text{MgSO}_4$ , filtered and concentrated. The crude product was purified by CombiFlash® chromatography with an eluent of petroleum ether and ethyl acetate (8:1) to afford 9 as a transparent liquid (147 mg, 90%).  $^1\text{H}$  NMR (400 MHz,  $\text{CDCl}_3$ ):  $\delta$  (ppm) = 4.14 (d,  $J = 2.3$  Hz, 4H,  $\text{CH}_2$ ), 3.75 (s, 4H,  $\text{CH}_2$ ), 3.53 (s, 4H,  $\text{CH}_2$ ), 2.43 (t,  $J = 2.5$  Hz, 2H,  $\text{C}\equiv\text{CH}$ ), 1.41 (s, 6H,  $\text{CH}_3$ ).  $^{13}\text{C}$  NMR (100 MHz,  $\text{CDCl}_3$ ):  $\delta$  (ppm) = 98.27, 79.85 ( $\text{C}_q$ ); 74.46 ( $\text{C}\equiv\text{CH}$ ), 69.29, 62.66, 58.77, 38.87 ( $\text{CH}_2$ ); 23.83 ( $\text{CH}_3$ ).  $m/z$  [ $\text{M}+\text{Na}$ ] $^+$  calcd. for  $[\text{C}_{14}\text{H}_{20}\text{NaO}_4]^+$ : 275.1254; found 275.1254.

## 2DCM

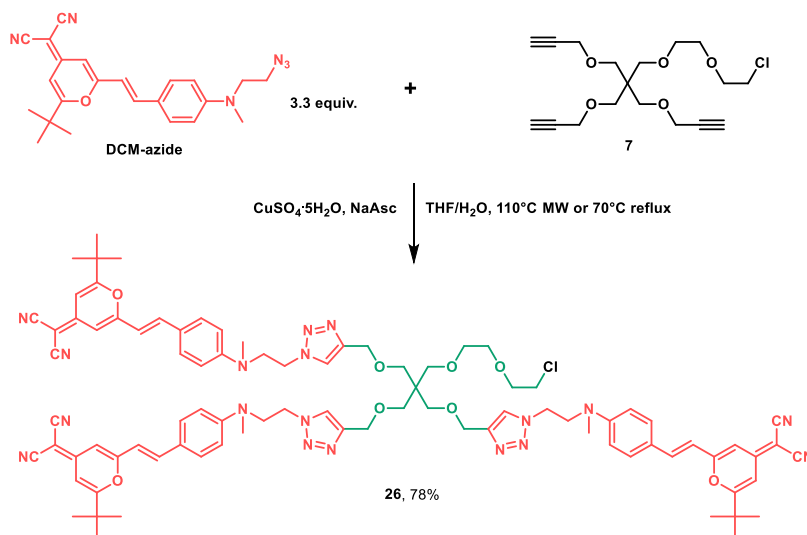


Scheme 21: Synthesis of **2DCM**.

Compound **9** (33 mg, 0.13 mmol), **DCM-azide**<sup>2</sup> (2.2 equiv.),  $\text{CuSO}_4 \cdot 5\text{H}_2\text{O}$  (0.4 equiv.) and sodium ascorbate (0.8 equiv.) were added together in a mixed solvent  $\text{THF}/\text{H}_2\text{O}$  (4 mL, 3:1, v/v) to a microwave reactor tube. The reaction mixture was kept irradiated with microwave, holding at  $110^\circ\text{C}$  for 30 minutes. After the reaction mixture returned to room temperature, it was poured into 0.1 M EDTA aqueous solution. The mixture was extracted with ethyl acetate (30 mL) for 3 times. The organic layer was washed with brine, dried over anhydrous  $\text{MgSO}_4$ . The crude product was purified by CombiFlash<sup>®</sup> chromatography with dichloromethane and ethanol as eluent (gradient, 100:0 to 90:10, v/v) to afford **2DCM** as red powder (113 mg, 82%). <sup>1</sup>H NMR (400 MHz,  $\text{CDCl}_3$ ):  $\delta$  (ppm) = 7.50 (s, 2H, triazole-*H*), 7.43-7.41 (m, 4H), 7.33 (s, 1H), 7.29 (s, 1H), 6.63 (d,  $J = 8.8$  Hz, 4H,  $\text{CH}_{\text{Ar}}$ ), 6.62-6.60 (m, 2H,  $\text{CH}=\text{}$ ), 6.53-6.49 (m, 4H,  $\text{CH}=\text{}$ ), 4.60 (t,  $J = 6.2$  Hz, 4H,  $\text{CH}_2$ ), 4.56 (s, 4H,  $\text{CH}_2$ ), 3.94 (t,  $J = 6.0$  Hz, 4H,  $\text{CH}_2$ ), 3.66 (s, 4H,  $\text{CH}_2$ ), 3.43 (s, 4H,  $\text{CH}_2$ ), 2.88 (s, 6H,  $\text{NCH}_3$ ), 1.37 (s, 18H, *t*-Bu), 1.36 (s, 6H,  $\text{CH}_3$ ). <sup>13</sup>C NMR (100 MHz,  $\text{CDCl}_3$ ):  $\delta$  (ppm) = 172.08, 160.02, 156.91, 149.89, 145.52 ( $\text{C}_\text{q}$ ); 137.98, 129.97, 123.55 ( $\text{CH}_{\text{Ar}}$ ); 115.82, 115.71 ( $\text{C}_\text{q}$ ); 114.02 ( $\text{CH}_{\text{Ar}}$ ); 112.10, 105.95, 102.58 ( $\text{CH}=\text{}$ ); 98.37 ( $\text{C}_\text{q}$ ); 69.65, 64.96, 62.91 ( $\text{CH}_2$ ); 58.32 ( $\text{C}_\text{q}$ ); 52.56, 47.69 ( $\text{CH}_2$ ); 38.89 ( $\text{CH}_3$ ), 36.83 ( $\text{C}_\text{q}$ , *t*-Bu); 28.28, 23.88 ( $\text{CH}_3$ ). HRMS (ESI-HRMS):  $m/z$   $[\text{M}+\text{H}]^+$  calcd. for  $[\text{C}_{60}\text{H}_{69}\text{N}_{12}\text{O}_6]^+$ : 1053.5458; found 1053.5454.

### 5.1.2.2 3DCM

## Compound 26

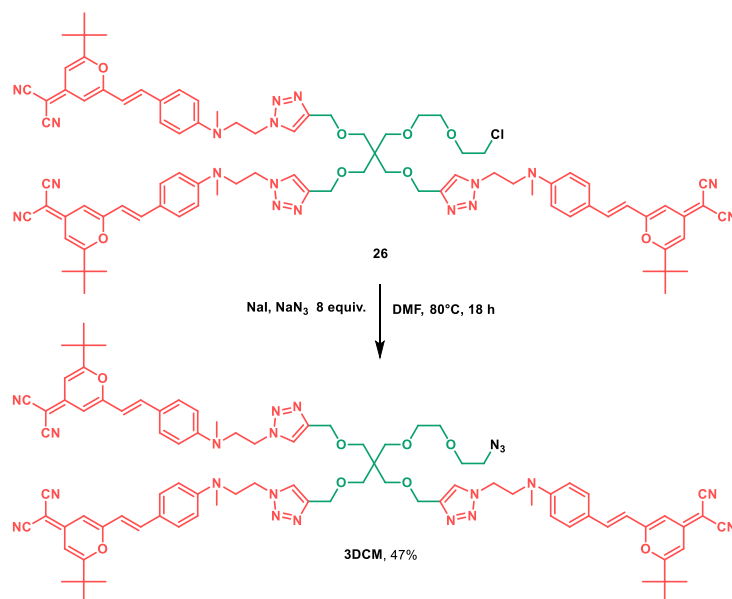


Scheme 22: Synthesis of trichromophoric compound **26**.

Compound **7** was prepared from pentaerythritol according to the reported method.<sup>195</sup> Compound **7** (50 mg, 0.14 mmol), **DCM-azide** (3.3 equiv.),  $\text{CuSO}_4 \cdot 5\text{H}_2\text{O}$  (0.4 equiv.) and sodium ascorbate (0.8 equiv.) were added together in a mixed solvent  $\text{THF}/\text{H}_2\text{O}$  (4 mL, 3:1, v/v) to a microwave reactor tube. The reaction mixture was kept irradiated with microwave, holding at  $110^\circ\text{C}$  for 30 minutes. After the reaction mixture returned to room temperature, it was poured into 0.1 M EDTA solution. The mixture was extracted with ethyl acetate (30 mL) for 3 times. The organic layer was washed with brine, dried over anhydrous  $\text{MgSO}_4$ .

The crude product was purified by CombiFlash® chromatography with dichloromethane and ethanol as eluent (gradient, 100:0 to 90:10, v/v) to afford compound **26** as red powder (170 mg, 78%). <sup>1</sup>H NMR (400 MHz, CDCl<sub>3</sub>): δ (ppm) = 7.53 (s, 3H, triazole-*H*), 7.43-7.41 (m, 6H), 7.32-7.27 (m, 3H), 6.63 (d, *J* = 8.8 Hz, 6H, *CH*=), 6.59-6.58 (m, 3H, *CH*=), 6.54-6.50 (m, 6H, *CH*=), 4.60 (t, *J* = 6.2 Hz, 6H, *CH*<sub>2</sub>), 4.52 (s, 6H, *CH*<sub>2</sub>), 3.93 (t, *J* = 5.6 Hz, 6H, *CH*<sub>2</sub>), 3.70 (t, *J* = 6.0 Hz, 2H, *CH*<sub>2</sub>), 3.58 (t, *J* = 5.6 Hz, 4H, *CH*<sub>2</sub>), 3.49 (m, 2H, *CH*<sub>2</sub>), 3.41-3.38 (m, 8H, *CH*<sub>2</sub>), 2.87 (s, 9H, *NCH*<sub>3</sub>), 1.37 (s, 27H, *t*-Bu). <sup>13</sup>C NMR (100 MHz, CDCl<sub>3</sub>): δ (ppm) = 172.11, 160.05, 156.92, 149.92, 145.66 (C<sub>q</sub>); 137.99, 129.98, 123.64, 123.53 (CH<sub>Ar</sub>); 115.87, 115.72 (C<sub>q</sub>); 113.95, 112.12, 105.93, 102.57 (CH=); 71.36, 71.05, 70.51, 69.29, 64.96 (CH<sub>2</sub>); 58.22 (C<sub>q</sub>); 52.71, 47.56 (CH<sub>2</sub>); 45.37 (C<sub>q</sub>), 43.25 (CH<sub>2</sub>), 38.82 (NMe), 36.79 (C<sub>q</sub>), 28.28 (CH<sub>3</sub>, *t*-Bu). HRMS (ESI-HRMS): *m/z* [M+H]<sup>+</sup> calcd. for [C<sub>87</sub>H<sub>98</sub>N<sub>18</sub>O<sub>8</sub>Cl]<sup>+</sup>: 1557.7498, 1558.7532; found 1557.7498, 1558.7529.

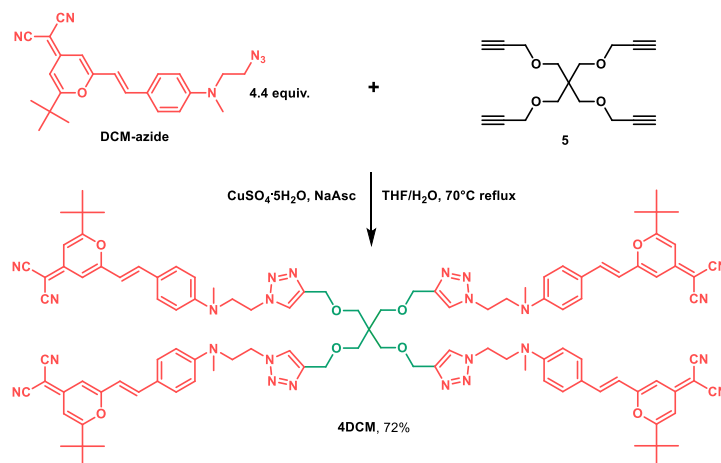
### 3DCM



**Scheme 23:** Azidation to yield **3DCM**.

To a solution of compound **26** (136 mg, 87 μmol) in DMF (5 mL), NaI (0.1 equiv.) and NaN<sub>3</sub> (8 equiv.) were added. The reaction mixture was heated up to 80°C and kept for 18 hours. After concentration, the residue was diluted in EtOAc (20 mL), washed successively with water and brine, dried over MgSO<sub>4</sub>, concentrated and purified by CombiFlash® chromatography with dichloromethane and ethanol (gradient, 100:0 to 90:10, v/v) to yield (*EEE*)-**3DCM** as a red solid (64 mg, 47%). <sup>1</sup>H NMR (400 MHz, CDCl<sub>3</sub>): δ (ppm) = 7.54 (s, 3H, triazole-*H*), 7.41 (d, *J* = 8.7 Hz, 6H, *CH*<sub>Ar</sub>), 7.32-7.27 (m, 3H), 6.64 (d, *J* = 9.2 Hz, 6H, *CH*=), 6.58-6.57 (m, 3H, *CH*=), 6.53-6.49 (m, 6H, *CH*=), 4.60 (t, *J* = 6.0 Hz, 6H, *CH*<sub>2</sub>), 4.52 (s, 6H, *CH*<sub>2</sub>), 3.93 (t, *J* = 6.0 Hz, 6H, *CH*<sub>2</sub>), 3.64-3.61 (m, 2H, *CH*<sub>2</sub>), 3.58-3.56 (m, 2H, *CH*<sub>2</sub>), 3.52-3.49 (m, 2H, *CH*<sub>2</sub>), 3.42-3.39 (m, 8H, *CH*<sub>2</sub>), 3.33 (t, *J* = 5.2 Hz, 2H, *CH*<sub>2</sub>), 2.87 (s, 9H, *NCH*<sub>3</sub>), 1.37 (s, 27H, *t*-Bu). <sup>13</sup>C NMR (100 MHz, CDCl<sub>3</sub>): δ = 172.07, 160.04, 156.88, 149.90, 145.61 (C<sub>q</sub>); 138.01, 129.95, 123.60, 123.42 (CH=); 115.84, 115.72 (C<sub>q</sub>); 113.88, 112.07, 105.85, 102.48 (CH=); 71.05, 70.55, 70.08, 69.91, 69.25, 64.91, 58.02 (C<sub>q</sub>); 52.65, 50.82, 47.51, 45.33 (C<sub>q</sub>); 38.76 (NMe), 36.73 (C<sub>q</sub>), 29.79 (CH<sub>2</sub>), 28.22 (CH<sub>3</sub>, *t*-Bu) ppm. HRMS (ESI-HRMS): *m/z* [M+H]<sup>+</sup> calcd. for [C<sub>87</sub>H<sub>98</sub>N<sub>21</sub>O<sub>8</sub>]<sup>+</sup>: 1564.7902, 1565.7936; found 1564.7915.

## 5.1.2.3 4DCM

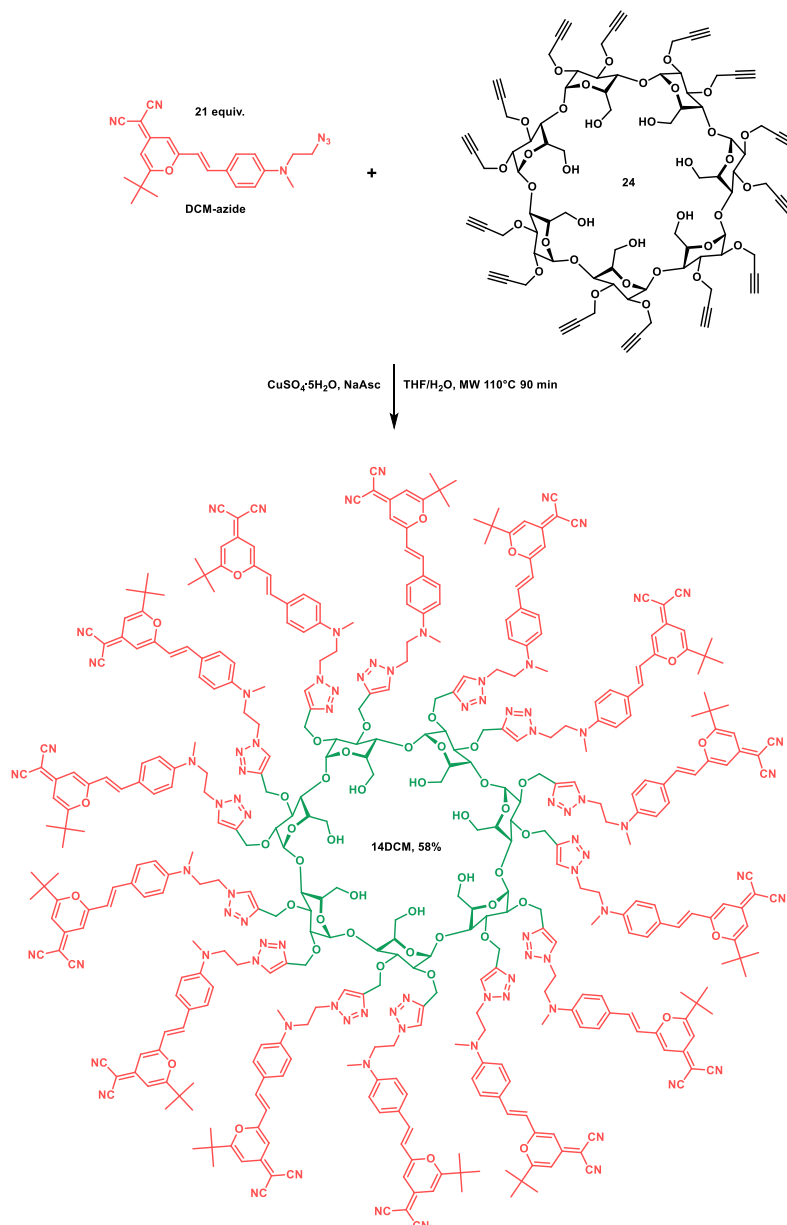


Scheme 24: Synthesis of tetrachromophoric 4DCM.

Compound **5** was prepared from pentaerythritol according to the reported method.<sup>136</sup>

Compound **5** (50 mg, 0.14 mmol), **DCM-azide** (1.1 equiv.),  $\text{CuSO}_4 \cdot 5\text{H}_2\text{O}$  (0.1 equiv.) and sodium ascorbate (0.2 equiv.) were added together to a mixed solvent THF/ $\text{H}_2\text{O}$  (4 mL, 3:1, v/v). The reaction mixture was kept stirring for 24h at room temperature. After that the reaction mixture was poured into 0.1 M EDTA solution, then extracted with ethyl acetate (30 mL) for 3 times. The organic layer was washed with brine, dried over  $\text{MgSO}_4$ , concentrated, then purified with CombiFlash® chromatography with petroleum ether and ethyl acetate (gradient, 100:0 to 50:50, v/v) as eluent to afford **4DCM** as a red powder (56 mg, 58%).  $^1\text{H}$  NMR (400 MHz,  $\text{CDCl}_3$ ):  $\delta$  = 7.55 (s, 2H, triazole-*H*), 7.53 (s, 2H, triazole-*H*), 7.43-7.39 (m, 8H), 7.32-7.27 (m, 4H), 6.63-6.57 (m, 12H, *CH*=), 6.53-6.47 (m, 8H, *CH*=), 4.62-4.60 (m, 8H, triazole- $\text{CH}_2$ ), 4.52-4.50 (m, 8H, triazole- $\text{CH}_2\text{O}$ ), 4.01-3.91 (m, 8H,  $\text{CH}_2\text{N}$ ), 3.42-3.35 (m, 8H,  $\text{CH}_2$ ), 2.86 (s, 12H,  $\text{NCH}_3$ ), 1.36 (s, 36H, *t*-Bu) ppm.  $^{13}\text{C}$  NMR (100 MHz,  $\text{CDCl}_3$ ):  $\delta$  = 172.07, 160.03, 156.87, 149.89, 145.40 ( $\text{C}_q$ ); 137.97, 129.94, 123.78, 123.43 (*CH*=); 115.86, 115.70 ( $\text{C}_q$ ); 113.92, 112.05, 105.86, 102.48 (*CH*=); 68.08, 64.91 ( $\text{CH}_2$ ); 58.01 ( $\text{C}_q$ ); 52.63, 47.52 ( $\text{CH}_2$ ); 38.72 (NMe); 36.73 ( $\text{C}_q$ ); 28.21 ( $\text{CH}_3$ , *t*-Bu) ppm. HRMS (ESI-HRMS):  $m/z$  [ $\text{M}+\text{H}$ ]<sup>+</sup> calcd. for  $[\text{C}_{109}\text{H}_{117}\text{N}_{24}\text{O}_8]^+$ : 1889.9481; found 1889.9483.

### 5.1.2.4 14DCM

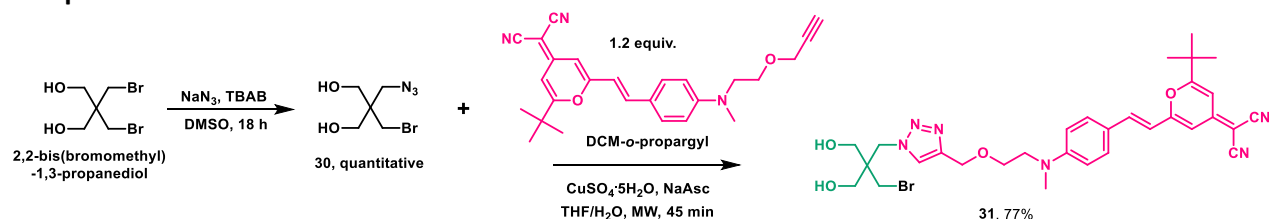


**Scheme 26:** Synthesis of 14-valent **14DCM**.

Compound **24** was prepared from  $\beta$ -CD according to the reported method.<sup>154</sup>

Compound **24** (5 mg, 30  $\mu$ mol), **DCM-azide** (21 equiv.),  $\text{CuSO}_4 \cdot 5\text{H}_2\text{O}$  (7 equiv.) and sodium ascorbate (14 equiv.) in a mixed solvent THF/H<sub>2</sub>O (3 mL, 2:1, v/v) were introduced into a microwave reactor tube. The reaction mixture was kept irradiated at 110°C for 90 minutes. After that the reaction mixture was poured into 0.1 M EDTA solution. The mixture was extracted with ethyl acetate (30 mL) for 3 times. The organic layer was washed with brine, dried over  $\text{MgSO}_4$ , concentrated, then purified with CombiFlash® chromatography with petroleum ether: dichloromethane (90:10, v/v) and dichloromethane: methanol (gradient, 10:90 to 95:5, v/v) as eluent to afford **14DCM** as a red powder (12 mg, 58%).  $m/z$   $[\text{M}+\text{Na}]^+$  calcd. for  $[\text{C}_{406}\text{H}_{434}\text{N}_{84}\text{NaO}_{49}]^+$ : 7295.4044, MALDI-TOF found 7295.

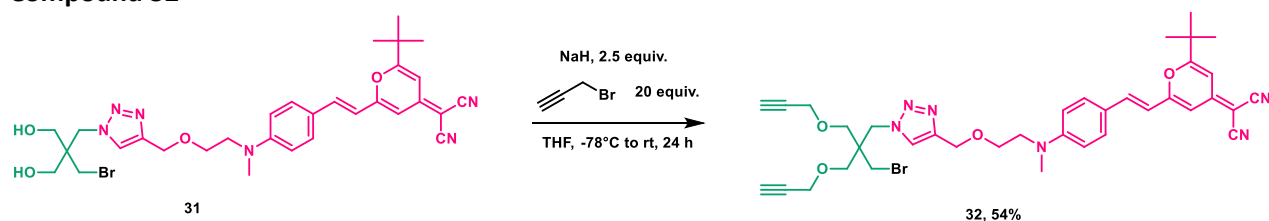
## Compound 31



Scheme 30: Synthesis of DCM contained compound 31.

Compound **30** was prepared from 2,2-bis(bromomethyl)-1,3-propanediol according to the reported method.<sup>193</sup> Compound **30** (1 g, 4.46 mmol), **DCM-o-propargyl** (1.2 equiv.),  $\text{CuSO}_4 \cdot 5\text{H}_2\text{O}$  (0.4 equiv.) and sodium ascorbate (0.8 equiv.) were added together in a mixed solvent THF/ $\text{H}_2\text{O}$  (3 mL, 2:1, v/v) to a microwave reactor tube. The reaction mixture was kept irradiated with microwave, holding at  $110^\circ\text{C}$  for 30 minutes. After that the reaction mixture was poured into 0.1 M EDTA solution. The mixture was extracted with ethyl acetate (30 mL) for 3 times. The organic layer was washed with brine, dried over  $\text{MgSO}_4$ , concentrated, then purified with CombiFlash<sup>®</sup> chromatography with petroleum ether and ethyl acetate (gradient, 20:80, v/v) as eluent to afford **31** as a red powder (2.19 g, 77%).  $^1\text{H}$  NMR (400 MHz,  $\text{CDCl}_3$ ):  $\delta$  = 7.60 (s, 1H, triazole-*H*), 7.43 (d,  $J$  = 9.2 Hz, 2H), 7.35-7.30 (m, 1H), 6.72 (d,  $J$  = 8.7, 2H,  $\text{H}_{\text{Ar}}$ ), 6.60 (d,  $J$  = 1.8 Hz, 1H,  $\text{CH}=\text{}$ ), 6.52 (d,  $J$  = 1.8 Hz, 1H,  $\text{CH}=\text{}$ ), 6.48 (s, 1H,  $\text{CH}=\text{}$ ), 4.65 (s, 2H, triazole- $\text{CH}_2$ ), 4.48 (s, 2H, triazole- $\text{CH}_2\text{O}$ ), 3.74 (t,  $J$  = 5.5 Hz, 2H,  $\text{CH}_2\text{N}$ ), 3.64 (t,  $J$  = 5.5 Hz, 2H,  $\text{CH}_2\text{Br}$ ), 3.57-3.53 (m, 4H,  $\text{CH}_2\text{OH}$ ), 3.07 (s, 3H,  $\text{NCH}_3$ ), 1.37 (s, 9H, *t*-Bu) ppm.  $^{13}\text{C}$  NMR (100 MHz,  $\text{CDCl}_3$ ):  $\delta$  = 172.08, 160.41, 157.02, 150.93, 145.06 ( $\text{C}_q$ ); 138.49, 129.86, 124.75 ( $\text{CH}=\text{}$ ); 122.43, 116.03, 113.03 ( $\text{C}_q$ ); 112.05, 105.60, 102.49 ( $\text{CH}=\text{}$ ); 68.06, 64.71, 62.51, 52.11, 49.65 ( $\text{CH}_2$ ); 45.87, 39.24, 36.75 ( $\text{C}_q$ ); 34.14, 29.81 ( $\text{CH}_2$ ); 28.25 ( $\text{CH}_3$ , *t*-Bu) ppm. HRMS (ESI-HRMS):  $m/z$  [ $\text{M}+\text{H}$ ]<sup>+</sup> calcd. for  $[\text{C}_{31}\text{H}_{38}\text{BrN}_6\text{O}_4]^+$ : 637.2133; found 637.2129.

## Compound 32



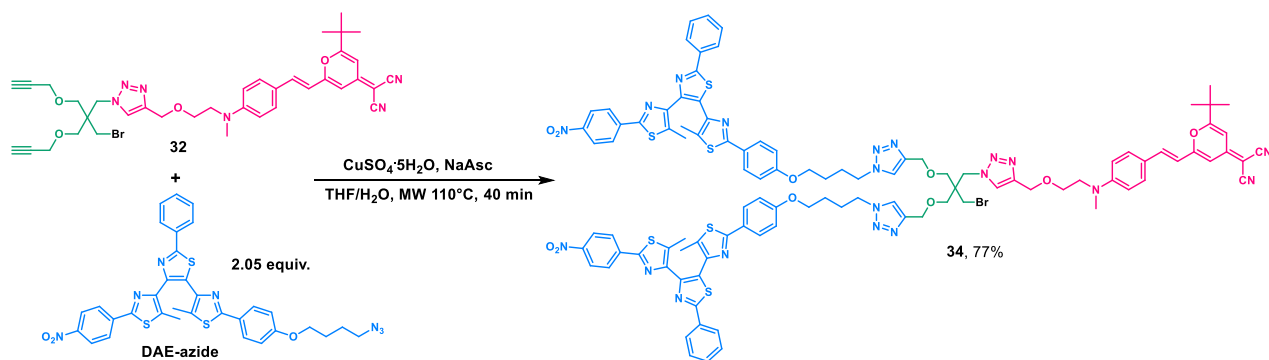
Scheme 31: Synthesis of target compound 32 and byproduct 33.

To a solution of compound **31** (123 mg, 0.65 mmol) in THF (5 mL), sodium hydride (60% dispersion in mineral oil, 2.5 equiv.) was added under argon at  $-78^\circ\text{C}$  under vigorous agitation. Then propargyl bromide (20 equiv.) was added immediately to the reaction mixture. These two steps were carried out within 5 minutes. After that, the reaction mixture was allowed to be warm up to room temperature for 24 h. Saturated  $\text{NH}_4\text{Cl}$  aq. was added to quench the reaction and the reaction mixture was extracted by dichloromethane (20 mL) for 3 times. The organic layer was washed with brine, dried with anhydrous  $\text{MgSO}_4$ , filtered and concentrated in sequence. The crude product was purified by CombiFlash<sup>®</sup> chromatography with an eluent of petroleum ether and ethyl acetate (gradient, 20:80, v/v) to afford **32** as a red solid (74 mg, 54%).  $^1\text{H}$  NMR (400 MHz,  $\text{CDCl}_3$ ):  $\delta$  = 7.61 (s, 1H, triazole-*H*), 7.42-7.39 (m, 2H), 7.35-7.30 (m, 1H), 6.71-6.68 (m, 2H), 6.60-6.47 (m, 3H), 4.64-4.62 (m, 2H, triazole- $\text{CH}_2$ ), 4.46-4.45 (m, 2H, triazole- $\text{CH}_2\text{O}$ ), 4.18-4.09 (m, 4H,  $\text{OCH}_2\text{C}\equiv\text{CH}$ ), 3.74-3.71 (m, 2H,  $\text{CH}_2\text{N}$ ), 3.64-3.60 (m, 2H,  $\text{CH}_2\text{Br}$ ), 3.51-3.38 (m, 4H,  $\text{CH}_2\text{OH}$ ), 3.06 (s, 3H,  $\text{NCH}_3$ ), 2.47 (t,  $J$  = 2.2 Hz, 1H,  $\text{C}\equiv\text{CH}$ ), 2.44 (t,  $J$  = 2.2 Hz, 1H,  $\text{C}\equiv\text{CH}$ ), 1.37 (s, 9H, *t*-Bu) ppm.  $^{13}\text{C}$  NMR (100 MHz,  $\text{CDCl}_3$ ):  $\delta$  = 171.99, 160.32, 156.94, 150.87, 144.86 ( $\text{C}_q$ ); 138.45, 129.85, 124.78 ( $\text{CH}=\text{}$ ); 122.39, 115.86 ( $\text{C}_q$ ); 112.96, 112.00, 105.56, 102.45 ( $\text{CH}=\text{}$ ); 79.06, 75.50 ( $\text{C}_q$ ); 69.17, 67.90, 64.65, 62.23, 58.86 ( $\text{CH}_2$ ); 57.68 ( $\text{C}_q$ ); 52.07, 50.01 ( $\text{CH}_2$ ); 45.29 ( $\text{C}_q$ ); 39.24 ( $\text{NMe}$ ); 36.72 ( $\text{C}_q$ ); 34.20 ( $\text{CH}_2$ ); 28.22 ( $\text{CH}_3$ , *t*-Bu) ppm. HRMS (ESI-HRMS):  $m/z$  [ $\text{M}+\text{H}$ ]<sup>+</sup> calcd. for  $[\text{C}_{37}\text{H}_{42}\text{BrN}_6\text{O}_4]^+$ : 713.2446; found 713.2442.





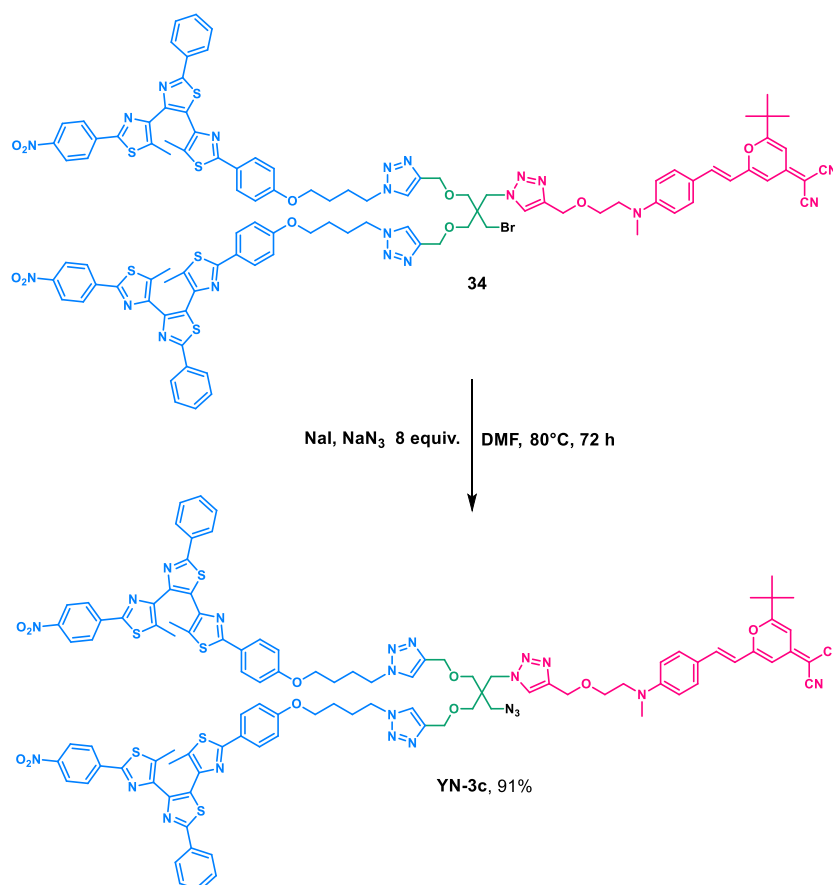
## Compound 33



**Scheme 33:** Synthesis of **34**.

Compound **32** (25 mg, 0.04 mmol), **DAE-azide** (2.05 equiv.),  $\text{CuSO}_4 \cdot 5\text{H}_2\text{O}$  (0.4 equiv.) and sodium ascorbate (0.8 equiv.) were added together in a mixed solvent  $\text{THF}/\text{H}_2\text{O}$  (3 mL, 2:1, v/v) to a microwave reactor tube. The reaction mixture was kept irradiated with microwave, holding at  $110^\circ\text{C}$  for 40 minutes. After that the reaction mixture was poured into 0.1 M EDTA solution. The mixture was extracted with dichloromethane (30 mL) for 3 times. The organic layer was washed with brine, dried over  $\text{MgSO}_4$ , concentrated, then purified with CombiFlash<sup>®</sup> chromatography with dichloromethane and ethanol (gradient, 95:5, v/v) as eluent to afford **34** as a red powder (55 mg, 77%).  $^1\text{H}$  NMR (400 MHz,  $\text{CDCl}_3$ ):  $\delta$  = 8.15-8.12 (m, 4H,  $\text{H}_{\text{Ar}}$ ), 8.05-8.03 (m, 4H,  $\text{H}_{\text{Ar}}$ ), 7.87-7.83 (m, 8H,  $\text{H}_{\text{Ar}}$ ), 7.68 (s, 1H, triazole-*H*), 7.65 (s, 2H, triazole-*H*), 7.48-7.46 (m, 6H,  $\text{H}_{\text{Ar}}$ ), 7.38 (d,  $J$  = 8.7 Hz, 2H), 7.33-7.29 (m, 1H), 6.90 (d,  $J$  = 8.7 Hz, 4H,  $\text{H}_{\text{Ar}}$ ), 6.67 (d,  $J$  = 8.7 Hz, 2H,  $\text{H}_{\text{Ar}}$ ), 6.56 (m, 1H), 6.49 (m, 1H), 6.45 (s, 1H), 4.60-4.59 (m, 6H), 4.48-4.43 (m, 6H), 4.03 (t,  $J$  = 5.7 Hz, 4H,  $\text{OCH}_2$ ), 3.72-3.69 (m, 2H), 3.61-3.59 (m, 2H), 3.41 (s, 2H,  $\text{CH}_2\text{Br}$ ), 3.37-3.32 (m, 4H,  $\text{CH}_2$ ), 3.03 (s, 3H,  $\text{NCH}_3$ ), 2.67 (s, 6H,  $2 \times \text{CH}_3$ ), 2.13 (s, 6H,  $2 \times \text{CH}_3$ ), 1.87-1.81 (m, 8H,  $\text{CH}_2$ ), 1.35 (s, 9H, *t*-Bu, DCM) ppm.  $^{13}\text{C}$  NMR (100 MHz,  $\text{CDCl}_3$ ):  $\delta$  = 171.98, 167.27, 164.14, 160.40, 150.93, 148.12, 147.57, 144.49, 143.40, 139.30 ( $\text{C}_q$ ); 138.52 ( $\text{CH}=\text{}$ ); 135.80, 133.57, 131.61 ( $\text{C}_q$ ); 130.47, 129.91, 129.58, 129.13, 127.98, 126.81, 126.68, 124.28, 122.96, 114.87, 112.96, 112.02, 105.54, 102.48 ( $\text{CH}=\text{}$ ); 68.87, 67.85, 67.22, 64.84, 64.63, 52.09, 50.35, 50.14 ( $\text{CH}_2$ ); 44.92, 41.47 ( $\text{C}_q$ ); 39.26 ( $\text{CH}_3$ ); 36.74 ( $\text{C}_q$ ); 34.73, 32.06, 29.83, 29.19 ( $\text{CH}_2$ ); 28.26 ( $\text{CH}_3$ ), 27.34, 26.30 ( $\text{CH}_2$ ); 22.76 ( $\text{CH}_3$ ); 20.57, 19.57, 14.26 ( $\text{C}_q$ ); 13.21, 12.44 ( $\text{CH}_3$ ); 11.57 ( $\text{C}_q$ ) ppm.

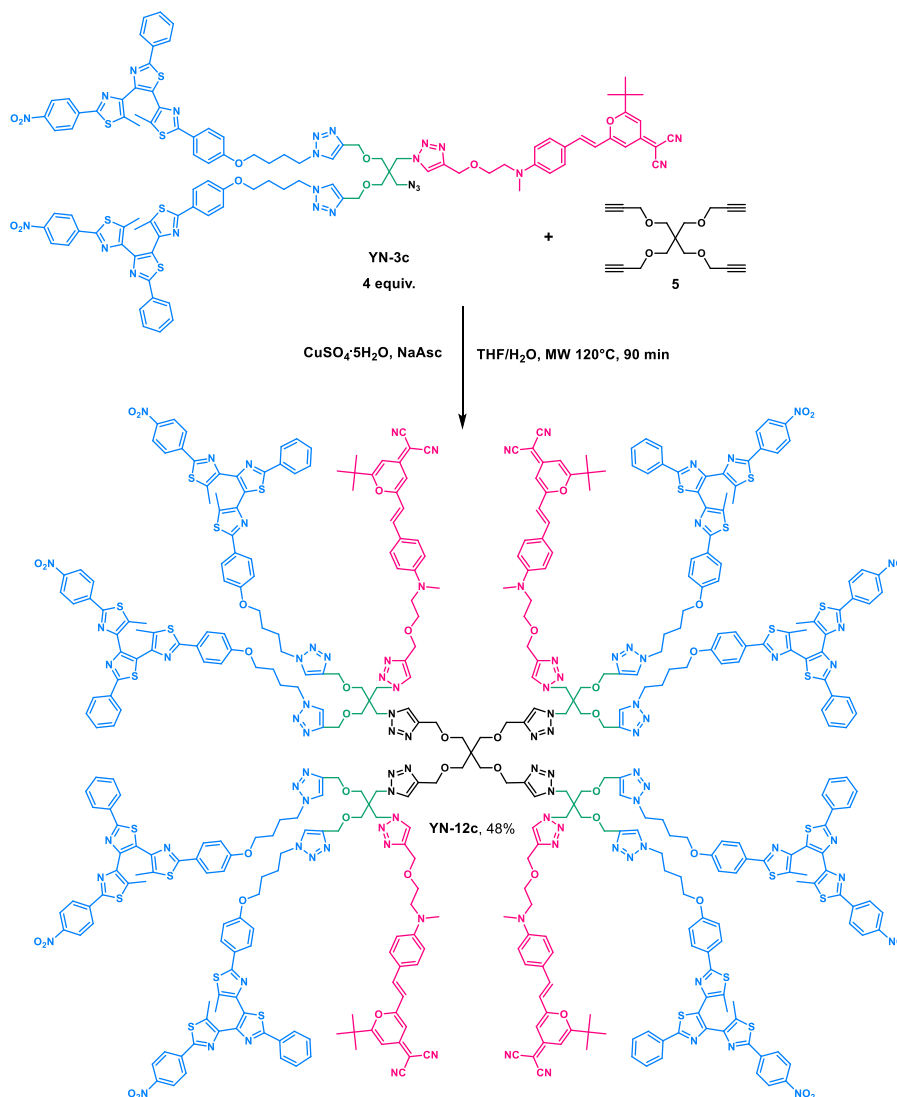
YN-3c



Scheme 33: Synthesis of **YN-3c**.

To a solution of compound **34** (56 mg, 27  $\mu\text{mol}$ ) in DMF (10 mL), NaI (0.1 equiv.) and  $\text{NaN}_3$  (8 equiv.) were added. The reaction mixture was heated up to  $80^\circ\text{C}$  and kept for 72 hours. After concentration, the residue was diluted in EtOAc (20 mL), washed successively with water and brine, dried over  $\text{MgSO}_4$ , concentrated and purified by CombiFlash<sup>®</sup> chromatography with dichloromethane and ethanol (gradient, 100:0 to 90:10, v/v). After The crude was purified by CombiFlash<sup>®</sup> chromatography with an eluent of dichloromethane and ethanol (gradient, 95:5, v/v) to yield **YN-3c** as a red solid (50 mg, 91%).  $^1\text{H NMR}$  (400 MHz,  $\text{CDCl}_3$ ):  $\delta$  = 8.13-8.10 (m, 4H,  $\text{H}_{\text{Ar}}$ ), 8.05-8.02 (m, 4H,  $\text{H}_{\text{Ar}}$ ), 7.87-7.81 (m, 8H,  $\text{H}_{\text{Ar}}$ ), 7.66 (s, 1H, triazole-H), 7.63 (s, 2H, triazole-H), 7.48-7.45 (m, 6H,  $\text{H}_{\text{Ar}}$ ), 7.38 (d,  $J$  = 8.7 Hz, 2H), 7.32-7.26 (m, 1H), 6.89 (d,  $J$  = 8.7 Hz, 4H,  $\text{H}_{\text{Ar}}$ ), 6.66 (d,  $J$  = 8.7 Hz, 2H,  $\text{H}_{\text{Ar}}$ ), 6.55 (d,  $J$  = 1.8 Hz, 1H), 6.48 (d,  $J$  = 2.3 Hz, 1H), 6.44 (s, 1H), 4.60-4.59 (m, 6H), 4.47-4.42 (m, 6H), 4.02 (t,  $J$  = 5.7 Hz, 4H,  $\text{OCH}_2$ ), 3.71-3.68 (m, 2H), 3.60-3.58 (m, 2H), 3.41 (s, 2H,  $\text{CH}_2\text{Br}$ ), 3.36-3.31 (m, 4H), 3.02 (s, 3H,  $\text{NCH}_3$ ), 2.66 (s, 6H,  $2\times\text{CH}_3$ ), 2.12 (s, 6H,  $2\times\text{CH}_3$ ), 1.86-1.80 (m, 8H), 1.34 (s, 9H, *t*-Bu, DCM) ppm.  $^{13}\text{C NMR}$  (100 MHz,  $\text{CDCl}_3$ ):  $\delta$  = 172.01, 167.31, 160.36, 156.97, 148.11, 147.52, 144.39, 143.39, 142.26, 139.31 ( $\text{C}_q$ ); 138.50 ( $\text{CH=}$ ); 135.82, 133.55, 131.67 ( $\text{C}_q$ ); 130.50, 129.90, 129.14, 128.01, 126.83, 126.70, 124.88, 124.30, 122.61 ( $\text{CH=}$ ); 115.97, 115.90 ( $\text{C}_q$ ); 114.86, 112.99, 112.04, 105.59, 102.50 ( $\text{CH=}$ ); 69.36, 67.88, 67.19, 64.69, 64.55, 61.85, 52.12, 51.38, 49.37 ( $\text{CH}_2$ ); 45.84, 39.30, 36.76 ( $\text{C}_q$ ); 28.27, 27.33, 26.27 ( $\text{CH}_3$ ); 23.97, 20.92, 17.64 ( $\text{C}_q$ ); 13.24, 12.46 ( $\text{CH}_3$ ); ppm. HRMS (ESI-HRMS):  $m/z$  [ $\text{M}+\text{Na}$ ]<sup>+</sup> calcd. for  $[\text{C}_{103}\text{H}_{95}\text{N}_{23}\text{NaO}_{10}\text{S}_6]^+$ : 2028.5849; found 2028.5775.

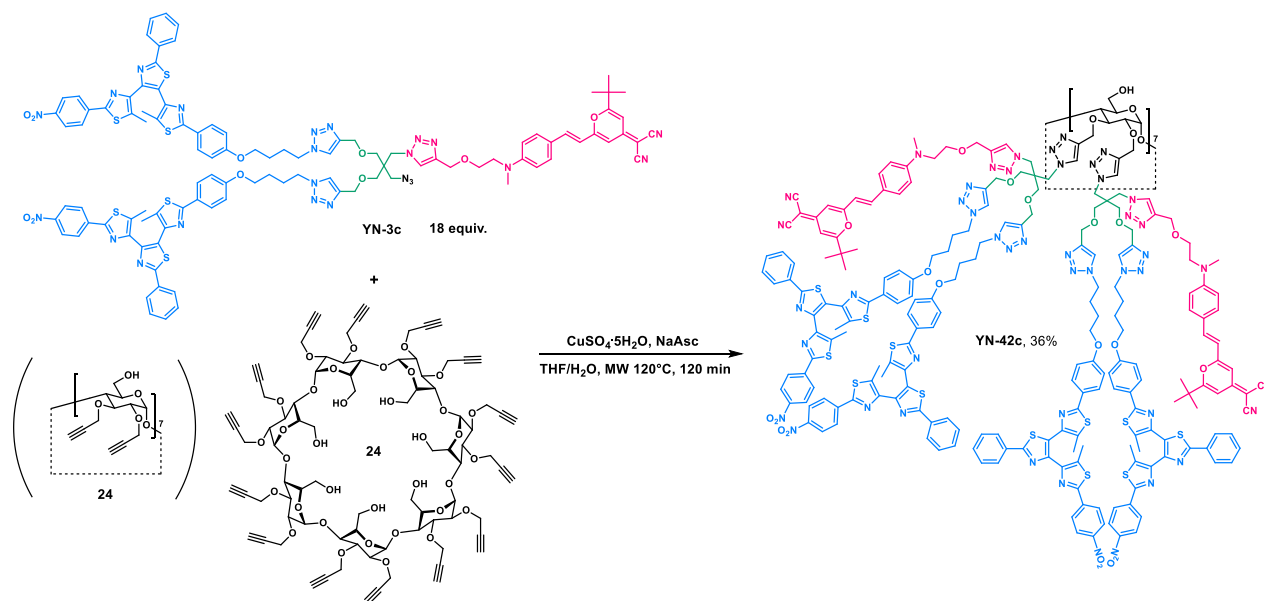
## 5.1.2.6 YN-12c



Scheme 34: Synthesis of YN-12c.

Compound **5** (1 mg, 0.04 mmol), **YN-3c** (4 equiv., 35 mg),  $\text{CuSO}_4 \cdot 5\text{H}_2\text{O}$  (7 equiv.) and sodium ascorbate (14 equiv.) were added together in a mixed solvent THF/H<sub>2</sub>O (3 mL, 2:1, v/v) to a microwave reactor tube. The reaction mixture was kept irradiated with microwave, holding at 120°C for 90 minutes. After that the reaction mixture was added ammonium solution, sonicating until all the solid dissolved. The reaction mixture was extracted with dichloromethane (30 mL) for 3 times. The organic layer was washed with brine, dried over  $\text{MgSO}_4$ , concentrated, then purified with CombiFlash® chromatography with dichloromethane and methanol (gradient, 100:0 to 95:5, v/v) as eluent to afford **YN-12c** as a red solid (17 mg, 48%).

## 5.1.2.7 YN-42c



Compound **24** (1.5 mg, 0.04 mmol), **YN-3c** (18 equiv., 32.5 mg),  $\text{CuSO}_4 \cdot 5\text{H}_2\text{O}$  (7 equiv.) and sodium ascorbate (14 equiv.) were added together in a mixed solvent THF/ $\text{H}_2\text{O}$  (3 mL, 2:1, v/v) to a microwave reactor tube. The reaction mixture was kept irradiated with microwave, holding at  $120^\circ\text{C}$  for 90 minutes. After that the reaction mixture was added ammonium solution, sonicating until all the solid dissolved. The reaction mixture was extracted with dichloromethane (30 mL) for 3 times. The organic layer was washed with brine, dried over  $\text{MgSO}_4$ , concentrated, then purified with CombiFlash<sup>®</sup> chromatography with dichloromethane and methanol (gradient, 100:0 to 95:5, v/v) as eluent to afford **YN-42c** as a red solid (12.5 mg, 37%).

## Reference

1. Y. Yu, N. Bogliotti, S. Maisonneuve, J. Tang and J. Xie, *Tetrahedron Lett.*, 2013, **54**, 1877-1883.
2. K. Ouhenia-Ouadahi, R. Métivier, S. Maisonneuve, A. Jacquart, J. Xie, A. Léaustic, P. Yu and K. Nakatani, *Photochem. Photobiol. Sci.*, 2012, **11**, 1705-1714.
3. L. Casimiro, S. Maisonneuve, P. Retailleau, S. Silvi, J. Xie and R. Métivier, *Chem. Eur. J.*, 2020, **26**, 14256-14256.
4. C. De Schutter, V. Roy, P. Favetta, C. Pavageau, S. Maisonneuve, N. Bogliotti, J. Xie and L. A. Agrofoglio, *Org. Biomol. Chem.*, 2018, **16**, 6552-6563.
5. D. Athanasiou, M. Aguila, J. Bellingham, W. Li, C. McCulley, P. J. Reeves and M. E. Cheetham, *Prog. Retin. Eye Res.*, 2018, **62**, 1-23.
6. K. D. Ridge and K. Palczewski, *J. Biol. Chem.*, 2007, **282**, 9297-9301.
7. H. Kamel, Vivo S10's Photochromic Rear Panel Enables For Interesting But Temporary Cover Designs, <https://www.lowyat.net/2021/246462/vivo-s10s-photochromic-rear-panel-enables-for-interesting-but-temporary-cover-designs/>.
8. Brahomos, Photochromic lenses, <https://brahmosindia.com/how-to-choose-adaptive-or-photochromic-lenses/>.
9. D. J. Wales, Q. Cao, K. Kastner, E. Karjalainen, G. N. Newton and V. Sans, *Adv. Mater.*, 2018, **30**, 1800159.
10. A. Dvornikov and P. Rentzepis, *Mol. Cryst. Liq. Cryst. Sci. Tech. Section A.*, 1994, **246**, 379-388.
11. C. C. Corredor, Z.-L. Huang, K. D. Belfield, A. R. Morales and M. V. Bondar, *Chem. Mater.*, 2007, **19**, 5165-5173.
12. M. Cacciarini, A. B. Skov, M. Jevric, A. S. Hansen, J. Elm, H. G. Kjaergaard, K. V. Mikkelsen and M. Brøndsted Nielsen, *Chem. Eur. J.*, 2015, **21**, 7454-7461.
13. X. Yao, T. Li, J. Wang, X. Ma and H. Tian, *Advanced Optical Materials*, 2016, **4**, 1322-1349.
14. J. Buback, M. Kullmann, F. Langhojer, P. Nuernberger, R. Schmidt, F. Würthner and T. Brixner, *J. Am. Chem. Soc.*, 2010, **132**, 16510-16519.
15. R. Klajn, *Chem. Soc. Rev.*, 2014, **43**, 148-184.
16. L. Kortekaas and W. R. Browne, *Chem. Soc. Rev.*, 2019, **48**, 3406-3424.
17. M. Irie, S. Kobatake and M. Horichi, *Science*, 2001, **291**, 1769-1772.
18. M. Irie, *Proc Jpn Acad Ser B Phys Biol Sci*, 2010, **86**, 472-483.
19. K. Amimoto and T. Kawato, *J. Photochem. Photobiol. C: Photochem. Rev.*, 2005, **6**, 207-226.
20. M. Irie, T. Fukaminato, K. Matsuda and S. Kobatake, *Chem. Rev.*, 2014, **114**, 12174-12277.
21. J. Calbo, A. R. Thawani, R. S. Gibson, A. J. White and M. J. Fuchter, *Beilstein J. Org. Chem.*, 2019, **15**, 2753-2764.
22. V. Marturano, V. Ambrogi, N. A. G. Bandeira, B. Tylkowski, M. Giamberini and P. Cerruti, *Phys. Sci. Rev.*, 2017, **2**.
23. S. Helmy, F. A. Leibfarth, S. Oh, J. E. Poelma, C. J. Hawker and J. Read de Alaniz, *J. Am. Chem. Soc.*, 2014, **136**, 8169-8172.
24. J. R. Hemmer, Z. A. Page, K. D. Clark, F. Stricker, N. D. Dolinski, C. J. Hawker and J. Read de Alaniz, *J. Am. Chem. Soc.*, 2018, **140**, 10425-10429.
25. J. E. Yap, L. Zhang, J. T. Lovegrove, J. E. Beves and M. H. Stenzel, *Macromol. Rapid Commun.*, 2020, **41**, 2000236.
26. S. O. Poelma, S. S. Oh, S. Helmy, A. S. Knight, G. L. Burnett, H. T. Soh, C. J. Hawker and J. Read de Alaniz, *Chem. Commun.*, 2016, **52**, 10525-10528.
27. B. Valeur and M. N. Berberan-Santos, *Molecular fluorescence: principles and applications*, John Wiley & Sons, 2012.
28. Y. Osakada, L. Hanson and B. Cui, *Chem. Commun.*, 2012, **48**, 3285-3287.
29. O. Nevskiy, D. Sysoiev, A. Oppermann, T. Huhn and D. Wöll, *Angew. Chem. Int. Ed.*, 2016, **55**, 12698-12702.
30. T. Fukaminato, S. Ishida and R. Métivier, *NPG Asia Mater.*, 2018, **10**, 859-881.

31. K. Uno, H. Niikura, M. Morimoto, Y. Ishibashi, H. Miyasaka and M. Irie, *J. Am. Chem. Soc.*, 2011, **133**, 13558-13564.
32. E. Barrez, G. Laurent, C. Pavageau, M. Sliwa and R. Métivier, *Phys. Chem. Chem. Phys.*, 2018, **20**, 2470-2479.
33. J. Su, T. Fukaminato, J.-P. Placiat, T. Onodera, R. Suzuki, H. Oikawa, A. Brosseau, F. Brisset, R. Pansu, K. Nakatani and R. Métivier, *Angew. Chem. Int. Ed.*, 2016, **55**, 3662-3666.
34. Y. Kim, H.-y. Jung, Y. H. Choe, C. Lee, S.-K. Ko, S. Koun, Y. Choi, B. H. Chung, B. C. Park, T.-L. Huh, I. Shin and E. Kim, *Angew. Chem. Int. Ed.*, 2012, **51**, 2878-2882.
35. P.-R. Hammond, *Opt. Commun.*, 1979, **29**, 331-333.
36. E. Marason, *Opt. Commun.*, 1981, **37**, 56-58.
37. J.-C. Mialocq and M. Meyer, *Laser Chem.*, 1990, **10**, 277-296.
38. J. Mialocq, X. Armand and S. Marguet, *J. Photochem. Photobiol. A: Chem.*, 1993, **69**, 351-356.
39. M.-k. Leung, C.-C. Chang, M.-H. Wu, K.-H. Chuang, J.-H. Lee, S.-J. Shieh, S.-C. Lin and C.-F. Chiu, *Org. Lett.*, 2006, **8**, 2623-2626.
40. Y. S. Yao, J. Xiao, X. S. Wang, Z. B. Deng and B. W. Zhang, *Adv. Funct. Mater.*, 2006, **16**, 709-718.
41. H. J. Yun, D. Y. Jung, D. K. Lee, A. K. Y. Jen and J. H. Kim, *Dyes Pigm.*, 2015, **113**, 675-681.
42. S. Hashimoto, R. Takagi, K. Okamura, A. Yabushita, T. Kobayashi and I. Iwakura, *Chem. Phys.*, 2021, **551**, 111326.
43. I. D. Petsalakis, D. G. Georgiadou, M. Vasilopoulou, G. Pistolis, D. Dimotikali, P. Argitis and G. Theodorakopoulos, *J. Phys. Chem. A*, 2010, **114**, 5580-5587.
44. P. Chatterjee, S. S. Dutta and T. Chakraborty, *J. Phys. Chem. B*, 2020, **124**, 4498-4511.
45. H. van Amerongen and R. Croce, *Photosynth. Res.*, 2013, **116**, 251-263.
46. P. Qian, D. J. K. Swainsbury, T. I. Croll, P. Castro-Hartmann, G. Divitini, K. Sader and C. N. Hunter, *Biochemistry*, 2021, **60**, 3302-3314.
47. A. P. Kulkarni, X. Kong and S. A. Jenekhe, *Macromolecules*, 2006, **39**, 8699-8711.
48. L. J. Patalag, J. Hoche, M. Holzapfel, A. Schmiedel, R. Mitric, C. Lambert and D. B. Werz, *J. Am. Chem. Soc.*, 2021, **143**, 7414-7425.
49. J. Pruchyathamkorn, W. J. Kendrick, A. T. Frawley, A. Mattioni, F. Caycedo-Soler, S. F. Huelga, M. B. Plenio and H. L. Anderson, *Angew. Chem. Int. Ed.*, 2020, **59**, 16455-16458.
50. P. Bonaccorsi, T. Papalia, A. Barattucci, T. M. G. Salerno, C. Rosano, P. Castagnola, M. Viale, M. Monticone, S. Campagna and F. Puntoriero, *Dalton Trans.*, 2018, **47**, 4733-4738.
51. F. M. Jradi, D. O'Neil, X. Kang, J. Wong, P. Szymanski, T. C. Parker, H. L. Anderson, M. A. El-Sayed and S. R. Marder, *Chem. Mater.*, 2015, **27**, 6305-6313.
52. D. K. Panda, F. S. Goodson, S. Ray and S. Saha, *Chem. Commun.*, 2014, **50**, 5358-5360.
53. V. Balzani, P. Ceroni, M. Maestri and V. Vicinelli, *Curr. Opin. Chem. Biol.*, 2003, **7**, 657-665.
54. I. Oh, H. Lee, T. W. Kim, C. W. Kim, S. Jun, C. Kim, E. H. Choi, Y. M. Rhee, J. Kim, W.-D. Jang and H. Ihee, *Adv. Sci.*, 2020, **7**, 2001623.
55. S. Nakazato, T. Takizawa and T. Arai, *Photochem. Photobiol. Sci.*, 2012, **11**, 885-888.
56. A. Momotake and T. Arai, *Polymer*, 2004, **45**, 5369-5390.
57. T. Mizutani, M. Ikegami, R. Nagahata and T. Arai, *Chem. Lett.*, 2001, **30**, 1014-1015.
58. A. Archut, G. C. Azzellini, V. Balzani, L. De Cola and F. Vögtle, *J. Am. Chem. Soc.*, 1998, **120**, 12187-12191.
59. J. Bahrenburg, C. M. Sievers, J. B. Schönborn, B. Hartke, F. Renth, F. Temps, C. Näther and F. D. Sönnichsen, *Photochem. Photobiol. Sci.*, 2013, **12**, 511-518.
60. M. Baroncini, S. d'Agostino, G. Bergamini, P. Ceroni, A. Comotti, P. Sozzani, I. Bassanetti, F. Grepioni, T. M. Hernandez, S. Silvi, M. Venturi and A. Credi, *Nat. Chem.*, 2015, **7**, 634-640.
61. A. Fihey, A. Perrier, W. R. Browne and D. Jacquemin, *Chem. Soc. Rev.*, 2015, **44**, 3719-3759.
62. F. G. Erko, L. Cseh, J. Berthet, G. H. Mehl and S. Delbaere, *Dyes Pigm.*, 2015, **115**, 102-109.
63. C. A. P. Goodwin, F. Ortu, D. Reta, N. F. Chilton and D. P. Mills, *Nature*, 2017, **548**, 439-442.
64. S. Valadkhan, K. Morris and A. Khajepour, *J. Intell. Mater. Syst. Struct.*, 2008, **20**, 131-142.
65. N. Balke, S. Jesse, Q. Li, P. Maksymovych, M. Baris Okatan, E. Strelcov, A. Tselev and S. V. Kalinin, *J. Appl. Phys.*, 2015, **118**, 072013.
66. N. Vaiana, S. Sessa and L. Rosati, *Mechanical Systems and Signal Processing*, 2021, **146**, 106984.



67. C. G. Burgess, D. H. Everett and S. Nuttall, *Pure Appl. Chem.*, 1989, **61**, 1845-1852.
68. A. V. Neimark, P. I. Ravikovitch and A. Vishnyakov, *Phys. Rev. E*, 2000, **62**, R1493.
69. S. Rodriguez, W. Casteels, F. Storme, N. C. Zambon, I. Sagnes, L. Le Gratiet, E. Galopin, A. Lemaître, A. Amo and C. Ciuti, *Phys. Rev. Lett.*, 2017, **118**, 247402.
70. A. Malyshev and V. Malyshev, *Phys. Rev. B*, 2011, **84**, 035314.
71. S. Imam, T. Deshpande, A. Guermoune, M. Sijaj and T. Szkopek, *Appl. Phys. Lett.*, 2011, **99**, 082109.
72. G. Assat, S. L. Glazier, C. Delacourt and J.-M. Tarascon, *Nat. Energy*, 2019, **4**, 647-656.
73. X. Zhao, B. Xiao, A. J. Fletcher, K. M. Thomas, D. Bradshaw and M. J. Rosseinsky, *Science*, 2004, **306**, 1012-1015.
74. R. Sessoli, D. Gatteschi, A. Caneschi and M. Novak, *Nature*, 1993, **365**, 141-143.
75. J. R. Pomeroy, E. D. Sontag and J. E. Ferrell, *Nat. Cell Biol.*, 2003, **5**, 346-351.
76. P. R. Hania, D. Thomsson and I. G. Scheblykin, *J. Phys. Chem. B*, 2006, **110**, 25895-25900.
77. H. Zhou, C. Qin, R. Chen, G. Zhang, L. Xiao and S. Jia, *Appl. Phys. Lett.*, 2014, **105**, 158\_151.
78. S. Maisonneuve, R. Métivier, P. Yu, K. Nakatani and J. Xie, *Beilstein J. Org. Chem.*, 2014, **10**, 1471-1481.
79. S. Maisonneuve, Thèse de l'ENS de Cachan, 2016.
80. M. Malkoch and S. G. Gallego, *Dendrimer Chemistry: Synthetic approaches towards complex architectures*, Royal Society of Chemistry, 2020.
81. R. Roy and M. Touaibia, *Comprehensive Glycoscience*, 2007, 821.
82. D. A. Tomalia, *Prog. Polym. Sci.*, 2005, **30**, 294-324.
83. D. A. Tomalia and J. M. Fréchet, *J. Polym. Sci., Part A: Polym. Chem.*, 2002, **40**, 2719-2728.
84. D. A. Tomalia, J. B. Christensen and U. Boas, *Dendrimers, dendrons, and dendritic polymers: discovery, applications, and the future*, Cambridge University Press, 2012.
85. M. Malkoch and S. García-Gallego, 2020.
86. M. Arseneault, C. Wafer and J.-F. Morin, *Molecules*, 2015, **20**, 9263-9294.
87. D. Astruc, E. Boisselier and C. Ornelas, *Chem. Rev.*, 2010, **110**, 1857-1959.
88. E. Abbasi, S. F. Aval, A. Akbarzadeh, M. Milani, H. T. Nasrabadi, S. W. Joo, Y. Hanifehpour, K. Nejati-Koshki and R. Pashaei-Asl, *Nanoscale Res. Lett.*, 2014, **9**, 247.
89. H. C. Kolb, M. Finn and K. B. Sharpless, *Angew. Chem. Int. Ed.*, 2001, **40**, 2004-2021.
90. B. Worrell, J. Malik and V. Fokin, *Science*, 2013, **340**, 457-460.
91. F. Himo, T. Lovell, R. Hilgraf, V. V. Rostovtsev, L. Noodleman, K. B. Sharpless and V. V. Fokin, *J. Am. Chem. Soc.*, 2005, **127**, 210-216.
92. O. David, S. Maisonneuve and J. Xie, *Tetrahedron Lett.*, 2007, **48**, 6527-6530.
93. S. Maisonneuve, Q. Fang and J. Xie, *Tetrahedron*, 2008, **64**, 8716-8720.
94. R. Métivier, I. Leray and B. Valeur, *Photochem. Photobiol. Sci.*, 2004, **3**, 374-380.
95. A. K. Agrahari, P. Bose, M. K. Jaiswal, S. Rajkhowa, A. S. Singh, S. Hotha, N. Mishra and V. K. Tiwari, *Chem. Rev.*, 2021, **121**, 7638-7956.
96. V. K. Tiwari, B. B. Mishra, K. B. Mishra, N. Mishra, A. S. Singh and X. Chen, *Chem. Rev.*, 2016, **116**, 3086-3240.
97. A. Joosten, J. P. Schneider, M. L. Lepage, C. Tarnus, A. Bodlenner and P. Compain, *Eur. J. Org. Chem.*, 2014, **2014**, 1866-1872.
98. R. Zhao, B. Li, Y. Wang and W. Hu, *Sensors*, 2018, **18**, 1134.
99. A. Tafrioucht, J. Rabah, K. Baczko, H. Fensterbank, R. Méallet-Renault, G. Clavier, F. Couty, E. Allard and K. Wright, *Dyes Pigm.*, 2021, **186**, 109031.
100. D. Bléger and S. Hecht, *Angew. Chem. Int. Ed.*, 2015, **54**, 11338-11349.
101. M. Baroncini, M. Canton, L. Casimiro, S. Corra, J. Groppi, M. La Rosa, S. Silvi and A. Credi, *Eur. J. Inorg. Chem.*, 2018, **2018**, 4589-4603.
102. D. Roke, S. J. Wezenberg and B. L. Feringa, *Proc. Natl. Acad. Sci.*, 2018, **115**, 9423-9431.
103. C. T. Kornman, L. Li, A. O. Weldeab, I. Ghiviriga, K. A. Abboud and R. K. Castellano, *Chem. Sci.*, 2020, **11**, 10190-10197.
104. F. Castiglioni, W. Danowski, J. Perego, F. K.-C. Leung, P. Sozzani, S. Bracco, S. J. Wezenberg, A. Comotti and B. L. Feringa, *Nat. Chem.*, 2020, **12**, 595-602.
105. S. L. Oscurato, M. Salvatore, P. Maddalena and A. Ambrosio, *Nanophotonics*, 2018, **7**, 1387-1422.

106. G. Das, T. Prakasam, M. A. Addicoat, S. K. Sharma, F. Ravoux, R. Mathew, M. Baias, R. Jagannathan, M. A. Olson and A. Trabolsi, *J. Am. Chem. Soc.*, 2019, **141**, 19078-19087.
107. K. Müller, A. Knebel, F. Zhao, D. Bléger, J. Caro and L. Heinke, *Chem. Eur. J.*, 2017, **23**, 5434-5438.
108. P. M. Toro, D. H. Jara, A. H. Klahn, D. Villaman, M. Fuentealba, A. Vega and N. Pizarro, *Photochem. Photobiol.*, 2021, **97**, 61-70.
109. B. Bai, M. Zhang, N. Ji, J. Wei, H. Wang and M. Li, *Chem. Commun.*, 2017, **53**, 2693-2696.
110. H. Karimi-Alavijeh, F. Panahi and A. Gharavi, *J. Appl. Phys.*, 2014, **115**, 093706.
111. M.-k. Leung, C.-C. Chang, M.-H. Wu, K.-H. Chuang, J.-H. Lee, S.-J. Shieh, S.-C. Lin and C.-F. Chiu, *Org. Lett.*, 2006, **8**, 2623-2626.
112. J. Y. Kim, S. S. Yoon and Y. S. Kim, *J. Nanosci. Nanotech.*, 2014, **14**, 5203-5206.
113. Z. Guo, W. Zhu and H. Tian, *Chem. Commun.*, 2012, **48**, 6073-6084.
114. M. Meyer, J. Mialocq and M. Rougee, *Chem. Phys. Lett.*, 1988, **150**, 484-490.
115. M. Meyer, J. C. Mialocq and B. Perly, *J. Phys. Chem.*, 1990, **94**, 98-104.
116. W. Rettig and W. Majenz, *Chem. Phys. Lett.*, 1989, **154**, 335-341.
117. J. Drake, M. L. Lesiecki and D. M. Camaioni, *Chem. Phys. Lett.*, 1985, **113**, 530-534.
118. M. Lesiecki, F. Asmar, J. Drake and D. M. Camaioni, *J. Lumin.*, 1984, **31**, 546-548.
119. X. Xu, R. Zhang, Z. Cao and Q. Zhang, *J. Theor. Comput. Chem.*, 2008, **7**, 719-736.
120. S. H. Nabavi, M. H. Khodabandeh, M. Golbabaee and A. Moshaii, *Int. J. Opt. Photon.*, 2018, **12**, 43-56.
121. B. Mennucci, *Int. J. Quantum Chem*, 2015, **115**, 1202-1208.
122. N. Minezawa and M. S. Gordon, *J. Phys. Chem. A*, 2011, **115**, 7901-7911.
123. Y. A. Bernard, Y. Shao and A. I. Krylov, *J. Chem. Phys.*, 2012, **136**, 204103.
124. N. Minezawa and M. S. Gordon, *J. Phys. Chem. A*, 2009, **113**, 12749-12753.
125. B. G. Levine, J. D. Coe and T. J. Martínez, *J. Phys. Chem. B*, 2008, **112**, 405-413.
126. M. Boggio-Pasqua, HDR de l'Université Toulouse III, 2015.
127. N. H. List, C. M. Jones and T. J. Martínez, *Chem. Sci.*, 2022, **13**, 373-385.
128. A. Toniolo, G. Granucci and T. J. Martínez, *J. Phys. Chem. A*, 2003, **107**, 3822-3830.
129. F. Lumento, V. Zanirato, S. Fusi, E. Busi, L. Latterini, F. Elisei, A. Sinicropi, T. Andruniów, N. Ferré, R. Basosi and M. Olivucci, *Angew. Chem. Int. Ed.*, 2007, **46**, 414-420.
130. B. Tollens and P. Wigand, *Justus Liebigs Annalen der Chemie*, 1891, **265**, 316-340.
131. M. Salkind, H. F. Ahern and A. A. Albert, *Ind. Eng. Chem.*, 1958, **50**, 1106-1114.
132. J. Liu, in *Nitrate Esters Chemistry and Technology*, ed. J. Liu, Springer Singapore, Singapore, 2019, DOI: 10.1007/978-981-13-6647-5\_7, pp. 341-375.
133. J. C. Parker, F. J. Di Carlo and I. W. Davidson, *Eur. J. Pharmacol.*, 1975, **31**, 29-37.
134. P. Kardar, M. Ebrahimi and S. Bastani, *Pigm. Resin Tech.*, 2014.
135. J. A. Payne, L. F. Francis and A. V. McCormick, *J. Appl. Polym. Sci.*, 1997, **66**, 1267-1277.
136. C. Sehad, T. C. Shiao, L. M. Sallam, A. Azzouz and R. Roy, *Molecules*, 2018, **23**, 1890.
137. T. Lenz, T. M. Klapötke, M. Mühlemann and J. Stierstorfer, *Propellants, Explosives, Pyrotechnics*, 2021, **46**, 723-731.
138. G. R. Newkome and C. Shreiner, *Chem. Rev.*, 2010, **110**, 6338-6442.
139. A. Mollard and I. Zharov, *Inorg. Chem.*, 2006, **45**, 10172-10179.
140. A. Chen, D. Wang, J. Bietsch and G. Wang, *Org. Biomol. Chem.*, 2019, **17**, 6043-6056.
141. M. C. Murguia, S. E. Vaillard and R. J. Grau, *Synthesis*, 2001, **2001**, 1093-1097.
142. J. Szejtli, *Chem. Rev.*, 1998, **98**, 1743-1754.
143. G. Crini, *Chem. Rev.*, 2014, **114**, 10940-10975.
144. C. O. Mellet, J. M. G. Fernández and J. M. Benito, *Chem. Soc. Rev.*, 2011, **40**, 1586-1608.
145. A. Martinez, C. Ortiz Mellet and J. M. Garcia Fernandez, *Chem. Soc. Rev.*, 2013, **42**, 4746-4773.
146. M. H. Asim, I. Nazir, A. Jalil, F. Laffleur, B. Matuszczak and A. Bernkop-Schnürch, *ACS Appl. Mater. Interfaces*, 2020, **12**, 7942-7950.
147. M. Hussain Asim, M. Ijaz, A. C. Rösch and A. Bernkop-Schnürch, *Coord. Chem. Rev.*, 2020, **420**, 213433.
148. W. Tang and S.-C. Ng, *Nature Protocols*, 2008, **3**, 691-697.

149. P. R. Ashton, R. Königer, J. F. Stoddart, D. Alker and V. D. Harding, *J. Org. Chem.*, 1996, **61**, 903-908.
150. M. Ortega-Munoz, J. Morales-Sanfrutos, F. Perez-Balderas, F. Hernandez-Mateo, M. D. Giron-Gonzalez, N. Sevillano-Tripero, R. Salto-Gonzalez and F. Santoyo-Gonzalez, *Org. Biomol. Chem.*, 2007, **5**, 2291-2301.
151. J.-B. Jiao, G.-Z. Wang, X.-L. Hu, Y. Zang, S. Maisonneuve, A. C. Sedgwick, J. L. Sessler, J. Xie, J. Li and X.-P. He, *J. Am. Chem. Soc.*, 2019, **142**, 1925-1932.
152. J. Boger, R. J. Corcoran and J.-M. Lehn, *Helv. Chim. Acta*, 1978, **61**, 2190-2218.
153. X.-P. He, R.-H. Li, S. Maisonneuve, Y. Ruan, G.-R. Chen and J. Xie, *Chem. Commun.*, 2014, **50**, 14141-14144.
154. S. Ward and C.-C. Ling, *Eur. J. Org. Chem.*, 2011, **2011**, 4853-4861.
155. C. Decroocq, D. Rodríguez-Lucena, V. Russo, T. Mena Barragán, C. Ortiz Mellet and P. Compain, *Chem. Eur. J.*, 2011, **17**, 13825-13831.
156. C. Decroocq, A. Joosten, R. Sergent, T. Mena Barragán, C. Ortiz Mellet and P. Compain, *ChemBioChem*, 2013, **14**, 2038-2049.
157. F. Ortega-Caballero, J. J. Giménez-Martínez and A. Vargas-Berenguel, *Org. Lett.*, 2003, **5**, 2389-2392.
158. M. Gómez-García, J. M. Benito, D. Rodríguez-Lucena, J.-X. Yu, K. Chmurski, C. Ortiz Mellet, R. Gutiérrez Gallego, A. Maestre, J. Defaye and J. M. García Fernández, *J. Am. Chem. Soc.*, 2005, **127**, 7970-7971.
159. M. Gomez-Garcia, J. M. Benito, A. P. Butera, C. O. Mellet, J. M. G. a. Fernández and J. L. J. n. Blanco, *J. Org. Chem.*, 2012, **77**, 1273-1288.
160. M. Gómez-García, J. M. Benito, R. Gutiérrez-Gallego, A. Maestre, C. O. Mellet, J. M. G. Fernández and J. L. J. Blanco, *Org. Biomol. Chem.*, 2010, **8**, 1849-1860.
161. Z. Shariatnia, in *Modeling and Control of Drug Delivery Systems*, ed. A. T. Azar, Academic Press, 2021, DOI: <https://doi.org/10.1016/B978-0-12-821185-4.00013-0>, pp. 153-182.
162. D. Nguyen, L. Tao and Y. Li, *Front. Chem.*, 2022, **9**.
163. D. Nicolaidis, *Molecular Simulation*, 2001, **26**, 51-72.
164. J. M. Yeomans, *Phys. A: Stat. Mech. Appl.*, 2006, **369**, 159-184.
165. A. C. Van Duin, S. Dasgupta, F. Lorant and W. A. Goddard, *J. Phys. Chem. A*, 2001, **105**, 9396-9409.
166. J. Wang, R. M. Wolf, J. W. Caldwell, P. A. Kollman and D. A. Case, *J. Comput. Chem.*, 2004, **25**, 1157-1174.
167. C. W. Priest, J. A. Greathouse, M. K. Kinnan, P. D. Burton and S. B. Rempe, *J. Chem. Phys.*, 2021, **154**, 084503.
168. S.-L. J. Lahey, T. N. Thien Phuc and C. N. Rowley, *Journal of Chemical Information and Modeling*, 2020, **60**, 6258-6268.
169. C. Caleman, P. J. van Maaren, M. Hong, J. S. Hub, L. T. Costa and D. van der Spoel, *J. Chem. Theory Comput.*, 2012, **8**, 61-74.
170. X. Daura, K. Gademann, B. Jaun, D. Seebach, W. F. Van Gunsteren and A. E. Mark, *Angew. Chem. Int. Ed.*, 1999, **38**, 236-240.
171. H. Matt, Python: from None to Machine Learning, (<https://python.astrotech.io/machine-learning/model-quality/principal-component-analysis.html> ).
172. C. R. Schwantes, D. Shukla and V. S. Pande, *Biophys. J.*, 2016, **110**, 1716-1719.
173. U. Sengupta, M. Carballo-Pacheco and B. Strodel, *J. Chem. Phys.*, 2019, **150**, 115101.
174. H. Liu, H. Zhong, Z. Xu, Q. Zhang, S. J. A. Shah, H. Liu and X. Yao, *Phys. Chem. Chem. Phys.*, 2020, **22**, 10968-10980.
175. T. Hempel, L. Raich, S. Olsson, N. P. Azouz, A. M. Klingler, M. Hoffmann, S. Pöhlmann, M. E. Rothenberg and F. Noé, *Chem. Sci.*, 2021, **12**, 983-992.
176. B. E. Husic and V. S. Pande, *J. Am. Chem. Soc.*, 2018, **140**, 2386-2396.
177. F. Nuske, B. G. Keller, G. Pérez-Hernández, A. S. Mey and F. Noé, *J. Chem. Theory Comput.*, 2014, **10**, 1739-1752.
178. H. Wu and F. Noé, *J. Nonlinear Sci.*, 2020, **30**, 23-66.

179. M. K. Scherer, B. Trendelkamp-Schroer, F. Paul, G. Pérez-Hernández, M. Hoffmann, N. Plattner, C. Wehmeyer, J.-H. Prinz and F. Noé, *J. Chem. Theory Comput.*, 2015, **11**, 5525-5542.
180. G. Pérez-Hernández, F. Paul, T. Giorgino, G. D. Fabritiis and F. Noé, *J. Chem. Phys.*, 2013, **139**, 015102.
181. L. Molgedey and H. G. Schuster, *Phys. Rev. Lett.*, 1994, **72**, 3634.
182. C. R. Schwantes and V. S. Pande, *J. Chem. Theory Comput.*, 2013, **9**, 2000-2009.
183. S. Klus, F. Nüske, P. Koltai, H. Wu, I. Kevrekidis, C. Schütte and F. Noé, *J. Nonlinear Sci.*, 2018, **28**, 985-1010.
184. G. Pinamonti, J. Zhao, D. E. Condon, F. Paul, F. Noè, D. H. Turner and G. Bussi, *J. Chem. Theory Comput.*, 2017, **13**, 926-934.
185. J. Sponer, G. Bussi, M. Krepl, P. Banáš, S. Bottaro, R. A. Cunha, A. Gil-Ley, G. Pinamonti, S. Poblete and P. Jurečka, *Chem. Rev.*, 2018, **118**, 4177-4338.
186. D. Maffeo, M. Lampropoulou, M. Fardis, Y. G. Lazarou, I. M. Mavridis, D. A. I. Mavridou, E. Urso, H. Pratsinis, D. Kletsas and K. Yannakopoulou, *Org. Biomol. Chem.*, 2010, **8**, 1910-1921.
187. L. Chen, L.-F. Zhang, C.-B. Ching and S.-C. Ng, *J. Chromatogr. A*, 2002, **950**, 65-74.
188. H. T. Le, H. M. Jeon, C. W. Lim and T. W. Kim, *Carbohydr. Res.*, 2014, **391**, 22-28.
189. K. Matsuda and M. Irie, *J. Photochem. Photobiol. C: Photochem. Rev.*, 2004, **5**, 169-182.
190. H. Tian and S. Yang, *Chem. Soc. Rev.*, 2004, **33**, 85-97.
191. C. Yun, J. You, J. Kim, J. Huh and E. Kim, *J. Photochem. Photobiol. C: Photochem. Rev.*, 2009, **10**, 111-129.
192. M. Morimoto and M. Irie, *Chem. Commun.*, 2005, DOI: 10.1039/B505256D, 3895-3905.
193. V. O. Rodionov, V. V. Fokin and M. G. Finn, *Angew. Chem. Int. Ed.*, 2005, **44**, 2210-2215.
194. L. Martínez, R. Andrade, E. G. Birgin and J. M. Martínez, *J. Comput. Chem.*, 2009, **30**, 2157-2164.
195. R. Ribeiro-Viana, M. Sánchez-Navarro, J. Luczkowiak, J. R. Koepppe, R. Delgado, J. Rojo and B. G. Davis, *Nat. Commun.*, 2012, **3**, 1-9.